The University Of Sheffield.

Spark Plasma Sintering as a powder processing route for pre-alloyed $Sm_2(Co, Fe, Cu, Zr)_{17}$ permanent magnets

by:

Alexander J. Mackie

A thesis submitted in partial fulfilment of the requirements for the degree of Doctor of Philosophy

The University of Sheffield
Faculty of Engineering
Department of Materials Science and Engineering
United Kingdom

Submission date: 30th September 2018

Abstract

The 'rare earth crisis' that occurred in 2011 ignited research into mitigating and replacing the dependence on these elements in Rare Earth Permanent Magnets (REPM) and their applications. It is the former that this body of work is based upon. A method of increasing the bulk resistivity of a REPM, $Sm(Co, Fe, Cu, Zr)_{8.2}$ (henceforth referred to as $Sm_2(Co, Fe, Cu, Zr)_{17}$), through the addition of an electrically insulating material, CaF_2, to form a rare earth composite permanent magnet is studied. The aim of increasing the bulk resistivity is to minimise the irreversible demagnetisation and performance losses that occur within REPMs due to circulating eddy currents during operation of high frequency applications, such as electric motors and drives.

The project utilises an emerging sintering technology platform, Spark Plasma Sintering (SPS), to rapidly consolidate powders. The processing methodology for $Sm_2(Co, Fe, Cu, Zr)_{17}$ powders by the SPS technique has therefore been studied with the optimal processing parameters found for producing full dense specimens for study: 1050 °C to 1100 °C hold temperature, 100 °C/ min to 200 °C/ min heating rate, 51 MPa hold pressure and 5 minute hold time. $Sm_2(Co, Fe, Cu, Zr)_{17}$ permanent magnets require a characteristic multi-stage heat treatment to precipitate a cellular nanostructure which enhances the coercivity of the permanent magnets. The optimal heat treatment for the full density SPS processed $Sm_2(Co, Fe, Cu, Zr)_{17}$ magnets has also been studied, with the following achieving the largest coercivities and energy products:

1. Homogenisation - 1170 °C for 2 hours in an argon atmosphere. Cooled slowly in air to room temperature.

2. Ageing - 850 °C for 8 hours (for largest coercivity) or 16 hours (for largest $(BH)_{max}$) in argon atmosphere.

3. Slow cool (1 °C/min) from 850 °C to 400 °C in argon atmosphere. Quench in oil to room temperature.

This established processing route was then used to prototype isotropic $Sm_2(Co, Fe, Cu, Zr)_{17}$ and CaF_2 composite magnets and study the effect of the electrically insulating phase on the microstructure, and material and magnetic properties before and after heat treatment.

Acknowledgments

Five years. 1825 days. 43,800 hours (or thereabouts). There are many ways to describe how long it has taken to reach this destination, however it is with thanks to so many people that the journey was made (relatively!) light.

My two supervisors; Dr. Russell Goodall and Dr. Julian Dean, were always there to provide positive motivation and guide me along the way with their indispensable knowledge on metallurgy, magnetic materials and modelling. They were always able to make time to meet and on hand to read countless drafts, and their patience with me is commended! They have both been a great influence on me, developing my confidence and ability as a researcher and for that I am forever grateful.

The opportunity of a PhD would not have been afforded to me without the CDT Advanced Metallics Systems and therefore I owe many thanks to the academic members, project coordinators, and industrial partners who contributed to expanding my research, technical and professional skills. Special thanks must go to Dr. Claire Hinchliffe, who was at the center of it all.

The academic members of the University of Sheffield magnetic materials group also deserve a shout out. Prof. Dan Allwood, Dr. Tom Hayward, Dr. Nicola Morley and Dr. Rene Dost, all of whom were a pleasure to learn from and discuss research. I eventually grew to enjoy their probing questions when it was my turn to present at the weekly group meetings! Similar appreciation and thanks goes to everyone from J11 (and the magnetics lab from the early days), who could always be counted on when things got hectic and a trip to the Red Deer was needed. For the assistance and training provided, as well as general banter, I express gratitude to Mike Bell, Ben Palmer, Ian Woods, Kyle Arnold, Dr Lisa Hollands and Dr Cheryl Shaw, as well as my colleagues in the RADIUS research group.

Outside of research, I was able to learn so much about teaching as a GTA in the undergraduate teaching labs and am grateful to Dr. Julian Dean, Dr. Joanna Bates and the teaching staff for providing me the opportunity to take part.

To all my family and friends, l love you all. You were my biggest supporters, listening when I needed someone to listen and speaking when I needed someone to speak.

Lastly, my biggest thank-you goes to my girlfriend, Katie. I couldn't have done this without you. Your patience is immeasurable and you have always been there for me. You are a baller and I love you. Here's to the next chapter...

Publications

Two publications have been produced from the work of this project: the first resulted from the study of carbon contamination in SPS processed $Sm_2(Co, Fe, Cu, Zr)_{17}$ materials, and the second on the processing of $Sm_2(Co, Fe, Cu, Zr)_{17}$ powders by SPS, both of which their results are covered in detail in chapter 6. However, this serves as a reference to the publication:

Mackie, A. J., Hatton, G. D., Hamilton, H. G. C., Dean, J. S. & Goodall, R. "Carbon uptake and distribution in Spark Plasma Sintering (SPS) processed Sm(Co, Fe, Cu, Zr)z." Mater. Lett. 171, 14-17 (2016).

Mackie, A. J., Dean, J. S., and Goodall, R. “Material and magnetic properties of $Sm_2(Co, Fe, Cu, Zr)_{17}$ permanent magnets processed by Spark Plasma Sintering” J. Alloys Compd., vol. 770, pp. 765–770, (2019).

Contents

Acronyms

BS Back-Scattered.

DCEM Direct Current Electro-Magnet.

EDS Energy Dispersive (X-Ray) Spectroscopy.

EDX Energy Dispersive X-ray (Spectroscopy).

EPMA Electron Probe Micro-Analysis.

FD Finite Difference.

FE Finite Element.

FEM Finite Element Method.

FM Field's metal.

REE Rare Earth Element.

REPM Rare Earth Permanent Magnet.

SE Secondary Electron.

SEM Scanning Electron Microscopy.

SmCo Samarium Cobalt.

SPS Spark Plasma Sintering.

TM Transition Metal.

VDP Van Der Pauw.

WDS Wavelength Dispersive Spectroscopy.

XRD X-Ray Diffraction.

Nomenclature

$(BH)_{max}$	Energy product	J/m^3
2θ	Bragg diffraction angle	$^\circ$
α	Gilbert magnetic damping parameter	
$\bar{\theta}$	Average deviation angle	$^\circ$
χ	Susceptibility	
$\epsilon_{anisotropy}$	Micromagnetic anisotropy energy term	J/m^3
ϵ_{demag}	Micromagnetic demagnetisation energy term	J/m^3
$\epsilon_{exchange}$	Micromagnetic exchange energy term	J/m^3
ϵ_{Zeeman}	Micromagnetic Zeeman energy term	J/m^3
γ	Gyromagnetic ratio of the electron spin	rad/sT
λ	Wavelength	m
$\mathcal{N}_d$	Demagnetising factor	
μ	Permeability	H/m
∇	Del (gradient)	
Ψ	Magnetic scalar potential	
ρ	Bulk resistivity	$\mu\Omega \cdot cm$
$\vec{u_c}$	Crystal c-axis unit vector	
$\vec{u}(\vec{r}, t)$	Magnetisation unit vector	
a	Crystallite long axis diameter	μm
A_{ex}	Exchange stiffness	J/m

B	Magnetic induction or flux density	T
b	Crystallite short axis diameter	μm
bH_c	Coercive force	kA/m
D	Mass density	g/cm^3
E_t	Total free energy	J/m^3
f	VDP correction factor	
H	Magnetic field	kA/m
H_A	Anisotropy field	kA/m
H_d	Self-demagnetising field	kA/m
H_N	Nucleation field	kA/m
I	Electric current	A
iH_c	Intrinsic coercivity	kA/m
J	Polarisation. Equivalent to μ_0M	T
J_r	Remanent polarisation or remanence. Equivalent to M_r and B_r	
J_s	Saturation polarisation. Equivalent to $\mu_0 M_s$	T
J_r/J_{max}	Degree of alignment	
K_b	Boltzmann constant	$1.38 \times 10^{-23}\, m^2 kg/s^2 K$
K_1, K_2	Magneto-crystalline anisotropy constants	MJ/m^3
M	Magnetisation	kA/m
R	Resistance	Ω
T_c	Curie temperature	$^\circ C$
V	Potential difference	V
$vol.frac$	Volume fraction	
$wt.\%$	Weight percentage	%

Chapter 1

Introduction

Introduction

Rare earth permanent magnets (REPM) are essential components in a wide-range of every-day, industrial, and aerospace applications Such general examples include, but not limited to; electric motors/generators, actuators, sensors and computer hard-drives. The two most commonly used REPM materials are grouped into the Nd-Fe-B-type and Sm-Co-type permanent magnets. Both families of REPMs achieve the necessary magnetic and material properties required for high performance and demanding applications through interactions between the ferromagnetic transition metal elements (Fe and Co) and heavy rare-earth elements (REE) (Nd, Dy and Sm) [1]. Growth in the REPM market is ever increasing and expected to continue as demand for power generation and conversion grows globally [2, 3]. Leading up to 2011, violent fluctuations in the supply and pricing of the rare earth materials, which are primarily mined and processed in China, led to the 'rare earth crisis' [1, 3]. While pricing and supply of critical rare earth materials have since become manageable (as of 2017) [4], the 'rare earth crisis' instigated a significant shift in the focus of REPM research away from subtle microstructure optimisation and towards the mitigation of the REEs within permanent magnets, and ultimately aiming for rare earth-free permanent magnets. It is the philosophy of the former that this research project is based upon and in particular study is made of the $Sm_2(Co, Fe, Cu, Zr)_{17}$-type REPM.

Nd-Fe-B-type magnets have a much lower Curie temperature than $Sm_2(Co, Fe, Cu, Zr)_{17}$ permanent magnets and are generally more susceptible to temperature related degradation of magnetic properties [5]. Nd-Fe-B magnets can improve their resistance to temperature induced demagnetisation through further alloying with dysprosium, another particularly expensive REE. However, when the oper-

ating conditions of REPM applications are in excess of 200 °C, $Sm_2(Co, Fe, Cu, Zr)_{17}$ is the REPM typically used.

During the operation of REPM containing electric motors or power generators, losses can occur as a result of electric currents that circulate at high frequencies within the conductive REPM. Known as eddy currents, this has the effect of heating the REPM, which if uncontrolled leads to irreversible demagnetisation, even in $Sm_2(Co, Fe, Cu, Zr)_{17}$. One low cost and relatively easy to implement method to mitigate these losses is to increase the resistivity of the REPM, which is inversely proportional to the eddy current losses [6–8]. Recent investigations have shown promising results for blended REPM powders with electrically insulating material, which have then been sintered to produce composite magnets which mostly maintain the magnets properties, but with significantly improved bulk resistivity. However, in this area there exists little study of high resistivity $Sm_2(Co, Fe, Cu, Zr)_{17}$ composite permanent magnets.

Project aims

Using an emerging powder sinter technology platform; Spark Plasma Sintering (SPS), the project aims are:

- Develop, understand and optimise the processing methodology for commercial grade $Sm_2(Co, Fe, Cu, Zr)_{17}$ alloy powders to produce near-theoretical density magnets via SPS technique.
- Establish and implement a heat treatment for the $Sm_2(Co, Fe, Cu, Zr)_{17}$ magnets processed by SPS to increase the hard magnetic properties.
- Prototype isotropic $Sm_2(Co, Fe, Cu, Zr)_{17}$ and CaF_2 increased-resistivity composite magnets using the developed processing knowledge.
- Understand the effect of additional electrically insulating material to the material and magnetic properties and the potential application of the increased-resistivity $Sm_2(Co, Fe, Cu, Zr)_{17}$ and CaF_2 composite magnets.

Thesis structure

Chapters 2-4 make up the theory and literature review portion of this thesis. Chapter 2 provides background on magnetic theory, beginning with micromagnetic theory and covering hysteresis, magnetic reversal and coercivity mechanisms. This level of an understanding of magnetic theory is most applicable to the experimental study of hard ferromagnetic materials covered within this body of work. An

extensive literature review on $Sm_2(Co, Fe, Cu, Zr)_{17}$ permanent magnets, their applications and eddy current effects make up the rest of the chapter.

Chapter 3 details sintering theory and the SPS technique. Relevant literature on SPS processed materials is also provided, with emphasis on REPMs. Chapter 4 covers the Finite Element Method (FEM) and its use in micromagnetic modelling and simulation for the analysis of the demagnetisation mechanics of REPMs.

In chapter 5, the experimental methodologies used, as well as preliminary studies, are explained in detail. This chapter also explains the how the FEM models are generated and summarises how demagnetisation of the magnetic model is simulated. This chapter is referenced throughout the thesis and where slight changes are made to the experimental method or parameters used, the base methodology is summarised in this chapter.

Chapters 6-8 are the results chapters. The study of the SPS technique used in the sinter of $Sm_2(Co, Fe, Cu, Zr)_{17}$ powders in covered in chapter 6. Here, a detailed study of the SPS processing parameters is detailed with the aim to identify the optimal parameters to achieve full density. The specimens produced within the study are analysed for their material and magnetic properties to examine their relationships with material density.

In chapter 7, the identified SPS processing parameters are used to produce full density $Sm_2(Co, Fe, Cu, Zr)_{17}$ specimens, which are subjected to a study of a specific heat treatment necessary to precipitate a cellular nanostructure within the $Sm_2(Co, Fe, Cu, Zr)_{17}$ grains and significantly enhance the coercivity of the magnet. The general structure of the heat treatment is consistent with those typically used for powder sintered $Sm_2(Co, Fe, Cu, Zr)_{17}$, although the individual stages and the ageing time are investigated with respect to the magnetic properties.

Chapter 8 brings together the knowledge developed from the previous chapters to produce blended $Sm_2(Co, Fe, Cu, Zr)_{17}$ and CaF_2 composite magnets of varying weight percentages using the SPS technique. A systematic study is conducted investigating the effect of the electrically insulating material on the microstructure, and material and magnetic properties both before and after heat treatment. This includes analysis of the resistivity, and the magnetic coercivity and energy products, which are compared to identify the optimal weight addition of CaF_2 which provides the largest bulk resistivity enhancement, while maintaining the magnetic properties viable for permanent magnet applications.

Chapter 2

Magnetic theory

2.1 Overview of magnetic theory

An understanding of magnetism and the properties of ferromagnetic materials, with focus on REPMs and how to characterise them, is necessary to provide the basis for the analysis and understanding of the technical details within this project. However, the absolute fundamentals of magnetic theory, which deal with the intrinsic properties and interactions at the atomic scale, are largely omitted. If information on these topics are required, established academic text books such as 'Magnetism and Magnetic Materials' by Coey and 'Modern Magnetic Materials: Principles and Applications' by O'Handley are recommended, amongst others [9–12], and have been used as the basis for this overview. The choice to bypass these topics is made because the research conducted is primarily concerned with macroscopic, bulk properties of ferromagnetic materials. These materials and their properties are well described by micromagnetic theory, which uses continuum magnetic energies to describe observed magnetic phenomena at the mesoscale. This simplification links observed magnetic phenomena, such as magnetic domains, to features within the microstructure of the material.

A general description of the material and magnetic properties of REPMs, with focus on $Sm_2(Co, Fe, Cu, Zr)_{17}$, as well as a literature review of notable and present studies, including high-resistivity phase additions concludes this chapter.

2.1.1 History of magnetism

The discovery of magnetic materials is cited to Magnesia in ancient Greece, for which it lends its name, where magnetised rocks, known as lodestone and particularly rich in a ferrimagnetic mineral - magnetite, (Fe_3O_4) showed unsual, 'magical' properties of attraction and repulsion [9]. A practical application was discovered for

magnetised lodestone rocks when fashioned into a 'spoon' like shape, which allowed it to orientate itself under influence of the Earth's magnetic field. This primitive form of the compass was improved on in around 1064 CE with the discovery that iron could acquire a thermoremanent magnetisation when quenched from red-hot temperatures [9]. Ferromagnetic steel needles produced by this method aligned with the Earth's field when suspended in air or floated on water and became the basis of the conventional compass. Compass technology, rediscovered in Europe centuries later, was indispensable in geo-navigation and ushered a defining age for naval exploration and cross-continental trade.

Many theories for the causes of the unique and unusual properties of the magnet were debunked with the first modern example of scientific approach by William Gilbert and his publication of 'De Magnete' in 1600. Using a sphere of lodestone as a model for the Earth, dubbed a terella, Gilbert observed the dipole direction with a horizontal compass and dip circle. From his observations, Gilbert explained the Earth acted like a great magnet and a compass points geographic north because of the location of the Earth's magnetic south pole. Acting like a great magnet with a far reaching magnetic field, it is this property of the Earth that protects life from the harmful solar wind, a stream highly energetic charged particles emitted from the Sun.

Following on from Gilbert's methodology, a study of the nature of magnetism began with the interaction between two magnets by Michell in 1750, and followed up by Coulomb in 1785, yielding an inverse square law, analogous to Coulomb's relationship of the force between two electric charges. With a defined relationship of the force acting between magnets, the concept of a magnetic field, $\vec{H}$, magnetic poles and potentials were developed, although it was quickly realised that 'magnetic charges' could not be separated, unlike electric charges.

Electromagnetic fields, flux and magnetisation

While studying current carrying electric wires in 1820, Hans-Christian Ørsted noticed a magnetic compass needle was deflected when in close proximity to the wire. Upon further investigation, he proposed a current-carrying electric wire produced a circumferential magnetic field. Not long after, André-Marie Ampére and Dominique-François Arago discovered that a wound wire carrying electric current produced a magnetic field of equivalence to a small bar magnet. These experiments displayed how moving electric charges created a magnetic field, connecting the sciences of electricity and magnetism. This new field of science was developed further with

Maxwell's equations, which describe all electrical and magnetic phenomena, static and dynamic [9, 13]. Maxwell's equations expanded the field theory of electromagnetism and introduced a number of different types of magnetic fields.

$\vec{B}$ is the primary magnetic field, or B-field, and measured in units of $\mathrm{A\,m^{-1}}$ or T. It is a measure of the flux produced by an electric current or the flux density of a magnet.

An applied magnetic field may be used to magnetise a material and can thus be described as the magnetising force or magnetic field strength, $\vec{H}$. In a vacuum, the primary B-field and auxiliary H-field are made equivalent by the following equation:

$$\vec{B} = \mu_0 \vec{H} \tag{2.1}$$

μ_0 is the permeability of free space with a value $4\pi 10^{-7}$ in a vacuum with units Henrys per meter. Materials can be defined by their response to an applied field. Within a material, the constant of proportionality relating $\vec{B}$ to $\vec{H}$ is a global property of the magnet, μ, and is determined experimentally.

For most materials, $\vec{B}$ and $\vec{H}$ are related linearly. However, for types of materials where the relationship between B and H is non-linear, they are defined as ferromagnetic (or ferrimagnetic, but we focus on the former) and they exhibit hysteresis; a property where the state of the system is dependent on its history. In the context of a ferromagnetic material; for a given applied field, the flux density has more than one possible value and the measured flux will depend on how the magnet was magnetised. The relationship between the magnetic flux density and the applied field for a ferromagnet is given by:

$$\vec{B} = \mu_0(\vec{H} + \vec{M}) = \mu_0 \vec{H} + \vec{J} \tag{2.2}$$

$\vec{M}$ is the magnetisation induced within the material and $\vec{J}$ is the magnetic polarisation, measured in $\mathrm{A\,m^{-1}}$ and T respectively. The magnetisation of the material is the summation of the individual magnetic moments of individual atoms per unit volume. If a non-zero field is applied, the magnetisation is related to the auxiliary magnetic field, $\vec{H}$ by the equation:

$$\vec{M} = \chi \vec{H} \tag{2.3}$$

The susceptibility of the material, χ, is a measure of a material's response to an external field and is dimensionless. Ferromagnetic materials have large, positive susceptibilities ($\chi > 1$) relative to paramagnetic or antiferromagnetic materials.

2.2 Micromagnetism

By the early twentieth century, the atomic origin of magnetism could be explained with quantum mechanics and was used to calculate the intrinsic magnetic properties of spin-ordered materials. However, there existed no link between the atomic-scale magnetic properties and Maxwell's phenomenological theory, which used volume averaged permeabilities and susceptibilities, with no derivation from first principles. Eventually, the two length scales were bridged with the experimental observations by Barkhausen [14] and later, Sixtus and Tonks [15, 16], of magnetic domain propagation in ferromagnetic materials under magnetic fields, evidencing magnetic interactions at the mesoscopic scale. Theory at this length scale was developed by Felix Bloch, who described domain walls as the intermediate region between adjacent *domains* where the magnetisation vector gradually rotates across a finite width due to competing magnetic energy terms [9].

Domain structure was developed further by Landau and Lifshitz, who introduced a mesoscopic continuum expression for the exchange energy in ferromagnetic materials. This approximation allowed the atomic-scale structure of the material to be discounted when trying to analytically model ferromagnetic behaviour. Building on experimental and theoretical developments, William Fuller Brown Jr. published two papers, which became the foundation of the modern theory of micromagnetism [17, 18].

The premise of micromagnetism is the magnetisation is represented by a smoothly varying function of position, $\vec{M(r)}$, with the magnitude of the magnetisation constant everywhere within the volume (or domain) and equal to the saturation magnetisation, M_s. The saturation magnetisation (or polarisation), is the maximum value attained for a magnetic body when every dipole moment is aligned parallel.

This method of simplifying the magnetic structure of a ferromagnetic body allows micromagnetism to describe the magnetic state of the system through a minimisation of the total free energy, ε. The total free energy is comprised of key intrinsic magnetic energy terms developed through micromagnetic theory of a ferromagnetic body: exchange energy, anisotropy energy, Zeeman energy and self-demagnetising energy:

$$\varepsilon_{tot} = \varepsilon_{exchange} + \varepsilon_{anisotropy} + \varepsilon_{Zeeman} + \varepsilon_{demag} \tag{2.4}$$

The exchange, magneto-crystalline anisotropy and magneto-elastic energy are derived through atomic-scale electro-static effects. The self-demagnetisation and Zeeman energies are macroscopic magneto-static effects which involve the interaction of the body with its own self-created magnetic field or with a steady or slowly changing applied magnetic field. Minimisation of the free energy, which is dictated by the

dominant micromagnetic energy term, reflects a local or an absolute energy minimum and at equilibrium allows the spatial distribution of the magnetisation $\vec{M}$ to be calculated.

2.2.1 Exchange energy

The exchange energy is a description of the quantum-mechanical derived exchange interaction, expressed within the magnetic continuum. Exchange acts in ferromagnetic materials such that the lowest energy state of an atomic system is where electron spins are aligned parallel [11, 12]. The exchange interaction is why ferromagnetic material behave differently to other types of magnetic materials. A detailed description and derivation of the contiuum expression of the exchange energy is provided by Kronmüller [13], with the resulting micromagnetic exchange energy term described as:

$$\varepsilon_{exchange} = \int A_{ex} \left(\nabla \frac{\vec{M(r)}}{Ms} \right)^2 d^3r \tag{2.5}$$

The implication of the exchange energy is a minimisation in the energy term when the magnetisation, $\vec{M(r)}$ is parallel throughout the entire magnetic volume. A_{ex} is the exchange stiffness and is a property of the atomic and electronic arrangement within the crystal lattice.

$$A_{ex} \approx \frac{k_B T_C}{2a_0} \tag{2.6}$$

K_b is the Boltzmann constant and T_C is the Curie temperature at which local magnetic dipoles moments have enough thermal or kinetic energy to overcome their ordering. In the case of ferromagnetic materials, this is the transition temperature from a ferromagnetic to a paramagnetic state. a_0 is the lattice parameter of the crystal lattice.

2.2.2 Magneto-crystalline anisotropy energy

Magnetic materials can possess magnetic anisotropy such that the magnetisation will naturally orientate itself in a particular direction. Magnetic anisotropy can arise from a material's atomic and crystal structure, an applied stress or material shape. These sources of magnetic anisotropy all have their own associated anisotropy energy, however they are non-cumulative and only the largest energy takes precedence. In the discussion of REPMs, magneto-crystalline anisotropy, which is the energy associated between the interaction of the individual magnetic

dipole moments and the electric field of the crystal, is the dominant source of magnetic anisotropy.

The magnetic moments that arise from electron spins and atomic angular orbital momentum can sometimes be strongly coupled. Magneto-crystalline anisotropy, which exists in some form for all crystalline materials, is due to the interaction between the spin-orbit coupling of electrons and the anisotropic crystal field of the crystal lattice. The strength of the spin-orbit interaction correlates with atomic weight and as such, is significant in the ferromagnetic TM elements and the heavy REEs.

For all crystal structure types, there will exist defined, lower-energy crystallographic axes that the magnetic moments prefer to align along. Magnetic saturation along these preferred directions (or any symmetrically shared directions in the crystallographic arrangement) requires relatively lower fields and these directions are defined as an 'easy axis' of magnetisation. Comparatively, if magnetisation is attempted in another direction, it is 'harder' to reach saturation as more energy is required to overcome the spin-orbit coupling and reorientate both the spin and orbital moments of the electrons within the crystal lattice. Figure 2.2.2 shows the characteristic initial magnetisation paths and fields required to reach saturation along easy and hard axes. The difference in energy between the two curves defines the magneto-crystalline anisotropy energy. Note, while not shown in figure 2.2.2, the same value for the magnetic saturation is eventually achieved in all directions.

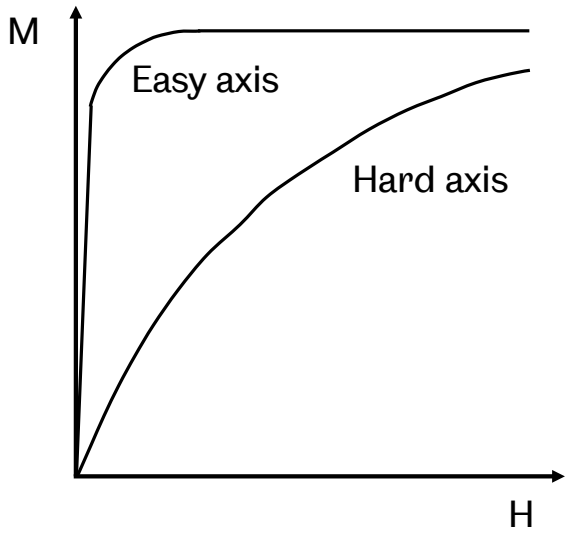

Figure 2.1: Schematic showing the magnetisation curves for a ferromagnet magnetised by an applied field orientated along the crystal easy and hard directions.

Permanent magnets are typically described as having uniaxial magneto-crystalline anisotropy. This means there is one easy axis, typically the c-axis <0001>, and all other orientations are defined as hard axes. Hexagonal, orthorhombic and tetragonal are examples of crystal structures which possess uniaxial anisotropy and the energy cost in reorientating the magnetisation in these structures is much larger in comparison to other crystal structures which posses high orders of symmetry, such as cubic.

The magneto-crystalline energy is described by phenomenological expressions, which are power series expansions that reflect the crystal symmetry [13]. For uniaxial crystal structures, the angular dependence of the anisotropy energy per unit volume is a function only of the angle, θ, between the magnetisation vector and the hexagonal c-axis. The anisotropy energy per unit volume is made equivalent to the first two terms of the expansion:

$$u_a = \frac{u_0}{V_0} = K_1 \sin^2\theta + K_2 \sin^4\theta \tag{2.7}$$

The easy magnetisation direction (hexagonal c-axis) is parallel to the Cartesian z-axis. K_1 and K_2 are empirically derived magneto-crystalline anisotropy constants, with units of J/m^3. They are temperature dependent and decrease on approach to the Curie temperature. For most ferromagnetic materials $|K_1| \gg |K_2|$ and therefore, K_2 is often neglected. Where $K_1 > 0$ the easy axis is parallel to the hexagonal c-axis. For the case $K_1 < 0$, the hexagonal c-axis is the hard axis, with an easy plane perpendicular to it.

2.2.3 Magneto-static energy

Self-demagnetising energy

The sources and sinks of magnetic fields are visualised using fictitious magnetic 'poles' or 'charges', which form at material surfaces perpendicular to the magnetisation direction. When a ferromagnetic material is magnetised to saturation by an applied magnetic field, a spontaneous macroscopic field is created by the magnetic material, called the stray field, $\vec{H_{stray}}$, which radiates from the 'north' pole and ends at the 'south' pole. Permanent magnets are ferromagnetic materials that are able to retain this state upon removal of a magnetising external field. An internal magnetic field also exists within the magnetised ferromagnet and, again, has field direction going north to south. This internal field is called the self-demagnetising field, $\vec{H}_d$, because it acts in the opposite direction of the magnetisation, $\vec{M}$ and the applied field, $H_{applied}$, which also permeates through the magnetic volume. An schematic of applied and induced magnetic fields in a ferromagnetic body is shown in figure 2.2.

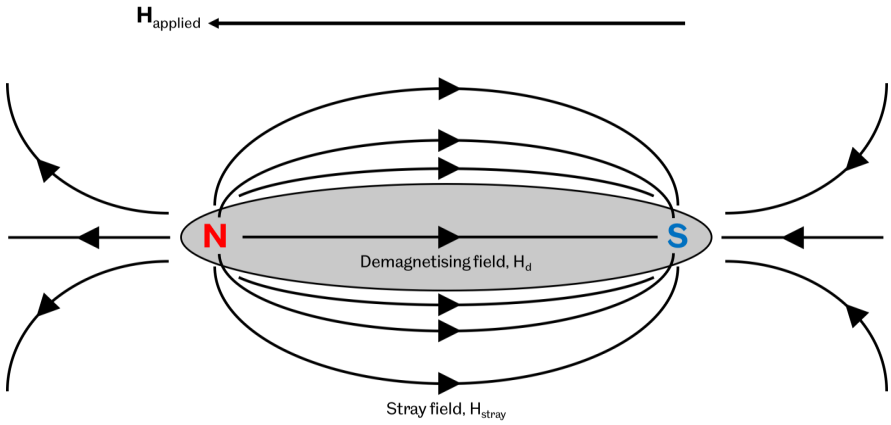

Figure 2.2: The stray field, $\vec{H_{stray}}$ around a ferromagnetic prolate spheroid. The magnetisation. $\vec{M}$ is in the same direction of the applied field $\vec{H_{applied}}$, while the self demagnetising field, $\vec{H}_d$ is in the opposite direction.

The effective field, H_{eff} describes the resultant magnetic field acting within the ferromagnetic body and is the difference between the applied field and the self-demagnetising field:

$$\begin{aligned} \vec{H_{eff}} &= \vec{H_{applied}} - \vec{H}_d \\ &= \vec{H_{applied}} - \mathcal{N}_d M_s \end{aligned} \tag{2.8}$$

$\mathcal{N}_d$ is the demagnetisation factor and can take values $0 \leqslant \mathcal{N}_d \leqslant 1$ depending on the shape of the medium. Using a prolate spheroid as an example in figure 2.3 a), $\vec{M}$ (indicated by the arrow) is orientated along long axis (a) and less surface charges are created in comparison to (b) where $\vec{M}$ is orientated along the short axis. $\mathcal{N}_d$ is largest with the magnetic orientation along the short axis. As such, this is the origin of shape anisotropy. The demagnetising factor varies for different shapes and a detailed derivation can be found in Aharoni [11]. Generally, for bulk REPMs, the magneto-crystalline anisotropy dominates over shape anisotropy, however defects and pores can be sources of magnetic charges, which lend to self-demagnetising fields reducing the nucleation field for magnetic reversal.

The energy cost in creating a stray field is the summation of individual interactions of magnetic dipoles with the self-demagnetising field created by other dipoles. Derivation of self-demagnetising energy can be found in by both Aharoni and Coey [9, 11], with the resultant micromagnetic energy term:

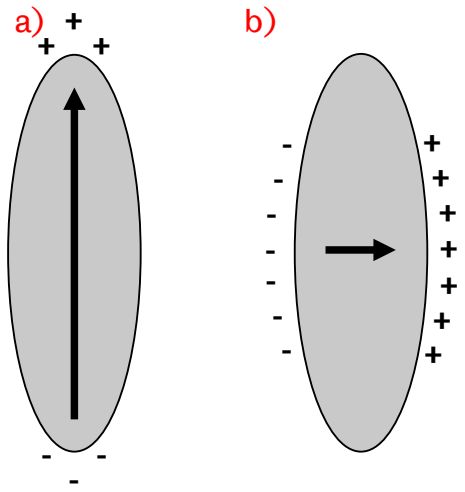

Figure 2.3: The shape anisotropy for a ferromagnetic prolate spheroid. The magnetisation, shown inside the ferromagnetic body, creates less surface charge when orientated along the long-axis. This is the basis for shape anisotropy.

$$\varepsilon_{demag} = -\frac{1}{2}\int \mu_0 \vec{M} \cdot \vec{H}_d d^3r \tag{2.9}$$

The self-demagnetising field energy is minimised by the charge/pole avoidance principle, which dictates the lowest energy configuration is found when $\vec{M}$ creates minimal surface or volume magnetic charges/poles. The minimisation of the self-demagnetising field facilitates the formation of magnetic domains.

Zeeman energy

Another magneto-static energy term exists upon the application of an applied magnetic field to a ferromagnetic material. Known as the Zeeman energy, this describes the potential energy of individual magnetic moments, which experience a torque in the direction of the applied magnetic field vector. The Zeeman energy is the statistical average over the magnetic volume of the individual magnetic dipole moments in the magnetic field. Minimisation of the Zeeman energy term is achieved with alignment of the $\vec{M}$ and the applied field, $\mathrm{H_{applied}}$.

$$\varepsilon_{Zeeman} = -\mu_0 \int \vec{M} \cdot \vec{H_{applied}} d^3r \tag{2.10}$$

2.2.4 Domains and domain walls

If the exchange energy was the only micromagnetic energy term used to describe the free energy; the natural state of all ferromagnetic materials would be uniform alignment of all the individual magnetic dipole moments throughout the

medium. However, the existence of the other magnetic energy terms, such as the self-demagnetising energy and magneto-crystalline anisotropy energy, compete with the exchange energy to form, in the absence of an applied field, multiple magnetic domains to minimise to total free energy (assuming the magnetic volume is above the single-domain limit).

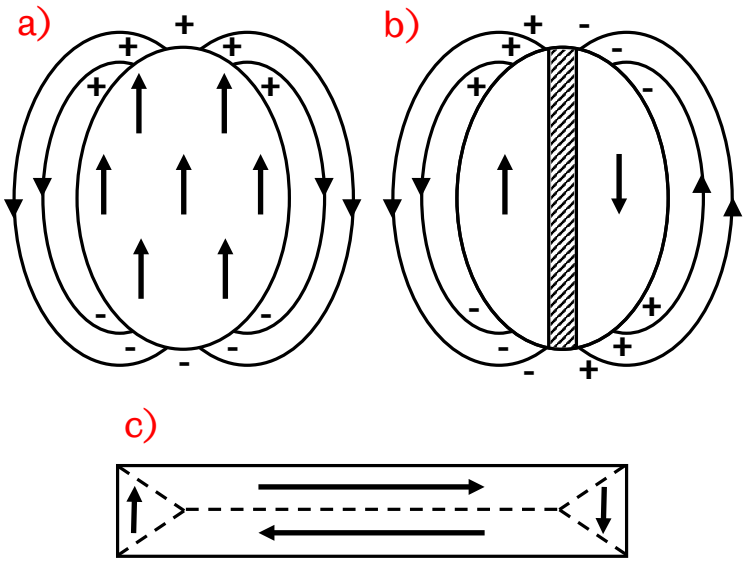

Figure 2.4: Schematic showing the reduction in magnetic surface charges (a) of a ferromagnetic body when a second domain is created (b). The reduction in the stray field energy is halved in (b), however this is offset by the energy, γ_w, of the domain wall (shaded region). (c) shows an exaggerated example of enclosure domains within a magnet with cubic crystal structure.

The origin for the formation of a multi-domain state can be explained by the charge avoidance principle; a simplified model that assume magnetic 'charges' (or magnetic poles) as sources of the stray self-demagnetising field at surfaces normal to the magnetisation vector. Charge can also accumulate within the volume where the divergence of the magnetic field is non-zero. Without anisotropy, the magnetisation in the bulk could simply continuously rotate to avoid charge creation and this configuration, a vortex domain, is observed in magnetically soft (small magneto-crystalline anisotropy) materials. In magnetically hard (large magneto-crystalline anisotropy) ferromagnetic materials, the magnetisation within magnetic body will split into mesoscopic domains, within which the magnetisation is homogeneous throughout and orientated along the crystallographic easy axis. Forming domains allows the energy associated with the stray field to be reduced by minimising the number of magnetic 'charges' created. An example between a single and two-domain state is shown in figure 2.4 a) and b).

In this simple example, the energy associated with the magnetic stray field is halved by the formation of two domains. Within domains, the exchange energy and magneto-crystalline energy are minimised by the long-range, uniform magnetisation along an easy axes. However, between adjacent domains, there exist domain walls where the magnetisation rotates from the orientation in one domain to another. An example of such feature is highlighted by the shaded region in figure 2.4 and rotation of the magnetisation increases the local exchange and magneto-crystalline anisotropy energy. Therefore, there is an energy cost in the formation of domains. In general, formation of domains will continue until a balance is reached between minimisation of the magnetic stray field energy is equivalent to the cost of creating a domain wall.

In cubic crystal structures, enclosure domains can form which allow complete charge avoidance at the surfaces and in the volume, as symmetry within the cubic crystal structure allow multiple easy axis directions. An example of this type of phenomena is given in figure 2.4 c). This type of domain structure is difficult to achieve in uniaxial crystal structures, which lack similar orders of symmetry. Imaging of domain structures can be done using Kerr microscopy, which uses the interaction of polarised light with the magnetisation vector of the domains to identify contrast. An example of typical uniaxial domain structure of a thermally demagnetised $Sm_2(Co, Fe, Cu, Zr)_{17}$ magnetic material is shown in figure 2.5.

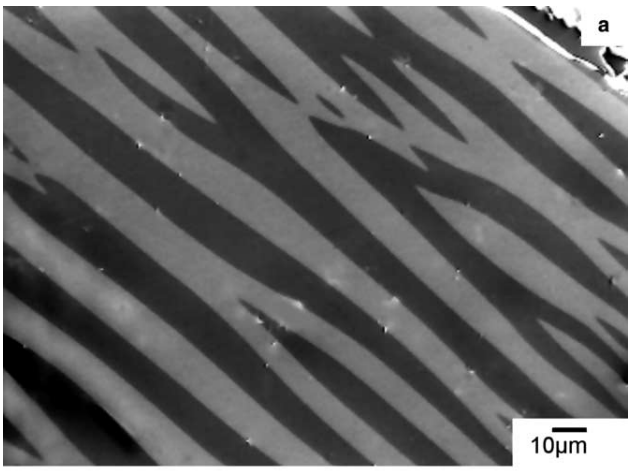

Figure 2.5: Kerr microscopy image taken of a homogeneous coarse-grained as-cast $Sm_2(Co, Fe, Cu, Zr)_{17}$ alloy. Wide domains are separated by 180° domain walls on the surface of a grain with the magnetic easy c-axis almost parallel to the imaging plane. [19] ©2006 John Wiley and Sons, licence granted for reuse in thesis (licence number 4196770830418).

Bloch domain walls

Within domains walls the magnetisation direction changes and deviates away from the easy axis leading to an increase in the exchange and anisotropy energy. Bloch walls are a type of domain wall in which the magnetisation deviates 180° through the plane of the domain wall and creates no divergence. Therefore, no magnetic charge is created by rotation in a Bloch domain wall and there is no contribution from the demagnetisation stray field energy. Figure 2.6 shows a schematic depicting the rotation of the magnetisation along the x axis in a Bloch domain wall between two domains. Bloch domain walls are associated with bulk ferromagnetic materials.

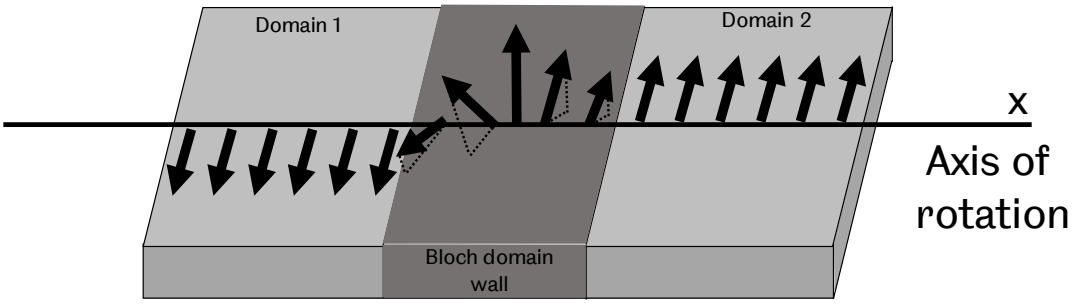

Figure 2.6: The local magnetisation across a Bloch domain wall. The magnetic moments (arrows) rotate out of the plane of the material.

Competition between the exchange and magneto-crystalline anisotropy energies define the exchange length, l_{ex}, which is the maximum length at which local magnetic dipole moments are parallel. Another way of looking at it is the shortest scale at which there can be deviation in the magnetisation vector. For hard ferromagnetic materials, l_{ex} is calculated using the following:

$$l_{ex} = \sqrt{\frac{A_{ex}}{K_1}} \tag{2.11}$$

The exchange stiffness, A_{ex} and K_1 were introduced and defined in sections 2.2.1 and 2.2.2 respectively. The exchange length can also define the width of the Bloch domain wall, as the local magnetisation is rotated 180° between domains. Therefore, the width of a Bloch domain wall is defined:

$$\delta_{BW} = \pi l_{ex} \tag{2.12}$$

The exchange energy favours wide domain walls, with gradual rotation of the magnetic moments minimising the misalignment of local magnetic moments. Conversely, the magneto-crystalline anisotropy energy favours narrow domain walls, with sharp

rotation of the magnetic moments between domains and avoiding deviation away from the easy axis.

Domain wall motion and pinning

In multi-domain ferromagnetic materials, the application of sufficient magnetic field will force the domain(s), whose easy axes are orientated closest to the applied field vector, to grow in size. Domain growth occurs by wall motion, with the applied field applying a pressure on the domain wall, itself related to the change in the Zeeman energy across the domain wall. In real magnetic materials, domain wall motion may be interrupted by defects within a heterogeneous micro-structure, with such examples as voids, dislocations, pores and precipitates. Barkhausen jumps are evidence of domain wall motion overcoming local pinning effects.

The wall energy per unit area in a uniaxial crystal is given by equation 2.13.

$$\gamma_w = 4\sqrt{A_{ex}K_1} \tag{2.13}$$

Defects in the microstructure pin domain walls as their exchange stiffness, A_{ex} or magneto-crystalline anisotropy constant, K_1 differ to that of the bulk. A statistical study of the pinning forces created by features, such as vacancies, pores and dislocations, is covered in detail by Kronmüller [13]. From this study, strong pinning will arise when a point defect has the dimensions comparable with that of the domain wall width, δ_{BW}. The strongest pinning effect occurs in planar defects, in which the entire domain wall has to overcome the pinning effect. The pinning effect is either an energy 'barrier' or a 'well' depending on the difference in energies of the domain wall interacting with the defect and the bulk. In either case, domain wall pinning is one source of magnetic hardness in ferromagnetic materials, which in combination of their long-range order of magnetic moments, give rise to the material property of hysteresis.

2.3 Hysteresis

Hysteresis describes the condition that a measurement is dependent on the history of the state and is a feature synonymous with ferromagnetic materials. This phenomena is characterised by the trace of a magnetisation loop when measuring either $\vec{M}$ or $\vec{B}$, while cycling the auxiliary field, $\vec{H_{applied}}$. Analysis of the hysteresis loop can provide a number of important properties used to characterise permanent magnets. An arbitrary example of a $\vec{M} - \vec{H}$ loop, along with the expected domain state at key points, is shown in figure 2.7.

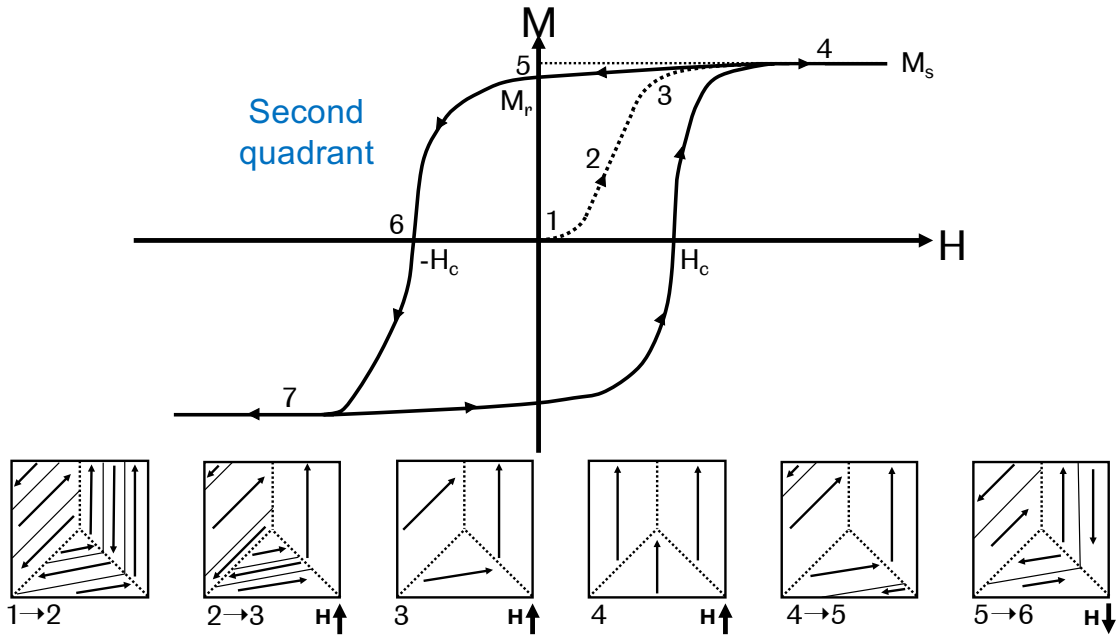

Figure 2.7: An example trace of a major hysteresis loop, measuring the magnetisation of a ferromagnetic material. Arrow-heads indicate the trace direction. Below the loop are simplified examples of the domain structure at key points during a loop trace. Dashed lines represent grain boundaries, solid lines represent domain boundaries and arrows indicate the magnetisation direction within the domain. The H-field direction is also indicated at each stage.

2.3.1 Initial magnetisation curve

When allowed to cool from the Curie temperature in the absence of a magnetic field, each grain within a ferromagnetic material will exist in a low-energy, multi-domain configuration, which attempts to reduce the self-demagnetising stray-field energy to zero. In an ideal ferromagnet in this state, there is no net magnetisation and this is the origin (section 1) of the initial magnetisation curve in figure 2.7.

If a magnetic field is applied in the vertical direction, the domains within each grain with easy axes orientated closest to $\vec{H_{applied}}$ will grow through domain wall motion at the detriment of other domains. Initially reversible (section 2), removal of the applied field allows the now present self-demagnetising field to return the ferromagnet to a state of zero net magnetisation. At these low applied magnetic fields (approximately $0 \leq M/M_s \leq 0.1$) [9], the domain walls do not have enough energy to overcome pinning sites and therefore domain growth is elastic.

If greater fields are applied, the pinning forces can be overcome and domain growth is irreversible (between sections 2 to 3). In this region, after removal of

the auxiliary field, the self-demagnetising field is not large enough to overcome the pinning potential of defects in the microstructure and so the magnet exists in a meta-stable state with a retained net magnetisation. Application of even greater fields continues the growth of the most favourably orientated domain in each grain until single domain grain states are reached (section 3).

Saturation is achieved with reversible rotation of the magnetisation vector in each single domain grain away from the easy axes and in alignment of $H_{applied}$ (section 4). The magnetisation of the ferromagnet at saturation is M_s and the field required to saturate a ferromagnet is H_s.

The initial magnetisation curve of a ferromagnetic material, such as REPM, gives insight into how the magnet holds onto its magnetisation [20]. Figure 2.8 shows the difference in the initial magnetisation curve shape between a pinning-based ferromagnet (solid line) and a nucleation-based ferromagnet (dashed line) [21]. In this example, the pinning-based magnet has a much lower susceptibility, χ, (gradient of the curve) at low applied fields, compared to the nucleation-based magnet. nucleation-based magnets saturate very quickly from the demagnetised state, while a pinning-based magnet requires larger fields to overcome the strong pinning effects and reach saturation [20].

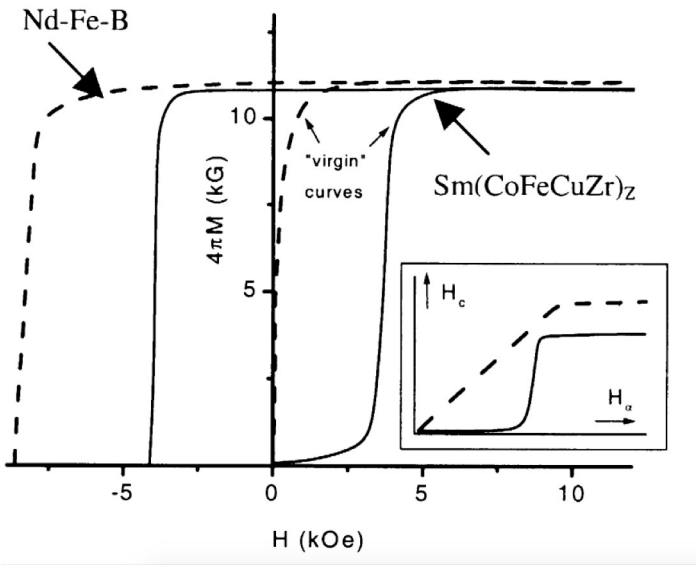

Figure 2.8: Initial magnetisation and demagnetisation curves for a 'pinning' based magnet (full line) and a 'nucleation' based magnet (dashed line). The inset schematic shows the dependence of the coercive field on the maximum applied magnetisation field, $H_{applied}$, for the two different coercivity mechanisms [21] ©1999 Elsevier, licence granted for reuse in thesis (licence number 4197000479134).

2.3.2 Magnetisation curves

Magnetisation curves are traced out by cycling the applied auxiliary field. If saturation is achieved, the corresponding loop traced out is defined as a major hysteresis loop, else for sub-saturation fields, minor hysteresis loops are measured. From the saturated state in figure 2.7 (section 4), a reduction of the applied field will see the ferromagnet attempt to reduce its free energy through minimisation of the magneto-crystalline anisotropy by rotation of the magnetisation within domains back towards their respective easy axes. Upon complete removal of the applied field, some grains return to a partial multi-domain state to reduce the self-demagnetising field energy (section 4 to 5). New reversed domains can be nucleated at sharp edges and corners of grains and at volume and surface defects.

At zero applied field, a magnetically hard ferromagnet (as exampled in figure 2.7) retains most of its magnetisation and exists in this meta-stable domain state. A REPM is engineered into this state either through nucleation hardening or domain wall pinning (or combination of both). This point of the magnetisation curve defines the retained magnetisation/polarisation (or induced flux) of the ferromagnet and is known as the remanence or remanent magnetisation/polarisation/flux (M_r, J_r or B_r respectively) and is a significant property of a permanent magnet, as it indicates the strength of its stray magnetic field.

Applying the auxiliary field in the opposite (negative) direction, the region traced out by the hysteresis loop is referred to as the second quadrant. In this region, the ferromagnetic body is demagnetised and therefore the information contained in the second quadrant tells of how magnetically hard and/or resistant to demagnetisation the magnet is (section 5 to 6). In an ideal hard ferromagnet, which has an anisotropic distribution of aligned easy axes, the magnetisation will remain approximately constant well into the second quadrant due to engineered magnetic hardening mechanisms. However, in real ferromagnetic materials, defects within the microstructure result in the magnetisation always reducing slightly due to the growth of the reversed domains, whose magnetisation vector lies closest to the reversal field vector. Figure 2.9 shows a schematic of the processes in effect.

The point at which the demagnetisation curve crosses the axis (section 6) is the intrinsic coercivity, iH_c, for a $\vec{M}$-$\vec{H}$ loop (or the coercive force, bH_c, for a $\vec{B}$-$\vec{H}$ loop). Coercivity, in both $\vec{M}$-$\vec{H}$ and $\vec{B}$-$\vec{H}$ loops, is a measure of the field required to return the ferromagnet from a magnetised to demagnetised state. Ferromagnetic materials can be described either as 'hard' or 'soft' based on the

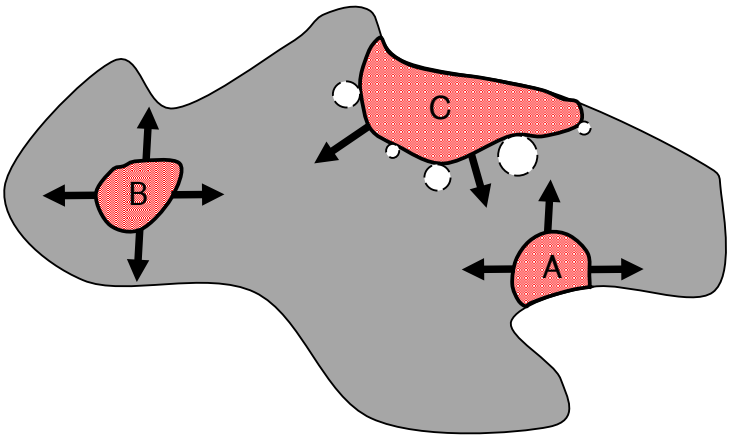

Figure 2.9: Examples of the processes involved in magnetisation reversal during demagnetisation in the second quadrant of a hysteresis loop. Red shaded regions are reversed domains and arrows show the direction of Bloch domain wall propagation. White dashed circles represent pinning sites. A is a reversed domain that nucleates at a surface asperity. B is a reversed domain nucleated in the bulk of the material. C is a reversed domain that has grown sufficiently large that it trapped by pinning sites. Adapted from [9].

value of the coercivity, with the distinction defined by Coey at around $400\,\mathrm{kA\,m^{-1}}$ [1]. High performance REPMs are engineered to have very large coercivities, often exceeding $2000\,\mathrm{kA\,m^{-1}}$ [2]. The demagnetised state of the magnet at section 6 is much different to the, now inaccessible, virgin demagnetised state at the origin. Further application of the auxiliary field in the negative direction will see the magnet again reach saturation (section 7), albeit with the magnetisation in the opposite direction as before in section 4. A full loop is traced out if the external field is cycled once again in the positive direction, mimicking the processes just described.

A $\vec{B}$-$\vec{H}$ loop can be extrapolated from a $\vec{M}$-$\vec{H}$ loop by use of equation 2.2 from section 2.1.1. The same processes as described throughout the $\vec{M}$-$\vec{H}$ loop occur in the $\vec{B}$-$\vec{H}$ loop, although the measured coercive force, $\mathrm{bH_c}$, will be smaller than $\mathrm{iH_c}$. The shape of the loop is much different, as shown in figure 2.10, and this is most clear in that saturation does not result in a plateau, a result of equation 2.2. The 'knee' of a $\vec{B}$-$\vec{H}$ is used to gauge stability of the permanent magnet during operation, when the magnet may be subjected to demagnetising fields during operation. For stable performance, it is expected that the 'knee' is absent from the second quadrant and lies below the axis.

The $\vec{B}$-$\vec{H}$ loop also allows a further material property to be calculated from the

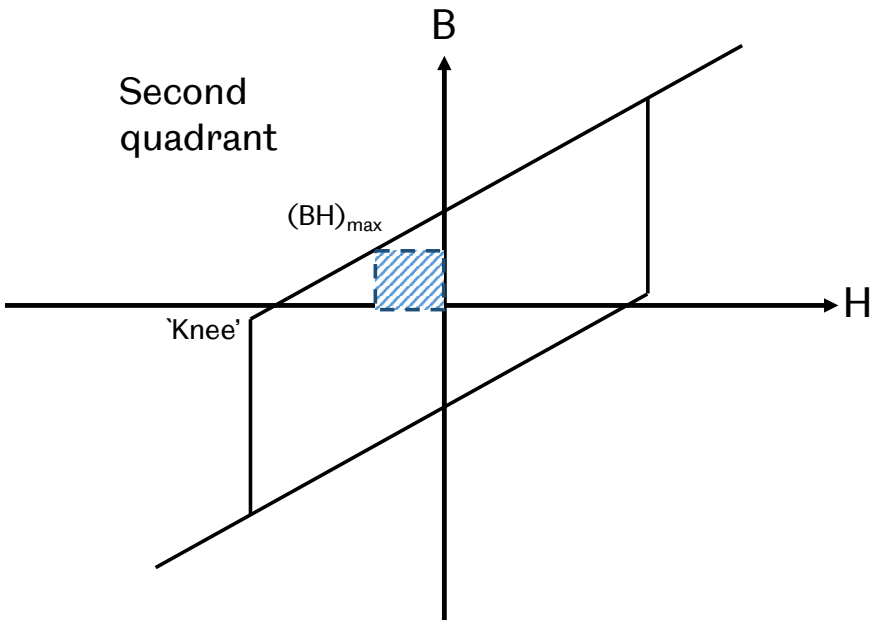

Figure 2.10: An ideal B − H hysteresis loop showing additional features in comparison to a M − H loop.

hysteresis loop, known as the energy product or energy density, $(\mathrm{BH})_{\max}$, with units of $\mathrm{kJ\,m^{-3}}$. Permanent, hard ferromagnetic materials are engineered to produce large stray fields, which allow the permanent magnet to do 'work' without expenditure of energy. The maximum energy product represents the largest product value of the magnetic induction and the applied field in the second quadrant of the $\vec{B} - \vec{H}$ diagram. Largely a figure of merit for permanent magnets, rather than an intrinsic property of the magnet, it can be represented as the largest rectangle area inscribed on the normal curve, as shown in figure 2.10 and is equivalent to twice the energy stored in the magnet's stray field when the normal curve is linear throughout the second quadrant and the 'knee' lies below the x-axis [9, 10]. Similarly, for a $\vec{M}$-$\vec{H}$ loop, the maximum energy products are achieved in large, square demagnetisation curves, such that $\mathrm{M_r} = \mathrm{M_s}$ and $\mu_0 \mathrm{iH_c} > \frac{1}{2}\mu_0 \mathrm{M_r}$. Under these conditions, the theoretical maximum energy product achievable for a hard ferromagnet is:

$$(BH)_{max} = \frac{1}{4\mu_0}(\mu_0 M_s)^2 \tag{2.14}$$

The energy product in commercial permanent magnets has increased significantly with alloy development and microstructure optimisation over the last 60 years [2]. Larger energy products has allowed the volume of the permanent magnet required to produce an equivalent field to significantly reduce over time.

2.4 Properties of permanent magnets

Permanent magnets are, generally, ferromagnetic materials with large magneto-crystalline anisotropy. Their coercivity exceeds the permanent magnet's own self-demagnetising field, $H_c > H_d$, and retain their magnetisation in the absence of an applied field - the hysteresis loop extends well into the second quadrant. Large anisotropy fields, typically of magneto-crystalline origin, and/or domain wall pinning microstructures keep the permanent magnet from dividing into multiple domains and minimising the energy dense stray-field. Permanent magnets are therefore hard ferromagnetic materials put into a meta-stable energy state to exploit a large stray field as necessary for application.

Figure 2.11 represents how an increase of the energy density ($(BH)_{max}$) has allowed permanent magnets to reduce their volume and increase their functionality. This has been achieved through the discovery of new permanent magnet materials, along with material microstructure and processing method optimisation.

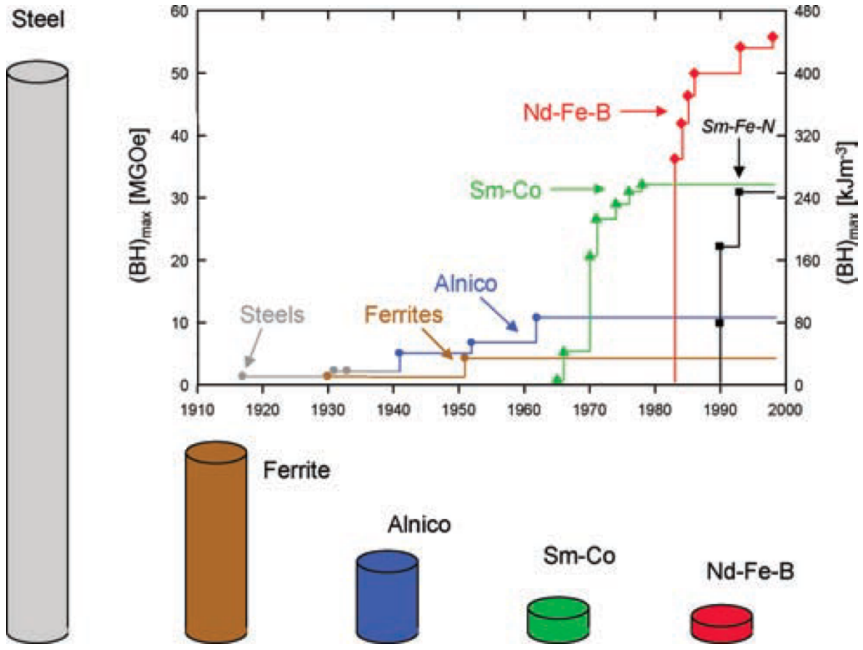

Figure 2.11: The energy density of hard magnetic materials developed over the twentieth century, as measured at room temperature. Also shown graphically is the relative volume required to produce a stray field of 100mT as measured 5mm from the pole [2] ©2011 John Wiley and Sons, licence granted for reuse in thesis (licence number 4197000886769).

The development of permanent magnets has been driven by a desirable increment of the energy density, which is most effectively done by maximising M_s, $M_r \approx M_s$,

and H_c, which maintained as greater than $\frac{1}{2}M_r$. However, real materials deviate from the ideal conditions for maximising the magnetic properties due to defects and misalignment of magnetic grains within the material and the microstructure. As such, $M_r < M_s$ and H_c is often, at best, 30% of the theoretical maximum coercivity of a permanent magnet [2], which is equivalent to the anisotropy field [13].

$$\mu_0 H_A = \frac{2K_1}{M_s} \tag{2.15}$$

H_A is the anisotropy field, which is the field required to coherently rotate the magnetic dipole moments within the volume away from the easy axis. $H_c < H_A$ because reverse domains nucleate at lower fields at sites such as volume and surface defects.

Another desirable property of permanent magnets is a large Curie temperature. As temperature rises, remanence and coercivity decrease as thermal energy overcome the magneto-crystalline anisotropy. The change in the magnetic properties with temperature can be measured and quoted as a coefficient of temperature, β for the remanent magnetisation/polarisation/flux or coercivity (for example, $\beta_{Hc} = dH_c/dT$) [22–24]. Generally, these coefficients are negative but their effect is minimised if the permanent magnet possess a large Curie temperature. The permanent magnet properties remain more stable with changes in the temperature and the magnet can operate at greater temperatures and more challenging conditions.

2.4.1 Rare-Earth Permanent Magnets

Theory

Ferromagnetic materials rarely possess both high magnetic saturation and coercivity. Using iron as an example; it has the largest M_s of any ferromagnetic material, but does not have uniaxial anisotropy. Its highly symmetric cubic crystal structure lacks sufficient magneto-crystalline anisotropy and thus K_1 is relatively small. Shape anisotropy can be used to compensate for high magnetic saturation, low magneto-crystalline anisotropy ferromagnetic materials as a way to engineer magnetic 'hardness'. Such examples are magnetic steel and AlNiCo-type permanent magnets and historically this is evidenced by the horse shoe shape synonymous with magnets.

Alloying has been used with great success to increase the magneto-crystalline anisotropy of ferromagnetic materials, usually through changes to the crystal structure which induce uniaxial magneto-crystalline anisotropy. This is best evidenced with the introduction of ferromagnetic REEs with the ferromagnetic TM elements. Through processing optimisation and composition development, the REPMs are the best examples of energy dense permanent magnets and are known for very large uniaxial magneto-crystalline anisotropies, while maintaining large

saturation magnetisation.

The REE encompass the lanthanide elements (lanthanum to ytterbium, and scandium and yttrium). The addition of the rare-earth elements to the transition metals in REPM alloys is to provide much of the uniaxial magnetocrystalline anisotropy, while also contributing to the ferromagnetic moment of the compound [1]. The spin-orbit coupling effect is strongest in heavy elements, as it scales with charge of the atomic nucleus and therefore with the atomic number [12]. The heavy REEs therefore possess a strong magneto-crystalline anisotropy.

Importantly, only certain REEs can couple and contribute positively to the ferromagnetic moment of the compound. Ferromagnetic materials are defined by the exchange interaction, which align the magnetic moments of valence electron spins in overlapping electron bands. In the ferromagnetic TMs: iron, nickel and cobalt, there is an overlap of the 3d and 4s band energies. Due to a positive exchange interaction within these elements, it is favourable for a significant, and importantly imbalanced, amount of valence electrons to align themselves parallel within the higher density of states 3d band [10]. The description of this effect, across unchanging band structures in TMs, is the basis of rigid-band theory and further information can be found in O'Handley [10].

Within REEs, the electrons in the 4f-band behave similarly to the 3d-band of the TM elements. Following Hund's rule third rule for the lowest energy configuration, for a less than half filled 4f-band (i.e. light REE - Sc - Gd), the orbital angular momentum number, **L**, and the spin angular momentum number, **S**, combine subtractively to provide the total angular momentum quantum number, **J**. When the 4f-band is more than half full (heavy REE - Y - Lu), **L** and **S** combine additively. Therefore, the orbital and spin moments are antiparallel for light REE and parallel for heavy REE. When combined with TM elements to form rare-earth transition metal (RETM) intermetallics, not all REEs will contribute positively to the net magnetic moment. Due to influence of the 5d-band in the REE, the interaction between the spins of the TM 3d-band and REE 4f-band are always anti-parallel. Therefore, under this condition and as a result of Hund's third rule, the coupling between the net magnetic moments of the TM and REE is ferromagnetic for light REE and antiferromagnetic for heavy REE [1].

General properties of REPMs

REPMs are known for their combined large magnetisation and coercivity. Generally, these properties are derived from the intrinsic magnetic properties of the REPM alloy; magnetic saturation and magneto-crystalline anisotropy, respectively. How-

ever, the microstructure is also significant with respect to the properties a REPM can possess [25]. The remanent magnetisation/polarisation (M_r/J_r) (or residual flux (B_r)) is strongly dependent on the alignment of magnetic grains, with respect to heir respective magneto-crystalline easy axes [26–28]. Magnetically anisotropic REPMs achieve remanent magnetisations close to their saturation magnetisation, which in turn optimises the energy product of the permanent magnet. The coercivity is strongly tied to the features and properties of the microstructure; such as the homogeneity, size and shape of the magnetic grains [13]. How the microstructure is engineered to maximise the coercivity of the REPM will depend on the type of mechanism that initiates, or describes, magnetic reversal. Generally, a homogeneous microstructure made up of uniform grains is beneficial to the coercivity [27, 29, 30]. Heat-treatments can also be an integral part of the processing route for REPMs which require homogenisation and/or optimisation of the phase structure. In particular, the $Sm_2(Co, Fe, Cu, Zr)_{17}$-type permanent magnets require a lengthy and complex multi-stage heat-treatment to generate a multi-phase, cellular nanostructure (within micrometer sized grains), which act to pin domain walls and achieve large coercivities.

There also exists a general, inverse relationship (1/D) between the grain diameter, D, and coercivity [25, 31–35]. Kronmüller and Fahnle [13] provides a comprehensive review of this relationship, which can be summarised as an increase of the coercive field as the grain size decreases in the mesoscale, where multi-domain states exist. A reduction in the grain size will increase the volume fraction of grain boundaries, which increase pinning sites to inhibit domain wall motion [36, 37]. Below the single-domain limit (which is typically around 200 nm to 300 nm for REPMs), the coercivity significantly enhances as magnetic reversal must occur through rotation of the magnetic dipoles, rather than domain wall motion. Peak coercivities can be achieved in nanoscale grain REPMs, with average grain diameters of around 20 nm to 40 nm [29, 35, 38]. Lower grain diameters (approaching 1 nm) see temperature effects dominate in what is referred to as a superparamagnetic state and a coercivity rapidly decreases with grain size [13]. When grain diameters are approximately of the order of tens of nanometers, the exchange coupling can be significant, which leads to an enhancement in the remanence [21, 27, 29, 36, 38].

Sintered permanent magnets make up the bulk of commercial REPM production [1, 25]. Sintering is a method of producing dense material from precursor powders by the application of heat, and sometimes pressure. The quality, shape and size of the precursor powder, as well as the sintering process, are strongly related to the microstructure of the bulk material. Common methods of processing the precursor

powders, such as jet milling, pulverise and control the distribution of powder size and shape, which is crucial to achieving a homogeneous microstructure after sintering [27]. Average powder diameters by this method can be around 5 µm to 10 µm [39, 40] and if the method is optimised to produce single crystal powders, their magneto-crystalline easy axes can be aligned to a high degree by a sufficiently large external magnetic field before consolidation via sintering [26].

To achieve sub-micron grain size, precursor powders are required to be of the same order. Achieving this can be difficult, as oxidation of the powders during the milling process becomes prevalent as particle diameters reduce past 5 µm, unless steps are taken to control the environment [27, 41]. Alternative methods, such as rapid solidification, HDDR and mechanical alloying can produce precursor powders/ribbons which are of the nanoscale, but are specialised processes [27, 42–47]. Texture can be induced in REPM magnets made by these methods through stress-induced grain deformation during a hot deformation process [27, 34, 47–50]. Hot deformation is the process of applying large pressures at temperatures below the melt and allowing the material's dimensions to change [48, 51].

2.4.2 Coercivity mechanisms of permanent magnets

Nucleation-based

Brown's expression gives the theoretical coercivity for a homogeneous, uniformly magnetised ferromagnetic ellipsoid [9]:

$$\mu_0 H_c \geq \frac{2K_1}{M_s} - \mathcal{N}_d \mu_0 M_s \tag{2.16}$$

However, Brown's paradox states that hard magnets produced throughout history have, at best, achieved coercivities equivalent to 20-30% of this predicted value [9, 27]. The most obvious initial explanation for the discrepancy, is the assumption that real materials are homogeneous. Defects and surface asperities within real materials are sources of strong local self-demagnetising fields. These imperfections therefore are sites for the nucleation of reverse domains, where in the second quadrant of the hysteresis loop the local reversal field is enhanced in their vicinity. The nucleation field, H_N, is the reversal field required to cause a deviation away from the uniformly magnetised domain state. The minimum size of a nucleated reversed domain is δ_w^3 and will expand through domain wall motion under influence of the reversal field, unless the pinned by defects [9]. Brown's expression can be expanded to include an additional coefficient, α, which accounts for the magnetic inhomogeneities caused by defects and imperfections.

The coercivities of REPM materials such as $SmCo_5$ and Nd-Fe-B-type are defined by nucleation-based reversal mechanisms and their coercivity increases with the nucleation field. Methods to increase H_N are referred to as 'nucleation hardening' and can be done by increasing the magneto-crystalline anisotropy, and/or the removal of nucleation sites, such as defects, irregularities and undesirable phases within the microstructure.

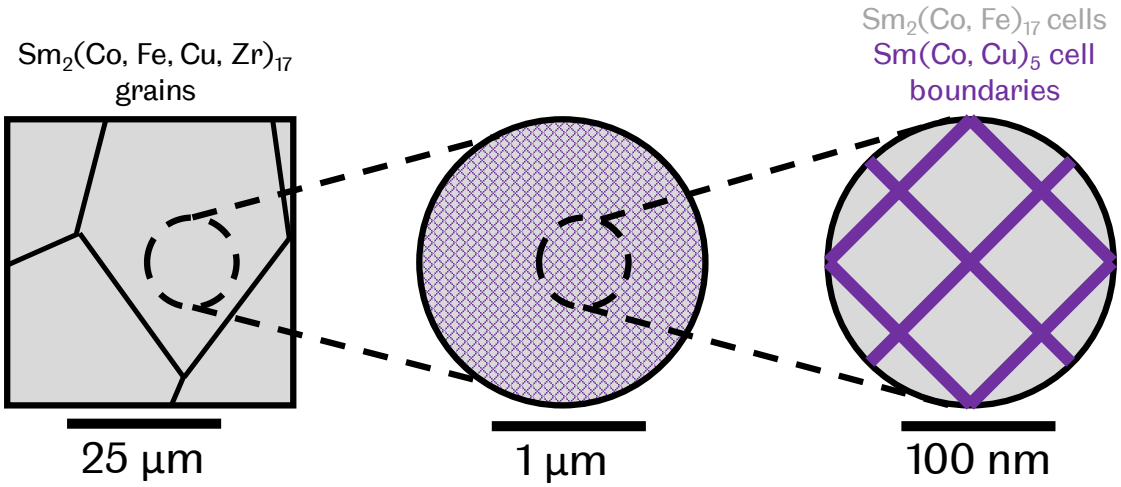

Figure 2.12: Schematic showing the microstructure of a typical $Sm_2(Co, Fe, Cu, Zr)_{17}$ permanent magnet at different length scales. Left shows the $Sm_2(Co, Fe, Cu, Zr)_{17}$ grains and grain boundaries. Right shows the nanostructured $Sm_2(Co, Fe_{17}$ cell and $Sm(Co, Cu)_5$ cell boundary phases within the $Sm_2(Co, Fe, Cu, Zr)_{17}$ grains. A separate Zr-rich lamellar phase is not shown in this schematic. Scale bars are approximate.

Pinning-based

$Sm_2(Co, Fe, Cu, Zr)_{17}$-type magnets are defined by a coercivity mechanism known as domain wall pinning. The nucleation field in these materials are comparably lower than the aforementioned nucleation-based REPMs, however their large coercivities are achieved by engineering an optimised microstructure which is able to trap domain walls and impede the motion of reverse domains. Large fields are required to overcome these energy barriers and instigate complete magnetic reversal throughout the magnet. The pinning structure, comprised of cell and cell boundary phase (as well as a lamellar phase), is precipitated in the $Sm_2(Co, Fe, Cu, Zr)_{17}$ grains after a multi-stage heat treatment process A schematic of the structure is shown in figure 2.12.

The theory behind the pinning coercivity of $Sm_2(Co, Fe, Cu, Zr)_{17}$ has been studied analytically by Kronmüller [52]. The cellular nanostructure within the $Sm_2(Co, Fe, Cu, Zr)_{17}$ grains pin domain walls via a difference in the domain wall energy at the boundary between the cell and cell boundary phases. Their analytical model, showing the magnetisation vectors of a domain wall pinned at an abrupt boundary between two phases I and II, is shown in figure 2.13.

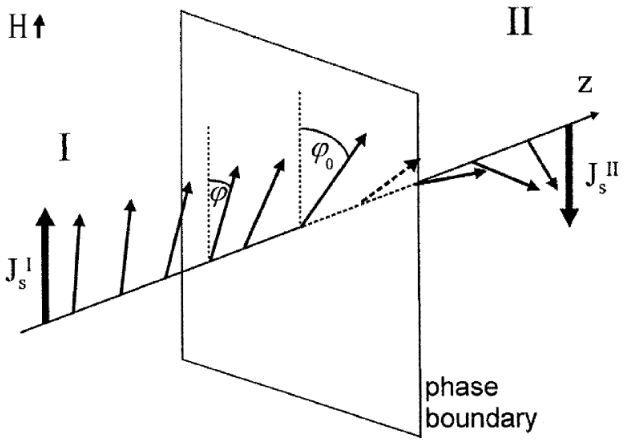

Figure 2.13: Spin configuration of a domain wall pushed into a phase-boundary by an applied field. ϕ denotes the angle between the spin vector and the easy axis. ϕ_0 is the critical angle at which the domain wall is spontaneously moved into the secondary phase [53] ©2002 Elsevier, licence granted for reuse in thesis (licence number 4197001040629).

The phase boundary represents an abrupt changes to the intrinsic magnetic property constants, K_1, J_s and A_{ex}. Using this simplified model, in which the magnetisation vector varies by an angle ϕ_0 from the azimuth at the phase boundary, then at a critical angle, ϕ_0^{crit}, the position of the domain wall becomes unstable. Kronmüller used this description to derive the field required to spontaneously move the domain wall from phase I into II, which defines the coercivity in the analytical model [52, 53].

$$H_c = \frac{2K_{II}}{J_{II}} \frac{1 - \epsilon_K \epsilon_A}{(1 + \sqrt{\epsilon_A \epsilon_J})^2} \tag{2.17}$$

The ratio of the magnetic material constants for phases I and II are given by $\epsilon_{\text{A}} = \frac{\text{A}_{\text{I}}}{\text{A}_{\text{II}}}$, $\epsilon_{\text{J}} = \frac{\text{J}_{\text{I}}}{\text{J}_{\text{II}}}$ and $\epsilon_{\text{K}} = \frac{\text{K}_{\text{I}}}{\text{K}_{\text{II}}}$.

In high performance permanent magnetic materials, it is desirable to have a large spontaneous magnetisation, such that a large energy can be stored in the stray field, and a high Curie temperature, so that the magnet has excellent temperature

stability. Therefore, an ideal permanent magnet has $\epsilon_J = \epsilon_A \simeq 1$. Implementing this conditions leads to a modification in equation 2.17.

$$H_c = \frac{K_{II}}{2J_{II}}(1 - \epsilon_K) \tag{2.18}$$

In this scenario, the field required to de-pin the domain wall is therefore optimised if ϵ_K is minimised, relating to phase 1 being magnetically 'soft' and phase II magnetically 'hard', or visa-versa. High-performance $Sm_2(Co, Fe, Cu, Zr)_{17}$ permanent magnets utilises domain wall pinning by engineering a nano-structured configuration of 'soft' and 'hard' phases; $Sm_2(Co, Fe)_{17}$, with $K_1 = 5.0\,MJ/m^3$ and $Sm(Co, Cu)_5$, which can range from a 'soft' $K_1 = 1.9\,MJ/m^3$ [54] to 'hard' $K_1 = 9.0\,MJ/m^3$ [55], depending on the alloying composition; specifically the copper content in the cell boundaries.

2.5 The development of SmCoFeCuZr magnets

The samarium based permanent magnets were developed first, with $SmCo_5$ in the late 1960s [56, 57] and later with the $Sm_2(Co, Fe, Cu, Zr)_{17}$-type magnets. The binary phase diagram for the Sm-Co system is shown in figure 2.14. Quinary system phase diagrams are difficult to construct and as such do not exist for $Sm_2(Co, Fe, Cu, Zr)_{17}$ permanent magnet alloys. However, ternary phase diagrams for Sm-Co-Fe [58] and Sm-Co-Cu [59] systems can be used to infer the preferred distributions within the $Sm_2(Co, Fe, Cu, Zr)_{17}$ microstructural phases [60].

The purpose of iron in $Sm_2(Co, Fe, Cu, Zr)_{17}$, and in REPMs in general, is to enhance the magnetic saturation and energy product, while the other alloying elements are added to generate a pinning-based microstructure. For the $SmCo_5$-type permanent magnets, no stable 1:5 phase exist for Sm(Co, Fe) alloys [9]. Initial investigations into single phase Sm_2Co_{17} and $Sm(Co_{1-x}, Fe_x)$ predicted large energy products, however, in practise these theoretical values could not be achieved due to low coercivities and inhomogeneous, multi-phase microstructures [58, 65, 66].

Through these developments, investigations began to focus on two-phase precipitation-hardened-type REPM. The addition of Cu in the form of the alloy $Sm(Co_{1-x-y}, Fe_x, Cu_y)$ [65] were able to achieve energy products of $207\,kJ/m^3$ with a developed heat treatment below 900 °C [66–68], an improvement on commercial $SmCo_5$ at $140\,kJ/m^3$ to $160\,kJ/m^3$ [66]. The addition of copper at weight additions of 10-12% [69] was found to enhance the coercivity through precipitation of a two-phase cellular nanostructure [70], comprised of 1:5 and 2:17 stoichiometries, which pin domain walls at their boundary [9, 13, 54, 66, 71]. Attempts to enhance the energy product in these alloys with greater concentrations of Fe and decreased

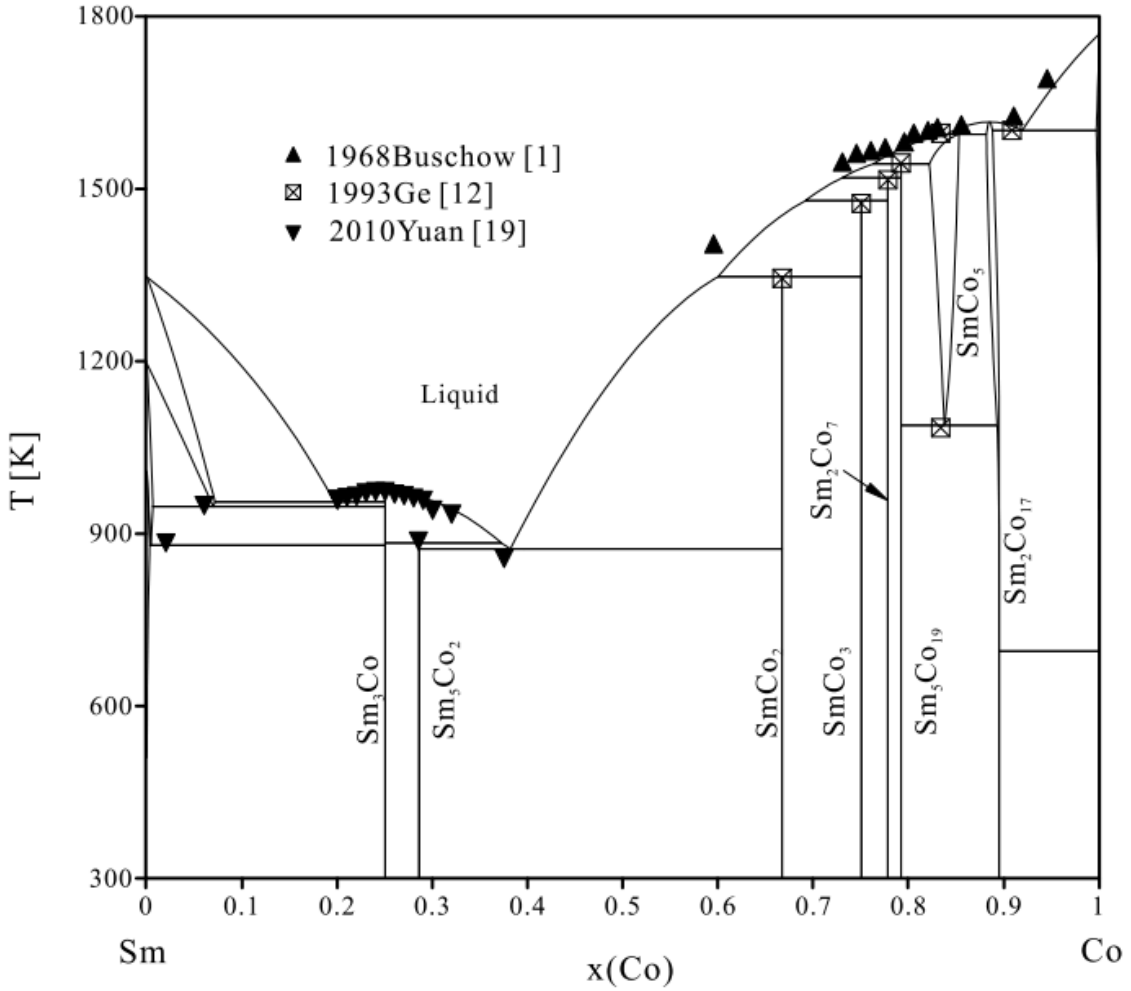

Figure 2.14: Experimental phase diagram for SmCo system comprised of data from [57, 61–64]. ©2011 Elsevier, licence granted for reuse in thesis (licence number 4307761424666).

Cu content destroyed the two phase microstructure, forming a magnetically soft Co-Fe phase and destroying the coercivity [72, 73]. Investigations which sought to stabilise the rhombahedral 2:17 (2:17R) cells and hexagonal 1:5 (1:5H) cell boundary nanostructure found the addition of small amounts of zirconium surpressed the formation of the Co-Fe phase [69]. Further refinement of the alloy composition and multi-stage step-aged heat treatment of $Sm(Co_{0.65}Fe_{0.28}Cu_{0.05}Zr_{0.02})_{7.7}$ by Mishra et al. achieved an energy product of $262\,kJ/m^3$ [74].

TEM bright-field images in figure 2.15 show an optimised cellular nanostructure within grains of $Sm_2(Co, Fe, Cu, Zr)_{17}$ after full heat treatment. Highlighted are the 2:17R $Sm_2(Co, Fe)_{17}$ pyramidal cells (A), 1:5H $Sm(Co, Cu)_5$ cell boundaries (B) and Zr rich lamellar Z-phase (C) [19].

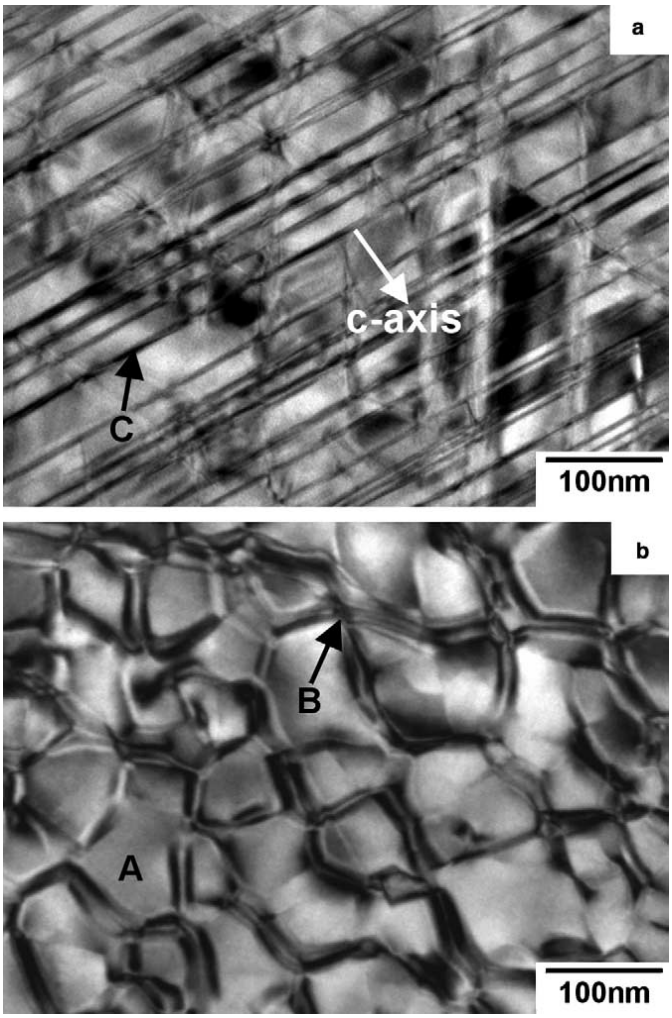

Figure 2.15: TEM bright-field images of optimised cellular nanostructure for high-temperature grade $Sm(Co_{0.784}Fe_{0.100}Cu_{0.088}Zr_{0.028})_{7.19}$. Alignment (C-axis of 2:17R phase) parallel (a) and perpendicular (b) to imaging plane. (A) highlights the 2:17R cell phase, (B) the 1:5H cell boundary phase and (C) the Z-phase [19] ©2006 Elsevier, licence granted for reuse in thesis (licence number 4196770830418).

2.5.1 Heat treatment and microstructure generation

The general form of a heat treatment for a $Sm_2(Co, Fe, Cu, Zr)_{17}$ permanent magnet is shown in figure 2.16.

The heat treatment of $Sm_2(Co, Fe, Cu, Zr)_{17}$ can be summarised by the following stages [13, 75–77]:

- Homogenisation [54, 78–82]
- Isothermal ageing [19, 23, 52, 75, 76, 78, 79]
- Slow cooling and quench [74, 75, 78, 79, 83, 84]

The pinning strength and coercivity for $Sm_2(Co, Fe, Cu, Zr)_{17}$ is strongly

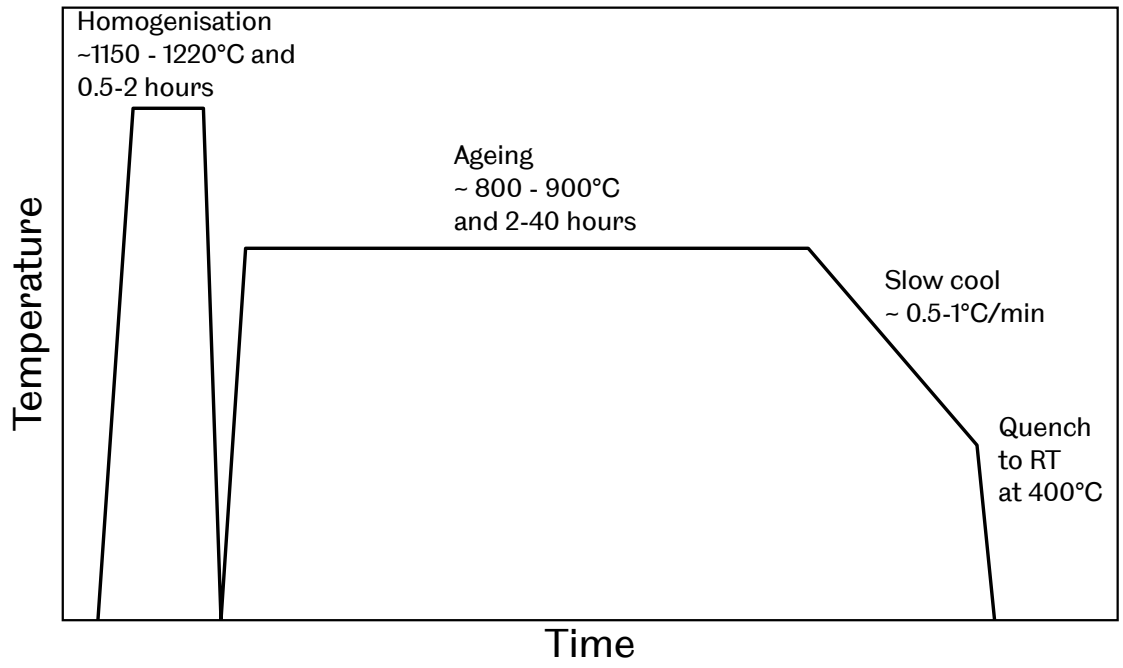

Figure 2.16: Schematic of the heat treatment used for $Sm_2(Co, Fe, Cu, Zr)_{17}$ magnets.

linked to the morphology and uniformity of the precipitated cellular and lamellar nanostructure. The alloying composition and heat treatment used will affect the size and shape of the 2:17R cells, thickness of 1:5H cell boundaries and elemental content within each phase. $Sm_2(Co, Fe, Cu, Zr)_{17}$ is a quinary system and the heat treatment shown in figure 2.16 is made up of multiple parameters over three stages, achieving the best magnetic properties for a specific application, such as; high room temperature coercivity or high temperature properties, is time consuming and complex. No 'one-size-fits-all' heat treatment exists for $Sm_2(Co, Fe, Cu, Zr)_{17}$ alloys, however in this section, the changes that occur within the $Sm_2(Co, Fe, Cu, Zr)_{17}$ grains, structurally and chemically, for a general heat treatment process are described.

The first stage is required to homogenize the microstructure into a single 1:7R or 2:17H phase. Homogenisation typically occurs between 0.5 and 2 hours at temperatures ranging from 1140 °C to 1200 °C [75, 79] and is followed by quenching to room temperature to retain much of the supersaturated single phase.

There is ambiguity and debate as to the stoichiometry and crystal structure of the high temperature phase. Several authors have identied the high temperature phase as a hexagonal 2:17 (2:17H) structure, with traces of 2:7R/2:7H structure [54, 60, 77–79]. However, Maury et al. believe it to be a hexagonal 1:7-type structure, which equates to a disordered rhombohedral 2:17 structure [19, 75]. Maury et al.

argued that partial ordering of the 1:7 structure during cooling from homogenisation temperature forms periodic microtwins, which may create additional spots on the diffraction pattern that are misindexed as the 2:17H phase [75, 85].

The isothermal ageing stage occurs at temperatures between 800 °C to 850 °C and can last from 0.5 to 24 hours and even longer [19, 74, 76, 77, 86]. Ageing time and temperature are well studied parameters on their effect on the microstructure and magnetic properties for different compositions of $Sm_2(Co, Fe, Cu, Zr)_{17}$. A good summary is given by Hadjipanayis et al. [77] and Maury et al. [75].

Almost instantly in the isothermal ageing stage, rapid ordering of Co and Fe in place of Sm occurs within the 1:7H phase (which is described by Maury et al. as 'effectively a disordered 2:17R phase' [75]), nucleating an ordered 2:17R phase. The solubility of Cu in the 2:17R phase at 850 °C is low (≈4 at.%), which induces Cu to diffuse into the remaining 1:7H matrix with Sm. This alters into the 1:5 stoichiometry [75, 87], forming the cell boundaries with thickness ranging from 5 nm to 10 nm [19]. Other authors argue the 1:5H cell boundary phase does not form until until the slow cooling stage of the heat treatment and instead, during isothermal ageing, the precipitated phases are a mixture of other stoichiometry; 2:17, 2:7, 5:19 and/or 1:3 [5, 52, 60, 88]. The argument stems from an explanation to why the coercivity of the magnet, with a fully developed precipitated nanostructure, is so low ($< 100\,\mathrm{kA\,m^{-1}}$) [5, 52, 74, 88].

A platelet lamellar phase, also known as the z-phase, forms shortly after the cellular structure. The ultra-fine Z-phase, reported as either 1:3 [60, 75, 79, 84] or 2:17 stoichiometry [5, 67], (thickness range 1 nm to 3 nm [75, 79]) runs over the pyramidal 2:17R cells and 1:5H cell boundaries, and perpendicular to the c-axis. For the remainder of the isothermal heat treatment, the 2:17R cells and 1:5H cell boundaries develop and coarsen, while the density of the lamellar phase increases rapidly at first, before stabilising. The structure appears after ageing and is shown in figure 2.15.

After isothermal ageing, a slow cooling, typically $0.5\,^{\circ}\mathrm{C\,min^{-1}}$ to $1\,^{\circ}\mathrm{C\,min^{-1}}$ to 400 °C is performed. The $Sm_2(Co, Fe, Cu, Zr)_{17}$ magnet can then be held for several hours or instantaneously quenched to room temperature. The phase structure, bar potentially the cell boundary phase, does not change during the slow cooling stage. After slow cooling and quenching, the room temperature coercivity dramatically increases to over $2400\,\mathrm{kA\,m^{-1}}$ [52, 79]. The cell boundary phase is now unanimously a 1:5H structure [5, 19, 75, 84]. This phase structure, as well as a redistribution of the alloying elements, is the basis of the coercivity enhancement. During slow cooling, Fe moves into the 2:17R cells, Cu into the 1:5H cell boundaries and Zr into

the 1:3 lamellar phase [13, 19, 52, 76, 84]. Again, the main driving force is decreasing solubility with temperature of the elements out of respective phases [79]. This is evidenced in figure 2.17, which shows high resolution EDX elemental analysis across the cell boundary and cell phase before and after the slow cooling stage.

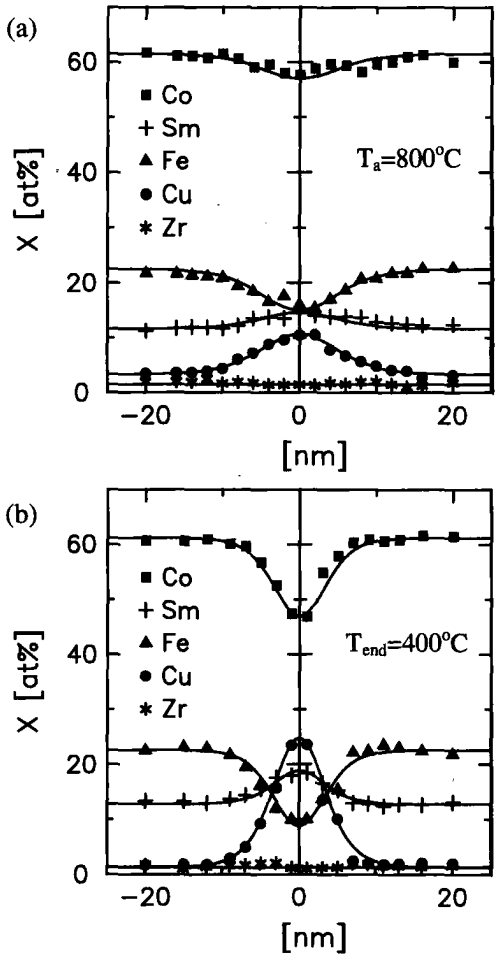

Figure 2.17: High resolution EDX elemental profiles for $Sm(Co_{bal}Fe_{0.22}Cu_{0.07}Zr_{0.04})_{7.4}$ alloy after ageing at 800 °C (a) and after slow cooling (1 °C min^{-1}) to 400 °C and quenching to room temperature (b). Middle of cell wall is located at z = 0 [52] ©2006 Elsevier, licence granted for reuse in thesis (licence number 4197001276884).

Redistribution of these elements leads to significant changes in the intrinsic magnetic properties across the cell and cell boundary. Fe enhances the saturation magnetisation of the 2:17R cells, while diamagnetic Cu dilutes the magneto-crystalline anisotropy, K_1, creating a steep K_1 gradient from the 2:17R cell into the 1:5H cell wall. Goll, Kronmüller and Stadelmaier [5] were able to relate the local Cu concentration across the cell boundary to an anisotropy energy profile (in terms of the K_1 constant), with help using data obtained by Lectard, Allibert and Ballou for the anisotropy constants K_1 of $Sm(Co_{1-x}Cu_x)_5$ alloys of varying Cu contents [89]. This

profile is shown in figure 2.18. Effectively, a domain wall energy 'barrier' or 'sink' (depending on the concentration of Cu within the cell boundaries) is created, which repel or attract domain walls and inhibit their movement [54, 90].

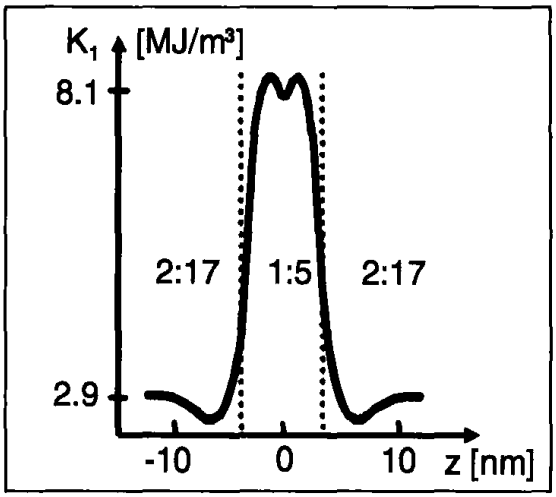

Figure 2.18: Calculated magneto-crystalline anisotropy constant K_1 using deconvolouted EDX profile, much like in figure 2.17 (b), after full heat treatment for $Sm(Co_{bal}Fe_{0.22}Cu_{0.07}Zr_{0.04})_{7.4}$ [52] ©2006 Elsevier, licence granted for reuse in thesis (licence number 4197001276884).

Calculating the strength of the pinning effect can be performed using the K_1 profiles and using a modified version of equation 2.18. A strong correlation between their analytically derived and experimentally measured coercivities for $Sm_2(Co, Fe, Cu, Zr)_{17}$ has been detailed by Kronmüller [13, 52], showing good agreement with pinning theory.

2.5.2 Study of alloying elements and their function in SmCoFuCuZr magnets

$Sm_2(Co, Fe, Cu, Zr)_{17}$ is based around the strong uniaxial magneto-crystalline anisotropy between Sm and Co, and therefore makes up, by weight, about 75% of the alloy composition. Cobalt also contributes to increase the Curie temperature (1100 K [27]) of the alloy. The exact effects of the transition elements on the magnetic properties are still debated, but their role and influence on the cellular nanostructure and magnetic properties has been evidenced in numerous systematic studies. These studies, which also investigate the ratio Sm to transition metals, known as the z-ratio, are summarised as follows.

The role of Fe

The addition of iron is primarily to increase the magnetisation of the magnet [70, 72] and, after heat treatment, is concentrated in the $Sm_2(Co, Fe)_{17}$ cells [79]. According to Ray [67], Fe stabilises the 2:17R cells in the presence of Cu. While Cu and Zr are more strongly linked with precipitation of the domain wall pinning 1:5H cell walls, Fe content has shown influence on the cell structure in $Sm_2(Co, Fe, Cu, Zr)_{17}$ magnets. Without Fe present, Sm(Co, Cu)-type alloys, aged at 800 °C, resulted in a microstructure consisting of a 1:5H phase and Co-Cu solid solution [70].

When the Fe content was increased in $Sm(Co_{bal}Fe_xCu_{0.078}Zr_{0.033})_{8.3}$ alloys (x = 0 to 0.244), there was no significant change in the average cell size at around 100 nm, or density of the lamellar phase [91]. For high-temperature $Sm(Co, Fe, Cu, Zr)_z$ alloys, where $z < 8$, the effect of the cell size with Fe content was different. In $Sm(Co_{bal}Fe_vCu_{0.128}Zr_{0.02})_{7.0}$ alloys, for low weight addition of Fe, smaller (around 50 nm and non-uniform cells were observed. Increase in the Fe content increased the average cell size and uniformity of the cells [77]. Excessive levels of iron, especially in the absence of Zr, see the 2:17R cell and 1:5H cell wall structure breaks down, with a Co-Fe phase is forming, and dramatic reduction in coercivity [67, 70, 72].

Cell size can be linked to the coercivity in $Sm_2(Co, Fe, Cu, Zr)_{17}$ magnets. For a fixed Cu content, larger 2:17R cells decrease the volume fraction of 1:5H cell boundaries, leading to an increase in coercivity, as the concentration of Cu in the cell walls is greater and so is the difference in domain wall energy.

For compositions of $Sm(Co, Fe, Cu, Zr)_z$ with $z > 8.0$, the presence of Fe showed no significant effect on the cellular nanostructure but did increase the magnetisation with Fe content [91]. However, the enhancement of magnetisation with Fe comes at a cost to the temperature dependence of the magnetic properties. Iron dilutes the effective magneto-crystalline anisotropy, K_{eff} of the magnet and thus has a negative effect on the Curie temperature and temperature coefficient of intrinsic coercivity, β_{Hc} [91]. Liu et al. showed for a composition of $Sm(Co_{bal}Fe_xCu_{0.078}Zr_{0.033})_{8.3}$, that an increase in the Fe content from 0 to 0.244 increased β_{Hc} from $-0.13\,\%/K$ to $-0.29\,\%/K$ (over the temperature range from room temperature to 474 K). Therefore, $Sm_2(Co, Fe, Cu, Zr)_{17}$ alloys designed for use at high and variable temperatures, need to minimise the Fe content as necessary to retain coercivity at high temperatures and maintain magnetic stability.

The role of Cu

Cu has a very important role in the formation of the cellular nanostructure, and in turn, the achievable magnetic properties [70]. Generally speaking, Cu stabilises

the 1:5H cell boundary phase in the presence of Fe [67]. In the absence of Zr, the cellular nanostructure in Sm-Co-Fe-Cu-type alloys only forms with relatively large Cu contents [77]. $Sm(Co_{bal}Fe_{0.1}Cu_yZr_x)_{8.5}$ magnets, where y = 0.088 and x = 0, the microstructure consisted of Cu-rich rod-like needles of the 1:5 phase within a 2:17 matrix [80, 92]. Further increment of Cu (y = 0.168) eventually precipitated a fine and uniform cellular structure (average cell size = 35 nm), forming after a short ageing (1 hour). The cellular structure was very sensitive to the length of heat treatment, with further ageing developing and coarsening the cells, before completely breaking down after 9 hours. The underdeveloped cellular structure of these Cu heavy alloys had low coercivities, which evolved over the heat treatment from 450 kA m^{-1} to 160 kA m^{-1} [80].

With Zr present, the 2:17R cell and 1:5H cell boundary nanostructure forms more readily with lower Cu content [92]. Measurements of TEM micrographs for $Sm(Co_{bal}Fe_{0.1}Cu_yZr_{0.04})_{8.5}$ magnets show the cell size decreased with increasing Cu content [77]. For this alloying compositon, M_s decreased and H_c increased initially, before slowly decreasing, as Cu content was increased [77]. $Sm(Co, Fe, Cu, Zr)_z$ alloys, with high Cu content and low z-ratio ($\approx$ z = 7.0-7.5) have lower room temperature coercivities than high z-ratio (z $\approx$ 8.0-8.5), but hold their coercivity at temperatures above 500 °C and above [77, 93, 94].

Cu importance towards the pinning potential and coercivity of $Sm_2(Co, Fe, Cu, Zr)_{17}$ magnets has already been stated in describing the structural and chemical changes during the heat treatment process. The pinning strength of the magnet can be characterised by the initial magnetisation curves, described previously in section 2.3.1, and they can be imaged through Lorentz microscopy, as shown in figure 2.19.

The content of Cu in the cell walls will affect the pinning mechanism of $Sm_2(Co, Fe, Cu, Zr)_{17}$ magnets. Figure 2.20 shows simulated anisotropy field, H_A profiles centred on the 1:5H cell wall and into the 2:17R cell for low and high Cu concentrations. In figure 2.20 a), the higher magneto-crystalline anisotropy of the 1:5H phase ompared to the 2:17R phase creates a energy 'barrier' for domain walls in the 2:17R phase near the 1:5H cell boundary. This is an example of repulsive pinning. In figure 2.20 b), a high Cu concentration reduces the magneto-crystalline anisotropy of the 1:5H phase, such that is lower than the 2:17R cell phase. Now, an energy 'well' exists for domain walls, which are trapped in the 1:5H cell wall. This is an example of attractive pinning and gives rise to the zig-zag pinning structure, shown in figure 2.19. For this type of pinning, it is essential for the cell boundary phase to be uniform, connected and between 5 nm to 10 nm thick [75], to fit domain walls, as defined by equation 2.12 [55].

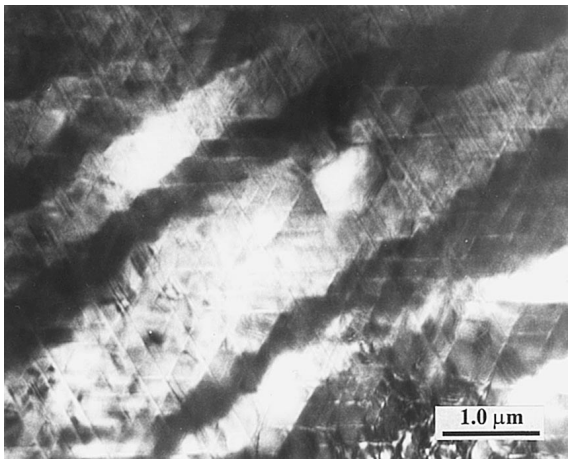

Figure 2.19: Serrated magnetic domains, pinned at cell boundaries in $Sm_2(Co, Fe, Cu, Zr)_{17}$ magnets and imaged by Lorentz electron microscopy (Foucault technique). Zig-zag structure of domain walls does not change with applied field. [21]

The Cu content in the 1:5H cell walls will depend on magnet alloy composition, cell size (equivalent to cell boundary density) and structure and parameters of the heat treatment process. Variation of these parameters allows the Cu content in the 1:5H cell boundaries to be controlled, either to minimise or maximise the Cu content to create the largest energy 'barrier' or 'well' and maximise the pinning field and coercivity, either at room temperature or for high temperatures. $Sm_2(Co, Fe, Cu, Zr)_{17}$ magnets with coercivities above $600\,kA\,m^{-1}$ at $500\,°C$ are generally high in Cu, low in Fe content and $z < 8.0$ (i.e. high in Sm content) [95].

The role of Zr

Zr is responsible for the formation of the fine structured lamellar z-phase that runs perpendicular to the c-axis [25]. Absent in TEM micrographs taken of Zr-free Sm-Co-Fe-Cu, the lamellar phase becomes instantly apparent with small Zr concentrations [80] $Sm(Co_{bal}Fe_{0.1}Cu_{0.088}Zr_{0.01})_{8.5}$ The lamellar phase develops early on during the ageing stage of the heat treatment of $Sm_2(Co, Fe, Cu, Zr)_{17}$ magnets, however its presence does not significantly contribute to domain wall pinning. This is evidenced with low coercivities ($< 100\,kA\,m^{-1}$) measured in specimens with fully developed cellular and lamellar structure after isothermal ageing and quenching to room temperature [13, 74]. Instead, the presence of the lamellar phase appears to stabilise the fine cellular structure and maintain uniformity over prolonged ageing times [74, 79, 92]. The formation of the $Sm(Co, Cu)_5$ 1:5H cell boundary phase is also achieved for lower concentrations of Cu, suggesting the lamellar z-phase promotes the segregation of Cu into the cell boundary phase through easier

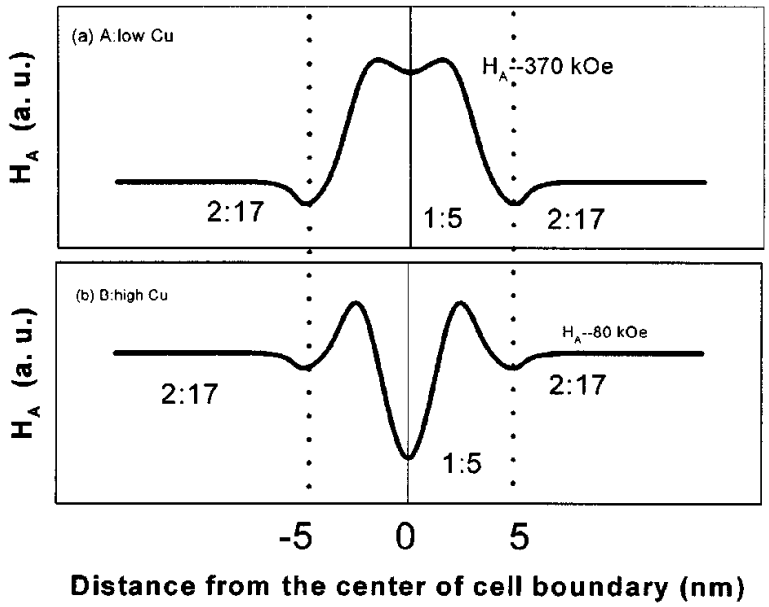

Figure 2.20: Simulated anisotropy field, H_A profiles, centred on the 1:5H cell wall and into the 2:17R cell for (a) low Cu concentration and (b) high Cu concentration [77]. ©2000 IEEE.

diffusion paths [92]. The diffusion of Cu into the 1:5H cell boundaries during the slow cooling stage of $Sm_2(Co, Fe, Cu, Zr)_{17}$ heat treatment creates the sharp domain wall energy difference between the two phases, which trap or repel domain walls. Substitution of Co for some Zr also allowed greater quantities of Fe to added to the alloy composition without formation of the soft magnetic Co-Fe phase [69].

The width of the lamellar phase did not change significantly with increasing Zr content, but the number density was shown to rapidly increase and then stabilise with additional Zr content (x = 0.01 - 0.08) in $Sm(Co_{bal}Fe_{0.1}Cu_{0.088}Zr_x)_{8.5}$ magnets [80]. The increased density of the lamellar phase with Zr content contributed to a decrease in the 2:17R cell size in studies of $Sm_2(Co, Fe, Cu, Zr)_{17}$ with fixed Cu contents. An initial increase in coercivity is observed as an ideal cell size and boundary phase volume fraction is reached, before decreasing as the Cu concentration decreases within the increasing volume fraction of 1:5H cell boundary phase [92]. Increasing the Zr content above 0.08 lead to formation of a 2:7 stoichiometry Sm-Co phase, leading to a decrease in the coercivity and high temperature properties [80].

2.6 Applications of REPMs

The purpose of a permanent magnet is to create an energy dense, stable magnetic field without the expenditure of energy. Sintered REPM offer the greatest energy

density for permanent magnets; extremely resistant to demagnetisation and, if textured, highly magnetic and energy dense. The external stray field of the permanent magnet is used to reliably interact with other material components in the 'air gap'. This general property makes them essential components for a wide-range of applications: electric motors/generators, actuators, sensors and components of computer hard-drives [9, 25, 96] and their usage is growing rapidly [2].

The resulting reduced volume of high performance REPMs such as Nd-Fe-B have seen dramatic advances in consumer and industrial devices where solenoids cannot be used. For example, small disk shaped REPMs, which may be used in a pair of head-phone speakers, with a diameter of 4 mm and height 2 mm, may have a $M = 1\,MA\,m^{-1}$. The magnetic moment of the material is therefore $\approx 0.1\,Am^2$. For a magnetic coil to produce to the same magnetic moment for similar dimensions, would require some 2000 ampere-turns [9]. In electric motors or generators, REPM are incorporated with solenoids to either create a torque to drive a rotor or, if driven, generate a current in the windings through Faraday's law of induction. Many variations of the electric motor exist and the REPMs may be situated on the stationary stator or the dynamic rotor [97]. The most commonly encountered electric generator is the simple bicycle dynamo, however increasingly more abundant are the large scale disc-type generators found in wind driven turbines. Aside from motors, actuators are another electromechanical application of permanent magnets which are produced in units of millions globally [25]. The most common utilisation are in computer hard drives, where REPM magnets are combined with current windings to precisely rotate the read/write head into the desired position. These devices have greatly benefited from more energy dense REPMs which, combined with other innovations in hard-drive technology, have reduced the size and improved the memory density of computer hard-drives.

Nd-Fe-B-type magnets are less expensive than SmCo-type and dominate maximum energy densities at room temperature. Thus, Nd-Fe-B-type magnets are the magnet of choice for room-temperature applications requiring REPMs [2]. However, for applications in which the environment is at high temperature ($>80\,°C$), the cost gap closes as dysprosium is required to be added to Nd-Fe-B-type magnets to improve their resistance to demagnetisation at elevated temperature [98].

The Sm-Co series of REPM find their uses in high temperature, corrosive and oxidising environments [20, 25, 96, 99]. In comparison to Nd-Fe-B, $Sm_2(Co, Fe, Cu, Zr)_{17}$ has a significantly larger Curie temperature (around 330 °C [96] and 800 °C [54] respectively) and excellent temperature stability of the coercive field at elevated temperatures [54]. As a result, above 150 °C, $Sm_2(Co, Fe, Cu, Zr)_{17}$ becomes the only viable REPM which can maintain performance and stabil-

ity at high temperature [99]. Specially designed high temperature grades of $Sm_2(Co, Fe, Cu, Zr)_{17}$ can even operate in environments where temperatures are above 400 °C [88, 93, 100, 101].

The applications that $Sm_2(Co, Fe, Cu, Zr)_{17}$ are therefore most suited to, and used almost exclusively, are in the military and aerospace industries [101–104]. These applications include accelerometers, gyroscopes and travelling wave tubes (TWT) [20, 25, 103], all of which benefit from the 'near-zero' temperature coefficient grades of $Sm_2(Co, Fe, Cu, Zr)_{17}$ [99]. TWT are used in aircraft and satellite radar and communications and require a narrow beam of electrons over the length of the tube, while coupling energy from an external helical coil [25, 103].

A drive within the military and aerospace industries is towards more electric aircraft to improve reliability, maintainability and supportability. Advancements in power generation, including magnetic bearings, aircraft integrated power units (IPU) and starter/generators internal to the aircraft propulsion system [103]. The operating temperature of the IPU is typically around 300 °C, with intent to operate at even higher temperatures in future design iterations [103]. For these types of application, specific grades of $Sm_2(Co, Fe, Cu, Zr)_{17}$ magnets are more beneficial. Where temperatures exceed 300 °C, SmCo-type permanent magnets have been shown to outperform Nd-Fe-B magnets in the power and torque generation of electric motors [101, 105].

Static applications of $Sm_2(Co, Fe, Cu, Zr)_{17}$ include magnetic annealing, where large, uniformly magnetised REPM segments are configured to create a long-range and uniform magnetic fields which are used to induce texture in a magnetic materials during annealing at temperatures in excess of 150 °C [9]. These non-uniform fields can also be created by careful arrangements of the REPMs, such as in Halbach arrays. These arrangements can be used for charged particle beam control and focussing electrons in cathode ray tubes and other electro-optic devices [25].

2.6.1 Oxidation and contamination of SmCoFeCuZr permanent magnets

During the lifetime of their operation, the magnetic properties of REPM degrade [102, 106, 107] which lead to losses in their application [108]. The degradation can arise when microstructural or phase changes occur at the surface of the magnet or when the operation of the magnet exceeds the working point of the magnet and irreversible, but not catastrophic, demagnetisation occurs within the magnet. With the application of $Sm_2(Co, Fe, Cu, Zr)_{17}$ permanent magnets at high temperature, and their coercivity mechanism defined by pinning rather than nucleation hardening, the degradation of magnetic properties over the life-cycle in for $Sm_2(Co, Fe, Cu, Zr)_{17}$

is linked to changes in the microstructure. In this work, oxidation and carbon contamination are most appropriate sources of microstructural changes [109] and a literature review of such effects is provided.

Oxidation

Numerous studies conducted into understanding and preventing oxidation in $Sm_2(Co, Fe, Cu, Zr)_{17}$ permanent magnets have ranged from the empircal; simple comparison of the hysteresis loops and magnetic properties after isothermal ageing [106], to detailed analytical study of the phases present within the surface oxide scale and internal oxidation zones (IOZ) [107, 110–113].

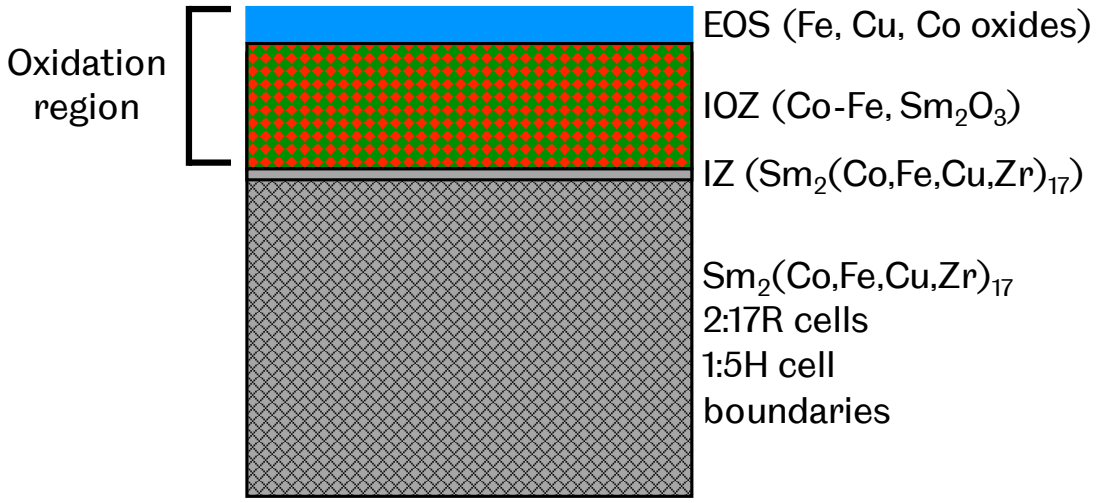

Figure 2.21: Schematic showing the structure of the oxidation region in $Sm_2(Co, Fe, Cu, Zr)_{17}$ magnets exposed to oxygen at temperatures >400 °C. The oxidation region is primarily made up of the External Oxidation Scale (EOS) and Internal Oxidation Zone (IOZ). Underlying affected region highlighted as the Inter-diffusion Zone (IZ). The unaffected $Sm_2(Co, Fe, Cu, Zr)_{17}$ cellular nanostructure lies underneath. Region thickness are implied and not to scale.

A schematic of the reported oxidation structure of $Sm_2(Co, Fe, Cu, Zr)_{17}$ is shown in figure 2.21. In general, there are two main oxidation regions, an external oxidation scale (EOS), which is free of Sm and primarily made up of oxides of Co, Fe and Cu, and a much thicker internal oxidation zone (IOZ) which is primarily a matrix of the soft magnetic Co-Fe, embedded with a fine precipitations of Sm_2O_3, as well as Cu and Zr [110, 111, 113, 114]. The EOS layer forms first as Co, Fe and Cu oxides form on the surface and grow outwards as the aforementioned elements diffuse from inside the $Sm_2(Co, Fe, Cu, Zr)_{17}$ material. The IOZ region grows as oxygen penetrates within the $Sm_2(Co, Fe, Cu, Zr)_{17}$ material and the 2:17R cells and 1:5H cell boundaries decompose as Sm is removed in the formation of Sm oxides. Co-Fe

forms in an absence of Sm, with fine precipitates of Sm_2O_3 and insoluble Cu and Zr dispersed throughout the IOZ region. Wang et al. reported after exposure to oxygen at 600 °C for 1 hour, their $Sm_2(Co, Fe, Cu, Zr)_{17}$-type magnet measured an EOS layer of thickness 1.4 µm and an IOZ region of thickness 10.4 µm. After 50 hours, the two regions grew to a depth of 11.6 µm and 173.3 µm respectively. Pragnell, Williams and Evans [111] noted the EOS layer did not exceed a thickness of 15 µm even after 300 hours at 600 °C or even 1000 hours at 300 °C. The internal oxidation is a much greater problem than the external oxidation due to the much larger extent of the IOZ and the destruction of the hard magnetic $Sm_2(Co, Fe, Cu, Zr)_{17}$ cellular nanostructure into the soft magnetic Co-Fe phase. A given specimen will experience magnetic losses proportional to the volume consumed by the oxidation zone [111]. Beneath the IOZ lies a smaller but notable region referred to as the interdiffusion zone (IZ). The IZ does not contain oxide precipitates, but is instead deficient in the necessary elements, such as Cu, which stabilise the 2:17R cell and 1:5H cell wall structure [67]. The affected cellular nanostructure becomes irregular and this effect is believed to contribute to irreversible magnetic losses [112–114].

Even with short exposure to oxidising environments, the magnetic properties of $Sm_2(Co, Fe, Cu, Zr)_{17}$ suffer and as the exposure time or oxidising conditions increase, so too does the degradation of the magnetic properties. Wang et al. details how exposure at 600 °C for 1 hour can have a notable effect on the shape of the $Sm_2(Co, Fe, Cu, Zr)_{17}$ specimen demagnetisation curve. After exposure for 10 hours, the coercivity reduced by nearly 30% [114]. These temperatures are more extreme than would be expected of he applications currently requiring $Sm_2(Co, Fe, Cu, Zr)_{17}$ magnets, but do show the affect on the magnetic properties if the internal oxidation zone reaches a depth of approximately 100 µm, as is the case in the 10 hour exposure specimen. This correlates with the increasing volume fraction and penetration depth of the aforementioned oxidation regions. The application of a nickel based coating to $Sm_2(Co, Fe, Cu, Zr, C)_{17}$ can protect and improve the resistance to oxidation in the most adverse and challenging environments [110, 115].

Carbon contamination

Carbon is another form of contaminant, along with oxygen, which can severely affect the microstructure and magnetic properties in commercial $Sm_2(Co, Fe, Cu, Zr)_{17}$ permanent magnets [109]. Several studies investigating potential uptake of carbon during the SPS process have used techniques such as EDS to measure the carbon concentration from the surface into the material [45]. In glass ceramic spinels, EPMA was used to identify contaminates as carbon, which reduced their transparency [116–120]. However, these studies could not conclude whether the car-

bon was a contaminant within the powder or whether it was a result of contact with the graphite mould. Studies by Tian et al. on the residual carbon in metal injection molded $Sm_2(Co, Fe, Cu, Zr)_{17}$ magnets with an organic binder found the carbon present in weight concentrations of 0.21 wt.% halved the coercivity and distorted the demagnetisation curve in comparison to carbon-free magnets [121]. When the weight percentage of carbon was 0.43 wt.%, the coercivity effectively reduced to zero. These studies were based upon having carbon mixed throughout the sintered magnet, rather than concentrated at the surface as would be expected from a diffusion process. Similar observations were made by Gong [122], whose investigations of $Sm_2(Co, Fe, Cu, Zr, C)_{17}$ melt-spun magnets saw the coercivity and energy products reduce significantly with the carbon weight percentage addition approximately 4 wt.%. It is noted that both of the studies of carbon in $Sm_2(Co, Fe, Cu, Zr, C)_{17}$ were not performed using the SPS technique. The reduction of coercivity and disruption of the demagnetisation curve was attributed to a break-up of the $Sm_2(Co, Fe, Cu, Zr, C)_{17}$ cellular nanostructure by removal of Zr through formation of ZrC [121]. Zr is critical to the formation and stabilsation of the 2:17R cells and 1:5H cell boundaries during heat treatment [79].

2.6.2 Eddy current effects in permanent magnets during operation

In the aforementioned applications of $Sm_2(Co, Fe, Cu, Zr)_{17}$ permanent magnets, the highly-dynamic and demanding environments [103] necessitate these REPMs to be mechanically strong (resisting the centrifugal forces subjected at high rotational frequencies), and magnetically hard, to resist demagnetisation, possess high Curie temperature to be stable at high temperatures and also be resistant to oxidation/corrosion and/or contamination. However, there are additional areas for material optimisation that reduce losses and/or irreversible demagnetisation incurred in the magnet during operation in machines, with these losses related to electromagnetic fields affecting the operation of the permanent magnets. Using electric motors as an example again, two common types of losses encountered are eddy current and hysteresis losses [123]. The latter type is the energy lost cycling the magnet through the hysteresis loop. REPMs are designed for magnetic stability and resistance to demagnetisation, so we expect these losses to be minimal in comparison to eddy losses. This assumption has been shown to be true in open circuit AC electric motors, where the 'working point' of the magnet is in the stable and square second quadrant of the hysteresis loop [123, 124]. Unless severe, irreversible degradation of the coercivity occurs for the permanent magnet, we can concern ourselves primarily with the study into the minimisation of the eddy current losses in REPMs.

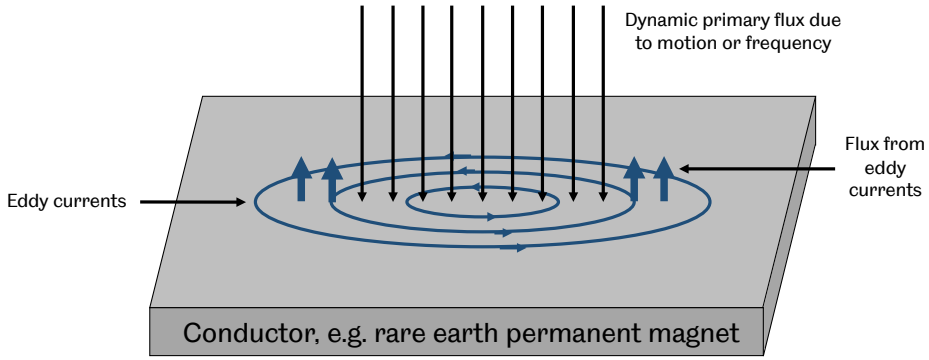

Figure 2.22: Schematic showing generation of eddy currents within a conductor.

The origin of the eddy currents, named after circulating eddies seen in turbulent fluids, is due to electrically conductive materials experiencing a change in flux density. Eddy currents are a circulating flow of electrons within the body of the conductor, which in this case is the permanent magnet material, which create a magnetic field. This response is described by Lenz's law, which states 'An induced current always flows in such a direction as to oppose its cause' [125]. A visual schematic of the effects are shown in figure 2.22.

In electrical machines, stray electromagnetic fields emanate from permanent magnets and/or coil windings within the machine, which are broadly collected as the 'air gap field'. During operation, movement through the air gap field over time create eddy currents within the permanent magnet.

While eddy losses are smaller relative to other types of power losses [97, 108], the eddy currents create heating within the magnet via Joule heating, which is proportional to the square of the electric current (RI^2) [126]. Raising the temperature of the permanent magnet beyond its specified operational temperature will result in significant irreversible demagnetisation, through nucleation of reversal domains, microstructural changes and oxidation effects [6, 108]. $Sm_2(Co, Fe, Cu, Zr)_{17}$ magnets have better temperature coefficients than Nd-Fe-B type magnets and tend to be used in applications where the operating temperature exceeds 250 °C [103, 127]. While $Sm_2(Co, Fe, Cu, Zr)_{17}$ is better equipped for temperature fluctuations, the eddy current effect will still be prominent in the conductive $Sm_2(Co, Fe, Cu, Zr)_{17}$ material and can cause partial, irreversible demagnetisation.

Laminations

Methods can be employed to reduce the eddy current effects. Segmentation, which can be axial or circumferential, involves cutting the magnet and applying an electrically insulating layer before reassembly [6, 126, 128]. While this is a successful method in reducing eddy current effects, by limiting their circulating area, it is a costly and time consuming processing method. Material wastage also occurs during segmentation, which for high performance, rare-earth containing REPMs, is highly undesirable, especially after the volatility in the pricing and uncertainty in sourcing the rare earth elements, such as Nd, Dy and Sm, during the 'rare-earth crisis' of 2011 [129].

2.6.3 High resistance materials

Studies investigating efficient, low-cost methods to reduce eddy current effects, which can be added into the current processing route for sintered rare earth permanent magnets have increased over the last decade. These have generally revolved around increasing the bulk resistance of the REPM, as the eddy currents are resistance limited and losses are inversely proportional to the resistivity of the magnet [6, 7, 130].

Energy dense REPM used in electric motors are inherently very conductive and their resistivities typically range from $70\,\mu\Omega\,\mathrm{cm}$, for samarium-based, to $200\,\mu\Omega\,\mathrm{cm}$, for neodymium-based, permanent magnets [131–133]. As most energy dense REPMs are produced by powder sinter method, the majority of studies have investigated the viability and effect of mixing electrically insulating material with the magnetic powders, either in the form of coating the precursor powder or through a blend, as a method of increasing the bulk resistivity.

Initial studies looked at producing thin polymer films at the surface of powders and compacting the powders to produce anisotropic magnets [134]. This method was very successful at increasing the resistivity and reducing eddy current losses, especially in the polymer coated $Sm_2(Co, Fe, Cu, Zr)_{17}$ type permanent magnets. However, this method of eddy resistance could not be processed at conventional temperatures and also limited the magnets operational temperature below $100\,^{\circ}\mathrm{C}$ due to softening of the polymer [134]. The polymer/magnet composite was also much lower in density and this impacted the magnetic flux and energy product of the material. Bonded permanent magnets suffer from the same limitations at elevated temperature [7].

Research has progressed away from polymers due to these reasons and onto other insulators of the type: fluorides, nitrides and oxides of boron, calcium, dysprosium, neodymium. In all cases, the introduction of insulating material increases the resistivity, however different success has been achieved by incorporating the non-conductive phases via differing processing methods; varying from coatings to blending and the formation of laminate layers.

Powder coatings

Isotropic, hot-pressed Nd-Fe-B powders coated with $NdF_{2,3}$ were investigated by Komuro et al. [135]. With a 200 nm average thickness, the fluoride coating increased the resistivity considerably, increasing from 140 µΩ cm to 1400 µΩ cm. The magnets were subjected to an alternating magnetic field of 20 Oe at 2 kHz and the temperature rise was measured to characterise the effect of eddy current generation. The increase in temperature for the coated powder magnet was $\frac{1}{8}$ compared to the non-coated magnet. The coated magnets measured the same coercivity as the un-coated comparison sample, while the magnetic flux was reduced by a percentage comparable to the volume percentage (9%) of the fluoride in the material.

Other studies of this nature have shown mixed results relating to the coating process and coating material used. Nd-Fe-B-type powders coated with SiO_2 showed only moderate increases in the resistivity (22% increase), before thicker coatings significantly diminished the coercivity of the magnet [136]. Nd-Fe-B-type powders coated with CaF_2 by different methods were reported by Zheng et al. in anisotropic, hot-deformed composite magnets [137, 138]. Hot deformation induces texture in the pressing direction and creates a layered insulating phase structure. Utilising a two-step coating process, Zheng et al. were able to achieve a resistivity of 847 µΩ cm, an increase of 268%, compared to the uncoated Nd-Fe-B magnet [137]. However, there was a considerable reduction in the coercivity of the magnet, likely due to oxidation from the prolonged coating process. Using a alternative liquid phase coating technique, Zheng et al. were able to improve on their previous results, maintaining the coercivity of the CaF_2 coated Nd-Fe-B magnets close to the uncoated Nd-Fe-B magnets, while also improving the resistivity by 258% [138]. Ferrite coated $Sm_2Fe_{17}N_3$ powders showed significant resistivity enhancement, with little effect on the coercivity, although full density was not achieved in these composite magnets [139].

It can be concluded from these studies that coating the precursor powder can be a very successful method of producing increased resistivity REPMs. However, it is clear that the process is sensitive to the type of insulating material and the

process used to coat the precursor powder. Achieving a consistent. sufficiently thick coating, while also avoiding oxidation, is essential to achieve a significant increase in the resistivity, while also avoiding degradation to the magnetic properties. Growing consistent thin films on precursor powders adds further complexity to the processing chain.

Blended powders

A much simplified method of introducing insulating material is to simply blend magnetic and insulating powders together before compaction. This methodology is enticing, as it can easily be introduced into current powder processing routes, instead of requiring additional coating and drying under inert conditions.

One study by Marinescu et al. investigated different fluorides ($CaF_2, NdF_3, \text{and} DyF_3$), added in fixed 5 wt.%, to Pr-Fe-B-type magnetic powders and compacted [8]. Hot deformation by die-upsetting was used to induced texture in the pressing direction and create a layered insulating phase structure in the composite magnet, as displayed in figure 2.23.

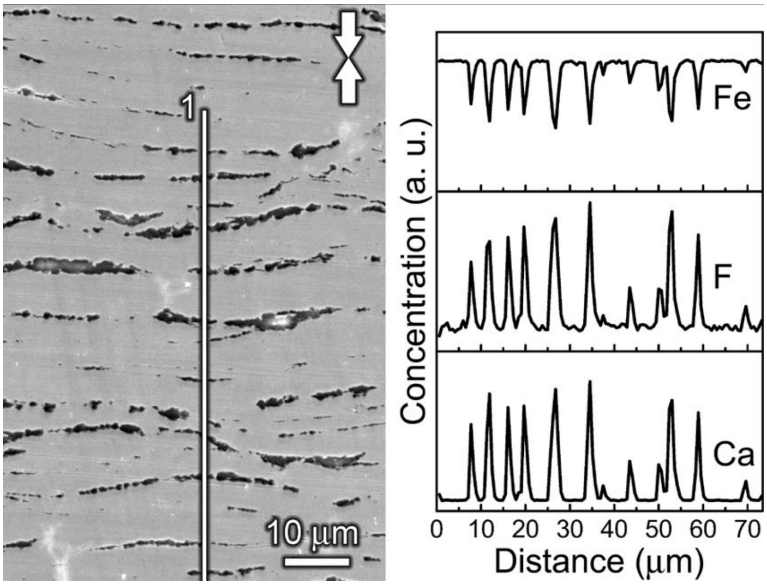

Figure 2.23: (Backscattered electron SEM image and concentration line scan for Pr-Fe-B with 5wt% CaF2 die-upset magnet. The starting point of the line scan is marked with 1. Arrows indicate the pressure direction. [8] ©2009 AIP Publishing LLC, licence granted for reuse in thesis (licence number 4197010958341).

The resulting layered structure increased the resistivity significantly in all composite magnet specimens when measured parallel to the texture direction. $873\,\mu\Omega\,\text{cm}$ was measured for the Pr-Fe-B and CaF_2 sample. However, the resistivity measured perpendicular to the texture direction was much lower - $200\,\mu\Omega\,\text{cm}$. Expectedly,

all studied composite specimens reduced their remanence with introduction of non-magnetic phases, but the coercivity either maintained or noticeably increased with the rare-earth fluorides. The addition of 5wt. % NdF_3 even improved the squareness of the demagnetisation curve. The introduction of heavy rare-earths via fluorides, interact with the grain boundary phase of Pr-Fe-B magnets to increase the local magneto-crystalline anisotropy and impede nucleation of reversed domains. The use of rare-earth fluorides or nitrides to enhance the coercivity by this method, known as grain-boundary diffusion, for Nd-Fe-B-type magnets is well documented [130, 140–142]. While no loss of coercivity was measured by Gabay et al. with the addition of CaF_2, Li et al. measured a decrease in the remanence, coercivity and energy product with increasing concentrations of non-layered CaF_2 in blended Nd-Fe-B-type composite magnets [133].

Zheng et al. investigated the use of oxides as an insulating material, varying weight additions of Dy_2O_3 with Nd-Fe-B-type magnets [143]. Dy_2O_3 reduced the coercivity compared to non-blended Nd-Fe-B, but increasing concentrations of Dy_2O_3 minimised this deleterious effect. Again, an interaction with the heavy rare-earth element Dy into the grain boundaries region, improved the local magneto-crystalline anisotropy. However, this effect was countered by the formation of Nd_2O_3 in the microstructure.

In all of these studies, reports of reduced anisotropy with weight addition of insulating material were discussed as remanence values decreased more rapidly than the volume percentage of non-magnetic phase. The oxides and fluorides deform less readily than the metallic magnetic material during the hot deformation process, resulting in comparably less texture.

Of the Sm-Co based high resistivity permanent magnets studied, it is predominantly the nucleation-based coercivity-type magnets $SmCo_5$ [144–146] and $Sm_2Fe_{17}N_3$ [139]. Studies by Gabay et al [144] investigated blending nanocrystalline powder flakes, produced by high energy ball milling (HEBM), of $SmCo_5$ various weight additions of mica, MoS_2, CaF_2, and B_2O_3. This method removed the requirement of hot-deformation to create a layered insulating material structure, with the high aspect ratio flakes distributing within the microstructure, naturally creating a layered structure after only hot pressing. B_2O_3 was most effective at enhancing the resistivity and created the 'best' microstructure as it melted during sintering, but was also most debilitating to the magnetic properties, again likely due to undesirable oxidation phases. At higher weight additions (10 wt.%), CaF_2 enhanced the resistivity by the most and also had the least effect on the magnetic properties, attributed to CaF_2 not interacting with the $SmCo_5$ phase.

Layered structures

Layered insulating phase structures can be created by hot deformation of composite magnets with coated or blended powders. Layered microstructures can also be produced by manually layering alternating magnetic and electrically insulating powders and sintering. By this method, anisotropy has to be introduced by use of magnetic field to reorientate the powders before compaction. This methodology was investigated by Chinnasamy et al. [7] with $Sm_2(Co, Fe, Cu, Zr)_{17}$ and Sm_2S_3 powders. Two layer widths, 50 µm and 190 µm, were investigated and an example optical micrograph showing the layered structure is shown in figure 2.24 (a).

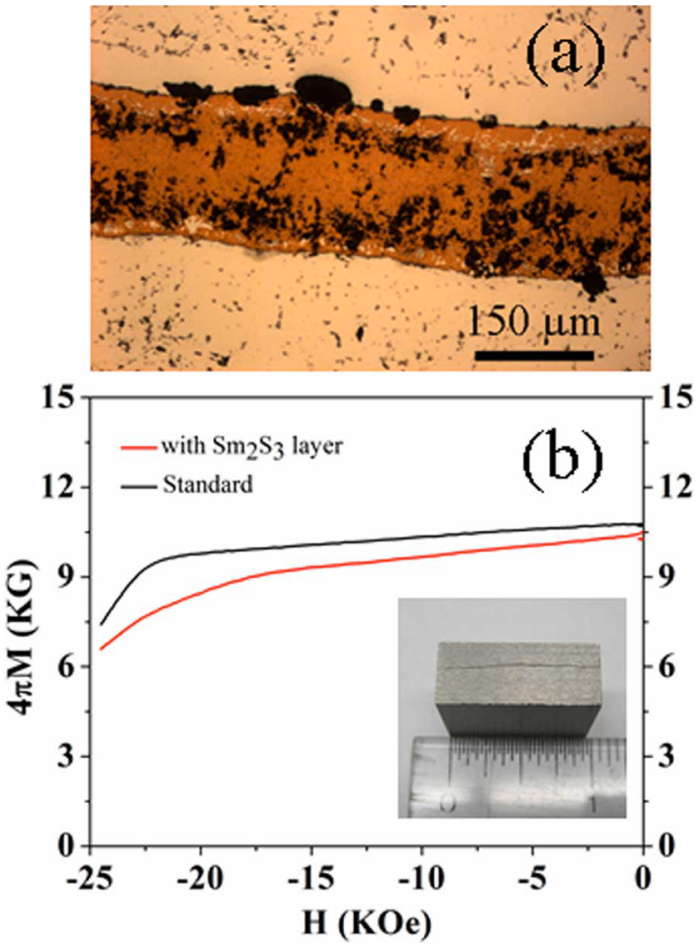

Figure 2.24: (a) Optical micrograph of composite magnet comprised of $Sm_2(Co, Fe, Cu, Zr)_{17}$ (light orange) and Sm_2S_3 laminate layer (dark orange). (b) Demagnetisation curve of the $Sm(Co, Fe, Cu, Zr)_z$ and Sm_2S_3 laminate layer sample and a standard EEC 2:17-27 grade $Sm(Co, Fe, Cu, Zr)_z$ magnet. (b) insert shows bulk specimen and layer structure. [7] ©2012 IEEE.

In figure 2.23 (b), the demagnetisation curves for a standard EEC 2:17-27 grade $Sm(Co, Fe, Cu, Zr)_z$ and 190 µm layer composite magnet shows the addition of the insulating layer reduces the remanent magnetisation and modifies the 'squareness'

of the demagnetisation curve. The coercivity remained unchanged and there was a slight reduction in energy product ($(BH)_{max}$) reduced from 223 kJ/m^3 to 200 kJ/m^3. However, the resistivity measured parallel to the alignment direction increased 30×, improving from 60 µΩ cm to 1845 µΩ cm. It was also reported that the addition of the electrically insulating layer reduced the mechanical properties of the magnet; with three-point bend tests measuring 60-70% of the original values. With large insulating layer thickness and reduced mechanical properties, these magnets may not be able to withstand the large centrifugal forces experienced in the rotor of high frequency power machines. Similar results have been observed by Gabay et al., in which they explored depositing a CaF_2 layer in Nd-Fe-B magnets, with a focus on the thickness and distribution of the layer [128]. Wang used a hybrid method of manually applying a layer of blended Nd-Fe-B-type powder and NdF_3, hot pressing and then die-upsetting. Noticeable enhancement of the resistivity and coercivity were achieved in the layered composite magnet containing 2 wt.% NdF_3. Further increase in insulating material content rapidly increased the resistivity, but began to reduce the coercivity, albeit to values higher than the standard. Overall, there was a continuous decrease in energy product [147].

Summary

Blending magnetic and electrically insulating powders offers the most efficient and practical method for improving the resistivity, and in turn reducing the eddy current heating effects using a more cost effective method, and minimising the losses incurred in REPM applications. In the majority of studies, a layered insulating phase structure is sought as this offers the largest improvement in resistivity, although this is in one direction. When hot deformation is used, texture is induced in the pressing direction, while the plane(s) of the layered insulating phase structure form perpendicular to the pressing direction. Eddy currents are created to oppose the change in flux that create them. If the anisotropic REPM is subjected to changes in flux in the opposite direction to their alignment, the eddy currents circulate within the planes between the laminate layers. The effect of increasing the bulk resistivity is bypassed in this scenario.

Chapter 3

Spark Plasma Sintering technique

3.1 Introduction

3.1.1 History of powder sintering

Ceramic materials

Sintering is a well established process by which powders or material are consolidated into a predominantly solid mass of material with improved material properties and without melting. It is a thermally activated process and therefore is achieved through the application of heat. Porosity is removed by diffusion of mass at the atomic scale and the process is driven by a decrease in free-surface energy [148]. Pressure is often accompanied with heating to enhance the densification process.

Historically, the practise was referred to as 'firing', as it was enabled by wood or charcoal fuelled fires. The earliest evidence of sintered materials can be found in ceramic pot pieces from 26,000 years [149]. As time progressed, techniques improved and the quality and range of sintered ceramic and earthenware items increased, as evidenced in archaeological sites across Egypt, China and the Middle East and by 1600 BC, the firing process improved sufficiently for the first porcelain items to be produced in China [149].

Brick is a material synonymous with building strong structures. It is made from sintering clay, a cheap and plentiful resource, and the discovery of the sintered material was followed by progressively larger and more complex building structures. More recently, the success of ceramic sintering has been realised in the production of cemented carbide dies and other extremely hard wearing materials that can only be produced by the sintering of powder.

Metals

Sintering is historically synonymous ceramics, but is also crucial to the production metallic materials as well. Sintered gold, silver, copper and bronze items have been found dating back to $\approx$ 3000 BC, while in Egypt, sintered iron artefacts trace back to $\approx$ 2800 BC [149].

In the 19th century, William Hyde Wollaston developed a consolidation process to produce high-quality platinum crucibles by way of sintering and this became the first published description of a powder sintered metal [149]. The process that Wollaston developed was followed and developed for the sintering of a wide, new range of metals. By the mid-19th century, powder sintered processed copper, silver and lead was common-place, with osmium and tungsten to follow by the beginning of the 20th century. The development and popularity of the electric lightbulb owes much to sintering as an essential processing step to produce tungsten filaments with functional life-times [149].

Ore induration, which is the process of taking pellets of ore and sintering in large furnaces became a common processing route for a number of materials over the last century. This processing method was developed with the rise of steel production during the 1940s and thereafter. The ease of transporting pellets, as well as the ability to reclaim waste iron dust through sintering back into pellets, made this method of processing very economical for industries at a time when national economies were in recovery.

3.2 Sintering methods

3.2.1 Thermally activated sintering

The historical success of the sinter process was developed through a trial-and-error approach, utilising an empirical understanding that 'firing' certain materials made them stronger. The technology required to understand the subtle changes at a microstructural level was, for the most part of history, not available to help develop and understand sinter theory. With optical microscopy and microstructure analysis development in the 1940s, combined with an understanding of atomic theory, basic quantitative sinter models emerged. These models were simplistic, but explored concepts such as surface tension between two particles [150] and surface diffusion to model neck growth and sintering [151].

The quantitative sinter models developed in coordination with improving observation techniques and equipment, allowing high magnification imaging of of neck formation by use of high-resolution electron microscopy. Modern sinter theory describes several different mechanisms of mass transport as methods which

contribute to the neck growth and porosity volume reduction between contacted particles. In the absence of pressure, the driving force for the several different mechanisms of mass transfer is a minimisation of surface energy; growth occurs to reduce the neck angle of curvature [152].

When particles are brought into contact, necks form at the contact point between particles due to inter-atomic attraction. Mass transport can occur by a number of different mechanisms, shown in figure 3.1 and summarised in table 3.1. Ashby developed sintering diagrams which describe the dominant mechanism of mass transport for a given sintering temperature and neck radius. It is important to note that not all mass transport mechanism contribute to the removal of porosity. All mechanisms contribute to neck growth, but only mechanisms 4, 5 and 6 promote densification [152].

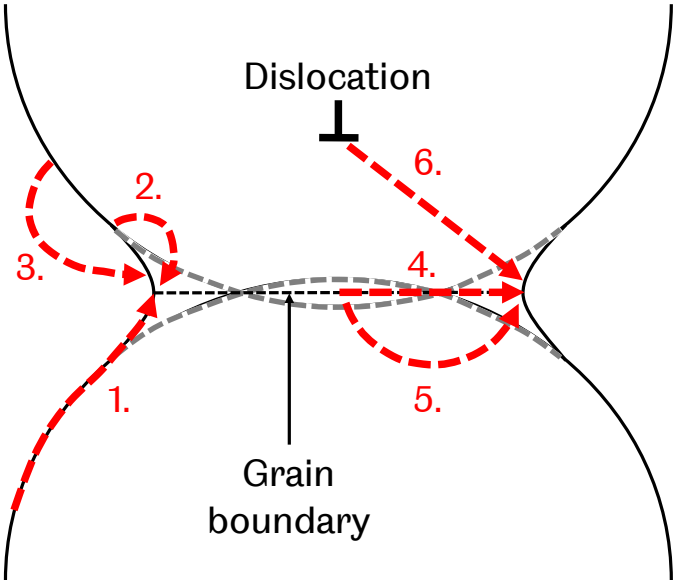

Figure 3.1: The mass transfer mechanisms in sintering. All mechanisms lead to neck growth, however only mechanisms 4, 5 and 6 cause densification

The surface-based mass transfer mechanisms (1 - 3) transport matter from one part of the pore to another. Driven by differences in curvature at the pore surface they do not bring the particle centres closer together and do not reduce porosity. These surface mechanisms have a relatively low activation energy, in comparison to the volume-based mass trafer mechanisms 4-6 and typically dominant at relatively low temperatures, with respect to the melting temperature of the material [153]. Once the pore becomes spherical, these low energy mass transfer mechanisms effectively stop, as the driving force has effectively been reduced to zero.

Mechanisms 4-6 transport mass from the within the material volume. Therefore, particle centres are brought closer together and porosity is reduced. The source of

Mechanism number	Transport path	Source of matter	Sink of matter
1	Surface diffusion	Surface	Neck
2	Lattice diffusion	Surface	Neck
3	Evaporation	Surface	Neck
4	Boundary diffusion	Grain boundary	Neck
5	Lattice diffusion	Grain boundary	Neck
6	Lattice diffusion	Dislocations	Neck

Table 3.1: Summary of six mass transport mechanisms that lead to neck growth. Mechanisms 1-3 do not lead to densification as mass transfer occurs only at the surface. Mechanisms 4-6 have mass transported from within the volume to the neck and bring the particle centres closer together, leading to densification

matter in these transport mechanisms include grain boundaries between the pores (at their contact point and from within the volume) and dislocations. These mechanisms only become dominant once pores have become spherical or when the temperature of sintering approaches the material melting point, as they are defined as high-energy mass transfer mechanisms, especially compared to mechanisms 1-3.

3.2.2 Pressure-assisted sintering

Figure 3.2 shows a schematic of powder particles, which can be an agglomeration of crystallites. Once intra-particle pores become closed and spherical, it can become difficult to remove the remaining porosity, no matter how how long the sinter process. Elimination of both intra-particle and inter-particle pores can be improved with the application of pressure to the sinter process.

Pressure increases the driving force for sintering and can lower the activation energy of the high energy mass transfer mechanisms 4-6 [155]. Pressure also has macroscopic effects through rearrangement and deformation of the powders, which help eliminate porosity via tessellation. However, if the powders are made up of an agglomeration of several crystallites then the particles can vary in shape. This will result in suboptimal tessellation and porosity can remain after particle sliding. In this instance, thermally activated processes are still necessary to achieve full density.

The last broad general mechanism for densification is through plastic deformation, where the applied stresses exceed the yield point of the material. It is an immediate effect and can create finer crystallites as they are fractured, improving densification through better tessellation, as agglomerates are broken up and increasing the contact points for more neck growth.

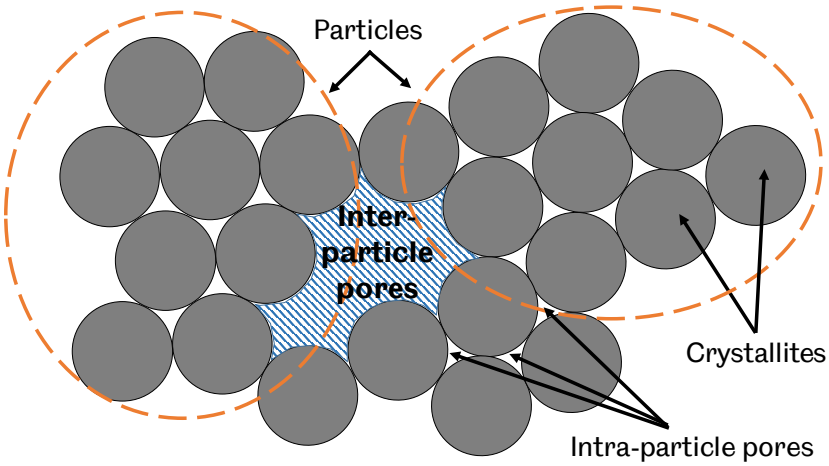

Figure 3.2: Schematic showing powder particles, which can be made up of an agglomeration of crystallites and have different shapes and contact surfaces. Porosity can be made up of intra-particle pores and inter-particle pores. Adapted from [154]

3.2.3 Current-assisted sintering

The use of electric current as a means to activate and aid powder sintering has been documented since the early twentieth century. Initially as part of an electric furnace arrangement, current was also directly passed through the material and/or crucible/mould and this method was referred to as electric current sintering. In 1922, d'Adrian combined a method dubbed 'spark sintering' with pressure [156] and in 1955, Lenel consolidated powders of titanium and zirconium [157] using the first commercial system of this nature. Subsequent work over the following decades [158, 159] has grown interest in the technique with reported benefits over conventional, electric current-free sintering methods (e.g. pressureless sintering, hot pressing and others). These benefits included lower sintering temperatures and faster sintering rates [160].

Another reported benefit in the current-assisted sintering of difficult materials is attributed to the effect of electromigration, or current-enhanced mass transport, which is a well documented effect, most often observed in semiconductor devices [161–163]. When large current densities are passed through a material, it can enhance diffusion through transfer of momentum from the flowing electrons to the ions within the material lattice. The passing of a large current density through a system during sintering has been well documented to enhance the reactivity of the material through the diffusion of elements within materials to the reacted layers [154, 164–167]. Enhanced mass transport by current effects has also been documented to enhance neck growth, leading to faster sintering and/or sintering at lower temperatures [168, 169].

3.3 Spark Plasma Sintering

3.3.1 Description of the system apparatus

Spark Plasma Sintering (SPS), is a method of powder consolidation which uses a combination of high current density and uniaxial load to apply heat and pressure directly to the powder. [153, 170]. SPS utilises either pulsed or continuous direct current (DC) during operation. Over the past few of decades, SPS has become an increasingly popular current-assisted sintering tool for material processing and research into a wide range of ceramic and metal alloys by this technique has increased exponentially [170]. SPS can be referred to by a variety of names: Field-Assisted Sintering Technique (FAST) [171–173], Current Assisted, Pressure Activated Densification (CAPAD) [153] and Pulsed Electric-Current Sintering (PECS) [168–170, 174]. However, SPS is the most popular nomenclature according to literature [170], although there is much debate as to whether sparking or plasma even occur during processing. However in this work SPS, will be used to refer to this low voltage, high current, pressure assisted sintering technique. A commercial FCT-Systeme GmbH SPS furnace is shown in figure 3.3.

Figure 3.4 show the main components of a commercial SPS machine. A powder containing, electrically conductive mould (or die), of which an example is displayed in figure 3.5, is placed within the furnace in contact with two electrodes, which provide both the current and load. A power supply provides high currents at low voltages (around 10 V). Due to the necessity for the mould material to be electrically and thermally conductive, high-purity graphite is often used, satisfying the requirement, while maintaining strong mechanical properties at high temperatures. The main vessel is a vacuum chamber which can be flooded with argon, nitrogen or air.

The power generator passes large continuous or pulsed DC current, typically 1000 A to 3000 A, through the mould (and powder if not an insulating material). For a 20 mm diameter sample, if it is assumed all the current is passed through the sample, the current density is of the order of $10^2\,\mathrm{A\,cm^{-2}}$ to $10^3\,\mathrm{A\,cm^{-2}}$. Heat is generated through resistive heating as described by the Joule equation (equation 3.1). Heating occurs within electrically conductive powder or is transferred directly to the powders by contact with the mould wall/punches. This direct method of applying heat to powders with careful control of the applied current allows SPS to achieve very high heating rates, a characteristic feature of the technique.

$$P = RI^2 \tag{3.1}$$

Figure 3.3: FCT-Systeme GmbH SPS furnace at the University of Sheffield (Sheffield, England)

Pressure can also be applied during the sinter process by hydraulic punches which administer uniaxial load. Limitations with the maximum pressure at temperature exist due to the material properties of the high density graphite mould. For example, a 20 mm diameter sample mould has a maximum pressure of ≈50 MPa. Use of reinforced graphite or steel moulds can facilitate the use of larger pressure. Utilising a combination of fast heating rates and high pressures, as well as current-related effects, allows SPS to consolidate powders to full density much quicker and at lower temperatures, when compared to conventional sintering process, such as pressure-less sintering and hot pressing. As well as these features, SPS has also been shown to consolidate powders of materials not possible by these conventional methods. [153].

3.3.2 History and development of current-activated, pressure-assisted sintering

It recent decades, the popularity of the SPS technique has increased rapidly due to the commercialisation of the technique and the reported sintering and material benefits, which are discussed in this section.

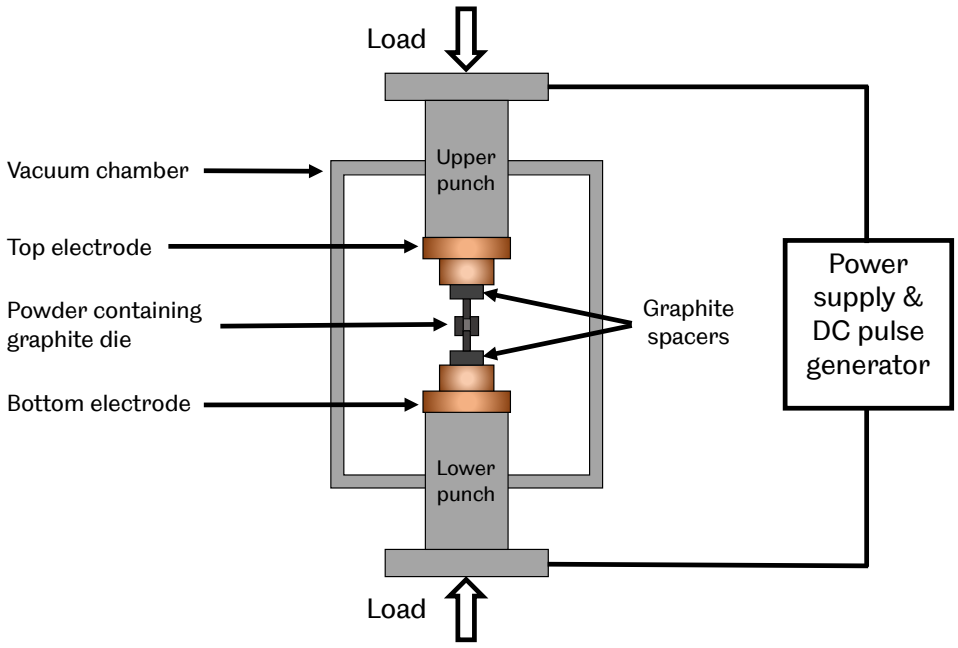

Figure 3.4: Schematic of a Spark Plasma Sintering (SPS) apparatus

Evidence of sparking or plasma

It has been proposed the enhanced sintering and fabrication of new materials by use of SPS was in part due to a sparking or plasma created in the gaps between particles [153, 175–177]. The sparking/plasma effect, created when DC current is pulsed through loose powder particles, was thought to, at least partially, remove surface oxidation layers on the powder particles and improve sintering by facilitating cleaner surface contacts [169, 176, 178]. Direct evidence of such effects have not been presented, but indirect evidence is shown in electric discharge patterns on insulator surfaces after processing and in elevated electric noise during processing [177]. Plasma is generally created by high voltages and facilitated by gases [153]. Typically, SPS functions at relatively low voltages, around 10 V, and materials are often processed under vacuum. Munir, Quach and Ohyanagi provide a comprehensive literature review on SPS and discuss the topic of sparking or plasma, concluding that no comprehensive evidence exists for metallic powders in SPS systems using a typical mould and under normal processing parameters [169]. Similar conclusions have been made by several authors, using a variety of techniques to observe or measure sparking or plasma formation [179–182].

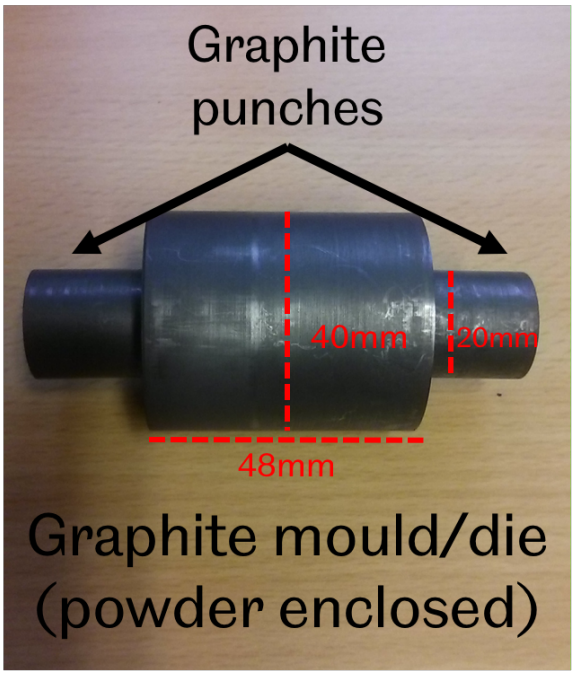

Figure 3.5: Example of graphite mould/die used in SPS. Product of Mersen UK.

Effect of pulsing current

While pulsing of the electric current during the sinter process likely does not result in sparking or plasma formation, as previously hypothesised, the general effect of current pulsing, as well specific features such as; pulse waveform, frequency and pattern, are topics that have also been explored separately for their effects on densification and microstructure for a variety of metal and ceramic powders. In studies of the pulse waveform and frequency, a measure of the power supplied to the material was found to be delivered at 0 Hz and no obvious effect on the densification or material properties were observed [183, 184]. Munir, Quach and Ohyanagi concluded from review of several studies covering a variety of materials that pulse pattern and pulse frequency had no measurable effect on the densification, grain growth or mass transport [169, 185]. However, Shen et al. found the pulse sequence (pulse on/off ratio) has an effect on the densification rate and grain size of alumina [175]. For low pulse on/off ratios, higher current densities are required for fixed heating rates, which had the effect of slightly reducing the densification temperature.

Current effects on reactivity

In section 3.2.3, electromigration was introduced as a non-thermal effect which can enhance mass transport and sintering. Investigations have shown the thickness of reaction layers are larger in current-assisted experiments, compared to systems that

just employ heat [154, 164–167]. However, in all of these studies, the investigated current densities as high as $10^7\,\mathrm{A\,cm^{-2}}$ and the experiments ran for hours. Both of these features atypical of SPS, where current densities are of the order $10^2\,\mathrm{A\,cm^{-2}}$ to $10^3\,\mathrm{A\,cm^{-2}}$ and sinter programs run of the order of tens of minutes.

Studies at $600\,\mathrm{A\,cm^{-2}}$ using standard SPS apparatus and tools were carried out by Anselmi-Tamburini et al. and Garay [186, 187]. While, these studies observed a noticeable increase in the thickness of the reacted phase in experiments where current was applied, the experiments occurred over relatively long time-scales, ranging from 20 minutes to 75 minutes. As one might expect, the length of the reacted phase region increased with the processing time.

Trzaska and Monchoux conducted thorough investigations [188] processing Ag-Zn over shorter time-scales; ranging from 2 to 20 minutes. Three different current density set-ups were used: zero, 'normal' $60\,\mathrm{A\,cm^{-2}}$ to $190\,\mathrm{A\,cm^{-2}}$ and a 'high' ($1000\,\mathrm{A\,cm^{-2}}$ to $1400\,\mathrm{A\,cm^{-2}}$). They concluded there was no significant variation in the the thickness of the reacted layer between zero, normal and high current density set-ups. Based on the evidence above, it can be concluded that any current induced effect on the reactivity of powders, under conventional SPS processing conditions, are only noticeable for extended sinter times; beyond 20 minutes.

Current effects on neck formation

For pre-alloyed powders, SPS is purely employed for the consolidation of the powder. As described in section 3.2.1, densification is facilitated by mass transfer to necks formed between contacted particles. Electromigration effects, if present in typical SPS apparatus, may positively influence the rate of neck growth and benefit densification.

To investigate such features, Frei, Anselmi-Tamburini and Munir [168] used a set-up involving copper spheres, while separating current and temperature variables by use of multiple graphite foils, which increased the resistance of the copper plates and controlled the current passed through the copper spheres in the experiment. Figure 3.6 show the fracture surface of necks formed after sintering at 900 °C for 60 minutes with different current values, ranging from 0 A to 1040 A. These images show clearly the effect of increased current on the diameter of the necks formed during sintering, although it is noted for very long processing times. In another study, Song found neck growth depended strongly on the local distribution of the current density [189]. A further study on neck formation conducted by Fu et al. [169] compared the SPS technique with hot-pressing of Cu-Ni and Fe-Cu spheres at different holding temperatures and processing times. Again, greater neck growth was measured in the SPS processed materials.

C2_frei_necks.png

Figure 3.6: SEM images showing the growth in neck formation between copper spheres and copper plates during SPS processing for 60 minutes at 900 °C for currents: (a) zero current, (b) 700 A, (c) 850 A, (d) 1040 A [168]

3.3.3 Processing parameters in SPS

The summary of studies on the non-thermal current effects in SPS have shown such effects to be minor in relation to the densification of powders using typical SPS apparatus and conditions. Thermal and pressure effects are therefore the most significant processes active during SPS with regards to the removal of porosity.

Figure 3.7 shows a typical thermal and pressure cycle used in SPS. Highlighted are the various components of the cycle which are the main processing parameters of the SPS technique, all of which can affect the density and material properties of the specimen. Numerous studies for various materials have investigated the sensitivity of the densified specimen to these parameters.

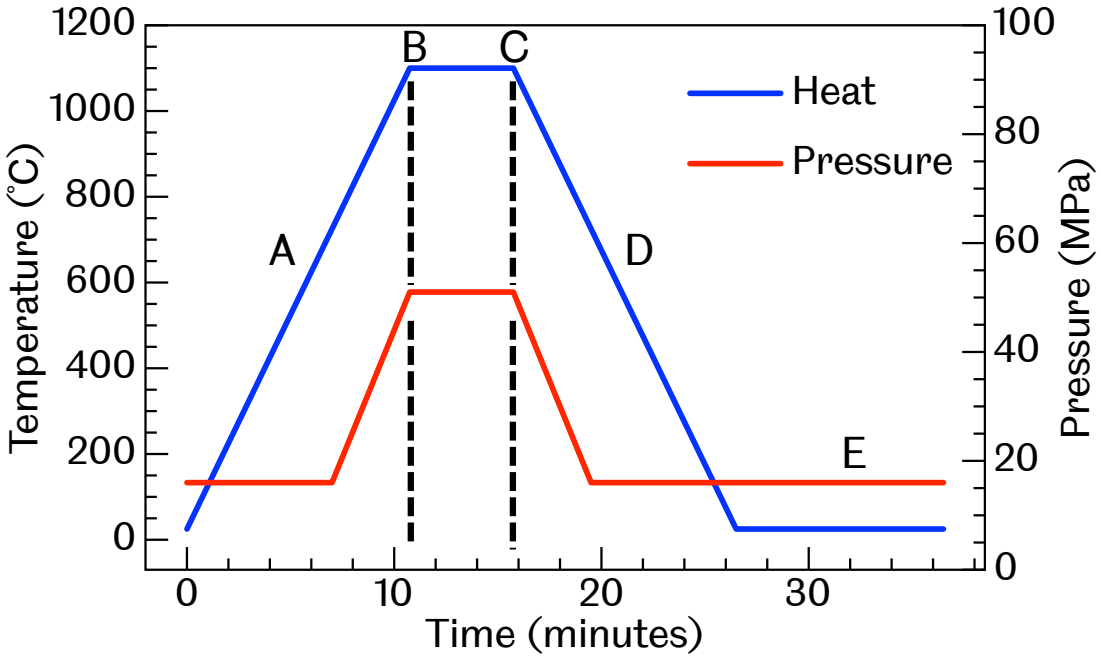

Figure 3.7: Schematic showing typical thermal and pressure cycle used in SPS. A highlights the heating/pressure rate, B-C highlights the holding time, temperature and pressure. Current is turned off at C. D highlights cooling/pressure removal rate (usually fixed) and E highlights the cool down.

Heating rate and holding temperature

One of the signature features of SPS are the fast heating rates (Highlighted 'A' in figure 3.7), which lead to much shorter processing times compared to other conventional sinter techniques. The heating rates achievable in commercial SPS systems range between 100 °C/ min and 600 °C/ min [171], and specialised research systems can achieve even higher heating rates. For comparison, hot pressing can achieve 50 °C/ min, but most apparatus are often limited to 10 °C/ min to 20 °C/ min [153].

To achieve certain material features or properties, fast heating rates are crucial. During the sinter process, a competition exists between grain coarsening and densification mass transfer mechanisms. Accessing holding temperature quickly bypasses the low-temperature grain coarsening effects and densification can occur with minimal grain growth. This feature has been explored with many different ceramic and metallic materials to produce fully-dense nanostructured specimens by SPS [45, 160, 170, 185, 190].

Study of materials such as alumina, zirconia, Fe-Ni and copper [171, 175, 185, 191] have shown an inverse relationship between the heating rate and grain size of the sintered material, consistent with the theory of quickly reaching the hold temperature minimises grain coarsening. Olevksy also showed this inverse relation in heating rate studies of aluminium and calculated that higher heating rates minimised surface diffusion, while enhancing grain boundary diffusion from within the particle volumes [192]. However, Zhang et al. observed no change in grain size with increasing heating rate for copper powders [193], while Weston et al. found grain size to increase slightly with heating rate for various titanium alloy powders [173].

A thorough study conducted by Zhou et al. [174] investigated the role of heating rate on the final density and grain size for Al_2O_3 ceramics and found the relationship changed with increasing holding temperatures. A plot of their results, shown in figure 3.8, can be divided into three sections in which the holding temperature and heating rate affect the grain size and density differently.

Section I: Holding temperatures below 1100 °C An increase in heating rate from 50 °C/ min to 300 °C/ min had no effect grain size and increased the relative density of alumina slightly, albeit to a still low level. At this stage, the holding temperature was too low for full densification to occur and it makes little difference how quickly the sample reaches the holding temperature.

Section II: Holding temperatures between 1100 °C to 1150 °C The heating rate again had little effect on the grain size. However, an increase in heating rate saw a sharp increase in relative density from 76.6% to 91.3% at 1150 °C. This is in agreement with other studies where, for a high enough sinter temperature; the quicker a sample is taken to the holding temperature, the greater the density.

Section III: Holding temperatures between 1200 °C to 1400 °C At 1200 °C, the lower heating rate achieved noticeably higher density. This can be explained as the processing time is longer overall. At this holding temperature, there is also very little grain coarsening and grain size continues to be independent of heating rate. Increasing the holding temperature to 1300 °C and beyond saw both samples achieve identical, near-theoretical densities. However, there is now a significant effect on the grain size of the samples. Generally, as the holding temperature increased, so too did the grain size for both heating rates. However, this effect was most significant at 50 °C min^{-1}, with grain growth increasing exponentially. Grain growth was suppressed when the heating rate increased to 300 °C/ min.

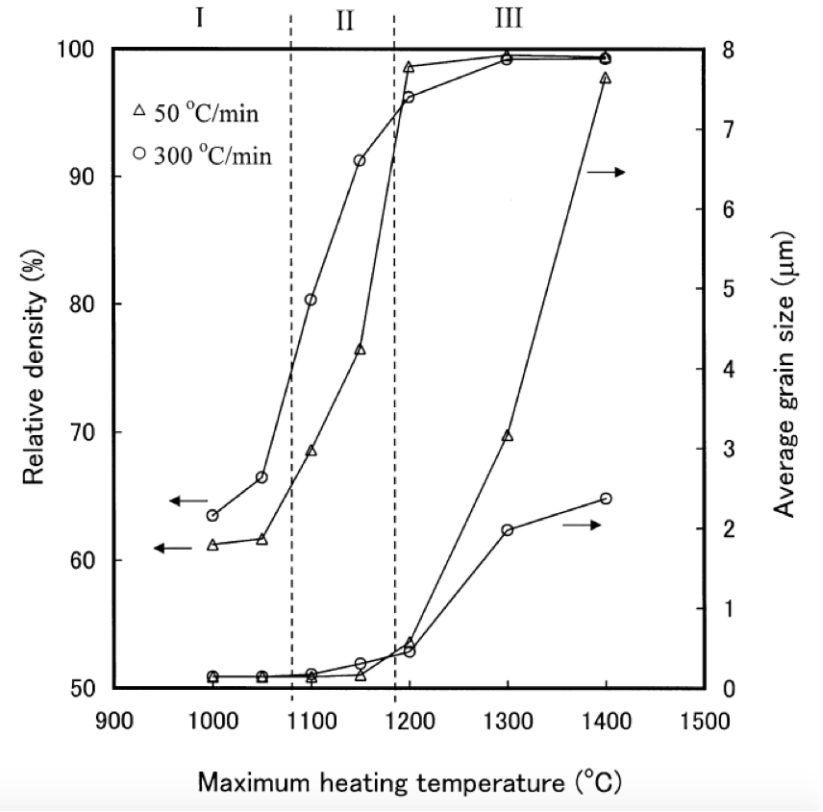

Figure 3.8: Relative density and grain size in relation to the holding temperature for two heating rates 50 °C/ min and 300 °C/ min for Al_2O_3 (alumina) [174] ©2004 Elsevier, licence granted for reuse in thesis (licence number 4197050763525).

Zhang et al. also reported for a fixed heating rate of 80 °C min^{-1} the holding temperature significantly affected the grain size of nanocrystalline copper [193]. Grain growth was suppressed and near full density was achieved when the sinter temperature was 600 °C. However, above 700 °C the grains coarsened exponentially. Shen et al. [175] investigated several heating-rates ranging from 50 °C/ min to 600 °C/ min at 1300 °C and 1400 °C holding temperatures and 0 minutes dwell time for SPS processed alumina. At either holding temperature, when the heating rate was < 400 °C min^{-1}, relative densities measured were around 99%. Higher heating rates saw a drop in relative densities to around 90%. The results were explained as such high heating rates and zero holding time created very large thermal gradients within the material, which likely lead to the outer part of the sample consolidated and the inner material retaining a lot of porosity. Shongwe et al. [191] also saw a decrease in relative density in Fe-Ni alloys processed at 1100 °C as the heating rate was increased up to 150 °C/ min. Studies by Stanciu et al. on SPS processed $\alpha - Al_2O_3$ and $MoSi_2$ observed no variation in final density whether samples were processed at 50, 250 and 700°C/ min [171], a conclusion also reported by Weston et al. for titanium alloys up to 200 °C min^{-1} [173].

Across both ceramic and metal materials there is a strong relationship between the heating rate and holding temperature, and the densification and grain size of the sintered material. Most literature generally show higher heating rates minimise grain coarsening. However, the holding temperature can significantly influence this relationship and if the holding temperature is very high, grain growth can be significant, even for the highest heating rates. Generally, the relative density increases across all materials with the holding temperature. However, caution must be taken when using very high heating rates, which can lead to large temperature gradients and lower relative densities in the specimen. If the specimen is not allowed to homogenise its temperature, partial densification of the specimen can occur.

Pressure

The application of pressure during the sintering process is well established from the traditional hot pressing technqiue as beneficial towards the consolidation of powders, and can lower the sintering temperature required to achieve full density [148, 155]. The role of pressure, with regards to the SPS technique, and the resulting density, grain size and sinterability of multiple ceramic and metallic materials are summarised in reviews by Munir [169] and Garay [153]. Munir states pressure has an extrinsic and intrinsic effect on the powder when applied during the sinter process. The former describes the role of pressure in the rearrangement and break-up of agglomerated powders, which increases the contact points for necks to

form within the system. Agglomeration is a particular problem in achieving full density when using nano-scale powders due to inhomogeneity in the density of the green compact due to different packing fractions as inhomogeneous agglomerates are brought together [194]. The intrinsic effect of pressure on the sintering is the lowering of the chemical potential for the powders [160], increasing diffusion related mass-transport, as well as influencing other effects such as viscous flow, plastic flow and creep [169]. These extrinsic and intrinsic effects combine to reduce the sintering temperature required to achieve full density, as well as reduce grain coarsening effects.

There are practical limits to the maximum pressure available in conventional SPS set-ups, which are due to the mechanical properties at high temperature of the mould material. For a 20 mm inner-diameter mould made of high-density, high-purity graphite, the upper limits of pressure are around 51 MPa. Modifications can be made if larger holding pressures are required. Materials such as ceramic reinforced graphite or stainless steel allow larger values of pressure, but are more expensive [153]. Novel set-ups have also been explored, which combine graphite and ceramic parts to allow current and heat transfer but also reinforce the mould structure. Using such a set-up, Anselmi-Tamburini et al. were able to study bulk ZrO_2 material at extremely high pressures up to 1 GPa [195]. For fixed heating rates and hold times, the sinter temperature required to achieve 95% relative density was reduced from 1350 °C to 900 °C when the pressure applied was increased from 40 MPa to 800 MPa. Over this pressure range the average grain size reduced from 200 nm to 15 nm. Studies using standard SPS apparatus, and therefore lower maximum pressures, saw an increase in relative density with pressure at fixed temperatures for zirconia and aluminium [185, 196]. However, the grain size remained approximately constant [185]. The influence of pressure on the relative density appears to be strongest in metals compared to ceramics [153]. This is because metals are much more sensitive to mechanical deformation mechanisms, such as plastic flow.

Grasso et al. used experimental and computer models to examine another potential effect of pressure to the flow of current through the SPS machine and graphite mould. They reported an increase in pressure reduced the contact resistance between the vertical punch and mould contact, resulting in lower gradients in the thermal and electric fields across the punch/mouldsample assembly [197]. This can contribute to improved densification and overall homogeneity across the sample.

The influence of pressure in SPS processing is generally positive with regards to densification of powders. Pressure improves the thermal sinter process by improv-

ing contact between particles through agglomeration break up and also improving thermal and electric current flow through the mould. For high enough pressures, plastic deformation of the powders also improves increase the density. These effects help to reduce the temperatures required for the sinter process.

Munir [169] covers numerous studies of pressure effects in SPS, which also investigate specific topics, such as the effect of applying the pressure during heating or once the sample has reached the sintering temperature and the rate at which pressure is applied.

3.4 SPS processed REPM

A generalised processing route for powder-sintered bulk REPMs is described as follows [25, 198, 199], although modified methods exist to produce nanocrystalline precursor powders and nanograined REPMs. A good summary of the latter method(s) is covered by Gutfleisch [27].

- Melting of alloy under vacuum
- Crushing
- Milling
- Alignment of powders by magnetic field
- Pressing or pre-sinter to form green-compact
- Sintering and annealing
- Machining and/or coating
- Magnetising

No new REPM alloys have been discovered with the same commercial viability as the SmCo and Nd-Fe-B series since the late twentieth century. Over this time much focus has thus been given to the optimisation of the microstructure in current REPM materials to improve their magnetic performance. SPS has been utilised as a technique to batch process REPM which feature meta-stable phases unattainable via conventional processing methods [200], composite materials [201–203] and higher densities at lower sinter temperatures [204, 205]. The rapid processing of the SPS technique also makes for an efficient prototyping tool of near-net shape materials. As well as this, the ability to produce nanostructured grains is a highly desirable property for nucleation based REPMs [13] and as such, Nd-Fe-B-type permanent

magnets have been a primary focus of studies of SPS processed REPMs [40, 50, 51, 190, 206–214].

Beneficial properties, attributed to the SPS process, have been reported in Nd-Fe-B-type magnets with improved corrosion and oxidation resistance [39, 206]. $Nd_{15.5}Dy_{1.0}Fe_{bal}Co_{3.0}B_{6.8}Al_{1.0}$ powders consolidated by SPS had a homogeneous microstructure. The average grain size of 6 µm was approximately the same as the precursor powder and half the average grain size for a similar composition magnet produced by conventional pressure-less sintering [206]. The authors noted a difference in the distribution of the Nd-rich phase in the microstructure between the SPS and conventionally processed sample. In the conventionally processed sample, the Nd-rich phase is finely distributed along the inter-grain boundary between the $Nd_2Fe_{14}B$ grains. In the SPS processed sample, the Nd-rich phase agglomerated at triple point junctions between the $Nd_2Fe_{14}B$ grains. The Nd-rich phase is a pathway for corrosion and oxidation propagation [39] and therefore the SPS processed sample performed considerably better in corrosion and oxidation tests as corrosion propagation was suppressed, as evidenced in figure 3.9. However, the difference in distribution of the Nd-rich phase also reduced the coercivity of the SPS processed magnet slightly. It is also noted that in optimising the SPS processing parameters for Nd-Fe-B, an increase of pressure applied, from 30 MPa to 50 MPa, reduced the remanence. A similar study, with pressures up to 300 MPa, presented similar results [211]. This was attributed to high pressures destroying the degree of alignment induced in the powders by magnetic field before the sinter process. The $(BH)_{max}$ of the SPS processed Nd-Fe-B-type magnet was 239 kJ m^{-3} and the conventional sinter magnet was 248 kJ m^{-3}. Nd-Fe-B-type magnets processed by SPS measured similarly excellent magnetic properties in comparison to conventionally processed equivalents, but showed improved mechanical properties with optimised processing parameters [40].

Mo et al. reported in SPS processed anisotropic $Nd_{15}Dy_{1.2}Fe_{bal}B_{6.0}Al_{0.8}$ magnets the microstructure was sensitive to the holding temperature. For fixed heating rates and pressures, the holding temperature ranged form 760 °C to 850 °C, which saw the density increase, a result consistent with other materials processed by the SPS technique. As density increased, so too did the remanence, until processed at 850 °C where the remanence lowered. The effect on coercivity was more complex, initially increasing, then decreasing and peaking when processed at 810 °C. The best magnetic properties were linked to the most uniform and developed microstructure, with a select few SEM backscattered images shown in figure 3.10. The reported magnetic properties of these SPS processed Nd-Fe-B-type magnets were near identical to those of conventional magnets, although again pressure had the effect

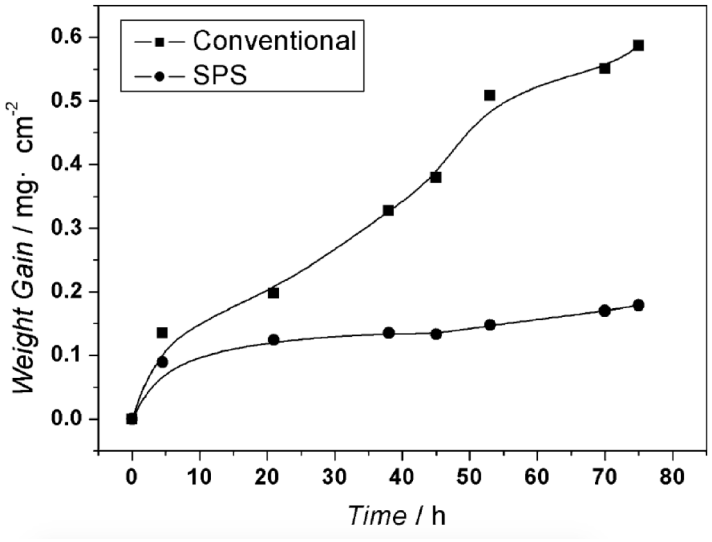

Figure 3.9: Oxidation reaction kinetics of SPS processed Nd-Fe-B-type magnets and conventionally sintered Nd-Fe-B-type magnets at 80 °C in 80% relative humidity atmosphere [39] ©2004 Elsevier, licence granted for reuse in thesis (licence number 4197050915841).

of reducing the remanence through a reduction of the degree of alignment.

Exploiting the capabilities of SPS have seen numerous magnetic material studies conducted exploring nanocrystalline melt-spun powders/ribbons. In the previous chapter, it was described how coercivitity increases as grain size decreases and this is most evident when the average grain size is below the single domain limit of the magnetic alloy. For nucleation based REPMs, this requirement is met when average grain size is below a few hundred nanometers [13]. These materials also utilise hot deformation/die-upsetting, introduced in the previous chapter, as a method to induced texture and magnetic anisotropy [27, 48]. Rapid consolidation using SPS combined with hot-deformation has seen anisotropic, nanostructured Nd-Fe-B-type magnets free of Dy additions achieve energy products as high as 293 kJ m^{-3} [51, 190, 208, 209].

High-energy ball milling of the precursor powders is a method which can produce amorphous powders in preparation for processing by SPS [37, 216, 217]. Utilising this methodology, isotropic $SmCo_5$ was produced by SPS with an average grain size of 40 nm, which resulted in excellent room temperature coercivity of 2270 kA m^{-1} and high temperature coercivity of 715 kA m^{-1} at 773 K [216]. The high temperature coercivity exceeded that of specially designed $Sm_2(Co, Fe, Cu, Zr)_{17}$ magnets for high temperature applications [94] However, as the magnets had an isotropic distribution of grain c-axes, the remanence and energy product were relatively low. An extra processing step utilising die-upsetting could improve the alignment

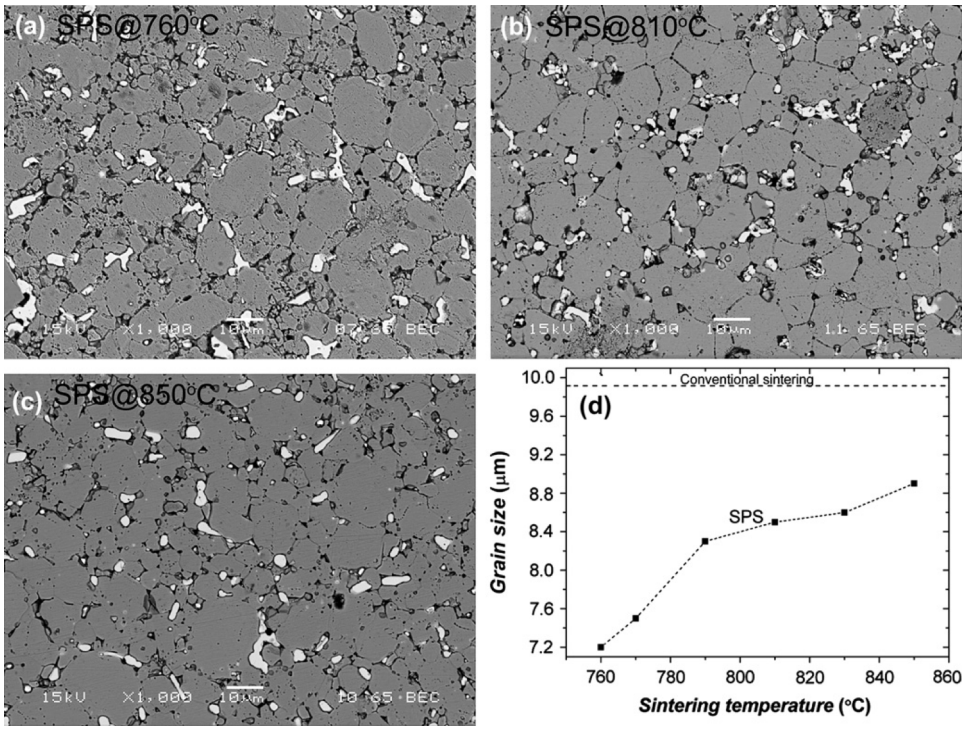

Figure 3.10: Microstructures of the Nd-Fe-B type magnets sintered at (a) 760 °C, (b) 810 °C, (c) 850 °C, together with (d) mean grain size as a function of SPS temperature [215] ©2007 Elsevier, licence granted for reuse in thesis (licence number 4197051063138).

of magnetic grains and improve the energy product of nanocrystalline magnets produced by amorphous powders. Care has to be taken however not to over process the powders, which often lead to oxidation and detrimental soft-magnetic phases and low coercivities for REPMs [45, 218].

Modification of the SPS technique have been used to consolidate and texture materials on the timescale of seconds. Flash SPS uses largely the same apparatus of conventional SPS but through a critical combination of electric field and temperature a power surge event occurs (referred to as the 'flash event'), which results in a nearly instantaneous densification of the powder material in mere seconds [219]. During Flash SPS, the material is not constrained by a mould, and thus densification effectively occurs simultaneously with hot deformation, removing the need for a secondary processing step to induce texture into isotropic materials. A review of flash SPS; covering the materials, mechanisms and modelling of the technique is given by Yu et al. [220].

Castle et al. [50] used flash SPS to consolidate melt-spun powders of Nd-Fe-Dy-Co-B-Ga, with comparison to a sample produced by standard SPS method. Initially, the authors were able to show using a two-step process (30s pre-sintering

step, followed by a 10s flash-sinter step), near theoretical densities could be achieved, with the specimens also exhibiting nanoscale, plate-like grains. As the heating power increased, a higher degree of alignment was measured as a result of anisotropic grain growth and consequent improved grain alignment, which occurred via hot deformation during the flash sinter stage. A follow-up study was able to improve on the conceptual investigation through a thorough optimisation of the flash SPS processing parameters [34]. As a result, Castle et al. were able to produce a Dy-free Nd-Fe-Co-Ga-Al-B magnet from melt-spun ribbons, which had a fine grain structure below the single domain limit. The coercivity of the optimally processed specimen was 14% larger ($1438\,\mathrm{kA\,m^{-1}}$ than the commercial Dy-containing Nd-Fe-B-type magnet. A high degree of alignment induced during the flash SPS process resulted in a remanent polarisation and energy product comparable to the commercial magnet as well. Further studies are needed to confirm the viability of the flash SPS technique for magnets. However, Castle et al. [34, 50] have demonstrated that the flash SPS technique, when performed under optimal and controlled conditions, is a very enticing powder processing method for REPM, which can potentially be produced more economically and simplifying the processing route for REPM powders/ribbons which could not be fully aligned by magnetic fields before the sintering stage.

In general, Sm-Co based alloys sintered by SPS are relatively unexplored. Nanocrystalline structures achieved with high-energy, balled milled powders in combination with the rapid SPS process have been studied [216], as well as hard-soft magnetic phase composites [202], but most studies have focussed on producing Sm-Co based magnets comprised of meta-stable phases, often unattainable by conventional processing methodologies which require higher sintering temperatures to achieve densification [36, 37, 217, 221, 222].

SPS processed isotropic $Sm(Co_{0.74}Fe_{0.1}Cu_{0.12}Zr_{0.04})_{7.4}$ at temperatures below 800 °C produced magnets with a single 1:7 stoichiometry structure [36]. Sintering at these lower temperatures also inhibited grain coarsening, with an inferred average grain size of 28 nm. To compensate for the low sinter temperatures, high pressures of 500 MPa were used, achieving 98% relative density. Figure 3.11 shows the nanocrystalline $Sm(Co_{0.74}Fe_{0.1}Cu_{0.12}Zr_{0.04})_{7.4}$ magnet exhibiting large coercivities, both at room temperature and at 500 °C, without the need to precipitate the cellular nanostructure associated with $Sm_2(Co, Fe, Cu, Zr)_{17}$ magnets. Matsumoto et al. have also investigated $Sm_2(Co, Fe, Cu, Zr)_{17}$ alloys with SPS, but only detailed the relative density with respect to the sinter temperature used [223]. In turn, they show that powders processed by SPS can achieve full density at temperatures much lower than conventional metallurgy processes. No details were provided with regards

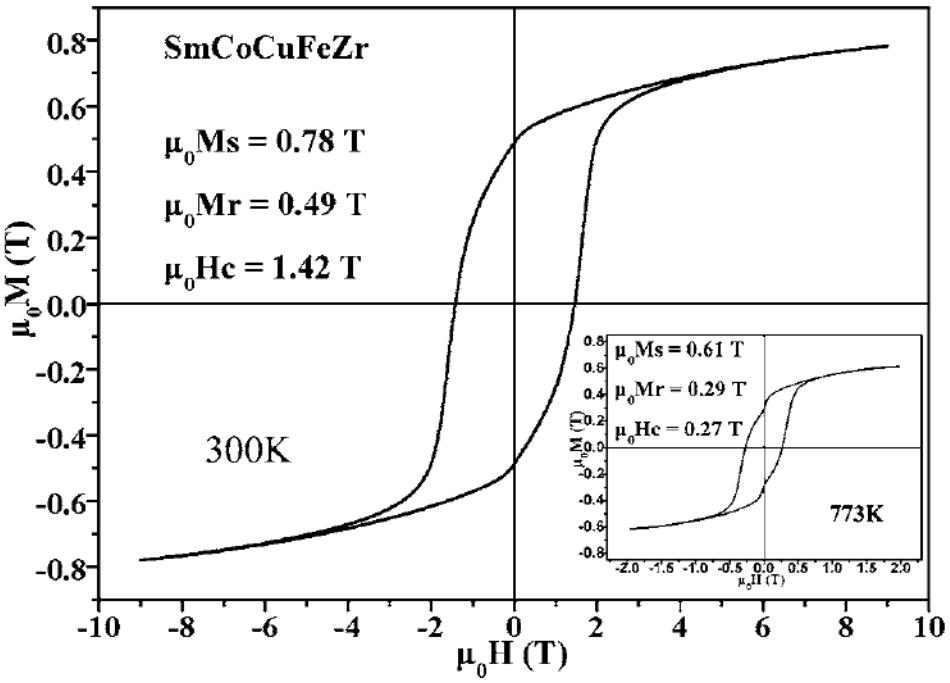

Figure 3.11: Hysteresis loop for SPS processed $Sm(Co_{0.74}Fe_{0.1}Cu_{0.12}Zr_{0.04})_{7.4}$ magnet with applied field, H_{app}, from -9 T to 9 T at 300 K. Inset shows high temperature hysteresis loop at 773 K for field ranging -2 T to 2 T [36] ©2009 AIP Publishing LLC, licence granted for reuse in thesis (licence number 4197051167711).

to the magnetic properties or phase composition. [223].

3.5 Summary

To summarise, SPS has been shown to produce a wide range of ceramic, metallic and magnetic materials with desirable features such as: nanoscale grain structure, unique phases and improved magnetic and material properties. The processing parameters; heating rate, holding temperature and pressure, have the largest effect on the microstructure and material properties. The magnetic properties are often comparable to those achieved by conventional processing methods, although the texture of anisotropic magnets can be disrupted if high pressures are used. A balance must be found, as higher pressures allow full densification at lower temperatures when unique phases and grain size minimisation is sought. Hot deformation may ultimately be better suited for SPS processing of REPMs, however this adds an further processing step. The SPS technique is still relatively novel for REPMs and improvements are expected with processing parameter optimization and alloying specifically designed for shorter processing of the SPS process. The rapid batch processing of the SPS technique has also demonstrated viability as a prototyping

tool for new alloy and composite magnet materials.

Chapter 4

Finite Element Modelling

4.1 Introduction

The development of permanent magnets for most of history has been empirically dictated. However, REPMs have benefited in their optimisation from the development of micromagnetic theory and, most recently, computational modelling and simulation. Engineers can now utilise numerical methods to solve micromagnetic equations to better understand magnetic reversal and predict magnetic properties, as well as show visually ferromagnetic magnetic behaviour. Increasing the magnetic hardness, either through the reduction of nucleation sites or by optimising the pinning field, is a critical aspect in REPM research for ever-more demanding applications, where stability, reliability and performance are critical. Modelling and simulation are ever more present and important in science and engineering as computer technology has advanced exponentially over the twentieth and into the twenty-first century.

The properties and performance of REPM developed by powder sinter route are linked to several, broadly grouped processing variables: alloying composition, powder morphology, processing parameters and heat-treatment. These variables will dictate the phases present, as well as the size and shape of microstructural features. Current REPM materials are believed to already be optimised in terms of their chemistry and so it is in the optimisation of the microstructure where improvement on current magnetic material properties are to be found [2]. With reducing computational cost and time, modelling and simulation are powerful tools which provide control over microstructures and micromagnetic properties, which could not easily be replicated by experiment. These include the influence of magnetic interactions between grains, misalignment of the magnetic grains, porosity, grain boundaries and non-magnetic phases. A better understanding of the

magnetic system and engineering of the microstructure improves REPM material efficiency. This is a critical aspect of future REPM usage and development [1, 2, 224].

This chapter reviews micromagnetic modelling for REPMs. A brief introduction of the original analytical micromagnetic models begins the chapter, which in turn led to the development of numerical models and finite element method (FEM) of modelling, which is the type of micromagnetic modelling used in this work. A literature review of the main areas of research in REPM FEM modelling and simulation are summarised, which typically cover the two common REPMs; NdFeB and $Sm_2(Co, Fe, Cu, Zr)_{17}$-type, before concluding with areas in REPM research and development that could benefit from the use of FEM.

4.2 Micromagnetic modelling of ferromagnetic materials

4.2.1 Analytical models and finite difference method

Hysteresis behaviour and reversal mechanisms in ferromagnetic materials are very complex processes to model at the atomistic level. Micromagnetic and continuum theory simplify the behaviour of domains and domain wall motion within granular structures, without the computation of the fundamental behaviour and interaction of atomic spins. However, even in the most basic scenarios, few micromagnetic equations can be solved analytically by continuum theory. Behaviour solvable by analytically methodology are planar domain walls [53, 225] and the law of approach to ferromagnetic saturation [13]. However, analytically solutions only provide a quantitative solution to the nucleation or coercive field, and do not necessarily provide insight into the reversal process. The Stoner-Wohlfarth model is the simplest analytical model, comprised of uniformly magnetised ellipsoids with uniaxial shape or magneto-crystalline anisotropy, which exhibits hysteresis [9, 226]. The Stoner-Wohlfarth model can predict the maximum coercivity of a ferromagnetic material, equal to the anisotropy field, H_a [9] and an ensemble of randomly orientated Stoner-Wohlfarth particles define the lower limit of $M_r = 0.5M_s$ for isotropic magnets, where remanence enhancement is non-existent. However, real REPMs are far more complex, with large, irregular grain volumes, multi-domain states and interactions between grains influencing the nucleation of reversal domains.

Numerical methods solve micromagnetic equations by finding an equilibrium state for a given applied field and can be developed to predict the path of magnetisation for non-uniform, interacting magnetic volumes. The total free energy,

equation 2.4 and introduced in the magnetics chapter, is minimised at each time or field step, which provides the effective field acting on $\vec{M(r)}$.

$$\varepsilon_{tot} = \varepsilon_{exchange} + \varepsilon_{anisotropy} + \varepsilon_{Zeeman} + \varepsilon_{demag} \tag{4.1}$$

Traditional numerical investigation of reversal mechanisms were also limited to few small, simple ellipsoid particles [227]. Early methods introduced particle-particle interactions utilising a theoretical treatment of the exchange interaction by implementation of a molecular field between single domain, single component amorphous material by Callen, Liu and Cullen [228]. This model was implemented by Hadjipanayis and Gong to calculate the coercivity of Nd-Fe-Al-B-Si melt spun ribbons and compared favourably with experimentally values [229].

The development of larger-scale, irregular models with particle-particle interactions coincided with the implementation of computer aided modelling. Micromagnetic continuum theory was adapted for computer modelling and from this, two primary numerical techniques were developed to account for heterogeneous microstructures and short and long-range interactions between particles. Finite difference (FD) [230, 231] and finite element (FE) [232] replace the continuous domain with a discreet set of lattice points, at which either FD operators or FE algebraic equations are solved [233]. A detailed description of both methods is provided by Fidler and Schrefl [233]. In summary, both techniques calculate the effective field, $\vec{H}_{eff}$, through minimisation of the micromagnetic energy terms in equation 2.4, and integrate the Landau-Lifshitz or Gilbert equation [233]), which allows the magnetisation direction to be tracked for each time or field step. This simulates the magnetic moment at each lattice point in both time and space with respect to an applied field. The Landau–Lifshitz Gilbert equation is shown in figure 4.2 with variables $\vec{J}$ = polarisation, t = time, γ = electron gyromagnetic ratio, which accounts for precession, α = Gilbert magnetic damping parameter.

$$\frac{\partial \vec{J}}{\partial t} = -\left|\gamma\right| \left(\vec{J} \times \vec{H_{eff}}\right) + \frac{\alpha}{J_s}\left(\vec{J} \times \frac{\partial \vec{J}}{\partial t}\right) \tag{4.2}$$

FD method is generally the quicker to simulate, but is restricted to simple simple parallelepiped volumes and fixed mesh structures of regular lattice points [233]. FE allows variable mesh structures and can model complex shape volumes, but at a greater computational cost [233]. Fukunaga and Inoue [234] used FD method to model the effect of exchange and the magneto-static interaction on approximately 8000 isotropic Nd-Fe-B-type grains of varying size. The authors showed that the exchange interaction enhanced the remanence above the Stoner-Wohlfarth lower limit,

$M > 0.5M_s$, and reduced the coercivity in the smallest grains around 10 nm. Their model agreed well for these small diameters with the theoretical model proposed by Callen, Liu and Cullen [228] and experimental results of Hadjipanayis and Gong [229]. At these diameters, the exchange interaction extended over most of the grain, influencing the magnetisation vector of the grain. The magneto-static interaction, simulated separately, made no change to the hysteresis of larger magnetic grains up to 500 nm. Their FD models did not allow magnetic inhomogeneity within grains and so domain-walls were omitted, which is unrealistic for large grains. Therefore, the FD models over-estimated the coercivity for grains $>$ 50nm compared with the experimentally derived results. The lack of intra-granular magnetic inhomogeneity also explained why the magneto-static interaction had negligible effect in their simulations.

4.2.2 Finite element method

While effective for modelling large number of volumes, simple parallelepipeds do not accurately represent the inhomogeneous and non-uniform microstructures of sintered REPM. The influence of irregularity and geometry are known empirically to be important to the reversal mechanism of REPMs, especially as the demagnetising field and magneto-static interactions are shape, rather than size, dependent. Finite element method (FEM) discretises the geometry in many smaller elements and thus can model much more complex geometries. FEM is a well established method of computer modelling in a number of fields, including structural analysis, fluid dynamics and electro-magnetic field computation [235]. Figure 4.1 shows an example of a large particle meshed with many smaller elements. In two-dimensions, each mesh element is typically a triangle, while in three-dimensions they are a prism. In both cases, at each element vertices is a nodal point. Fidler and Schrefl cover in detail the general approach of the FE method [233]. For micromagnetic simulations, the nodal points are where the magnetic free energy is minimised and the effective field at each time or field step is calculated.

Small elements are not only advantageous to model arbitrary shapes, but are also required to track dynamic changes within the model. To accurately model hysteresis, micromagnetic FEM models require the mesh size to be small enough to identify magnetic inhomogeneity in the volume and track nucleation and/or domain wall motion. For magnetic reversal in hard ferromagnetic materials, the mesh elements are required to be comparable to the domain wall width, δ_{BW} [236, 237]. Introduced in the magnetics theory chapter, δ_{BW} is related to the smallest

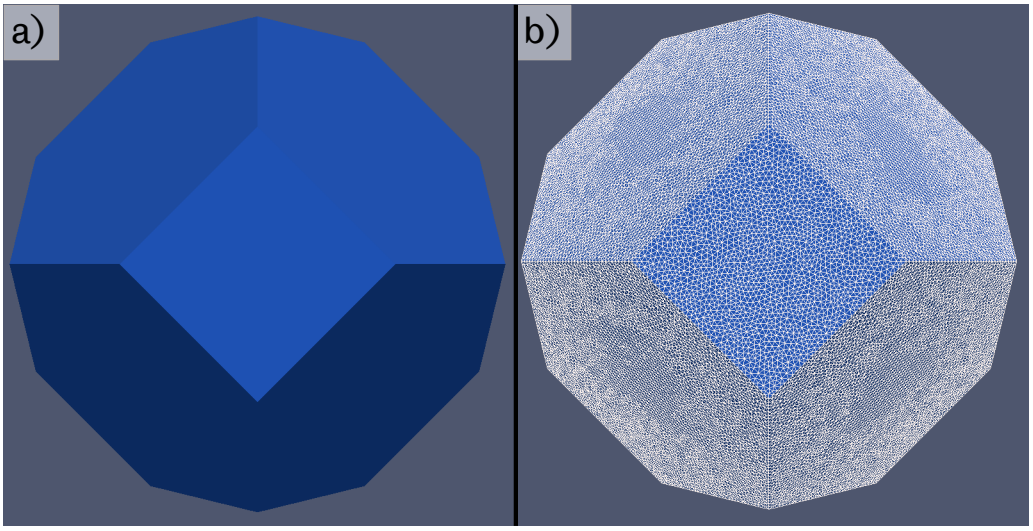

Figure 4.1: a) Example particle generated by voronoi tessellation with a diameter of ≈300 nm. b) shows surface mesh of finite elements with an average cell edge length 4.5 nm

length scale of magnetic deviation and is dependent on the exchange stiffness, A_{ex}, and magneto-crystalline anisotropy constant, K_1, of the material. For hard ferromagnetic materials, with uniaxial anisotropy, δ_{DW} ≈4 nm to 10 nm. Therefore, for granular models of REPM with structures of average diameters exceeding hundreds of nanometers, the number of elements are of the order of millions. At each time or field step, this equates to millions of calculations at every nodal point. Adaptive meshing can also be incorporated, such that the FE mesh elements are refined in critical areas of the model. This allows greater precision where, for example, reversed domains may nucleate, at sharp edges or corners of grains or to model grain boundaries [236].

The use of finite elements to represent arbitrary geometries comes at a great computational cost, requiring more complex mathematics. Therefore, the size and scale of models used in FEM studies are often much smaller than that of FD. FEM was first applied to solve numerical micromagnetics of a single prolate spheroid by Fredkin and Koehler in 1989 [238]. Due to its simplicity, the model lacked the inter-particle interactions as shown in figure 4.2. However, it evidenced magnetic properties of a single particle calculated by numerical FEM treatment were the same as those predicted by conventional analytical equations. To reduce computational cost, early studies of REPMs were confined either to two-dimensional models, removed magnetic inhomogeneity within the magnetic grains [231, 234] or neglected inter-particle interactions [239]. Today, with much improved computing power and improved mathematics, modern FEM studies are

required to be three-dimensional, multi-grain and include both the exchange and magneto-static interactions. However, multi-grain micromagnetic FEM models are generally limited grain diameters of the order of hundreds of nanometers, although recent studies have emerged analysing grain volumes in the micrometer scale [32, 240].

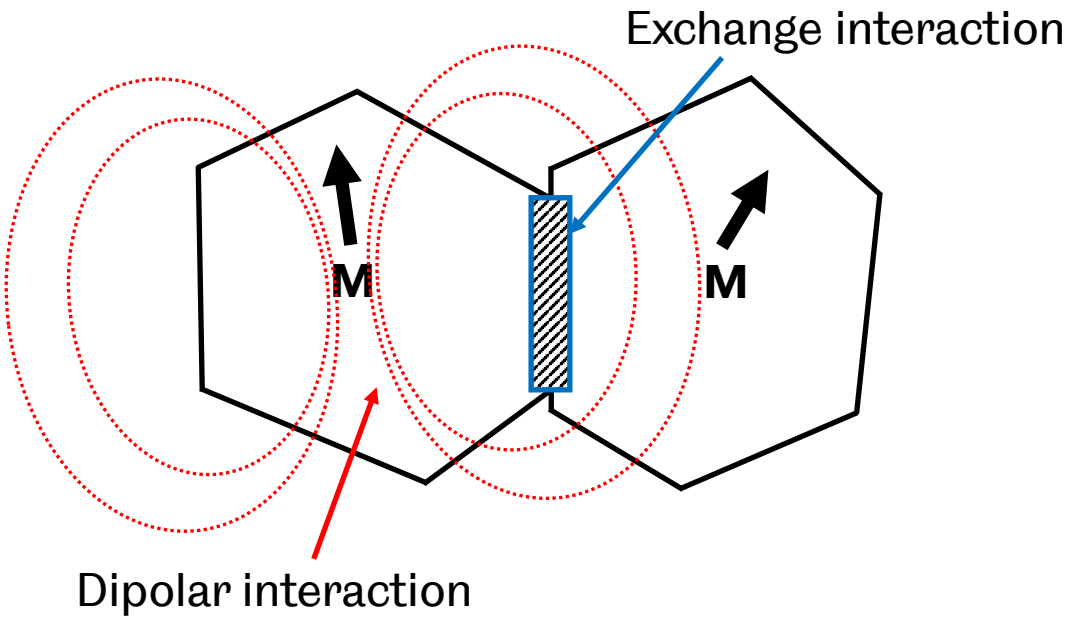

Figure 4.2: Schematic showing short range exchange and long range magneto-static interactions between two misaligned grains. Magnetisation vector is indicated at centres. Adapted from [233].

4.3 Literature review of micromagnetic FEM REPM modelling and simulation

4.3.1 Inter-particle interactions

The Stoner-Wohlfarth model predicts, for an ensemble of randomly distributed, non-interacting particles, $M_r = 0.5M_s$ [9, 226]. However, experimental data show isotropic, nanocrystalline permanent magnets with remanence up to 40% larger than those of non-interacting particles [38, 42, 44]. For isotropic, grains around 10 nm to 30 nm in diameter, the exchange interaction, which has a length scale for hard magnetic materials of a few nanometers, aligns the magnetic moments across the boundary of neighbouring magnetic grains, which enhances the alignment within the magnet and noticeable increases the remanent magnetisation [13]. The

influence of the exchange and magneto-static interactions on the remanence and coercivity and the grain size has therefore been a well studied topic in numerical micromagnetic FEM REPM models and simulation [233].

In a highly influential paper, Schrefl et al. [241] showed in a multi-grain model, that included both the long-range magneto-static and short-range exchange interactions, that isotropic, homogeneous nanocrystalline $Nd_2Fe_{14}B$ magnetic material with a mean grain diameter $< 20\,\text{nm}$ saw significant remanence enhancement due to the exchange interaction.

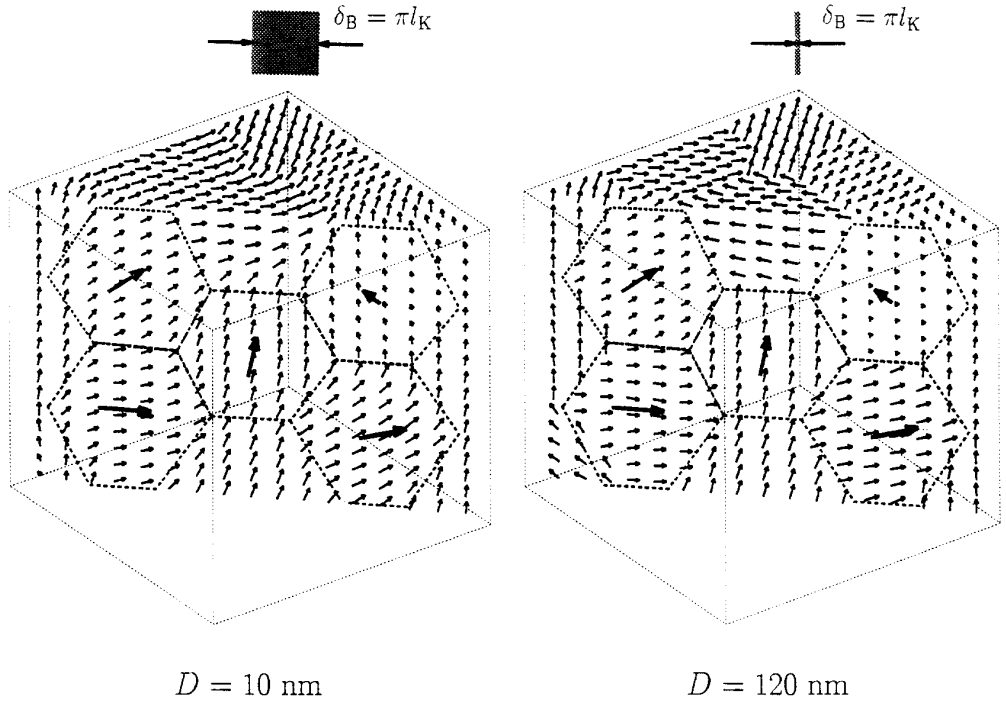

Figure 4.3: Distribution of the spontaneous magnetisation at $H_{applied} = 0$ for isotropic nanocrystalline Nd_2Fe14B models of 35 grains. The grain diameter is different in both models and the relative width of a domain wall is also referenced. This highlights the length scale of the exchange interaction. All arrows have the same arbitrary length and dotted lines refer to grain-boundaries. Big arrows indicate the easy axis of the grain. [242] ©1996 Elsevier, licence granted for reuse in thesis (licence number 4197070295163).

Figure 4.3 shows area of influence of the exchange interaction, approximately the Bloch domain wall length shown at the top of the figure, extends well into most of the smaller magnetic grains, influencing the magnetic moment vectors to deviate away from their easy-axes and improving the remanent magnetisation, M_r [242, 243]. The influence of the exchange interaction diminishes in larger grains, as displayed in the model on the right of figure 4.3. However, misalignment of

M_r away from the easy axis across neighbouring grains increases the energy of the magneto-crystalline energy term and reducing the energy barrier for magnetic reversal and reducing the coercive field.

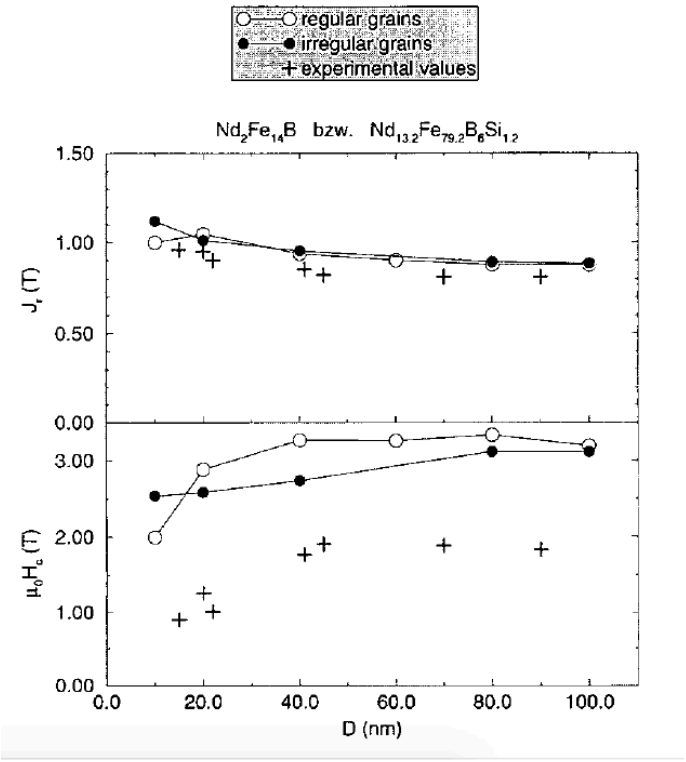

Figure 4.4: Remanence, J_r, and coercivity, $\mu_0 H_C$, calculated by numerical methods as a function of grain diameter, D. Experimental results (plus signs) are taken from study by Manaf et al. [38][242] ©1996 Elsevier, licence granted for reuse in thesis (licence number 4197070295163).

These observations were also reported in the studies of isotropic nanocrystalline Nd-Fe-B-type magnets by Fischer et al. [242, 244]. Figure 4.4 shows the relationship between remanence and coercivity as a function of grain diameter in the FEM micromagnetic models of Fischer et al. These results also show as grain diameter increased, the influence of the exchange interaction reduced; lowering magnetic remanence. However, as magnetic coupling is reduced, so too did the magnetic inhomogeneity across grain-boundaries, which improved coercivity. Therefore, grains smaller than 50 nm, the leading magnetic energy terms are the exchange and magneto-crystalline anisotropy. Above 50 nm, the long range magneto-static self-demagnetising field dominates and creates magnetic inhomogeneity in the corners and edges of the granular volumes [245, 246]

The magneto-static interaction in grain diameters beyond the nano-scale have

recently been studied [32, 240]. Bance et al. studied single grains of cubic and spherical shape, ranging in grain size from 40 nm to 1000 nm, while Sepehri-Amin et al. used irregular multi-grain models up to 2.7 µm. Sepehri-Amin et al. had to compromise with their mesh elements being an order of magnitude larger than the domain wall width of Nd-Fe-B magnets and concede their simulations over-estimate the nucleation field as a result.

Both studies reported a decrease in the coercivity with increasing grain size above the nanoscale. An increase in the magneto-static self-demagnetising field with grain diameter increased the torque applied to M_r near the edges and corners of grains, rotating the local magnetisation out of the easy axis and reducing the coercive field. For these large, microscale grain diameters the exchange interaction was negligible. Bance et al. described a logarithmic decrease in the coercivity, consistent with other studies of large single-grain particles [237, 243, 247].

Another result of their study, Sepehri-Amin et al. were also able to show the resistance to demagnetisation at elevated temperatures improved with reducing grain size [32]. Using magnetic properties derived from experiment at different temperatures, the authors ran several demagnetisation simulations for grain diameters up to 130 nm. The smaller self-demagnetising stray-fields encountered in the finer grain models with effective demagnetisation constant, $\mathcal{N}_{eff}$, close to zero, were less susceptible to magnetic reversal at elevated temperature. However, their elevated temperature simulations did not account for micro-structural defects, which are the other source of nucleation sites in the nucleation model of coercivity.

The size distribution and shape of particles are also microstructure features which have been shown to influence the magnetic properties and demagnetisation of hard magnetic materials. In two-dimension studies, Schrefl, Fidler and Kronmüller compared demagnetisation curves of uniform and inhomogeneous granular models. The inhomogeneous model showed lower remanence and coercivity in comparison to the uniform microstructure. It was shown using graphical representations of the microstructures with the absolute values of the stray field overlaid that where an ensemble of small grains collected, the effect of the stray fields was $\approx 15\%$ higher. The larger stray-field effects lead an area of reduced magnetisation and the stronger stray-field act to reduce the coercive field. The coercivity of a collection of Nd-Fe-B-type cubic grains has also been shown to be lower than the equivalent collection of dodecahedron grains, again an effect of greater self-demagnetising fields at the sharp corners of the cubic grains [240, 247].

4.3.2 Hard and soft phase magnetic composites

Melt-spinning is a rapid-quench method which produces nanocrystalline ribbons or flakes from the melt, which can then be consolidated by SPS to produce materials with nanoscale grains [47, 208]. REPMs produced this way exhibit exchange coupling between grains, and enhanced remanence and $(BH)_{max}$ [42, 44]. Exchange coupled magnets have been proposed as composite permanent magnet materials which combine nanoscale hard and soft magnetic phases to push beyond the theoretical magnetic properties of conventional REPM materials, such as Nd-Fe-B and $Sm_2(Co, Fe, Cu, Zr)_{17}$-type [21]. The soft magnetic phases provide the large magnetisation, while the hard magnetic phase provides the coercivity. FEM micromagnetic models have been used to show the potential of exchange coupled composite magnet materials and investigate the interaction between the hard and soft magnetic phases, their structure and their distribution.

Schrefl et al. investigated the volume fraction and size distribution in two-dimensional, isotropic $Nd_2Fe_{14}B/\alpha - Fe$ composite models [241]. Significant remanence enhancement ($J_r/J_s = 0.92$) and exchange hardening was observed in composite models where the grain size was 10 nm, which is approximately twice the domain wall width of the hard $Nd_2Fe_{14}B$ phase [13]. Exchange hardening of the soft magnetic phases due to exchange coupling with neighbouring hard magnetic grains was less prevalent in larger grain models. In these fine grained models, the volume fraction of the soft magnetic $\alpha - Fe$ phase could reach 75% without significant detriment to the coercivity. In models with a favourable distribution of easy-axes and hard/soft magnetic phases, energy products in these simulated composite magnets exceeded $500\,kJ/m^3$. Fischer et al. produced a similar study in three-dimensional isotropic nanocrystalline $\alpha - Fe/Nd_2Fe_{14}B$ models, and reported for $\approx$10 nm magnetic grains, the soft phase can account for 55% of the total volume fraction and enhance the remanence by 50% [242]. The extra degree of freedom for the magnetic moments in the soft magnetic phase evidently reduce the volume fraction of the soft magnetic phase before deleterious effects on the coercivity.

Fidler and Schrefl brought further insight using a detailed 343 irregular grain, multi-phase model, consisting of hard magnetic $Nd_2Fe_{14}B$, and soft magnetic Fe_3B and $\alpha - Fe$ phases [233, 248]. These simulations again showed remanence enhancement and exchange hardening occurred when the average grain diameter was 15 nm to 20 nm. Lower coercivities were reported for the smallest grain diameters, around 10 nm, where strong exchange coupling between neighbouring hard magnetic grains rotated the magnetic moments across the grain boundaries, creating magnetic inhomogeneity away from the easy axis. This magnetic inhomogeneity lowers the energy barrier for magnetic reversal, thus lowering the coercivity. When the

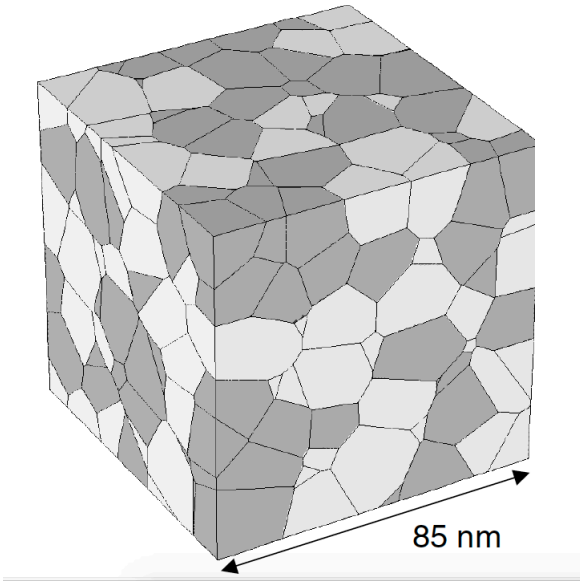

Figure 4.5: 343 grain model of nanocrystalline hard-phase $Nd_2Fe_{14}B$ (light grains), and soft-phases $\alpha - Fe$ and Fe_3B (dark grains) [233] ©2000 IOP Publishing, licence granted for reuse in thesis (licence number 4197081259332).

grain diameter was greater than 20 nm, the large soft magnetic phases affected the squareness and coercivity of the composite magnet demagnetisation curves. Interestingly, the remanence was also reduced in the larger grain models, where the self-demagnetising field induced closure domains within the large soft magnetic phase regions. These effects were also observed in the studies of Schrefl [235] and in FEM studies of irregular grain structure by Fischer et al [242]. Fischer compared their numerical data favourably with empirically derived laws for the remanence and coercivity in nanocrystalline composites.

4.3.3 Grain boundaries, inter-granular phases and misaligned grains

Ideal nucleation-based sinter magnets are comprised of magnetic grains, separated by a grain boundary phase. The transition region between the grain and grain boundary phase is ideally sharp within one atomic layer [249]. In real permanent magnets, however, grain boundaries and inter-granular regions are never defined as sharp transitions and there exists a region of inhomogeneity. There is deviation in the local intrinsic magnetic parameters between grains, which affect domain wall dynamics and can be sources of nucleation. There may also exist a variety of inter-granular phases, which further contribute to the inhomogeneity of the local microstructure. Figure 4.6 shows a typical backscattered SEM microstructure of

a Nd-Fe-B-type magnet. The hard magnetic $Nd_2Fe_{14}B$ grains (dark regions) are separated by thin, inter-granular phases (bright/white regions), rich in Nd, which also feature at triple-junctions. The influence of these inter-granular phases on the adjacent hard magnetic grains via the exchange and magneto-static interactions cannot be studied experimentally at the point of reversal. Therefore, the effect of grain boundaries and inter-granular phases within the microstructure on the magnetic properties of REPMs has become another well studied area of micromagnetic FEM modelling.

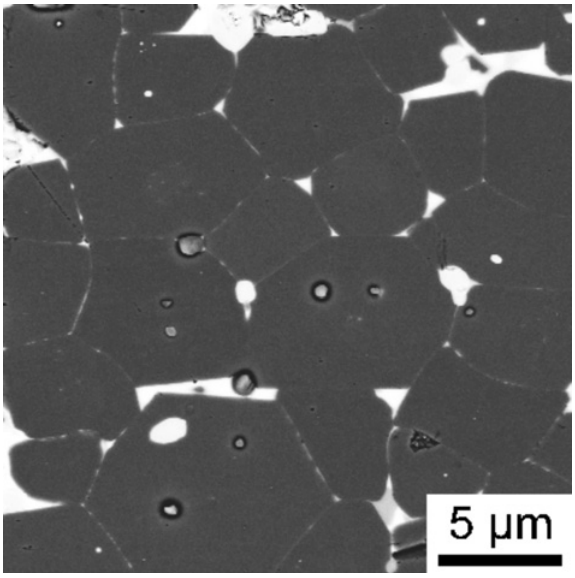

Figure 4.6: BS SEM image showing typical microstructure of a Nd-Fe-B-type permanent magnet. Dark regions correspond to $Nd_2Fe_{14}B$ phase, white regions are Nd-rich inter-granular phases [30] ©2012 Elsevier, licence granted for reuse in thesis (licence number 4197081447921).

Granular models, comprised of uniform, nanocrystalline $Nd_2Fe_{14}B$, with 3 nm thick grain-boundary regions of reduced magnetic parameters were performed by Fischer and Kronmüller [243]. The intrinsic magnetic properties of grain-boundary region, A_{ex}, K_1 and J_s, were reduced to 1/10th and 1/100th of the bulk values. The calculated remanence and coercivity for varying grain sizes were then compared with experimental data of Manaf et al. [38]. Fischer and Kronmüller found that the condition where exchange and magneto-crystalline anisotropy were reduced (magnetic saturation kept unchanged) best fit the comparison experimental values for M_r and H_c. However, the demagnetisation process used in the study was a static computation of equilibrium magnetic state. More modern numerical techniques use a dynamic computation, which follows the gyromagnetic precession of the magnetisation vector towards equilibrium by integration of the Gilbert

equation [233]. In comparative studies, Fidler and Schrefl [248] found that the static computation calculates larger M_r and H_c values in comparison to dynamic computations. Taking this information into account, the micromagnetic FEM study by Fischer and Kronmüller's still provides insight into the magnetic ambiguity of the grain-boundary region.

The different Nd-rich inter-granular phases in Nd-Fe-B-type magnets are ambiguous, with such uncertainties as to whether they are paramagnetic or ferromagnetic and crystalline [30]. However, it is well reported that their presence can improve the coercivity of Nd-Fe-B-type magnets by decoupling the $Nd_2Fe_{14}B$ grains, which comes at the expense of reduced remanence [233]. Fidler and Schrefl used FEM micromagnetic models identify visually the magnetic influence of the Nd-rich phase in nanocrystalline $Nd_2Fe_{14}B$ granular models with an inter-granular phase of varying magneto-crystalline anisotropy [233]. Initially, the inter-granular region shared the magneto-crystalline anisotropy of the bulk ($K_{1,IGR} = K_{1,bulk}$), and increased the misalignment of the easy axis between grains, which decreased the coercivity. Modelling the Nd-rich phase as non-magnetic ($K_{1,IGR} = 0$), the coercivity increased when the misalignment of the magnetic grains increased. The non-magnetic inter-granular region acted as a buffer between inter-granular coupling between $Nd_2Fe_{14}B$ grains and the misalignment of easy axis reduced the demagnetising field within the grains. High demagnetising fields are associated with highly aligned grains, which promote nucleation of reversed domains. The simulations were successful in explaining experimentally observed data [250].

The angular dependence of the applied field to the crystallographic easy axis has had a known deleterious effect on coercivity from Stoner and Wohlfarth's analytical model [226]. The non-interacting particles of Stoner and Wohlfarth shows a relationship between in the nucleation field and angular deviation of the applied field to be a minimum at 45°. However, real materials behave differently due to inter-granular interactions [250], as has been made evident by numerous micromagnetic FEM studies. Schrefl and Fidler have investigated the degree of alignment between isotropic, nanocrystalline Nd-Fe-B-type magnets in two-dimensional models [239]. These models, lacking the exchange interaction, found as misalignment increased between grains, the coercive field deviated from the theoretical nucleation field. When non-magnetic inter-granular phases were added to the model, the effects of misalignment were reduced and the coercive field was larger in comparison. These models were refined with the exchange interaction and again found misalignment in grains caused a reduction in the coercive field between particles, reducing H_N to approximately 30% of the theoretical maximum [251].

4.4 Pinning within precipitation hardened permanent magnets

4.4.1 Modelling the cellular nano-structure of precipitation hardened permanent magnets

The interaction of domain walls with pinning sites or phase boundaries and the effect on the pinning force or coercivity can be modelled and solved analytically by micromagnetic expressions. Kronmüller provides a detailed statistical analysis on the pinning field from point defects and planar defects [13]. This analysis was then used to derive an analytical expression for the coercive field based an abrupt phase boundary, of which the resulting equation was given as equation 2.18 in the magnetics theory chapter. This equation has been used in understanding the coercivity and pinning effect of the cellular nanostructure in $Sm_2(Co, Fe, Cu, Zr)_{17}$ permanent magnets [53]. The analytical model has also been developed for gradual changes in the intrinsic magnetic properties between the 2:17R cell and 1:5H cell boundary phase, as is the case in real permanent magnet nanostructures [84], using step changes in the intrinsic magnetic properties [252]. This has allowed features such as phase thickness to be incorporated into the model of the cellular nanostructure of $Sm_2(Co, Fe, Cu, Zr)_{17}$ permanent magnets. A similar analytical approach has also been presented by Skomski et al. which also investigate the different in domain wall energies across planar defects as sources of coercivity [253].

Numerical FE models add an extra level of insight with visual identification of the pinning process, as well as greater control over the cell and cell boundary structure, shape and volumes. The cellular nanostructure of $Sm_2(Co, Fe, Cu, Zr)_{17}$ permanent magnets is precipitated during a lengthy, multi-stage heat treatment. As discussed in the magnetic theory chapter, the morphology of he cell, cell boundary and lamellar phase are dependent on multiple variables, such as alloying composition, and the time and temperature of the heat treatment. FEM modelling has been used to identify the optimal $Sm_2(Co, Fe, Cu, Zr)_{17}$ precipitated structures for either room or high temperature coercivity [233, 254–257], which can then be replicated during processing and heat treatment. Similarly, the study of the different pinning mechanisms,repulsive pinning, where $K_1^{cell-boundary} > K_1^{cell}$, and attractive pinning, where $K_1^{cell-boundary} < K_1^{cell}$ [13], has been studied by FEM in relation to their pinning of domain walls and cell boundary structure.

Streibl et al [254] and Fidler and Schrefl [233] created three dimensional, $3 \times 3 \times 3$ grain models with 2:17 phase cells and 1:5 phase cell boundaries, as shown

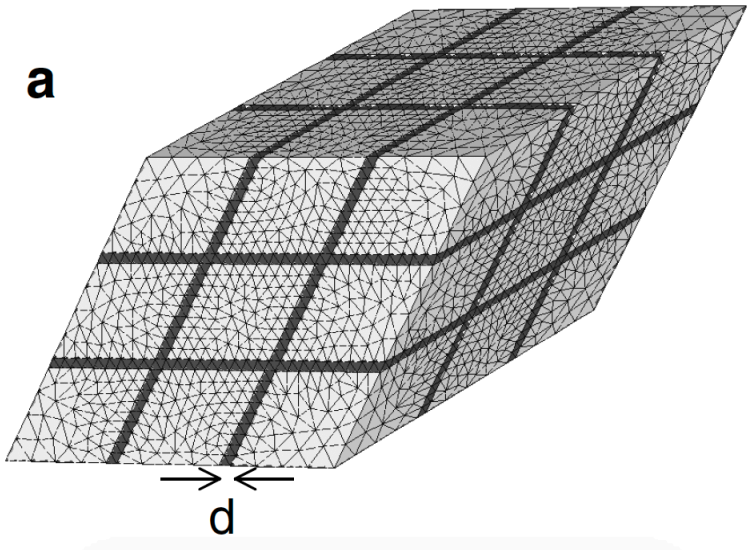

Figure 4.7: FE model used in three-dimensional micromagnetic simulation of Sm_2Co_{17} rhombic cells and cell-boundary $SmCo_5$ phase of varying thickness, d [233]

in figure 4.7. Studying an attractive pinning scenario, where domain walls are pinned within the cell boundary phase, they investigated the thickness, d, of the cell boundaries for varying cell sizes. Figure 4.8 shows the pinning field for cells, whose edge length was 100 nm, was maximum when the cell-boundary thickness was in the range $\approx$ 10 nm to 20 nm [233, 254].

Similar maximum coercivities were measured for cell boundary thicknesses in the range $\approx$10 nm to 20 nm by Scholz et al., who also performed simulations under attractive pinning scenarios and increased the cell boundary phase thickness up to 40 nm [255, 256]. These models show the maximimum pinning field is achieved for attractive pinning $Sm_2(Co, Fe, Cu, Zr)_{17}$ permanent magnets when the cell boundary thickness is greater than the domain wall width for the 1:5 cell boundary phase (8.5 nm using the instrinsic magnetic properties reported by Streibl [254]). If the cell boundary thickness is below the domain wall width of the 1:5H phase, the cell boundary physically can not contain and thus pin the domain wall.

Scholz et al. [255] also noted for models where the cell-boundary thickness was more than four times the domain wall width, the demagnetisation curve was not rectangular and had a step feature. Here, the cell-boundary region was large enough for nucleation of reversed domains to initiate at the edge, before domain walls could move into the cell-boundary phase and be pinned. The step feature is generated when, at higher fields, the magnetically harder cellular phase also nucleates a reversed domain at the corner of the cell, resulting in a two-step demagnetisation

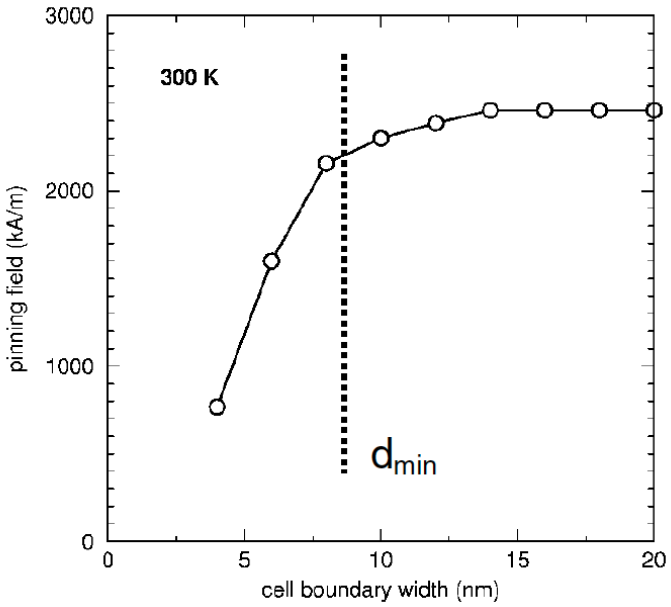

Figure 4.8: Calculated pinning field of precipitation hardened $Sm(Co, Fe, Cu, Zr)_{7-8}$-type magnet, with attractive pinning, as function of cell-boundary thickness, d. $d_m$in is the minimum thickness required to achieve high pinning field, roughly equivalent to the domain wall width of the cell boundary phase [233] ©2000 IOP Publishing, licence granted for reuse in thesis (licence number 4197081259332).

process.

The cell-boundary thickness in repulsive pinning $Sm_2(Co, Fe, Cu, Zr)_{17}$ permanent magnets have also been investigated by FEM micromagnetic models of Chen et al. [257]. They found, for cell edges fixed at 50 nm, the coercivity of their models increased with cell boundary thickness, up to 8 nm. For cell boundaries below $\leq$ 6 nm, they observed only a single-phase demagnetisation behaviour, indicating no domain wall pinning. For cell boundaries ≥ 6, a step-like feature, indicating a two-phase demagnetisation behaviour, was observed. This suggests that nucleation of magnetic reversal originates in the magnetically softer 2:17 cells, which are then pinned by the magnetically harder 1:5H cell boundaries. This analysis is entirely from simulated demagnetisation curve and evidence of reversal or pinning in the FEM models are not shown, however the results are in agreement with one-dimensional analytical models of Scholz et al. [55], which also show coercivity enhancement in repulsive pinning magnets increases with cell boundary thickness.

4.4.2 Investigations of magneto-crystalline anisotropy differences across the cell-boundaries in relation to the pinning field

Building on the analytical expressions presented by Kronmüller and Goll [53], FEM micromagnetic models and simulations have investigated the pinning effect with respect to the difference in the intrinsic magnetic properties between the 2:17R cell and 1:5H cell-boundary phases.

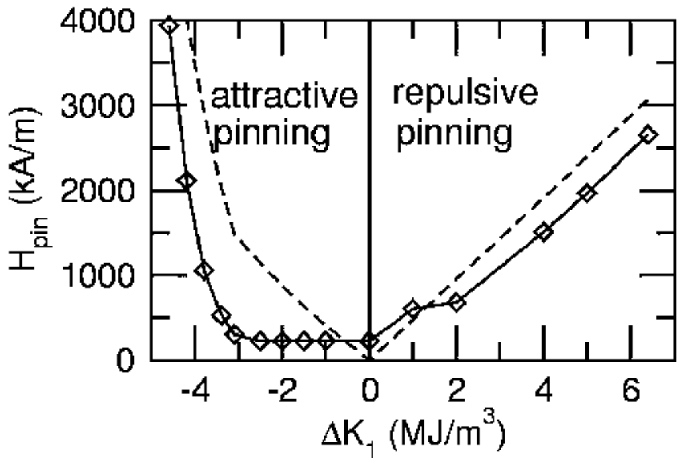

Figure 4.9: Pinning field as a function of difference in magneto-crystalline anisotropy constant between cell and cell-boundary phase in $Sm(Co, Fe, Cu, Zr)_{7-8}$ magnets. Comparison of three-dimensional micromagnetic results are made with one-dimensional analytical model (dashed curve) [258] ©2004 Elsevier, licence granted for reuse in thesis (licence number 4197090859664).

Three-dimensional, $3 \times 3 \times 3$ granular models, similar to those shown in figure 4.7, were used to simulate demagnetisation in $Sm_2(Co, Fe, Cu, Zr)_{17}$ permanent magnets for both attractive and repulsive pinning types [255, 256]. The magneto-crystalline anisotropy constant, $K_1^{cellboundary}$ of the cell boundary phase was increased or decreased relative to K_1^{cell}, inducing either attractive or repulsive pinning, as indicated by the x-axis in figure 4.9. Similarly, the exchange energy was also modified with ΔK_1 [258]. The cells in these models had a long axis length of 125 nm and the cell boundaries were 5 nm thick. Figure 4.9 shows the calculated pinning fields with ΔK_1, where the greatest pinning field is achieved when ΔK_1 is largest. The results are compared to date derived from Kronmüller and Goll's one-dimensional analytical model [53] and show good agreement in the repulsive pinning region with the FEM micromagnetic models of Scholz et al. [258]. There is divergence between the models in the attractive pinning region, where

in the FEM micromagnetic model the domain wall width increases as $K_1^{\text{cellboundary}}$ is reduced. Lower pinning fields are reported because the domain wall width in the cell boundary phase does not fit within the 5 nm cell boundaries. However, in for the lowest values of ΔK_1, which represent very large concentrations of Cu in the cell boundaries, the exchange interaction is significantly reduced and the cell boundary phase decouples the the 2:17R cells from one another [258].

For these models, a sharp transition existed from the cell to cell boundary phase, which may not exactly represent real materials. These models do well to show empirically derived trends, which compare favourably with experimental observations of $Sm(Co, Fe, Cu, Zr)_Z$ magnets. To further improve these models to accurately predict coercivities and magnetic performance, new techniques may need to include a gradient change of intrinsic magnetic properties over the cell-boundary. However, it can be concluded from these studies that to achieve large room temperature coercivities, the difference in magneto-crystalline anisotropy between the cell and cell-boundary phases is required, while also maintaining an appropriately thick cell-boundary phase in the attractive pinning situation.

4.4.3 Modelling the anomalous temperature effect in low-transition metal SmCo alloys

An area of focus in $Sm(Co, Fe, Cu, Zr)_z$ FEM micromagnetic modelling and simulation is that of the "anomalous" temperature effect which is observed in alloys with low transition metal content/high rare earth content (often summarised by their z-ratio ≤ 7.5) [259–261]. These alloys are usually deficient in iron and copper. These alloys typically have low room temperature coercivity, which remains relatively stable with or decreases relatively slowly with temperature, only to reach a maximum at high temperatures (>600 K). Here, there is a sudden change in the temperature coefficient for coercivity, which becomes positive, before becoming negative again as temperature increases again. Evidence of this unusual temperature/coercivity relationship, with comparison between two $Sm_2(Co, Fe, Cu, Zr)_{17}$ alloys, which have high and low iron and copper content, as well as Nd-Fe-B-type magnet, is given in figure 4.10 [262].

It is hypothesised that this effect is a result of either a change from a pinning-based coercivity mechanism to either a nucleation-based or rotation based mechanism [23, 262, 263], although other arguements are made that this effect is simply a result of a pinning based coercivity with a positive relationship with temperature [259, 260]. The latter explanation would be expected

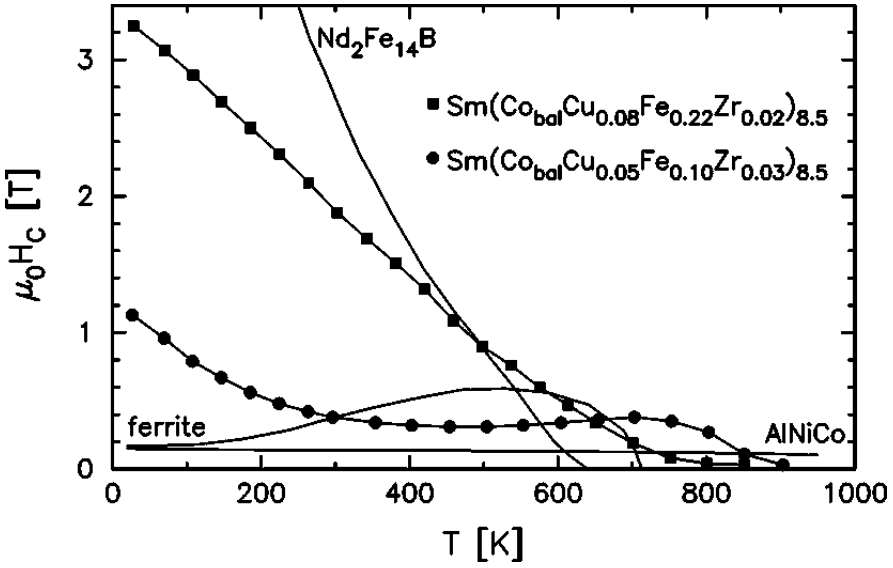

Figure 4.10: Temperature dependence of coercivity of transition metal-rich (square symbols) and transition metal-poor (circles) in comparison with other permanent magnetic materials. The anomalous temperature feature can be seen in the transition metal-poor plot at around 600 K to 800 K [259] ©2000 AIP Publishing LLC, licence granted for reuse in thesis (licence number 4197090940629).

to produce a linear relationship of coercivity that increases with temperature, although most data observe a minima before the anomalous temperature effect [263].

To better understand this phenomena, Rong et al. used FE models to investigate this behaviour using 64 cells, ranging in size from 20 nm to 100 nm and separated by a 8 nm cell boundary layer [264]. Temperature dependent values for A_{ex}, K_1 and J_s were assigned for the 2:17R cells and 1:5H cell boundary phases to emulate their temperature dependent properties. In all their simulations, the anomalous temperature effect featured in the coercivity temperature profile and the 100 nm cell models exhibited the overall best coercivity. These results are shown in figure 4.12.

Their models also showed characteristics of domain wall pinning in initial magnetisation curves for temperatures $\leq$ 800 K. Above 800 K, they observed magnetic reversal change to coherent rotation of the magnetic moments, which is reminiscent of single domain nanocrystalline nucleation magnets. Their explanation for this behaviour was prior to the onset of the anomalous temperature effect, the cell boundary phase approaches its Curie temperature ($T_c \approx 950$ K) and K_1 and A_{ex} decline rapidly. These effects decouple the magnetically harder 2:17R cellular phase, improving the coercivity and creating the bump observed in coercivity measurements at high temperatures. The isolated nanoscale 2:17R cells behave

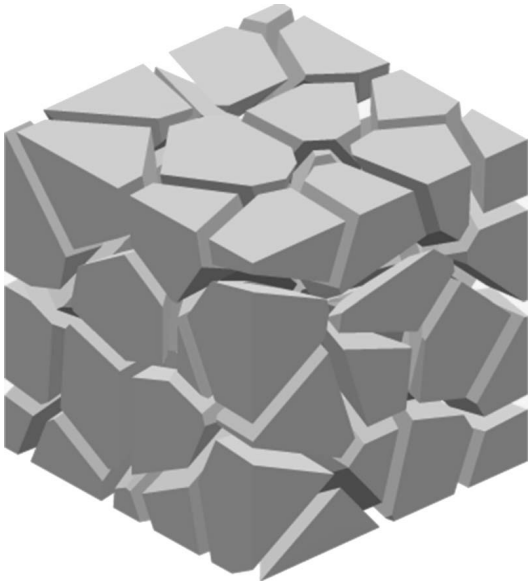

Figure 4.11: FE model used in three-dimensional micromagnetic simulations by Rong et al. Cells are Sm_2Co_{17} phase, with layer phase acting as cell-boundary $SmCo_5$ phase [264]

like single domain particles, with reversal by coherent rotation. As temperatures increase further, T_c is reached for the cell phase and the magnetic properties of the magnetic system deteriorate.

The simulations of Rong et al. did not include thermally activated processes, instead using intrinsic magnetic properties taken from experimental data at temperature. No experimental values at elevated temperatures were available for A_{ex}, so these values were estimated. However, their study is one of the most detailed on the temperature profile of the coercivity in $Sm_2(Co, Fe, Cu, Zr)_{17}$ magnets and their results appear to show changes in the coercivity mechanism at high temperature, as well as explain the anomalous temperature effect. These results agreed with prior studies of Chen et al. on cubic grain models, which also showed a transition from pinning based coercivity at temperature $\geq$700 K [24, 257]. A deviation between the two studies on the temperature at which the anomalous behaviour is onset is likely due to differences in model properties, such as cell size, boundary thickness and shape, as well as the temperature dependent intrinsic magnetic properties used in the FE model for A_{ex}, K_1 and J_S. Kronmüller and Goll have also shown, through a modification of their one-dimensional analytical model, that the coercivity mechanism of $Sm_2(Co, Fe, Cu, Zr)_{17}$ magnets can change from repulsive to attractive pinning, before again changing to a nucleation based coercivity, when the temperature reaches the Curie temperature of the 1:5 cell-boundary phase [23].

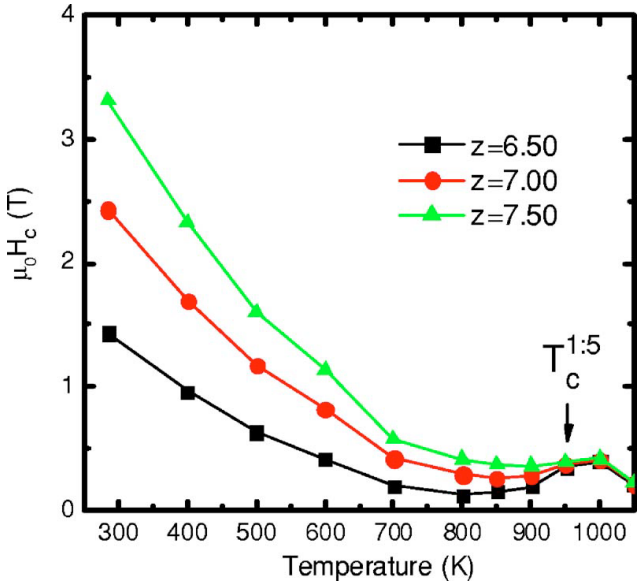

Figure 4.12: Numerically calculated coercivity versus temperature for three different models of $Sm(Co, Fe, Cu, Zr)_z$ precipitation hardened magnets. Here the z value is related to the cell length in each axis (with increasing z value the cell lengths are 20, 50 and 100 nm respectively [264] ©2006 AIP Publishing LLC, licence granted for reuse in thesis (licence number 4197100893829).

4.5 Summary

Modern FEM studies are required to be three-dimensional, multi-grain and include both the exchange and magneto-static interactions. Accurate models go further to replicate grain structures, typically limited to the nanoscale, and microstructural features such as size and shape inhomogeneities. Next generation models may look to incorporate microstructural defects to accurately model demagnetisation processes in real REPM materials. Defects, such as surface abnormalities and porosity within the volume, are significant sources of self-demagnetising fields and magnetic reversal nucleation. Without these features in the FEM model, simulated demagnetisation curves and predicted coercivities are over-estimated, in comparison to real REPM materials. Implementation of these features may is difficult, as they can be much larger than several nano-grains and require very fine meshing as they are sources of nucleation, so multi-grain models with defects may have to wait until computing power can handle magnetic systems of that scale. But there exists an opportunity for a single large magnetic particle to be studied with a single pore and simulate the effect on the demagnetisation process. Thermally activated processes are also features which could be implemented, which could be especially important towards modelling temperature degradation of the intrinsic magnetic properties, which will complement our empirically derived relationships. This is an area of FEM micromagnetic modelling currently active [233, 258, 265].

In this chapter, a summary of the methodology of micromagnetic FEM modelling and simulation has been provided, along with a review of the main research topics relating to REPM and relevant to the work conducted in this project. These topics primarily concern the inclusion of exchange and dipolar interactions, grain size, shape and phase distribution. The necessity for mesh elements to be of the order of 5 nm for hard ferromagnetic material models limits the size and scale of the magnetic model. However, this is not a significant problem when modelling the cellular structure of $Sm_2(Co, Fe, Cu, Zr)_{17}$ magnets, which are of the order of 100 nm after a typical heat treatment. Therefore, if the relationships between the model structure and parameters are taken into account when building our $Sm_2(Co, Fe, Cu, Zr)_{17}$ models, we are able to accurately simulate demagnetisation and test hypotheses and provide further confirmation to experimental data in our research project.

Outcomes of the literature review

The aims of the project were outlined in the introduction chapter. In summary; the intentions are to process and study $Sm_2(Co, Fe, Cu, Zr)_{17}$ powders to bulk theoretical density utilising the SPS technique and investigate the heat treatment process for these magnets. The developed knowledge of this processing route is then to be applied to prototype and produce increased resistivity $Sm_2(Co, Fe, Cu, Zr)_{17}$ and CaF_2 composite magnets.

In the previous chapters, a thorough literature review was collected and detailed notable past and current bodies of work within the fields of REPMs, sintering and FEM modelling, all of which are deemed relevant and influential to this work. Using this collected knowledge, the relevance and uniqueness of this project is justified in the following paragraphs.

The first aim of the project is a study of the processing methodology for $Sm_2(Co, Fe, Cu, Zr)_{17}$ microcrystalline powders using the SPS platform. Chapter 3 illustrated numerous studies which highlighted beneficial properties to REPMs through processing by the SPS technique. The retention of nanocrystalline grain size, a recurring feature of the SPS technique, was often the basis for favourable magnetic properties, such as enhanced coercivity, and was the underlying theme for most SPS related REPM studies. However, it was also evidenced how microcrystalline magnets processed by SPS measured comparable magnetic properties in comparison to conventional sintered magnets, but also exhibited improved corrosion resistance and mechanical properties [39, 40, 206, 215]. These studies were conducted with Nd-Fe-B-type magnets and, overall, the literature review showed far less attention has been given to the SPS processing of the Sm-Co series of permanent magnets. Sm-Co binary alloys were generally the focus of SPS based studies and almost always focused on nanocrystalline magnets. Of the two papers on SPS processing of the $Sm_2(Co, Fe, Cu, Zr)_{17}$-type magnetic alloy, one sought to produce nanocrystalline magnets [36], whilst the other only detailed the relationship between the sinter temperature [223]. Therefore, there has been minimal research into the processing of $Sm_2(Co, Fe, Cu, Zr)_{17}$ powders by the SPS technique. Without much precedence with this technique and this material, it is the aim of this project

to first investigate the SPS technique as a processing route for microcrystalline $Sm_2(Co, Fe, Cu, Zr)_{17}$ powders. The information gained from this work will include the reporting of the optimal processing parameters for producing bulk theoretical density specimens, identification of the critical areas of the processing route, such as carbon contamination and oxidation effects, and characterisation of the resulting microstructure of the $Sm_2(Co, Fe, Cu, Zr)_{17}$ magnets.

The literature review highlighted how crucial and well studied the heat treatment of sintered $Sm_2(Co, Fe, Cu, Zr)_{17}$ magnets are [52, 77]. Chapter 2 showed how every aspect of the heat treatment, from the $Sm_2(Co, Fe, Cu, Zr)_{17}$ alloy composition and specimen's dimensions, to the ageing temperature and cool down rate, can have a notable effect on the resulting precipitated microstructure, and ergo; the hard magnetic properties. With this in mind, no reported study of SPS processed $Sm_2(Co, Fe, Cu, Zr)_{17}$ magnets provide any detail on the specific heat treatment, which is because they derive their hard magnetic properties from a fine, nanoscale grain structure [36]. For this project, which works with microcrystalline powder and grain sizes, the heat treatment for the previously unexplored SPS processed $Sm_2(Co, Fe, Cu, Zr)_{17}$ magnets will require study. A typical heat treatment structure for conventionally sintered $Sm_2(Co, Fe, Cu, Zr)_{17}$ permanent magnets is used as a starting point for the study and is then adapted. The change in the magnetic properties with the different heat treatments will provide an indication towards the appropriate heat treatment structure and parameters, as well as in-direct evidence for the microstructural evolution, for the SPS processed magnets. The optimisation of the heat treatment for conventionally sintered $Sm_2(Co, Fe, Cu, Zr)_{17}$ permanent magnets has been an active area for nearly 50 years, and is still ongoing and not fully understood. Therefore, for this project; it is only the aim to build a foundation for the heat treatment of SPS processed $Sm_2(Co, Fe, Cu, Zr)_{17}$ magnets, which can used as a basis to improve on in future work.

The knowledge gained in the processing by SPS and subsequent heat treatment of the $Sm_2(Co, Fe, Cu, Zr)_{17}$ magnets will then be used to prototype high resistivity $Sm_2(Co, Fe, Cu, Zr)_{17}$ and CaF_2 permanent magnets. One method to reduce the burden of resources for REPMs is to improve their performance and life-cycle in application and reduce the volume of magnetic material require for use. The eddy losses incurred in REPM in electric motors was shown in the literature to be inversely proportional to the resistivity of the permanent magnet [266]. In high performance magnets, lamination of electrically insulating material are applied, which are expensive, both in wasted material and in the additional processing and man hours. Alternatively, for low cost applications; bonded magnets this

have excellent performance against eddy losses, but are limited to low operating temperatures due the polymer [134]. In the literature, a collection of studies showed numerous methods to increase the resistivity of high performance REPMs without the need for machining or coating after sintering. Some of these involved coating magnetic powders with a die-electric material, or artificially creating laminated microstructures through hot deformation. A large amount of variability was found in the literature study, with different methods and weight addition of different insulating material. Of interest was a method of mixing the magnetic and electrically insulating powders before the sinter process to increase the bulk resistivity isotropically, which offers a uniform reduction in eddy loss generation in all directions during application. This method also offers a quick and cheap way of introducing high resistivity permanent magnets into current sintered REPM processing routes. However, again it is noted the lack of study in this area for $Sm_2(Co, Fe, Cu, Zr)_{17}$ magnets, which are naturally more electrically conductive than Nd-Fe-B-type magnets [131], and thus are more susceptible to eddy losses, but are also important as they are the only commercial REPMs to operate at temperatures beyond the capabilities of Nd-Fe-B. It is unknown what affect mixing electrically insulating and non-magnetic material has on the delicate heat treatment of $Sm_2(Co, Fe, Cu, Zr)_{17}$ magnets. Therefore, it is another aim of this project to answer these questions for $Sm_2(Co, Fe, Cu, Zr)_{17}$ composite magnets, with additions of CaF_2, which was selected as a cost-effective electrically insulating material after showing promising results with numerous high resistivity Nd-Fe-B-type, and similar, permanent magnets [8, 128, 133, 137]. Processing and heat treatment methodologies learnt from the preceding chapters are adapted for the composite magnets and their magnetic properties and material properties detailed as to the effectiveness of the method and materials used to create high resistivity $Sm_2(Co, Fe, Cu, Zr)_{17}$ magnets for application.

This project uses FEM modelling and micromagnetic simulations to compliment the experimental studies and verify assumptions and test hypotheses. Micromagnetic modelling provides control and access to investigations of particular features within the microstructure of REPMs, which are not achievable or costly to perform on real specimens. Understanding the microstructure in permanent magnets and the mechanisms of magnetic reversal are crucial to developing high performance REPMs. To provide a background to the nature of this type of work, the literature review provided a comprehensive review of past and current FEM micromagnetic studies of REPMs in chapter 4.

In summary, much of the reported work focussed on the influence of the exchange interaction and the dipolar field on the nucleation of reversal domains, as

well as the relationship of microstructural features, such as; grain size/shape and grain boundaries, on the hard magnetic properties. Where this work is unique is in the incorporation of non-magnetic phases, between grains and randomly distributed within the microstructure, and their influence on magnetic reversal and macroscopic magnetic properties. The literature also highlighted the work of Scholz et al. [55, 255, 256, 258, 267], whom studied the morphology of the cellular precipitated nanostructure in heat treated $Sm_2(Co, Fe, Cu, Zr)_{17}$ magnets, with particular focus on the cell size and wall thickness, and their relationships with the pinning field and coercivity. This type of FEM $Sm_2(Co, Fe, Cu, Zr)_{17}$ model is developed within this project, as comparison is made with a uniform and an irregular cell and cell wall structure for, which aims to verify conclusions made from experimental studies of the $Sm_2(Co, Fe, Cu, Zr)_{17}$ microstructure on the nature that under/over-developed or contaminated microstructures are the cause of irreversible magnetic loses.

Chapter 5

Experimental methods

5.1 Introduction

This chapter describes the equipment used within the project to process $Sm_2(Co, Fe, Cu, Zr)_{17}$ powders into bulk magnets and characterise the material and magnetic properties, as well as microstructural features.

The techniques listed are well established and so description of their use will focus on the preparation and parameters used, rather than the technicalities. For any techniques or equipment we have developed ourselves; extra detail is provided in how we have tested the repeatability and validity of the measured data.

5.2 Powder processing

$Sm(Co, Fe, Cu, Zr)_{8.2}$ pre-alloyed powders, of which the composition was verified by X-ray fluorescence, were provided by Arnold Magnetic Technologies (Sheffield, UK). The exact composition of each alloying element is protected, but the overall alloying composition is a standard commercial grade (under the name Recoma 28), which is designed for high room temperature coercivity and 'squareness' in the demagnetisation curve [109]. Throughout the remainder of this report, the composition of these powders are simply referred to as $Sm_2(Co, Fe, Cu, Zr)_{17}$. Precursor powders were produced from the crushing of a highly controlled cast alloy. The commercial powders were then refined to an approximate size of around 10 µm using jet milling at their production facility in Lupfig, Switzerland. Jet milling is a process which refines and narrows the size distribution of powders. Coarse powder is fed into a milling chamber and high velocity inert gas jets force the powders to pulverise each other. Care must be taken to avoid oxidation (and other contaminants), as well as over-processing and particle welding [27]. Therefore, to accommodate the former risk, the process is performed under inert atmospheres to minimise contamination of

the fine powders. The coarse powders become refined over multiple impacts and are eventually collected using a specified classifying rotor. The typical average powder size of a jet milling process is around 5 µm to 10 µm [40, 41, 141, 215, 268]. Ultrafine particles are removed in a cyclone chamber; where lighter, smaller particles move to the top of the chamber and are removed, while the heavier, larger particles are collected at the bottom. As well as narrowing the size distribution of the powder alloy, the other aim of this processing stage is to produce single crystal particles. Single crystal particles contain no grain boundaries and are therefore defined by a single axis of magnetisation. During pulverisation the coarse, multi-grain powder particles will ideally fracture along the grain boundaries, eventually becoming single crystal particles. If the $Sm_2(Co, Fe, Cu, Zr)_{17}$ powders are single crystal particles, a high degree of alignment can be achieved with a sufficiently large magnetic field before the sinter stage.

The $Sm_2(Co, Fe, Cu, Zr)_{17}$ powders were stored in a Kilner (England, UK) clip-top jar, which was flooded with argon gas and sealed with wax film tape after each use to minimise oxygen and moisture contamination of the powders over the coarse of the project. However, handling of the powders occurred in air in preparation for the SPS process. The weighing of the powders using digital scales and transfer to the graphite moulds was performed under local exhaust ventilation with a calibrated flow rate of 0.4 m/per/second for health and safety. The same method was followed for the $Sm_2(Co, Fe, Cu, Zr)_{17}$ and calcium fluoride (CaF_2) composite powder mixtures, although with an additional mixing stage. After weighing, the composite powders were collected in a 60 mm diameter plastic container and rigorously mixed using a SpeedMixer DAC 800 (FlakTek Inc, USA); a bladeless mixing processor utilising rapid three-dimensional rotation. The mixing was not performed under an inert atmosphere and to create a homogeneous mixture, a three step mixing program was devised: two stages of continuous mixing at 800 rpm for 2 minutes, followed by one stage of continuous mixing at 1000 rpm for 1 minute. Upon completion of each stage, the container was removed and the composite powders inspected. Any excess powder was tapped and scrapped from the container walls using a weighing spoon to ensure all powders were mixed.

5.2.1 Powder alignment

For studies on the alignment of $Sm_2(Co, Fe, Cu, Zr)_{17}$ powders, pulsed or continuous DC magnetic fields were applied before compaction by SPS technique. Both methods of alignment provide a uniform magnetic field over the entirety of the powder containing graphite mould. Figure 5.1 shows a simple schematic of the powder alignment process.

In either case, approximately 13 g of $Sm_2(Co, Fe, Cu, Zr)_{17}$ powder was placed within a 20 mm inner-diameter graphite mould and enclosed as standard for the SPS process. This is described in more detail in section 5.2.2. Care was taken to enclose the powder but also provide room for the powders to rotate and reorientate under the applied magnetic field and also minimise contact/frictional resistances.

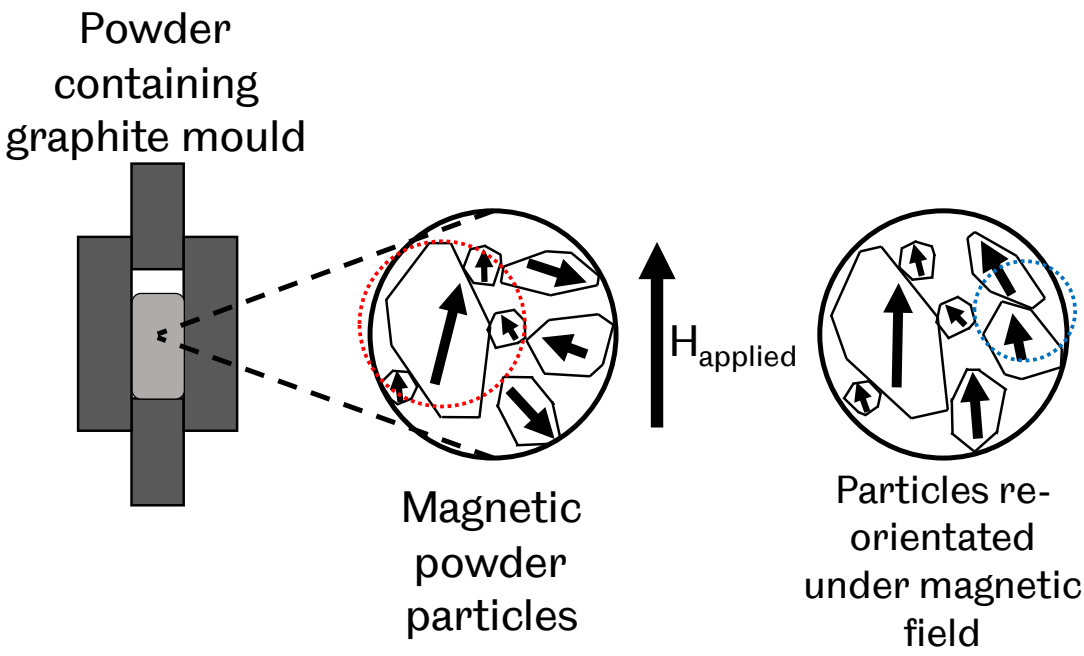

Figure 5.1: Schematic showing powder containing graphite mould with close-up giving an example of the random orientation of the powder particles. Arrows indicate the easy axis of particle. Red dashed circle highlights powder agglomerate of several individual particles. After magnetic field is applied, particles and agglomerate are re-orientated in field direction. Agglomerate is re-orientated collectively, but some of the individual particle easy axes can not align with field direction. Blue dashed line shows example where friction interferes with the re-orientation process.

Pulse magnetic fields were produced using a Hirst Magnetic Instruments (Falmouth, UK) pulse field magnetiser, which utilises a large capacitor bank, charged to 2000 V and discharged over 10 ms to pulse ≈2.5 T magnetic field, aligning the powders in the axial direction.

For continuous DC magnetic field powder alignment, a Newport instruments (Newport Pagnell, England) type A electro-magnet was used to align powders in the axial direction. The pole pieces of the electro-magnet were separated by an air-gap of 76 mm, providing a continuous and uniform magnetic field of 0.3 T across the entire graphite mould in the axial direction.

After pulse or continuous magnetic field powder alignment, a Specac (Kent, UK) hydraulic pellet press was used to compact the powders and 'lock' the alignment in place. 5 t (equivalent to 16 MPa) was applied to the graphite punches before the powder containing mould was transported to the SPS furnace for processing.

5.2.2 SPS

A general description of the SPS technique and how it compares to conventional sinter techniques was given in chapter 3. Here, a description of the equipment and processing methodology used to consolidate $Sm_2(Co, Fe, Cu, Zr)_{17}$ powders is accounted.

The SPS apparatus used in this project was FCT Systeme GmbH (Frankenblick, Germany) Spark Plasma Sintering furnace type HP D 25. For each specimen, approximately 13 g of $Sm_2(Co, Fe, Cu, Zr)_{17}$ powder was weighed out and set-aside. Similar quantities were also used for composite powder samples. This quantity of powder produced fully dense samples sufficient for characterisation with thickness between 4.0 µm to 4.5 µm.

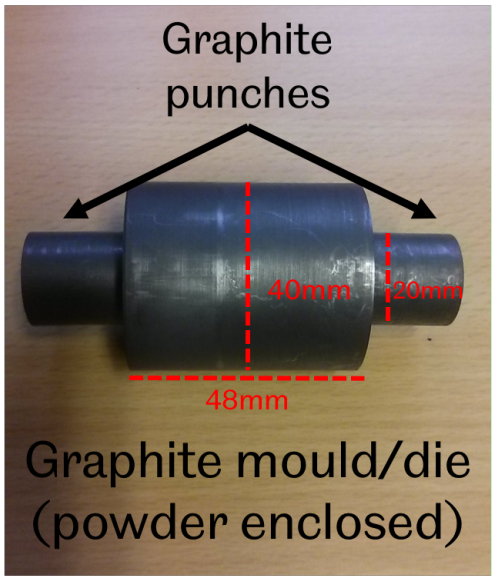

Figure 5.2: High density graphite mould with enclosed powder showing main components

For all materials studied, a 20 mm inner-diameter high density graphite mould (material grade 2333, produced by Mersen, UK) was used, with an annotated example shown in figure 5.2. To prepare the mould for the SPS process, the interior is lined with 0.35 mm thick graphite foil. This is done for every sample produced and is done so to prolong the use of the graphite mould and aid removal of the specimen after the SPS process. The bottom graphite punch is then inserted into

the mould and also covered with a 20 mm diameter piece of graphite foil. The weighed out powder is then carefully poured into the mould. Another piece of 20 mm diameter graphite foil is placed on top of the powder and the second graphite punch inserted to enclose and contain the powder.

If powder alignment is intended, the process then follows as described in section 5.2.1, otherwise the powders are cold compacted using a Specac (Kent, UK) hydraulic pellet press with 5 t (equivalent to 16 MPa applied to the powders. This is done to increase packing and contact between powders to improve current flow and heat transfer. The graphite mould is then placed within the SPS vessel and the processing parameters specified and uploaded directly to the on-board SPS computer system. 16 MPa is applied to the top graphite punch before the program starts to maintain good contact for current flow. The SPS vessel is then pumped to vacuum before flooding with 99.998% purity argon gas (BOC group, Guildford, England).

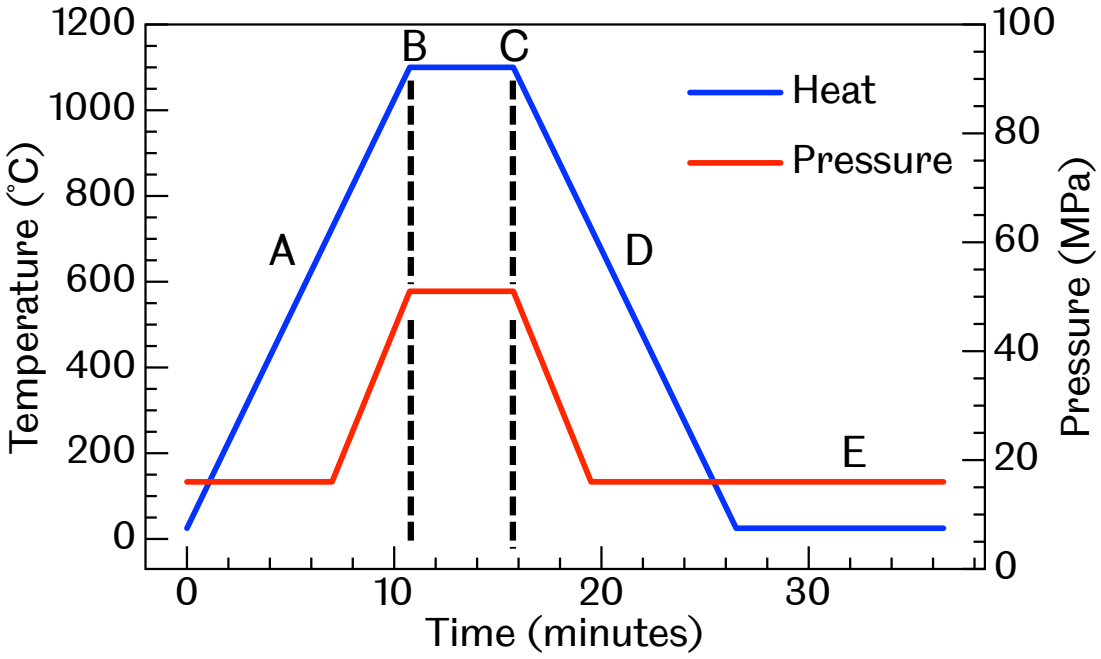

Figure 5.3: Schematic showing typical thermal and pressure cycle used in SPS. A highlights the heating/pressure rate, B-C highlights the dwell time, temperature and pressure. Current is turned off at C. D highlights cooling/pressure removal rate (usually fixed) and E highlights the cool down.

A typical thermal and pressure cycle is shown in figure 5.3, which also describes the main processing variables. Table 5.2.2 shows the range of processing parameters used in our study of SPS processed $Sm_2(Co, Fe, Cu, Zr)_{17}$ (and CaF_2 composite)

magnets. The DC current applied at maximum temperature was ≈1000 A which, if we assume all current flows through the 20 mm diameter graphite punch, equates to a current density of around 30 kA cm^{-2}. Pulsed electric current was not used in this project.

Heating rate	**(°C/ min)**	50 to 200
Hold temperature	**(°C)**	800 to 1100
Pressure	**(MPa)**	25 to 51
Holding time	**(min)**	5 to 10
Cooling rate	**(°C/ min)**	100

Table 5.1: Range of SPS processing parameters used to consolidate powders of $Sm_2(Co, Fe, Cu, Zr)_{17}$ (and CaF_2)

Upon completion of the processing cycle, the graphite mould was removed from the SPS vessel and the consolidated specimen removed from the mould. After SPS processing, the specimen is encased in adhered graphite foil. A quick, but gentle surface polish (120 grit/grade SiC abrasive paper at 150 rpm platen speed) was used on all surfaces to remove the adhered graphite until visibly abolished. The specimens were stored dry in individually labelled bags and catalogued in plastic storage boxes within an air environment.

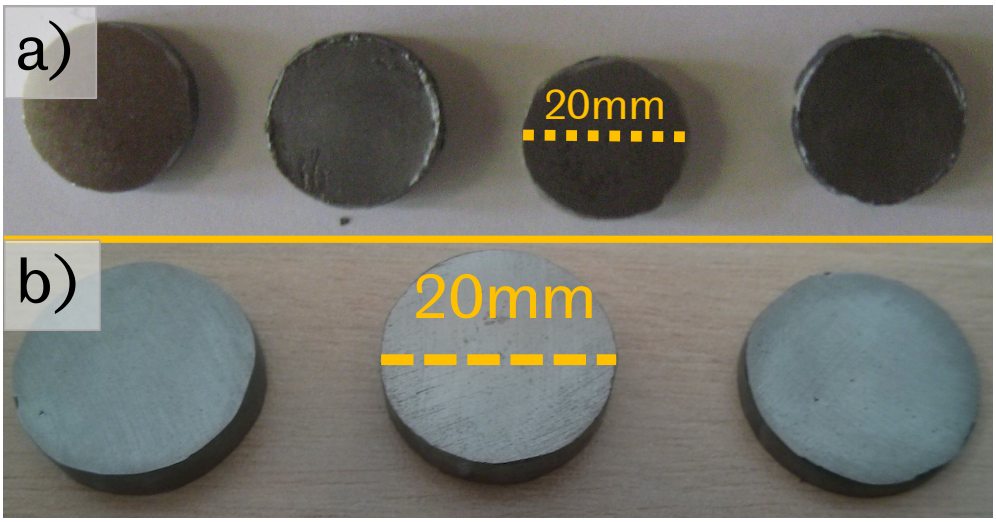

Figure 5.4: Example SPS processed $Sm_2(Co, Fe, Cu, Zr)_{17}$ specimens (a) with surface adhered graphite foil (b) after mechanical surface polish and removal

5.2.3 Heat treatment

Chapter 2 section 2.5.1 provided a detailed description of how and why the heat treatment is applied to sintered $Sm_2(Co, Fe, Cu, Zr)_{17}$ permanent magnets. For this project, heat treatments were performed using an Elite Furnace TSH18/75/300 (Leicestershire, England). The structure of the heat treatment used for the SPS processed $Sm_2(Co, Fe, Cu, Zr)_{17}$ magnets was based upon the typical heat treatment applied to conventional sinter processed $Sm_2(Co, Fe, Cu, Zr)_{17}$ magnets:

- Homogenisation at 1170 °C for 2 hours within an argon atmosphere
- Ageing at 850 °C for between 2 - 24 hours within an argon atmosphere
- Immediately following the ageing stage, slow cooling at 1 °C/ min to 400 °C within an argon atmosphere before removal of the sample from the furnace and quenched to room temperature in either water or quenching oil

The maximum continuous temperature for the Elite Furnace TSH18/75/300 is specified at 1800 °C, which is well above the maximum temperature of the heat treatment process. Across the chamber, type N thermocouples were used to maintain temperature stability, which is quoted to within ± 5 °C.

BOC 99.998% purity Pureshield Argon (Guildford, England) was used to provide an inert atmosphere during the heat treatment. Air was evacuated from the chamber through a continuous flow of argon gas throughout the heat treatment to maintain an inert atmosphere. A flowmeter was not used to quantify the flowrate, however based upon the quantity of gas supplied and a pressure of 2 bar; a single cylinder can be used for a heat treatment operation at 800 °C continuously for 4 days, giving an estimated flowrate of 0.01 l/ min. Gas tight end seals were used to maintain the inert atmosphere within the furnace chamber.

The quenching oil used was produced by Pennine Lubricants (Sheffield, England) and was a conventional grade designed for the heat treatment of a carbon alloy steels, with excellent resistance to oxidation and good water shedding properties.

5.3 Magnetic characterisation

Relating the induced field within a magnetic material to applied field allows characterisation of key magnetic parameters, which define the magnetic material and are used to design magnetic material devices and applications. A magnetometer is a device which measures magnetic field and several established techniques exist which utilise magnetometers to measure the magnetic properties and characteristics of bulk permanent magnets. Generally, magnetisation measurements can be

grouped into open or closed-circuit measurements. In open circuit measurements, there exists an air-gap between the specimen and the source of the applied magnetic field. Therefore, the applied field, $\vec{H_{app}}$ is not equal to the H field, $\vec{H_{sample}}$, within the sample due to the self-demagnetising effects, $\mathcal{N}_d M$.

$$\vec{H_{sample}} = \vec{H_{app}} - \mathcal{N}_d M \tag{5.1}$$

Open-circuit measurement techniques require a demagnetisation correction factor to properly characterise the magnetisation of the material, or the results need to be specified as pre-correction. If the correction factor is known, almost any shape of magnetic material can be measured. Vibrating Sample Magnetometer (VSM), Superconducting Quantum Interference Device (SQUID) and Pulsed Field Magnetometry [269] are established open-circuit flux methods of characterising permanent magnet materials. A review of such techniques is covered by Coey [9]

Closed-circuit magnetisation measurements are limited to flat geometry magnetic materials, such as blocks or cylinders with uniform cross-sections and parallel faces. The magnet is clamped between two pole pieces and this forms part of a closed magnetic circuit. As such, $\vec{H_{sample}} = \vec{H_{app}}$ and no demagnetisation correction factor is required. However, closed-circuit magnetisation measurement techniques are less sensitive than open-circuit methods and the maximum field achievable is limited by the material properties of the magnetic pole pieces [9]. One such closed-circuit measurement device, known either as a permeameter or hysteresisgraph, has been used in this project to characterise our SPS processed $Sm_2(Co, Fe, Cu, Zr)_{17}$ magnets.

5.3.1 Hysteresisgraph

Hysteresisgraph offers several advantages over other magnetisation measurement techniques for the type of magnetic specimens produced in this project. Measurement cycles are very quick for hysteresisgraph, typically producing a second quadrant demagnetisation curve within a minute. This is advantageous for the high number of samples produced throughout our investigation of the processing parameters of SPS and composite magnet specimens. The hysteresisgraph device is also designed for uniform and flat-faced cubic or cylindrical shaped specimens, removing the need for significant machining. Finally, as hysteresisgraph is a closed-circuit magnetic measurement technique, there are no demagnetisation correction factors required when analysis the demagnetisation curves.

A schematic of a hysteresisgraph is shown in figure 5.5. An electromagnet is used to produce a magnetic field which is directed through the high permeability, soft-magnetic iron pole pieces. The vertical position of the top pole piece can be

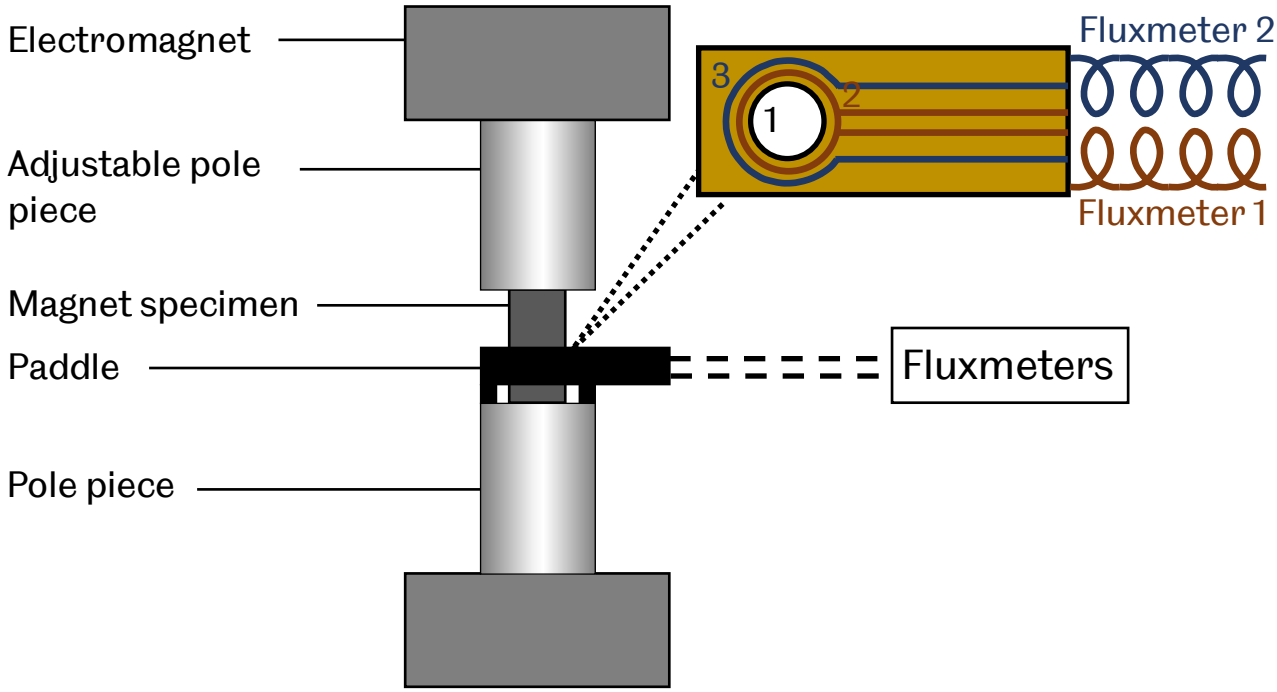

Figure 5.5: Schematic showing the main components of a hysteresisgraph. Also shown is schematic of the paddle which highlights opening (1), primary closed coil winding (2) which is connected to fluxmeter 1 and measures the magnetic flux of the magnet, and secondary coil winding (3) which is connected to fluxmeter 2 and measures the applied field.

adjusted, which allows a magnetic specimen to be placed between the two pole pieces. A paddle with an opening is inserted over the magnetic specimen and the top pole piece is lowered and brought into contact with the permanent magnet sample and locked in position. A prerequisite of this set-up is the height of magnet specimen must be greater than the thickness of the paddle, otherwise the magnet is not in contact with the pole pieces. If this condition is met, a closed magnetic circuit is formed, with the magnetic field directed through the sample by the pole pieces.

The paddle contains the coil windings which are used to measure the magnetic flux density of the magnet sample and the applied field during the experiment. A primary closed coil winding surrounds the magnet during measurement and is connected externally to a fluxmeter. This integrates the induced voltage in the coils as the flux of the magnet ($\vec{B}$) changes due to the applied field sweep. Separately, a secondary coil winding is used to measured the applied field, which does not fully enclose the sample and is connected to a second fluxmeter. Conversion between $\vec{B}$ and $\vec{M}$ is possible with $\vec{H}$ using equation 2.2. A schematic showing this configuration within the paddle used in this project is shown in figure 5.5.

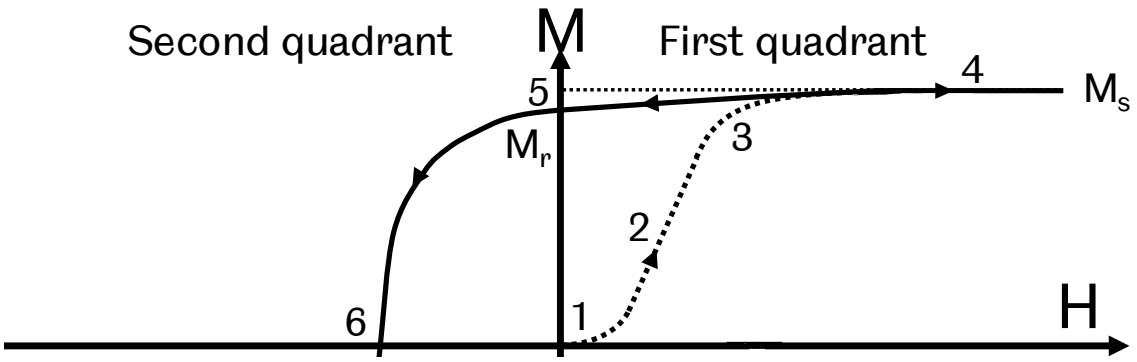

Figure 5.6: Partial hysteresis $\vec{M}$-$\vec{H}$ loop showing magnetisation to saturation and demagnetisation of a magnetic specimen during hysteresisgraph experiment.

Figure 5.6 shows an example partial $\vec{M}$-$\vec{H}$ hysteresis which a magnetic specimen may experience during experiment by hysteresisgraph. The electromagnet first applies a field initially in the 'positive' direction - the first quadrant of a hysteresis loop. REPMs are usually magnetised to saturation before experiment using a pulsed field magnetiser and are already at point 4 of the partial hysteresis loop in figure 5.6. Magnetically softer materials can be magnetised by the hysteresisgraph and the magnetisation of these magnets follows points 1 to 4. The applied field is then swept in the opposite direction (points 5 and 6), terminating when the magnetisation is negative and producing a demagnetisation curve. Hysteresisgraph produces a complete second quadrant of a full hysteresis loop, with example given in figure 5.7, which provides the standard magnetic parameters used to characterise permanent magnet materials. However, as a result the hysteresisgraph does not provide a full hysteresis loop for analysis.

Uncertainty in the flux measurement can arise from electrical drift in the, which needs to be monitored and corrected by zeroing before new measurements are made. Secondly, the iron pole pieces are not constructed from perfectly soft-magnetic magnetic material and retain some magnetic induction after every measurement. This can be monitored and corrected through use of a reference material, typically a nickel magnet, which is also used for calibration annually.

There are also practical limitations when measuring the magnetisation or flux of soft-magnetic materials. Hysteresisgraph is less sensitive in comparison to open-circuit measurement techniques [9] and magnetic materials with coercivity less than $10\,\mathrm{kA\,m^{-1}}(125\,\mathrm{Oe})$ are unreliable. Secondly, for magnetically-hard materials such as REPMs, there is a limit to the maximum field than can be applied. The

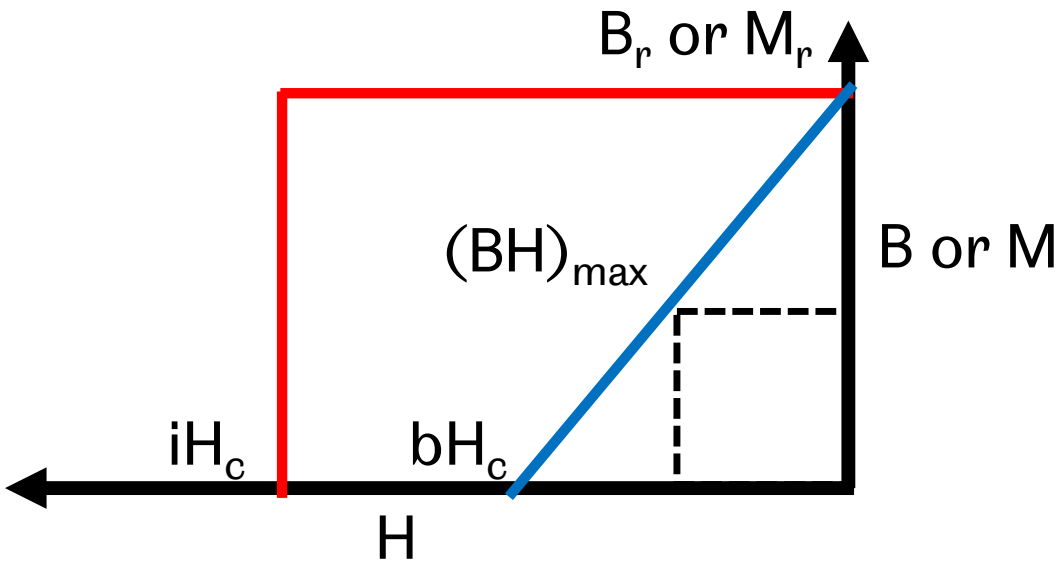

Figure 5.7: Example second quadrant produced by hysteresisgraph, showing both $\vec{M}$-$\vec{H}$ (red) and $\vec{B}$-$\vec{H}$ (blue) demagnetisation curves. Key permanent magnet properties are measured, such as remanence (M_r or B_r), coercivity (iH_c or bH_c) and energy product ($(BH)_{max}$)

soft-iron pole pieces become saturated at fields around $1800\,\mathrm{kA\,m^{-1}}$ (22.6 kOe). When saturated, the magnetic field created by the electro-magnet is not directed exclusively through the pole pieces and begins to spread out in the air-gap between the poles. This affects the magnetisation measurements and distorts the demagnetisation curve, however this effect can be corrected using a device known as a potential coil, which is described by Coey [9]. Generally, fields are limited to avoid this effect and therefore this also imposes a limitation in the coercivity that can be measured by hysteresisgraph. REPM typically have very large coercivities and when measured by hysteresisgraph a minimum value is measured. Hysteresisgraph serves as a quick initial characterisation of the magnetic properties. For absolute coercivity measurements, other magnetometer devices such as VSM or pulsed field magnetometry are required, but are significantly longer measurement methods.

5.3.2 Hysteresis methodology

The Magnet-Physik GmbH hysteresisgraph used in this project was situated at Arnold Magnetic Technologies (Sheffield, England). All software and apparatus was manufactured and calibrated by Magnet-Physik GmbH (Germany). For the 20 mm diameter samples produced by SPS, a JHT 26-4 paddle with embedded coils

to measure $\vec{B}$, $\vec{M}$ (or $\vec{J}$ and $\vec{H}$ was found most appropriate. The thickness of the JHT 26-4 paddle (3 mm) defined the minimum height of the SPS processed magnet samples required for measurement.

Pre-measurement, all samples were magnetised in the axial direction using a Hirst Magnetics pulse magnetiser using a pulsed field of 3.5 T (2800 kA m^{-1}). To begin the measurement process, the specimen face area was entered into the hysteresisgraph software. For each sample, the face area (A) of the sample is calculated using the mass (m), density (ρ) and thickness (t) of the sample and using the following equation.

$$A = \frac{m}{\rho \cdot t} \tag{5.2}$$

However this value sometimes exceeded the maximum surface area for a 20 mm diameter disc shaped specimen. A less accurate method simply calculates the face area from measurements of the specimen diameter, although this assumes perfect circular faces. A comparison of the magnetic properties for several SPS processed $Sm_2(Co, Fe, Cu, Zr)_{17}$ samples which varying divergence between the face areas derived from the two methods found the uncertainty to be constant across all ranges of divergence at around 5%. This uncertainty is applied to all measured magnetic properties as the error carried through based upon the surface area measurement. This systematic error is combined with the standard error from multiple measurements to give the uncertainty in the measured magnetic properties by hysteresisgraph.

The hysteresisgraph software allows the sweeping field and rate to be specified by controlling the max ($+I_{max}$), min ($-I_{max}$) and rate of change of the current ($\frac{dI}{dt}$) through the electro-magnet. To account for any potential self-demagnetisation before measurement, the field was first swept in the positive direction $+I_{max}$ = 50%. Demagnetisation in the second quadrant was set to $-I_{max}$ = 100% - however, a flag was set to cease the measurement when the demagnetisation curve passed the horizontal axis ($\vec{B} < 0$). dI/dt = 25% was found to provide the most appropriate data points, while maintaining an appropriate measurement speed. These parameters were found to produce the best quality demagnetisation curves for our magnet samples through trial-and-error, so specimens measured early in the project may have been measured under slightly different conditions. Where this has occurred, it is mentioned in the results chapters when discussing the data.

5.4 Material characterisation

5.4.1 Resistivity measurements

A linear arrangement of electrical probes is a classical method of resistivity measurement for bulk specimens [270]. To reduce uncertainties, samples by this method typically have to be cut to form test bars or bridge type geometries. However, this was difficult for brittle ceramic semiconductor materials. Leo Van der Pauw developed a measurement method that could be applied to arbitrary shaped samples [271]. The Van Der Pauw (VDP) method can measure almost any arbitrary geometry as long as the specimen has a uniform and parallel face, is solid and symmetrical, and approximately two-dimensional; such that the thickness of the sample is much smaller than the cross-sectional diameter. It is also essential to reduce measurement uncertainties to locate the electrical contacts at the periphery of the sample and contact area is significantly smaller than the diameter of the specimen. Such an arrangement of electrical contacts are shown in figure 5.8.

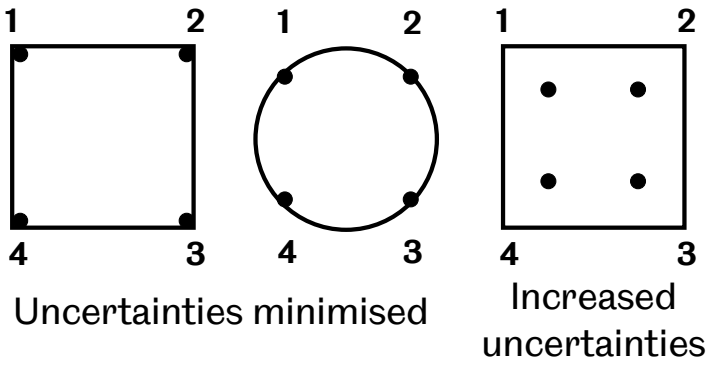

Figure 5.8: Desired arrangement of electrical contacts under Van der Pauw method

VDP derived an expression based on his new method of resistivity measurement [271]:

$$\exp\left(-\frac{\pi t}{\rho}R_{12,34}\right)+\exp\left(-\frac{\pi t}{\rho}R_{23,41}\right)=1 \tag{5.3}$$

't' is the thickness of the specimen, ρ is the resistivity of the material and $R_{12,34}$ is the measured resistance when the current is passed from contacts 1 to 2 and the potential difference is measured between contacts 4 and 3. In other words; $R_{12,34}=\frac{V_{34}}{I_{12}}$. Figure 5.8 can be used as a reference.

Reciprocity theorem (reversal of current and potential difference contacts) and

reversed polarity measurements allow additional measurements to be taken, which further increases the accuracy of the VDP method. Resistivity measurements can be summarised as horizontal and vertical, such that:

$$\begin{aligned} R_{horizontal} &= \frac{R_{12,34} + R_{21,43} + R_{34,12} + R_{43,21}}{4} \\ R_{vertical} &= \frac{R_{23,41} + R_{32,14} + R_{41,23} + R_{14,32}}{4} \end{aligned} \tag{5.4}$$

Equation 5.3 can be simplified and solvable if the shape of the specimen and arrangement of the probes possess a line of symmetry.

$$\rho_{horizontal} = \frac{\pi t}{\ln 2} R_{horizontal} f \tag{5.5}$$

$$\rho_{vertical} = \frac{\pi t}{\ln 2} R_{vertical} f \tag{5.6}$$

$$\rho_{VDP} = \frac{(\rho_{horizontal} + \rho_{vertical})}{2} \tag{5.7}$$

A correction factor, 'f', is added to amend the calculated resistivity, as real materials are not ideally symmetrical as postulated by VDPs method and there exist inhomogeneities in the material. VDP derived and calculated the correction factors for different values of $\frac{\mathrm{R_{horizontal}}}{\mathrm{R_{vertical}}}$ [271]. Figure 5.9 shows the experimental resistivity measurements of Cu and Al thin films of different shape and contact configurations by Ramadan et al., which compare favourably with VDP's numerically calculated correction factors (line (a)) [272].

A rig to measure resistivity using the VDP method was constructed with four Hirschmann (Germany) miniature spring-loaded nickel tip/gold pin test probes. The point-contact probes were arranged in a square array 14 mm apart, as shown in figure 5.10. The probes were set in a perspex top-plate, below which the sample was placed. The sample and probes were adjusted such that the probes lay as close to the sample periphery as possible. The height of the top plate was then adjusted to bring the probes into contact with the specimen and locked in place using screws. Two test leads connected the rig to an ISO-TECH IPS 2303 DC current power supply and TENMA 72-7732A multi-meter in series, while the other test leads were connected to a Keithely 2000 multi-meter. DC currents of 0.3 A to 0.4 A were used to measure the potential difference at room temperature across the sample for the various horizontal and vertical configurations. Testing at room temperature confirmed Ohm's law held in the range of these currents. To accurately measure the resistivity across the entire sample, eight measurements were made for

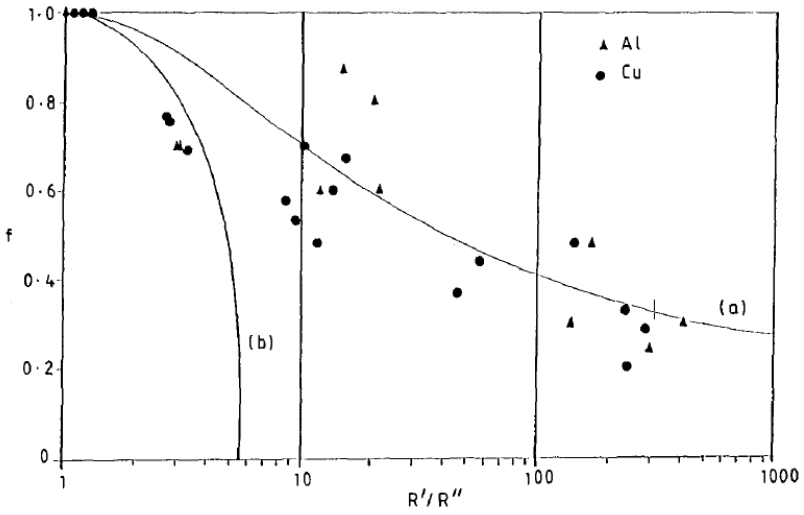

Figure 5.9: Graphical representation of the Van der Pauw correction factor plotted as a function of the ratio of $R_{horizontal}$ and $R_{vertical}$, represented by R' and R" respectively. Line (a) Van der Pauw's numerically calculated correction factor. The symbols represent experimentally derived results for Al and Cu thin film samples of different shapes and contact configurations [272] ©1994 Elsevier, licence granted for reuse in thesis (licence number 4197101135798).

each sample, as to meet the criteria of equation 5.4. Efficient measurements were made by switching the test leads to reverse the polarity of the DC current source and also switch test leads between the current source and Keithley multi-meter. The potential difference was allowed to stabilise after each measurement iteration and often an offset was taken and subtracted/added when the potential difference settled on a non-zero value with zero current applied. Two repeats were made per measurement direction to minimise uncertainty.

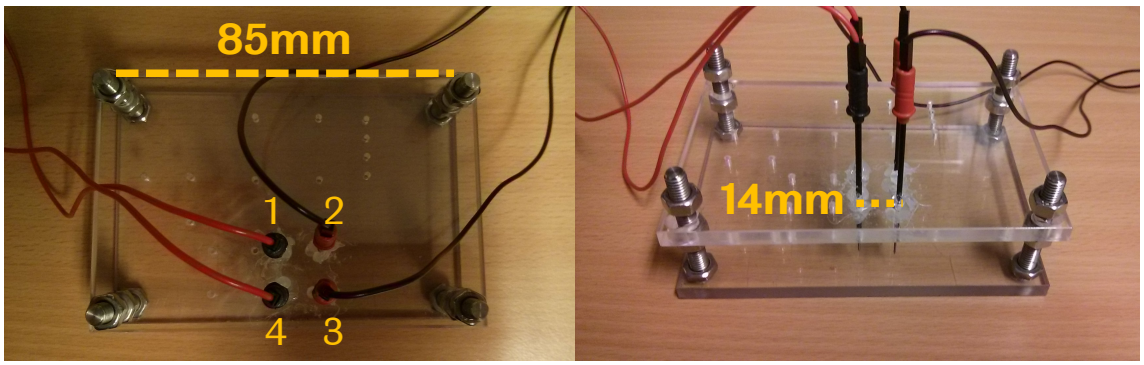

Figure 5.10: VDP method rig used to measure potential difference and resistivity in SPS processed $Sm_2(Co, Fe, Cu, Zr)_{17}$ and composite samples.

The VDP method is designed for specimens with diameters much larger than their height. The bulk samples produced by SPS using around 13 g of powder in the 20 mm mould configuration have thickness typically ranging from 3.5 mm to 5 mm. Studies by Kasl [273] and Weiss [274] both agree that inaccuracy in the VDP method may arise when the height (h) to diameter (D) ratio exceeds 0.5. Using the most extreme example for the specimens produced in this project; the maximum height h = 5mm is used and the minimum diameter is dictated by the probe displacement, D = 14mm (probes not at the periphery), the worst-case ratio of $\frac{\mathrm{h}}{\mathrm{D}} = 0.36$, which is well below the condition described by Kasl and Weiss. Therefore, it is expected that the Van Der Pauw method is suitable for the specimen dimensions produced by our SPS methodology.

Errors can also arise in the VDP method if the electrical probe placement is not at the periphery of the sample. Van der Pauw calculated the approximate uncertainty in the resistivity measurement, $\Delta\rho/\rho$, per probe, as a function of distance, l, and sample diameter, D [271].

$$\frac{\Delta\rho}{\rho} \approx \frac{-l^2}{2D^2 \ln 2} \tag{5.8}$$

Figure 5.11 plots the fractional error in the resistivity as a function of the probe displacement from the periphery of a 20 µm diameter specimen for a single electrical probe and for all four probes, assumed to be equally distant from the periphery.

The predicted uncertainty by VDP via equation 5.8 compared favourably with relative measurement errors in Van der Pauw method resistivitity measurements by Koon et al. [275]. The resistivity rig used in this project is designed to work for all potential samples produced by SPS using our 20 mm moulds. Due to slight variation in the geometry of the specimens produced by SPS and after varying degrees of surface grind on the edges during graphite foil removal, our resistivity rig does not locate the electrical probes exactly at the periphery as to accommodate all potential samples. Therefore, the probe placement is often to ideally positioned at the periphery. However, in the extreme case that each probes lies 2 mm from the perimeter, figure 5.11 shows the combined uncertainty arising from the probe displacement is small at 1.4%. Uncertainty may also arise due to contact resistance between the electrical contacts and the specimen [271]. However, this is expected to be even smaller than the probe displacement uncertainty through our use of point-contact probes, which minimise the contact area.

A similar level of uncertainty of around 1% was measured in the fluctuation of the D.C. current supply. However, the largest uncertainty in the resistivity measurements arose from the fluctuation in the potential difference measurements. Even

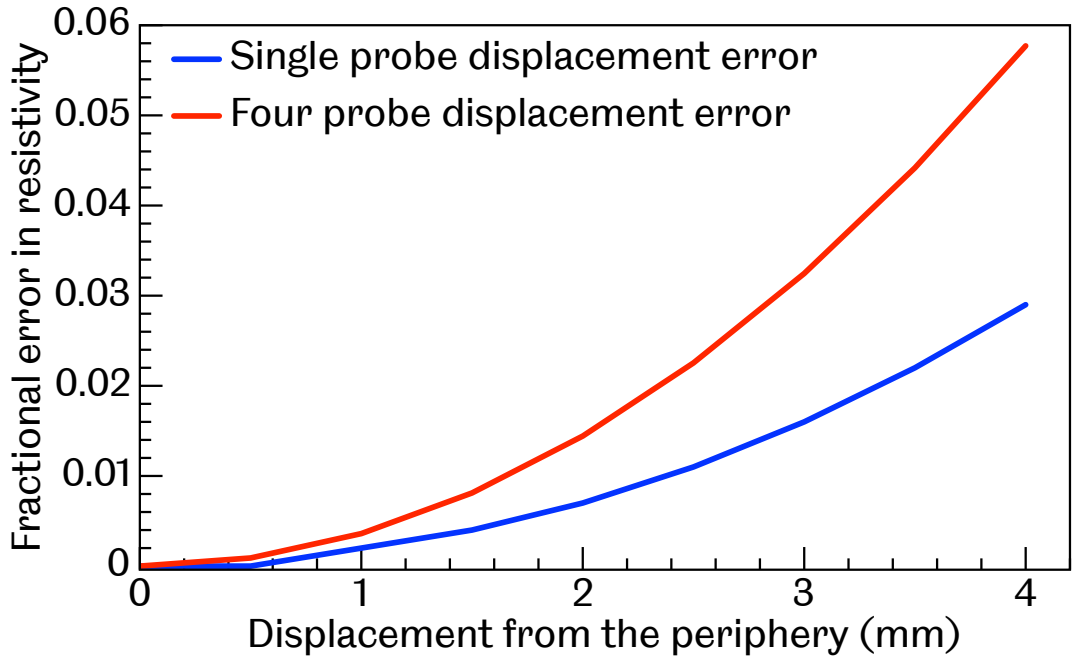

Figure 5.11: The fractional uncertainty in the resistivity due to probe displacement from the sample periphery, as per equation 5.8. D = 20 µm in this calculation. In the combined probe error, the distance from the periphery for all probes is equal

allowing time for these readings to settle, an uncertainty of 0.5 µV was assigned to the noise in the measured values of the order 10 µV, giving a percentage uncertainty of around 5%. Repeated measurements attempted to improve the statistical uncertainty of these measurements, however these systematic errors amounted to a total uncertainty of approximately 10% in the resistivity measurements.

5.4.2 X-ray diffraction phase analysis

X-ray Diffractometry (XRD) is a non-destructive method used to analyse crystallographic properties of bulk and powdered materials. The periodic arrangement of crystalline materials diffract X-rays incident on the material at different angles in relation to the crystal structure and atomic-plane spacing. Peaks in intensity occur due to constructive interference when conditions satisfy Bragg's law of diffraction, shown in equation 5.9. 'n' is an integer, which refers to the "order" of reflection, 'λ' is the wavelength of the incident X-rays, 'd' is the inter-planar spacing of the crystal and 'θ' is the angle of incidence.

$$n\lambda = 2d\sin(\theta) \tag{5.9}$$

Crystallographic analysis can be performed if a sample is rotated about the X-ray beam at an angle 'θ', with a detector also rotated at an angle (2θ). Characteristic

Bragg peaks will be located at specific '2θ' angles for certain crystal structures and lattice dimensions.

XRD 2θ phase analysis of bulk SPS processed and powder $Sm_2(Co, Fe, Cu, Zr)_{17}$ were performed using a Siemens D5000 GAXRD. The X-ray tube working conditions were 40 kV and 40 mA. A copper source was used to generate Kα_1 and Kα_2 X-ray radiation with an average wavelength, $\lambda = 1.541\,78$ Å. A fixed detector slit of 0.2 mm was used.

Powder and SPS processed samples were placed in aluminium crucibles, with bulk samples mounted using non-elastic Apiezon Q Sealing Compound putty. Care was taken to ensure the sample face was level with the rim of the aluminium crucible, which can shift peaks to lower and higher 2θ values if unaccounted for. For the majority of samples, full phase analysis was performed over 2θ angles ranging from 20° to 80°. After a short investigation into the scanning parameters, a step size of 0.02° and a scan rate of 19.2 s/step (total scan time of around 16 hours) was found to achieve the best intensity to noise ratio for peak identification and analysis of the bulk and powder specimens. The sample was rotated during measurement at a rate of 15 rpm to further boost peak intensities.

Analysis of Bragg peak positions and their intensities was performed using SIeve+ curve fitting software, which uses the International Centre for Diffraction Data (ICDD) PDF-4+ database for comparison of peak position and intensities [276]. Simulated profiles were based on Cu Kα_{1+2}.

5.4.3 Density measurements

Density measurements were performed using Archimedes' water immersion technique. Measurement of the bulk specimen mass in air and in distilled water can be combined with the known density of distilled water and air to calculate the density of the material through rearrangement of the following equation [277].

$$D = \frac{m_a}{m_a - m_b}(D_0 - D_{air}) + D_{air} \tag{5.10}$$

D is the density of the specimen, m_a, m_b are the specimen masses measured in air and in the liquid respectively, D_0 is the density of distilled water at a specified temperature, which is taken from a database programmed into the equipment, and D_{air} is the density of air, which is fixed at 0.0012 g/cm^3 [277]. Density measurements were performed using a commercial Mettler Toledo MS-DNY-43 and repeated three times to derive an average value and minimise statistical uncertainty.

5.5 Microscopy

5.5.1 Sample preparation

Microscopy was performed on specimen cross-sections, investigating the microstructure and composition. Samples were sectioned using a Buehler Isomet and MetPrep type 5 10-17-28 abrasive saw with a spindle speed of 2000rpm and a feed rate of 2 mm/ min. The sectioned specimens were then mounted in conductive bakelite and their surfaces prepared for microscopy using a Buehler Eco/AutoMet 300. An optimal surface grind was found to consist of initial stages of 400, 600, 1200 and 2500 grit/grade SiC paper using the following parameters for each stage:

Force applied to the mounted specimens = 25 N, plate rotational speed = 170 rpm, head rotational speed = 32 rpm (in the opposite direction to the plate i.e. contra mode) and each stage lasting around 1 minute.

To achieve a mirror-like finish, a series of polishing stages followed in the order of 6 µm, 3 µm (both diamond suspension) and 1 µm colloidal silica. The method used for the diamond suspension stages was a 3 minute polish with force = 15 N, plate rotational speed = 140 rpm, head rotational speed = 30 rpm in contra mode. The colloidal silica stage method was 5 minutes with force = 12 N, plate rotational speed = 130 rpm, head rotational speed = 28 rpm in contra mode.

For grain boundary studies, a chemical etchant was used to emphasise such features within the microstructure. Mounted and polished samples were submerged into a dilute citric acid (10%) and water solution, which was heated to 80 °C [278]. Between periodic submersion for 10 seconds, the microstructure was observed under a light microscope to confirm a visible granular structure.

For the imaging of powders by Scanning Electron Microscopy (SEM), powders were affixed to a micro-stand using conductive carbon tape and excess powder carefully removed. CaF_2 powders, which are electrically insulating, required gold coating using an EMSCOPE SC500 sputter coater. The powder-affixed micro-stand was placed within the chamber, which is then pumped to vacuum. Once achieved, the deposition current was set to 15 mA and the coating time set for 3 minutes.

5.5.2 Light microscopy

Light microscopy was performed using a Nikon Eclipse LV 150 digital microscope and Buehler Omnimet image and analysis software. In bright field mode, the pol-

ished sample is illuminated from above and contrast is created from attenuation and scattering of the transmitted light. In dark field mode, the unscattered light is excluded from the image, thus highlighting features such as pores and scratches, which scatter the most light.

5.5.3 Scanning Electron Microscopy (SEM)

Secondary and back-scattered imaging

SEM imaging was performed using an FEI Inspect F-50, imaging in secondary (SE) and back-scattered (BS) modes. Standard operating practices were followed, by insertion of the mounted sample into the SEM camber, pumping down to vacuum and bringing the imaging plane into focus. For the majority of images, a spot size of 3 was used with electron accelerating voltage at 20 kV.

SEM imaging is performed by directing an accelerated and focused beam of electrons at the material surface and detecting re-emitted electrons or X-rays from specific points as the beam is rastered across the area to be imaged. The interaction of the electrons is different for secondary and back-scattered and therefore provide different imaging information. Secondary electrons are detected as a result of multiple ionisation interactions close to the material surface, typically at depths of a few nanometers. SE mode is therefore used for high-resolution (greater than 1 nm) topological imaging of features, such as grain-boundaries and pores. Back-scattered electrons are the result of reflected electrons by elastic scattering between the incoming electrons and atom. These electrons probe at depths greater than those of secondary electrons and so the spatial resolution in BS is not as good as SE mode. However, BS mode can show contrast between phases present in the micro-structure as the intensity of the scattered electrons correlates strongly with atomic weight. BS imaging is useful to infer phase distribution and is complemented with further analysis by Energy Dispersive X-ray Spectroscopy.

Grain size measurement

Grain size measurement was performed using linear intercept method [279], which measures the lengths of random intercepts to calculate an average grain size. Light microscopy or SEM images of etched microstructure were analysed in imageJ [280] and manually measured across at least 10 lines in the horizontal and vertical directions in each image.

$$\bar{L} = \frac{L_{total}}{N_L} \tag{5.11}$$

$\bar{\mathrm{L}}$ is the average distance per intercept, $\mathrm{L_{total}}$ is the length of the line and $\mathrm{N_L}$ is the

number of grain boundary intercepts. $\bar{L}$ was calculated for each line, which was then used to calculate the average grain size, and standard error, in the horizontal and vertical directions.

Energy dispersive X-ray spectroscopy (EDS or EDX)

Energy Dispersive X-ray Spectroscopy (EDS or EDX) is a method of probing the elemental composition of a material. EDS was also performed on the FEI Inspect F-50 and also utilises a directed beam of highly energetic electrons to stimulate emission of characteristic X-rays in an interaction volume below the surface. The spatial resolution of EDS varies between light (low atomic number) and heavy (high atomic number) elements, but is generally of the order of $1\,\mu m^3$ [281]. An energy dispersive X-ray detector converts the photons of energetic X-rays into voltages, which are processed and analysed. Therefore, this method of detection and processing is known as energy dispersive spectroscopy. Elements are identifiable by characteristic peak positions (typically from the strongest Kα lines, but also satellite peaks of less energetic line transitions). If reference materials of known elemental compositions are used for comparison, the concentrations of elements in the specimen can be determined from their relative intensities.

Rastering the electron beam over the entire imaging area allows EDS to identify the elemental profile of an entire image. Small area and spot scans can also be performed to provide elemental identification of specific microstructural features. Line scans are used to measure changes in elemental composition across the microstructure. Elemental maps can show the spatial distribution again by rastering the electron beam over the imaging area and individually analysing, pixel by pixel, the elemental composition. For this project, elemental maps were generated with 1 µm step sizes, with dwell times ranging from 200 s to 250 s and total scans times up to 1 hour, which were found to provide sufficient detail in the spatial distribution of chemical elements.

EDS is limited to elements heavier than Be and care in the interpretation of the measured concentrations of elements lighter than Na is advised [281]). The interaction volume for EDS is also larger and probes depths greater than SE and BS imaging, and so the spatial resolution of elemental maps is worse than imaging in SE or BS mode. Similarly, when EDS spot or small area analysis is used at high magnification, the identified elements may not correspond to the area of interest in the image. If higher resolutions and improved sensitivities to lighter elements is required, a technique such as Wavelength-Dispersive X-ray Spectroscopy (WDS) can be used.

5.5.4 Electron Probe Micro-Analysis (EPMA)

EPMA works fundamentally the same as SEM. However, EPMA uses wavelength dispersive detectors to detect and measure the energies of emitted X-rays. WDS uses an arrangement of several crystals to diffract specific X-rays that satisfy Bragg's law (equation 5.9) onto a detector. The arrangement of the X-ray source, crystal and detector are carefully arranged for detecting specific elements. A typical EPMA will have multiple spectrometers, each with several crystals of different lattice spacings, such that all elemental wavelengths of interest can be diffracted and detected. The purpose of this arrangement is a much improved degree of sensitivity to X-rays of low energy and the detection of lighter elements than in comparison to EDS.

EPMA was used to image and map the spatial distribution of elements using a Jeol JXA-8500F. Sample preparation and imaging was performed at Johnson-Matthey technology centre (Sonning Common, England) Sectioned samples were mounted in Field's metal (32.5wt% Bi, 51wt% In and 16.5wt% Sn, Alfa Aesar, UK) rather than Bakelite to reduce ambiguity in carbon detected at the surface edges of the mounted specimen. The samples underwent a grinding and polishing process similar to that described in section 5.5.1 and plasma cleaning was further used to remove any residual organic contaminants after the polishing process. The Jeol JXA-8500F used an arrangement of five WDS detectors and one silicon drift diode (SDD) EDS detector for accurate elemental detection. The accelerating voltage was 20 kV with a step size of 1 µm and a dwell time of 50 ms.

5.6 LECO analysis

Elemental carbon and oxygen quantification was performed on sectioned samples using a LECO CS-844 and LECO-ON736 instruments respectively (AMG-S, Rotherham, England). For this type of analysis, $Sm_2(Co, Fe, Cu, Zr)_{17}$ specimens were sectioned and segments were taken either from the centre or edges of the specimen to quantify both internal and surface carbon concentrations. The internal segments also underwent surface polishing to remove around 1 mm of material from both the top and bottom faces to ensure the original surfaces were removed. Each segment was at least 0.2 g.

The LECO carbon measurement test is a destructive analytical technique which consists of an induction furnace and infrared cells. The furnace reaches temperatures up to 2000 °C and the sample segments are combusted in an oxygen atmosphere. The carbon concentration, either in weight percentage or parts-per-million, is inferred

through measurement of released CO_2, which is detected by infrared absorption [282]. For the oxygen measurement, the sample section is melted in a crucible under inert gas and the released oxygen reacts with hot graphite to form carbon monoxide. The carbon monoxide gas is detected using a non-dispersive infrared (NDIR) cell and the concentration quantified following the ASTM E1019 standard.

5.7 FEM micromagnetic modelling and simulation

5.7.1 Model generation

Granular structured models of $Sm_2(Co, Fe, Cu, Zr)_{17}$ and composite magnets and were created using a model generation code described in detail by Dean et al. [283]. An array of seed points are distributed within a three-dimensional box and a Voronoi tessellation is performed which create shapes with surfaces that fill the box. The model generation allows a number of parameters, such as number of grains, grain size and grain shape to be controlled. Models varied in size and scope, with grain numbers ranging from 8 to 14 volumes and grain sizes ranging from 90 nm to 150 nm. The regular distribution of seeds points can also be disturbed slightly to create an irregularly shaped granular structure. If required, the granular volumes can be shrunk to their centroid, by a defined fraction of the original volume, to create a core-shell type structure. Separate material and magnetic properties can then be assigned to the core and shell volumes. This core-shell type structure is useful to represent the cellular nanostructure of $Sm_2(Co, Fe, Cu, Zr)_{17}$ permanent magnets or features such as inter-grain phases/grain boundaries.

The granular structures are meshed using Gmsh, a three-dimensional finite element mesh generator [284]. Figure 5.12 shows a single particle (a) and its meshed elements at the surface (b). In this example, the total number of surface and volume mesh elements is just over 100,000 and the number of nodal points, which are located at the vertices of the prism-shaped elements, is around 20,000. The relative surface and volume mesh element sizes can be modified, such that finer meshing can be applied to the surfaces of grains and coarser meshing to the volume. This may be performed to reduce the number of elements overall, but retain the resolution of the mesh structure in areas where magnetic reversal is likely to occur [233].

Each grain, and core-shell, is assigned specific material and intrinsic magnetic properties: magnetic easy axis, defined by spherical coordinates, ϕ and θ, magnetisation/polarisation saturation, M_s or J_s, magneto-crystalline anisotropy constants, K_1 and K_2, exchange stiffness, A_{ex} and Gilbert magnetic damping parameter, α (which is explained in section 5.7.2). Magnetic isotropy or alignment can be implemented

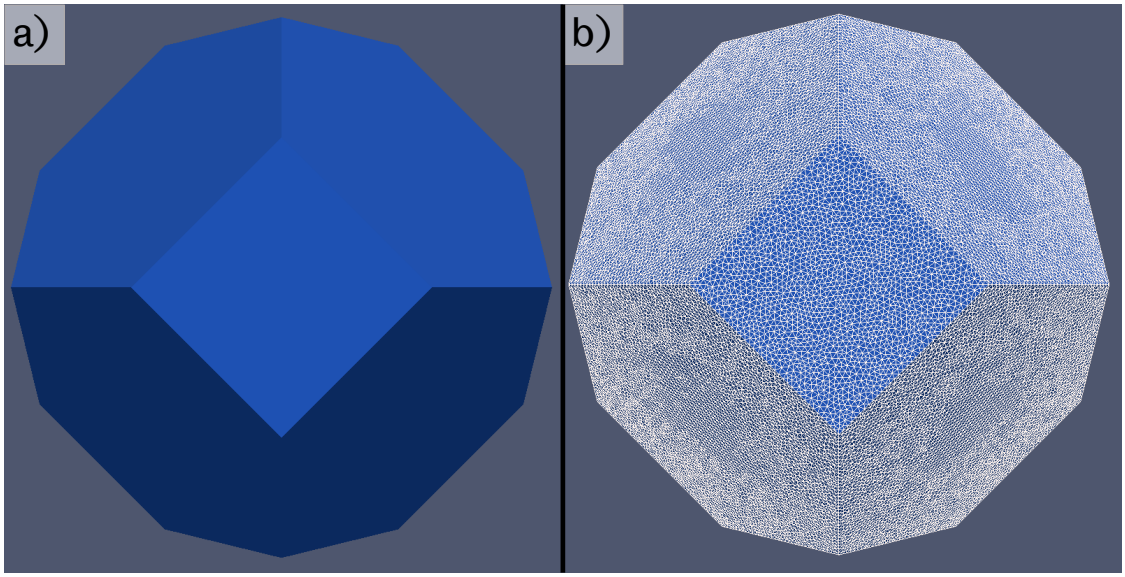

Figure 5.12: Single tetradecahedron grain (a) showing fine surface element structure after meshing (b)

Intrinsic magnetic property		**2:17R Sm_2Co_{17}** [54, 55]	**1:5H $SmCo_5$** [54, 55]	**CaF_2**	**Co-Fe** [285–287]
$\mathbf{J_s}$	**(T)**	1.32	0.8	2×10^{-8}	2.20
$\mathbf{K_1}$	**(MJ/m^3)**	5.0	9.0	0	-7.0×10^{-3}
$\mathbf{K_2}$	**(MJ/m^3)**	0	0	0	0
$\mathbf{A_{ex}}$	**(pJ/m)**	14	14	0	25
$\boldsymbol{\alpha}$		0.2	0.2	0.2	0.2

Table 5.2: Intrinsic magnetic properties used for different phases in FEM models of $Sm_2(Co, Fe, Cu, Zr)_{17}$ and composite magnets. CaF_2 phase in composite studies assumed to be diamagnetic and this is interpreted as having zero magnetic properties, however 2×10^{-8} is lowest allowed value for J_s in FEMME and Magpar packages.

into the model through a random or controlled normal distribution of easy axis. The intrinsic magnetic properties used for the different phases within our study of $Sm_2(Co, Fe, Cu, Zr)_{17}$ magnets and composite structures are shown in table 5.2.

5.7.2 Micromagnetic simulation packages

FEMME (SuessCo, Austria) and Magpar [288] are two FEM micromagnetics packages used within this project. Both were run using the University of Sheffield's Iceberg high performance computing cluster. Magpar differs from FEMME in that in uses parallel computing methodologies, reducing the computing cycle and thus has been used for large and complex magnetic models. Both packages have been developed from the same underlying micromagnetic theory, with a detailed descrip-

tion covered by Fidler and Schrefl [233]. In summary, the Gibb's free energy with respect to the magnetisation is minimised, which yields a stable energy state of the magnetic system at each nodal point. The magnetic polarisation, $\vec{J}(\vec{r},t)$, at each node is a function of space and time:

$$\vec{J}(\vec{r},t) = J_s \cdot \vec{u}(\vec{r},t) \tag{5.12}$$

$\vec{u}(\vec{r},t)$ is the magnetisation unit vector. The expression for the standard total free energy for a system within a certain volume:

$$E_t(\vec{J},\vec{\Psi}) = \int \left[\frac{A_{ex}}{J_s^2}(\nabla J)^2 - K_1 \left(\vec{u_c} \cdot \frac{\vec{J}}{J_s} \right)^2 - \vec{J} \cdot \vec{H_{app}} - \vec{J} \cdot \nabla \vec{\Psi} \right] dV \tag{5.13}$$

The micromagnetic energy terms in equation 5.13 in order are exchange, magneto-crystalline anisotropy (for a uniaxial system with the easy axis direction $\vec{u_c}$), the Zeeman energy relative to an applied field $\vec{H_{app}}$ and the stray field arising from magnetic dipole interactions. In this interpretation, a magnetic scaler potential Ψ has been introduced to simplify the long-range self-demagnetising field, with detail on this methodology described by Fidler [233].

Minimisation of equation 5.13 provides the effective field, $\vec{H_{eff}}$, which is the torque acting on the magnetisation vector at each nodal point.

$$\vec{H_{eff}} = -\frac{\delta E_t}{\delta \vec{J}} \tag{5.14}$$

A hysteresis loop can be calculated by this numerical approach through successive calculation of the energy minima after small changes in the applied field. This numerical micromagnetic method is described as the static approach and does not account for the path taken between energy minima states [235]. The dynamic approach accounts for gyromagnetic precession and damping of the magnetisation vector, which may alter the path leading to the final stable energy minima state. Static approaches have been shown to over-estimate numerically calculated coercivities in comparison to dynamic approaches in nanocomposite Nd-Fe-B type magnets [289] The Landau–Lifshitz Gilbert equation describes the path taken as the system proceeds to equilibrium [235]

$$\frac{\partial \vec{J}}{\partial t} = -|\gamma| \left(\vec{J} \times \vec{H_{eff}} \right) + \frac{\alpha}{J_s} \left(\vec{J} \times \frac{\partial \vec{J}}{\partial t} \right) \tag{5.15}$$

γ is the gyromagnetic ratio of the electron spin and α is the dimensionless Gilbert

magnetic damping parameter. The former introduces precession to the magnetic moment about the effective field vector, while the latter models material related damping to said precession.

The general approach taken to simulate a hysteresis loop using FEMME or Magpar is similar to the process described in section 5.3 with our characterisation of permanent magnets by hysteresisgraph.

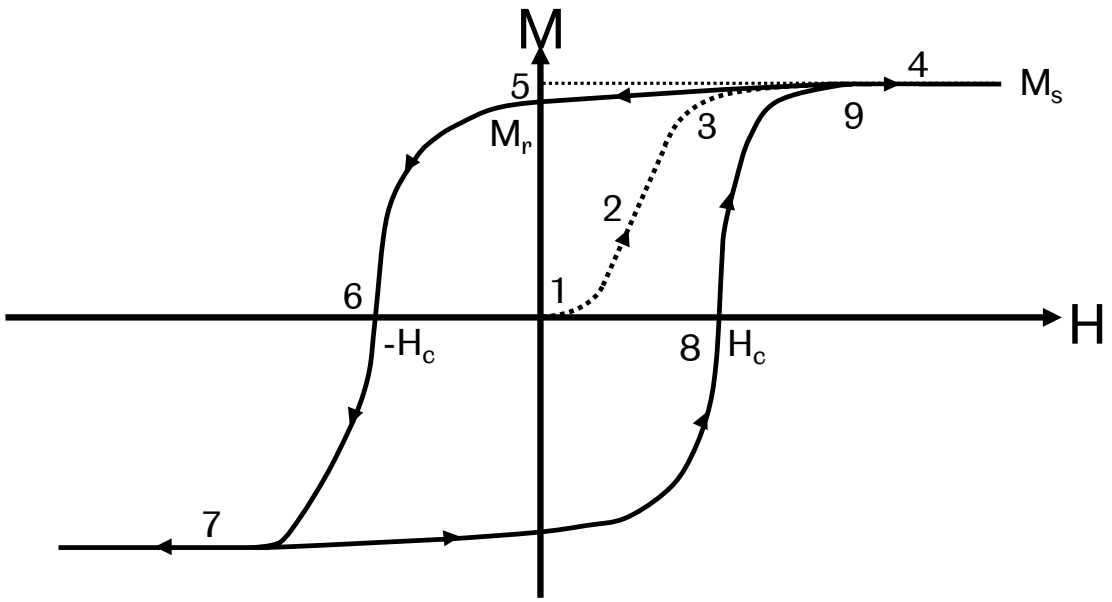

Figure 5.13: Full hysteresis from demagnetised state (1) to magnetically saturated state (4). Field sweep in the negative and positive x-directions produce partial hysteresis (demagnetisation) curve (5 and 6) or full hysteresis loop (4 to 9).

Using figure 5.13 as a reference, the magnetic model is first saturated by applying a high field between 10 T to 15 T in the positive x-axis direction (points 1 to 4 in figure 5.13. The initial magnetisation vectors in the magnetic model were set-up to be weighted in the positive x-axis, sometimes away from the easy axis, to further aid saturation. From point 4, the applied field is reduced and swept in the negative x-axis. A demagnetisation curve is traced out as the Gibbs free energy is minimised for each field step, with equation 5.15 describing the transient path [233]. From point 6, a full hysteresis loop can be simulated if the applied field is swept to saturation in the negative x-axis and then in the positive x direction.

Chapter 6

Spark Plasma Sintered SmCoFeCuZr magnets

6.1 Introduction

This chapter is concerned with the utilisation of the SPS technique to sinter a standard commercial grade of $Sm(Co, Fe, Cu, Zr)_{8.2}$ pre-alloyed powders. Following the literature review, a summary of the aims of the project were outlined. With little preceding study of the processing of $Sm_2(Co, Fe, Cu, Zr)_{17}$ by the SPS technique, it is required to investigate the main SPS processing variables; heating rate, holding temperature, holding time and holding pressure; firstly on the consolidation of the powders to produce dense specimens, and secondly on the effects on microstructure and magnetic properties. This is accompanied with a complimentary study of two magnetic field powder alignment techniques which could be incorporated into the processing route.

This chapter also details an investigation of carbon uptake into the $Sm_2(Co, Fe, Cu, Zr)_{17}$ material during the SPS process. Powders contained within the graphite mould are in direct contact with the graphite foil liner, and also potentially the mould, at elevated temperatures and pressures, which may allow carbon to diffuse into the surfaces of the sintered material. The literature review in chapter 2 highlighted how carbon contamination has been detected in materials processed by SPS [116, 290], and in particular has a serious affect on the magnetic properties of $Sm_2(Co, Fe, Cu, Zr)_{17}$ when the concentration of carbon exceeds 0.2 wt.% [121, 122]. The viability of the SPS technique towards processing of carbon-sensitive materials and its potential to produce optimised microstructures is therefore dependent on the extent of carbon uptake during the rapid sinter process. This study utilises EPMA to image the spatial distribution of carbon at the surfaces of sample cross-sections

in SPS and conventionally processed $Sm_2(Co, Fe, Cu, Zr)_{17}$, in addition to a thermal decomposition carbon detection technique (LECO-C) to quantify the relative carbon concentrations.

6.2 Powder characterisation

6.2.1 Crystallite size and shape

To begin the investigation into the processing of $Sm_2(Co, Fe, Cu, Zr)_{17}$ powders by SPS, physical characterisation of the powders is required. SEM has been used to image the $Sm_2(Co, Fe, Cu, Zr)_{17}$ powders in both SE and BS ('Z cont') imaging modes. Figures 6.1 and 6.2 show the particle sizes and shapes at various magnifications.

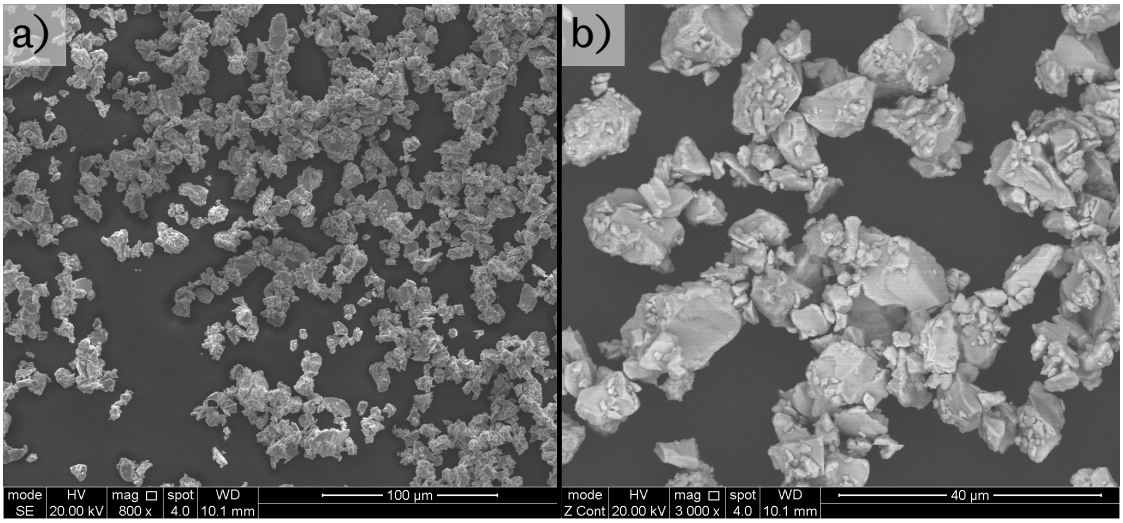

Figure 6.1: $Sm_2(Co, Fe, Cu, Zr)_{17}$ powder imaged by SEM at 800× (a) and 3000× (b) magnification

At relatively low magnification, figures 6.1 a) and b) show the $Sm_2(Co, Fe, Cu, Zr)_{17}$ particles have irregular shape and, by a visual inspection, the upper bound of particle size is between 30 µm to 40 µm. At higher magnifications, shown in figures 6.2 a) and b), the $Sm_2(Co, Fe, Cu, Zr)_{17}$ powder is mostly comprised of larger crystallites, approximately 10 µm to 30 µm in diameter, covered with much smaller crystallites of approximate diameters <2 µm. The particle shapes range from nearly spherical (most common in the smallest particles), to irregular ellipsoidal and cubic particles.

Measurement and distribution of $Sm_2(Co, Fe, Cu, Zr)_{17}$ crystallite size was performed for a sample of 150 random crystallites across the four SEM images shown in figures 6.1 and 6.2. For each crystallite, an estimation of the long axis diameter,

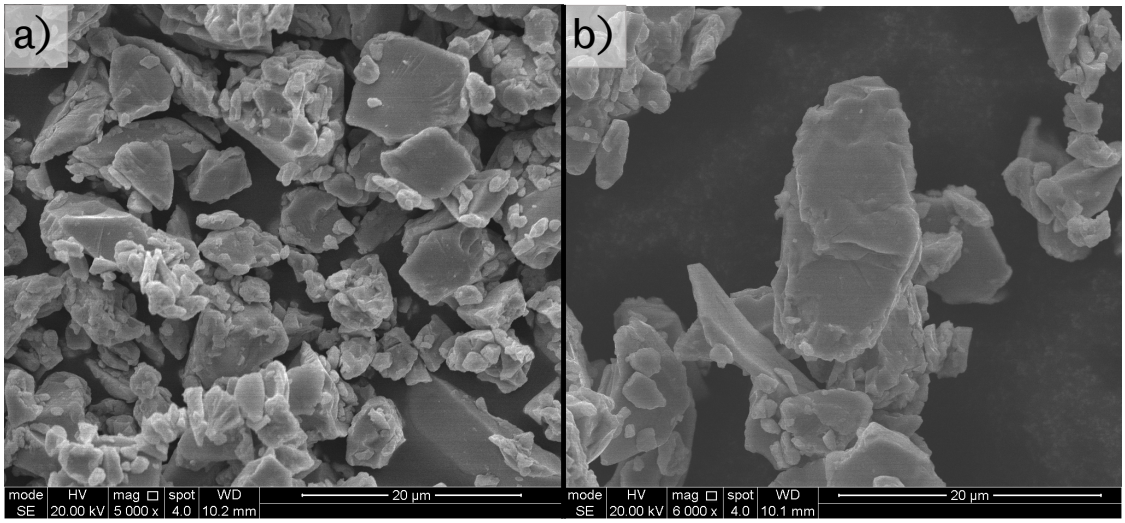

Figure 6.2: $Sm_2(Co, Fe, Cu, Zr)_{17}$ powder imaged by SEM at 5000× (a) and 6000× (b) magnification

a, of the crystallite was made and the axis perpendicular to this was then measured as the short axis diameter, b. The long and short axis diameters are also used to calculate the aspect ratio (a/b) for each crystallite, providing a quantification of crystallite geometry. It is noted that measurement of crystallite dimensions via microscopy image is of a two-dimensional projection for each crystallite and therefore prone to an under-estimate relative to their actual, three-dimensional shape.

Figure 6.3 shows the distribution for long and short axis measurement of $Sm_2(Co, Fe, Cu, Zr)_{17}$ powder crystallites. From this analysis, it is shown the majority of crystallites have dimensions below 10 µm. The long axis distribution is bimodal, with the major peak centred around 5 µm and minor peak around 15 µm. The short axis distribution is approximately Gaussian, although it could be argued for the presence of an emerging peak at 10 µm. Maximum magnification of 6000× limited accurate measurement in the smallest crystallites below 1 µm in size. The mean long axis diameter with 95% confidence limits was calculated to be, $\bar{a} = 5.9 \pm 0.8$µm. The mean short axis diameter was calculated as $\bar{b} = 4.2 \pm 0.6$µm. The average crystallite size from these two measurements is calculated as 5.0 ± 1.0µm. These values were calculated with a t-distribution value of 1.96 for a sample size of 150.

Figure 6.4 shows the distribution of crystallite aspect ratio. Reflecting the correlation in the major peak positions of the long and short axes, a significant majority of particles have measured aspect ratio of 1.5 or lower, which indicates the majority

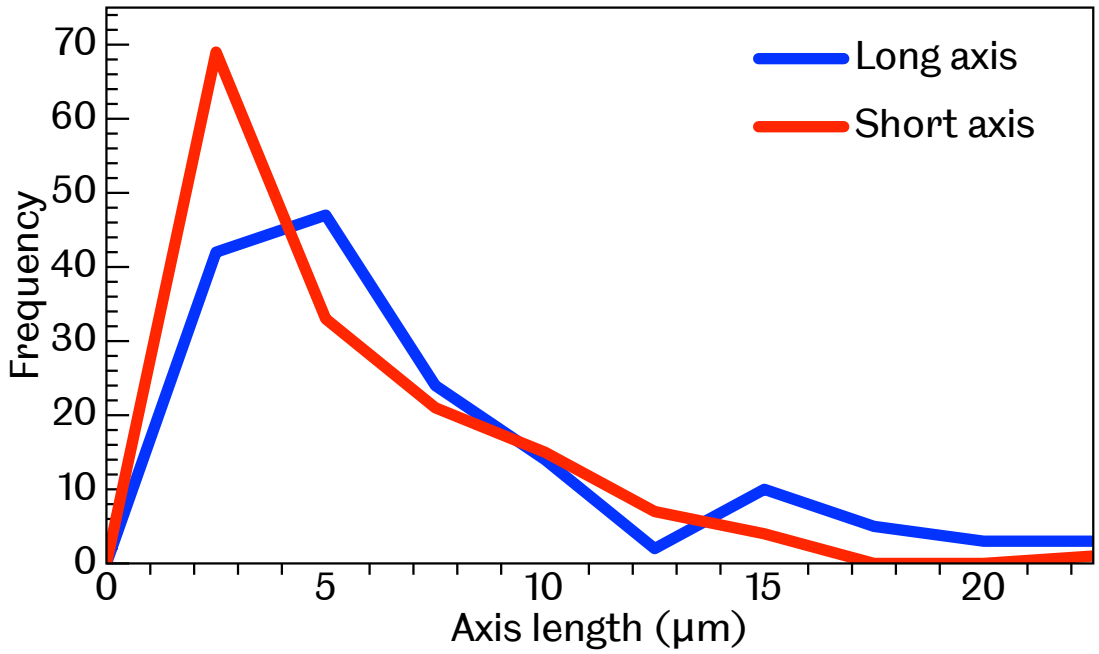

Figure 6.3: Distribution of long and short axis measurements for a sample size of 150 $Sm_2(Co, Fe, Cu, Zr)_{17}$ powder crystallites imaged by SEM.

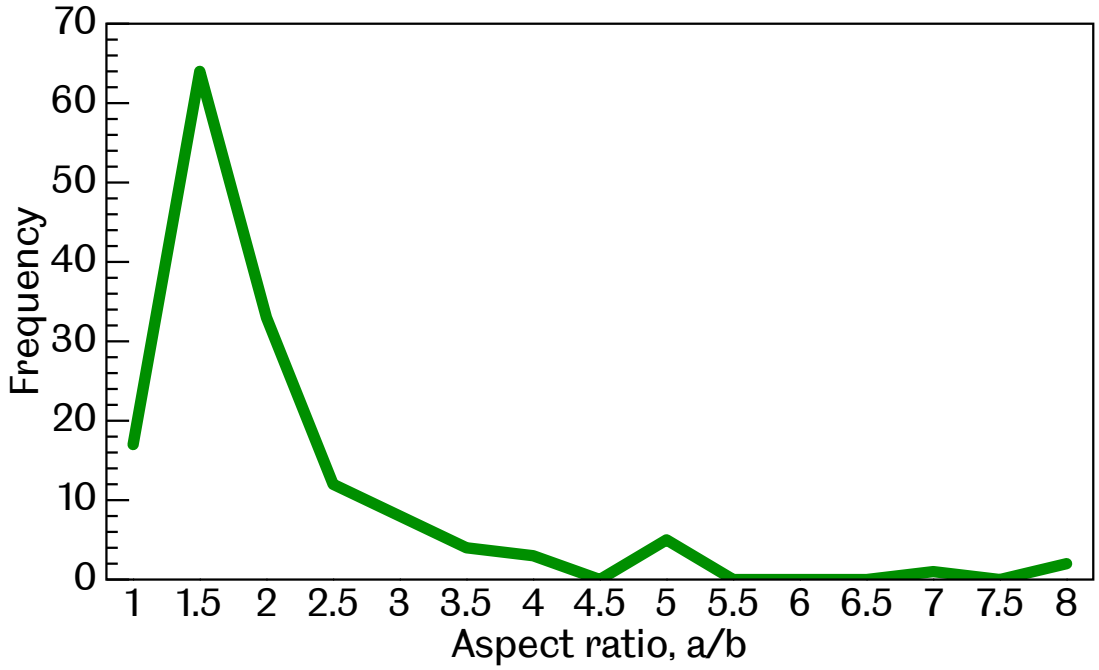

Figure 6.4: The calculated aspect ratio for a sample of 150 $Sm_2(Co, Fe, Cu, Zr)_{17}$ powder crystallites imaged by SEM

of the smallest particles are approximately equiaxed. Just under a third of crystallites sampled are elongated with an aspect ratio between 1.6 and 2.5. A clear example of one such crystallite is given in the centre of figure 6.2 b). A small peak for crystallites of aspect ratio = 5 highlights a small number of crystallites with very elongated geometries. The mean aspect ratio is 1.9 ± 0.2, while the median and mode are 1.5 and 1, respectively. The jet milling method used to produce the $Sm_2(Co, Fe, Cu, Zr)_{17}$ powders is able to produce a relative small distribution of powder size and the irregular geometries are characteristic of impact refinement method.

In general, the majority of crystallites that make up the powders of $Sm_2(Co, Fe, Cu, Zr)_{17}$ are around 5 µm, which is slightly smaller than the quoted size of 10 µm. The powder particles are made up of larger, irregular crystallites surrounded by noticeably smaller, equiaxed crystallites.

6.3 SPS processing parameters study

6.3.1 Heating rate and hold temperature

The immediate aim of powder processing by SPS is to produce fully dense $Sm_2(Co, Fe, Cu, Zr)_{17}$ samples, with the remanence and energy product of a permanent magnet strongly linked to the specimen's density [291]. From the literature available, the SPS processing parameters used specifically for $Sm_2(Co, Fe, Cu, Zr)_{17}$ powders are only specified by Zhang et al. [36]: Hold temperature 973 K (650 °C) for 5 minutes, pressure 500 MPa and a heating rate of 50 K/ min. The available SPS system (FCT Systeme GmbH Spark Plasma Sintering furnace type HP D 25) can emulate these parameters, however graphite moulds are limited to maximum applied pressures of 51 MPa. Zhang et al. achieved their far higher pressures using WC-Co moulds. If the maximum pressure available to us is used with a hold time of 5 minutes, the processing variables for study are reduced to the heating rate and hold temperature. It is expected that hold temperature and heating rate have the strongest influence on the sinter process, as the mass transfer mechanisms associated with porosity removal are temperature dependent.

To investigate the role of heating rate and hold temperature on the density, 11 $Sm_2(Co, Fe, Cu, Zr)_{17}$ specimens were processed by SPS with heating rates ranging from 50 °C/ min to 200 °C/ min and hold temperatures ranging from 800 °C to 1100 °C. For all specimens, the hold pressure and time were kept constant at 51 MPa and 5 minutes respectively. Table 6.3.1 catalogues the measured densities, where uncertainties were calculated from standard deviation of repeated measurements. The

densities of the specimens are reported as a percentage density relative to $8.4\,\mathrm{g/cm^3}$; the theoretical solid density for $Sm_2(Co, Fe, Cu, Zr)_{17}$ permanent magnets [131, 292].

Sample ID	**Hold temp. (°C)**	**Heating rate (°C/ min)**	**Density 1 (g/cm³)**	**Density 2 (g/cm³)**	**Density 3 (g/cm³)**	**Average density (g/cm³)**	**Relative density (%)**
1-31	800	100	6.304	5.980	5.987	6.090	72.50 ± 1.27
1-32	800	200	6.652	5.984	5.938	6.191	73.71 ± 2.75
1-01	1000	50	7.704	7.715	7.708	7.709	91.77 ± 0.04
1-02	1000	100	7.387	7.423	7.392	7.401	88.10 ± 0.13
1-07	1000	200	7.515	7.515	7.528	7.519	89.52 ± 0.05
1-10	1050	50	7.912	7.896	7.894	7.901	94.06 ± 0.07
1-11	1050	100	8.317	8.323	8.320	8.320	99.05 ± 0.02
1-12	1050	200	8.336	8.341	8.340	8.339	99.27 ± 0.02
1-13	1100	50	8.370	8.384	8.393	8.382	99.79 ± 0.08
1-20	1100	100	8.344	8.347	8.365	8.352	99.43 ± 0.08
1-21	1100	200	8.390	8.381	8.378	8.383	99.80 ± 0.04

Table 6.1: Measured densities for samples processed in heating rate and sintering temperature investigation. The relative density used is in reference to $Sm_2(Co, Fe, Cu, Zr)_{17}$ theoretical density of $8.4\,\mathrm{g/cm^3}$ [9]

The data shows an increase in density with the hold temperature used. Figure 6.5 [293] plots the average relative density against heating rate at different hold temperatures and a strong relationship is observed.

The lowest densities were recorded for the samples sintered at 800 °C, and at this temperature there is no significant effect on the density for the heating rates used. It is noted larger statistical uncertainties are associated with these specimens due to buoyancy errors (associated with trapped air within the porous bodies) during repeated measurements by Archimedes' water immersion technique. Zhang et al. were able to process fully dense nanocrystalline $Sm_2(Co, Fe, Cu, Zr)_{17}$ magnets by SPS at this temperature, however they used much higher pressures at 500 MPa [36].

When the hold temperature is increased to 1000 °C, the relative density increases significantly to $\approx 90\%$. While the hold temperature remained fixed, the sample processed with a heating rate of $50\,^{\circ}\mathrm{C\,min^{-1}}$ measured the highest density of this sinter temperature series, due to a longer overall processing cycle in comparison to the samples processed with heating rates of $100\,^{\circ}\mathrm{C\,min^{-1}}$ and $200\,^{\circ}\mathrm{C\,min^{-1}}$. Generally, the heating rate showed no significant trend with the sinter temperature at or below 1000 °C.

With a slight increase in the hold temperature to 1050 °C, full densification is now achievable and the heating rate becomes influential. For heating rates of 100 °C and above, the relative densities recorded improved to around 99%; approximately full density. Based on sintering theory, the higher heating rates bypass low temperature,

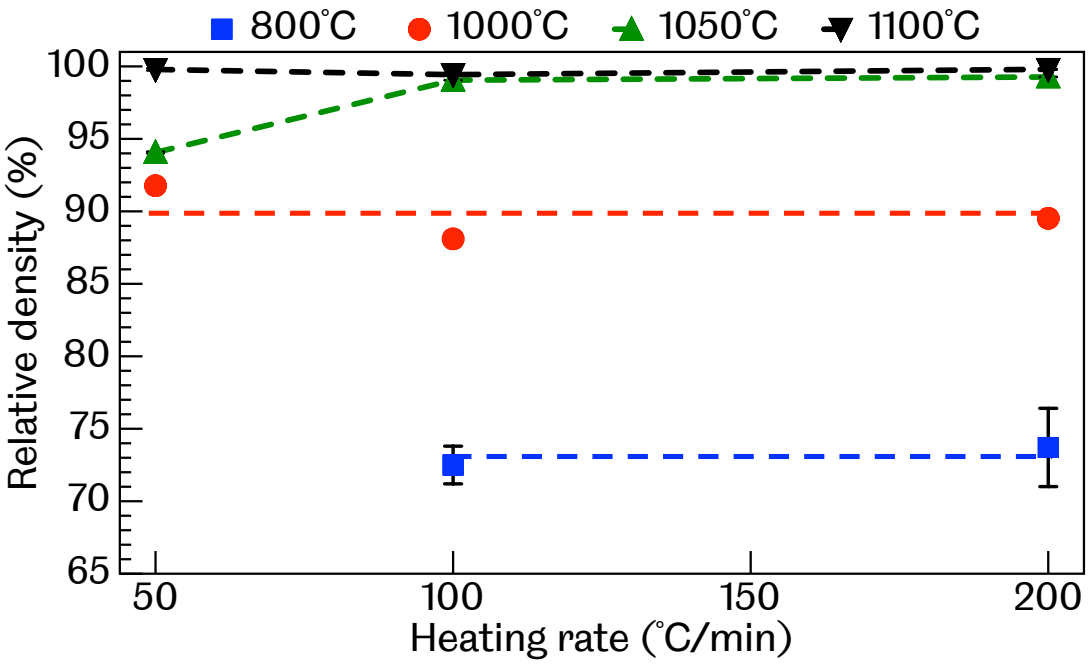

Figure 6.5: Relative density measured against heating rate for different hold temperatures for SPS processed $Sm_2(Co, Fe, Cu, Zr)_{17}$. The maximum pressure and hold time for all sample specimens were 51 MPa and 5 minutes respectively. Dashed lines are a trend line guide for the eye.

non-densifying mass-transfer mechanisms, and the majority of the processing is spent at the hold temperature, where the sinter mechanisms promote densification and dominate the sintering process. When the hold temperature is further elevated to 1100 °C, full densification is recorded for all specimens processed at the different heating rates studied.

The data presented in our study [293] compare well with the collected data [174, 175] in Garay's review on SPS processed Alumina [153] and show a similar relationship between hold temperature, heating rate and density.

A BS SEM microstructure image of the specimen processed at 1000 °C with a heating rate of 100 °C/ min is shown in figure 6.6. The under-processed microstructure is comprised of a large volume fraction of porous features, highlighted by the blue square, which are not entirely void, but instead appear to be comprised of un-sintered powder particles. These are markedly different from traditional pores, noted with black circle and 'p', which are spherical voids. This example of the microstructure, in combination with the data presented in table 6.3.1, confirms for the maximum available pressure of 51 MPa and a hold time of 5 minutes, the sintering of $Sm_2(Co, Fe, Cu, Zr)_{17}$ powders by SPS is insufficient at temperatures below 1000 °C, regardless of the heating rate used, as full densification is not

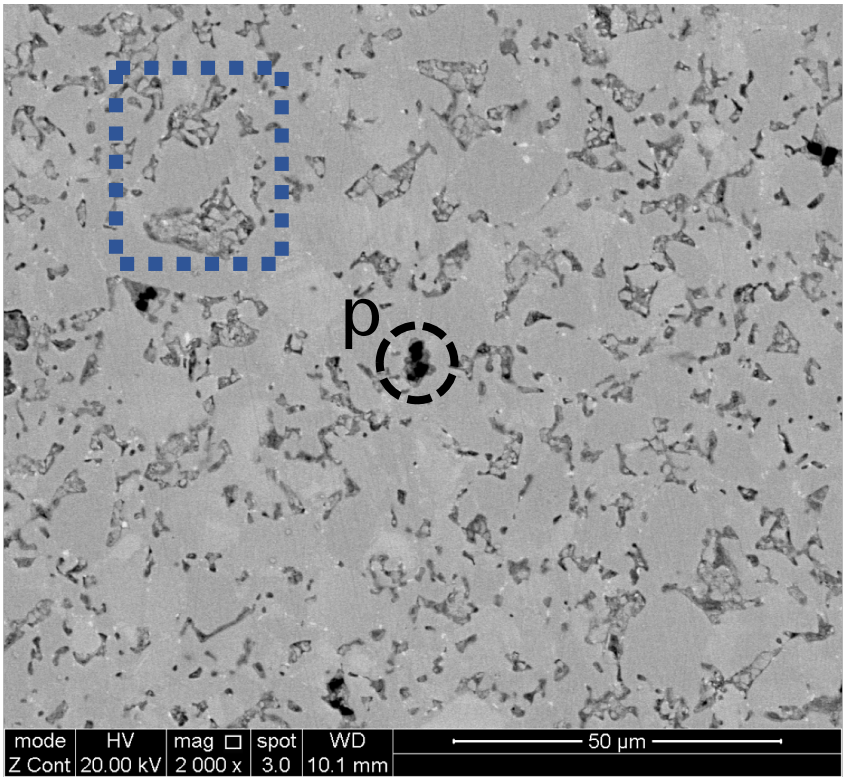

Figure 6.6: BS SEM image of a typical $Sm_2(Co, Fe, Cu, Zr)_{17}$ microstructure sintered by SPS at 1000 °C with a heating rate of 100 °C/ min. The blue square highlights porous areas of un-sintered $Sm_2(Co, Fe, Cu, Zr)_{17}$ particles, while the black circle and 'p' highlights void pores.

achieved and the material is too porous to be considered useful for permanent magnet processing.

The effect of the sinter time was also briefly investigated, to confirm whether extending the time spent at lower sintering temperatures improved densification. Two samples, processed at a maximum pressure of 51 MPa and a heating rate of 100 °C/ min, were sintered at 1000 °C for 5 and 10 minutes respectively. The 5 minute sample had a relative density of $90.83 \pm 0.02\%$, while the sample sintered for 10 minutes measured $93.01 \pm 0.06\%$, showing for certain materials or phases, which may require low temperatures for sintering, higher levels of densification can be reached by extending the hold time. With regards to $Sm_2(Co, Fe, Cu, Zr)_{17}$, conventional sinter methods occur at temperatures of around 1200 °C for between 1 - 2 hours [84].

Based on the heating rate and hold temperature study, the standard processing parameters for SPS processed $Sm_2(Co, Fe, Cu, Zr)_{17}$ established in this work are: 1050 °C to 1100 °C sinter temperature, 100 °C/ min to 200 °C/ min heat-

ing rate, 51 MPa pressure and hold time of 5 minutes. These parameters densify $Sm_2(Co, Fe, Cu, Zr)_{17}$ powders to full density in cycle times under 30 minutes. Henceforth, when referring to 'standard' SPS processing parameters for $Sm_2(Co, Fe, Cu, Zr)_{17}$ in this project, it is the aforementioned parameters that have been used. Where necessary, specific heating rates and hold temperatures will be disclosed.

6.4 Microstructure characterisation

6.4.1 Light microscopy and grain characterisation

Figure 6.7 a) shows an example bright-field light microscopy image of SPS processed $Sm_2(Co, Fe, Cu, Zr)_{17}$. This specimen has been processed under standard processing parameters and has a relative density of 99.92%. As such, there is clearly no evidence of significant un-sintered porous regions. The microstructure shown in figure 6.7 a) is typical throughout the specimen cross-section and is defined by two main features - a $Sm_2(Co, Fe, Cu, Zr)_{17}$ matrix phase (light in colour) and a grain boundary precipitate phase (black). However, some of these black features are identified as pores, which are highlighted as the brightest features in 6.7 b), where the image is viewed in dark-field mode. In this viewing mode, light scattered by uneven and rough surfaces is more favourably detected and porosity can clearly be identified. ImageJ analysis of 6.7 b) was used estimate the volume percentage of these pores at 0.26%, equating to density of 99.74%, relative to the theoretical value, which compares favourably with the density measured by Archimedes' water immersion technique.

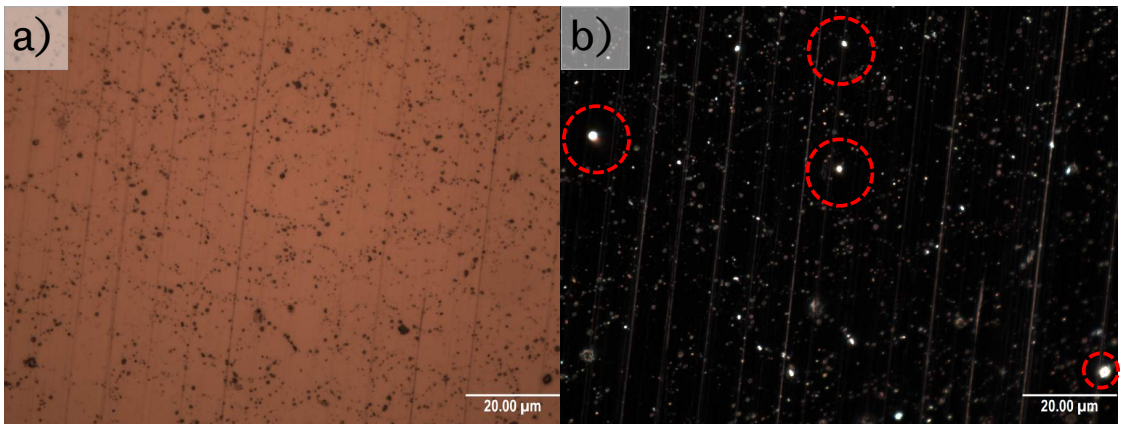

Figure 6.7: a) Bright-field and b) dark-field light microscopy image of SPS processed $Sm_2(Co, Fe, Cu, Zr)_{17}$ microstructure. Red circles highlight selected pores.

For comparison, figure 6.8 shows a similar light microscopy image for a conventionally sintered and heat treated $Sm_2(Co, Fe, Cu, Zr)_{17}$ sample. This specimen was provided by Arnold Magnetic Technologies (Sheffield, UK) and is of a similar alloy composition to the powders used in the SPS study. The same features inherent in the SPS processed microstructure are observed in the conventionally processed microstructure, which is dominated by a $Sm_2(Co, Fe, Cu, Zr)_{17}$ matrix phase with a distribution of a spherical and black precipitate phase along the grain-boundaries.

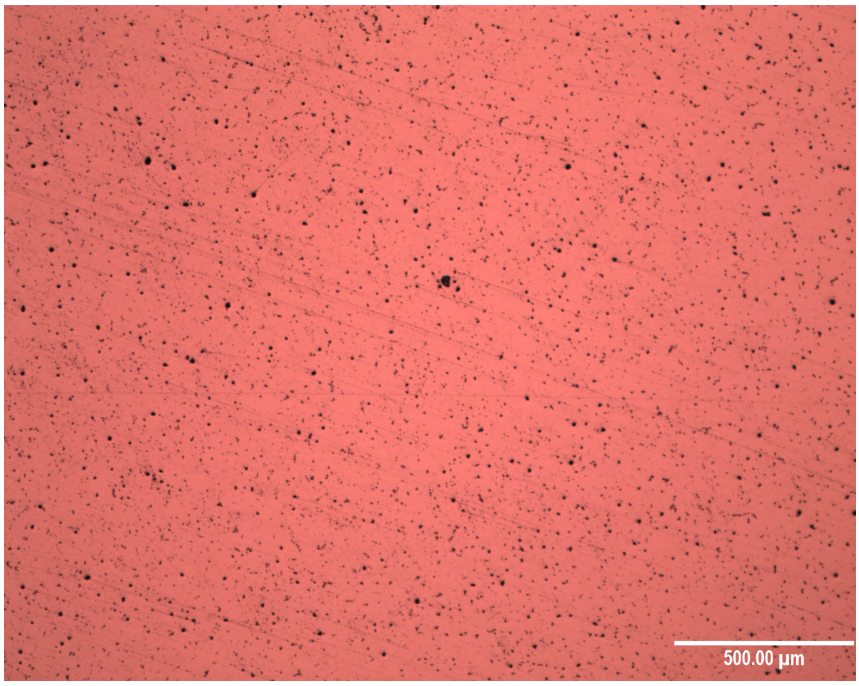

Figure 6.8: Light microscopy image of conventionally processed and heat-treated $Sm_2(Co, Fe, Cu, Zr)_{17}$ specimen provided by Arnold Magnetic Technologies.

Grain size measurement

Grain boundaries in $Sm_2(Co, Fe, Cu, Zr)_{17}$ material can be revealed using a 10% concentration citric acid and water solution at 80 °C as an etchant. Figure 6.9 shows an example of the revealed grain structure in a SPS processed $Sm_2(Co, Fe, Cu, Zr)_{17}$ specimen. The granular microstructure is comprised of irregularly shaped grains with varying grain sizes.

To measure average grain diameters, the linear intercept method was used in the horizontal and vertical axis of the image. For each measurement direction, twenty lines across two microscopy images of the same etched specimen were used to measure grain diameters. The mean grain diameter, with 95% confidence limit, in the horizontal axis was 9.0 ± 0.4µm and 8.0 ± 0.4µm in the vertical axis. The

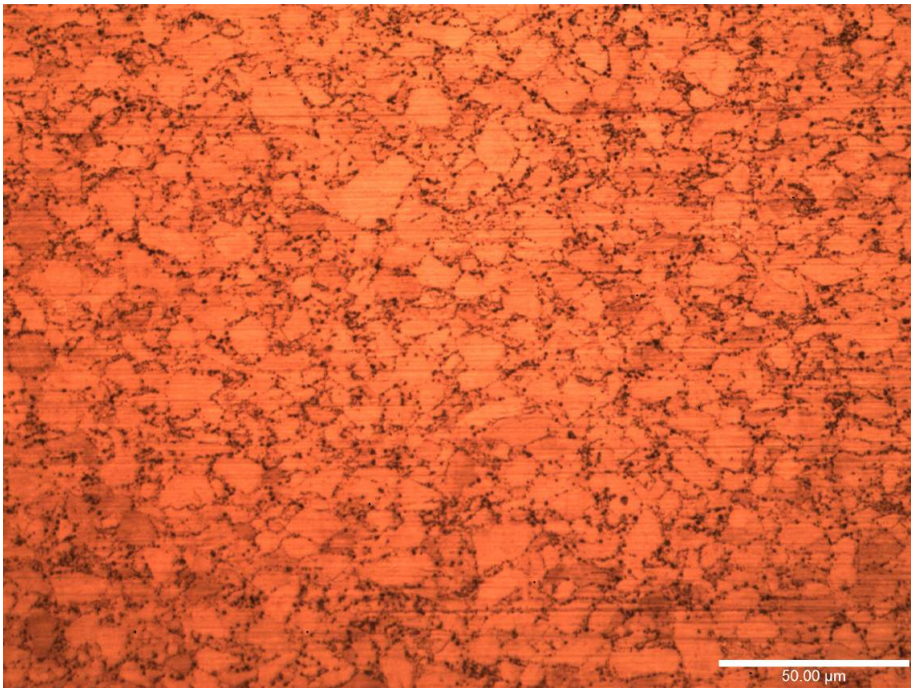

Figure 6.9: Optical microscopy of citric acid 10% solution etched SPS processed $Sm_2(Co, Fe, Cu, Zr)_{17}$.

average grain size from these two values is 8.5 ± 0.6µm. The uncertainty in these values were calculated using a t-distribution value of 2.

Comparison with the mean powder crystallite size provides insight into grain coarsening during the SPS process. Although a different method was used to measure the crystallite diameters of the $Sm_2(Co, Fe, Cu, Zr)_{17}$ powders, the long axis diameter can effectively be used as an upper bound estimation of the crystallite diameter. The mean long axis diameter of the powders was measured as $\bar{a} = 5.9 \pm 0.8$ µm and both horizontal and vertical grain measurements by linear intercept method in the SPS processed $Sm_2(Co, Fe, Cu, Zr)_{17}$ sample are greater than this value. This indicates minor grain coarsening occurred under the stated SPS processing parameters.

Using the mean horizontal and vertical grain diameter measurements by linear intercept method, we can approximate the mean aspect ratio for the SPS processed $Sm_2(Co, Fe, Cu, Zr)_{17}$ specimen and compare with the averaged aspect ratio calculated for the $Sm_2(Co, Fe, Cu, Zr)_{17}$ crystallites. This can offer insight into whether deformation of the grains occurs with the application of pressure during the sinter process. After SPS processing, a mean aspect ratio of 1.1 ± 0.1 is calculated, which is less than 1.9 ± 0.2; the equivalent for $Sm_2(Co, Fe, Cu, Zr)_{17}$ powder crystallites. The variation in the method of powder and grain size measurements is likely the main contributor to the disparity, however through application of 51 MPa of pressure

during the sinter process to the isotropically distributed irregularly shaped grains, and with slight grain coarsening occurring, the $Sm_2(Co, Fe, Cu, Zr)_{17}$ grains become more equiaxed during the SPS process, rather than more deformed and/or elongated.

Comparison of the grain sizes with an available conventional sinter method $Sm_2(Co, Fe, Cu, Zr)_{17}$ magnet is not directly comparable, as the provided $Sm_2(Co, Fe, Cu, Zr)_{17}$ magnets have undergone a full heat treatment. In the following chapter, where the SPS processed $Sm_2(Co, Fe, Cu, Zr)_{17}$ magnets are subjected to full heat treatments can comparison between the two processing methods effect on grain size be fairly made.

SEM and EDS analysis

SEM provides further microstructure imaging and analysis at greater magnification and resolution compared to light microscopy. Figure 6.10 shows a BS SEM image of an SPS processed $Sm_2(Co, Fe, Cu, Zr)_{17}$ specimen, sintered to full density under standard SPS processing parameters.

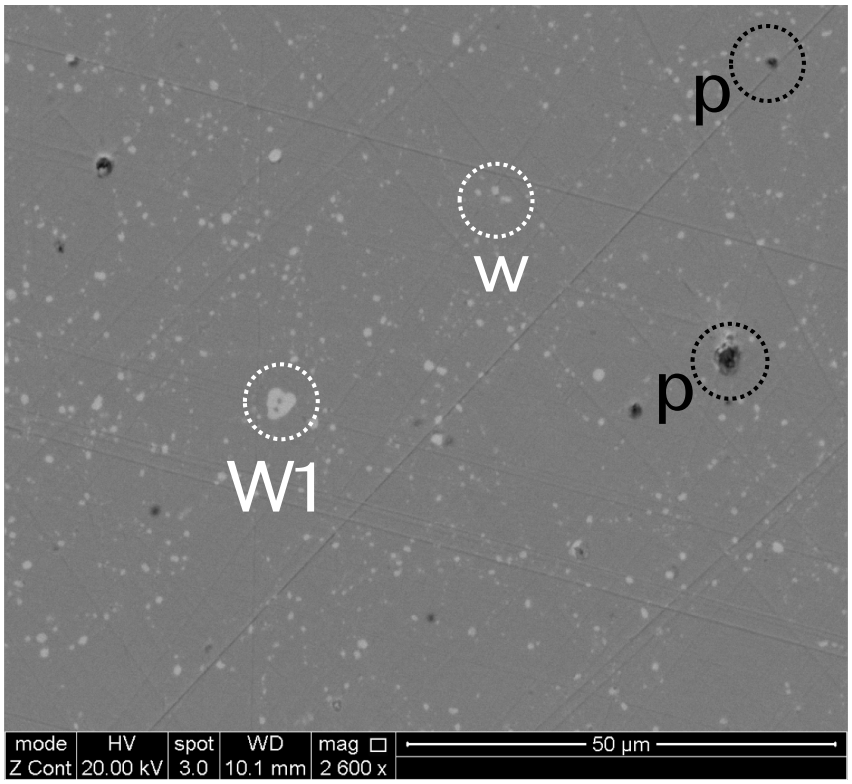

Figure 6.10: BS SEM image of a typical microstructure for SPS processed $Sm_2(Co, Fe, Cu, Zr)_{17}$ sintered at 1100 °C and 100 °C/ min. Letter 'p' highlights pore/voids, 'W' highlights Sm and O-rich white precipitate feature, 'W1' shows atypically large Sm and O-rich precipitate feature.

Complementing the light microscopy images, the microstructure is comprised of a $Sm_2(Co, Fe, Cu, Zr)_{17}$ matrix phase (grey), with a distribution of numerous precipitates (white, and highlighted by white circle and letter 'W') and some porosity/voids (highlighted by black circle and letter 'p').

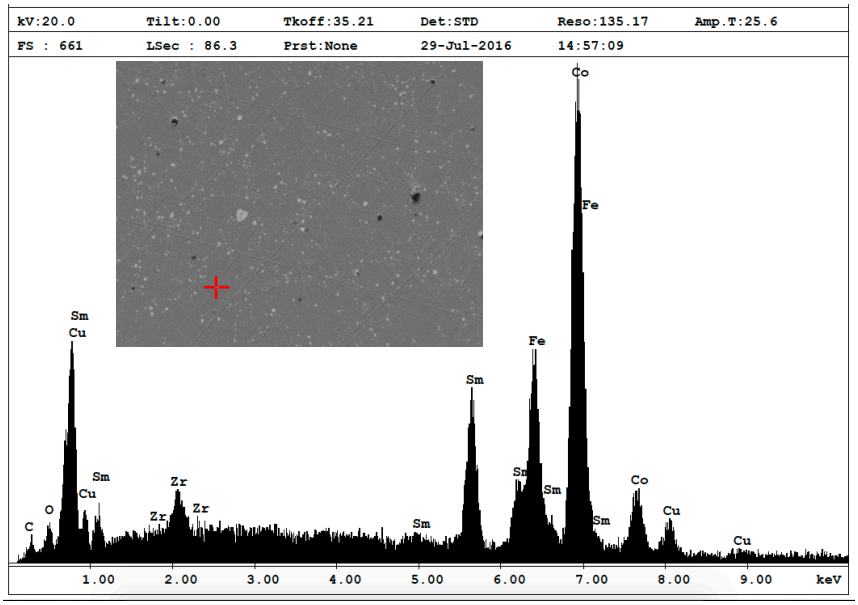

Figure 6.11: EDX spot analysis of the main matrix phase, highlighted in insert (red cross).

Figure 6.11 shows the location (red cross) of an EDS spot scan used to identify the elements present within the grey $Sm_2(Co, Fe, Cu, Zr)_{17}$ matrix phase. The resulting spectra, with corresponding elements attributed to peak positions, is one example of several matrix spot scans taken throughout the SEM image. Over these multiple scans, the peak positions and intensities did not change significantly. Expectedly, the matrix phase is predominantly comprised of the elements Sm, Co, Fe, Cu and Zr, with indication for trace amounts of C and O.

EDS spot analysis was also used to identify the elemental composition of the white precipitate features. Figure 6.12 shows the results of one such spectral analysis, showing the white precipitates are comparatively rich in Sm and O and poor in Co, Cu and Zr. Maury et al. identified these features as the Sm_2O_3 phase, which form along grain boundaries [75].

SEM of conventional sinter processed $Sm_2(Co, Fe, Cu, Zr)_{17}$ specimens by Maury et al. were also able to identify a Zr-rich phase, which featured as black precipitates within their microstructures [75]. In our study, EDS spot analysis of a similarly de-

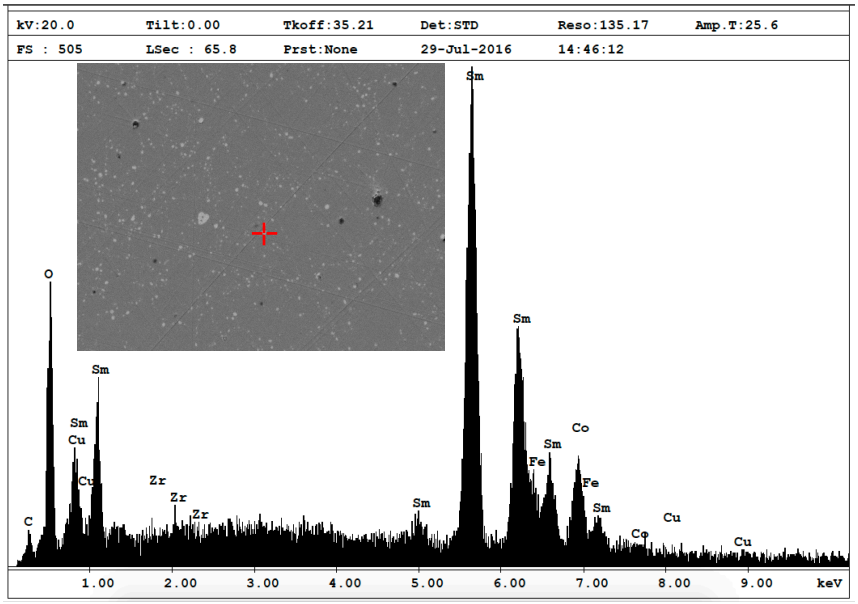

Figure 6.12: EDX spot analysis of a typical white precipitate feature, highlighted in insert (red cross).

scribed feature is shown in figure 6.13 and does not show elevated levels of Zr in this feature compared to the matrix or white precipitate phase. Zr comprises of a very small weight addition in the $Sm_2(Co, Fe, Cu, Zr)_{17}$ alloy, typically less than 2 wt.% and so the levels measured for this element are much lower than the other alloying elements. There are elevated levels of oxygen when comparing peak intensities with figure 6.11 and this is consistent in all of black features analysed. Therefore, it is concluded that the analysis of these features within the microstructure of the $Sm_2(Co, Fe, Cu, Zr)_{17}$ specimen studied are not the Zr-rich precipitates identified by Maury et al., but instead are likely voids or pores.

6.5 Material characterisation and properties

6.5.1 XRD phase analysis

XRD 2θ analysis was used to identify the phases present in the pre-alloyed $Sm_2(Co, Fe, Cu, Zr)_{17}$ powders and in a specimen (1-18) processed under the following parameters: $100\,^{\circ}C\,min^{-1}$ heating rate, 1100 °C hold temperature, 51 MPa hold pressure and 5 minutes hold time.

Figure 6.14 shows measured spectra and symbols used to represent identified peaks after phase analysis. Both the $Sm_2(Co, Fe, Cu, Zr)_{17}$ powder and SPS processed specimen are primarily comprised of the 2:17R phase, which has a rhombohedral symmetry and a crystal structure of the type Th_2Zn_{17}. The

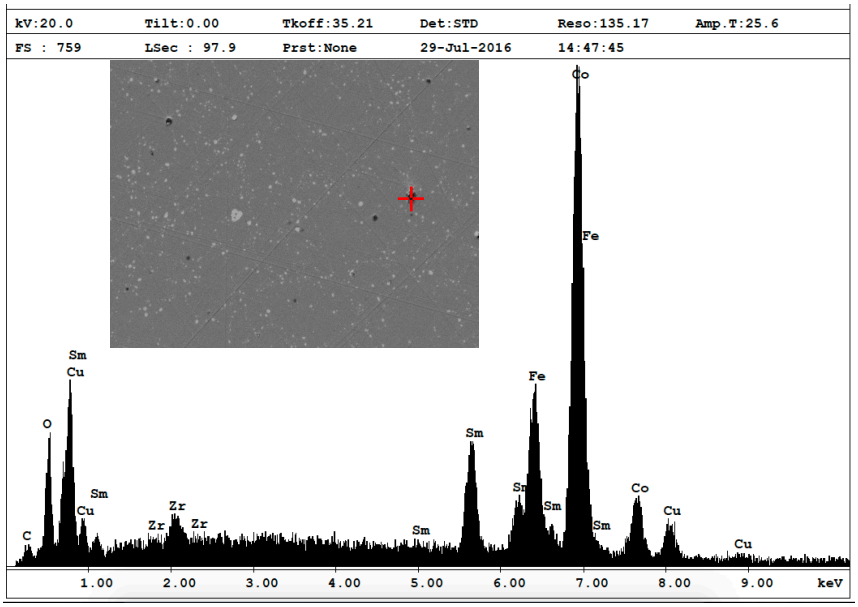

Figure 6.13: EDX spot analysis of a typical black feature, highlighted in insert (red cross).

stable, low temperature 2:17R phase is the most commonly identified phase in $Sm_2(Co, Fe, Cu, Zr)_{17}$ cast alloys and powders [37, 66, 75] and also regularly reported in conventional sinter processed $Sm_2(Co, Fe, Cu, Zr)_{17}$ magnets [80, 121]. Evidently, no significant phase changes occur within the $Sm_2(Co, Fe, Cu, Zr)_{17}$ material during the SPS sinter process.

A peak at 66 2θ can not be accounted for by the $Sm_2(Co, Fe, Cu, Zr)_{17}$ 2:17R phase. It could potentially be explained by a ZrC phase, which also has peaks at 33 2θ and 43.5 2θ, although these are obscured by the more prominent peaks of the 2:17R phase. A possible explanation for their presence is due to carbon uptake during the SPS process, where carbon is diffusing into the surface of the $Sm_2(Co, Fe, Cu, Zr)_{17}$ material and forming carbides with zirconium in the material [95]. Zirconium carbides have been observed in $Sm_2(Co, Fe, Cu, Zr)_{17}$ studies with carbon addition [121, 122]. However, this phase is only highlighted in figure 6.14 as a tentative identification, as any features within the $Sm_2(Co, Fe, Cu, Zr)_{17}$ microstructure could not be identified as Zr or C rich. It would be more likely that the grain boundary Sm_2O_3 phase would be present in the XRD spectra, which was numerous and easily identifiable in the SEM EDS analysis, but instead does not feature in any XRD 2θ study of SPS processed $Sm_2(Co, Fe, Cu, Zr)_{17}$.

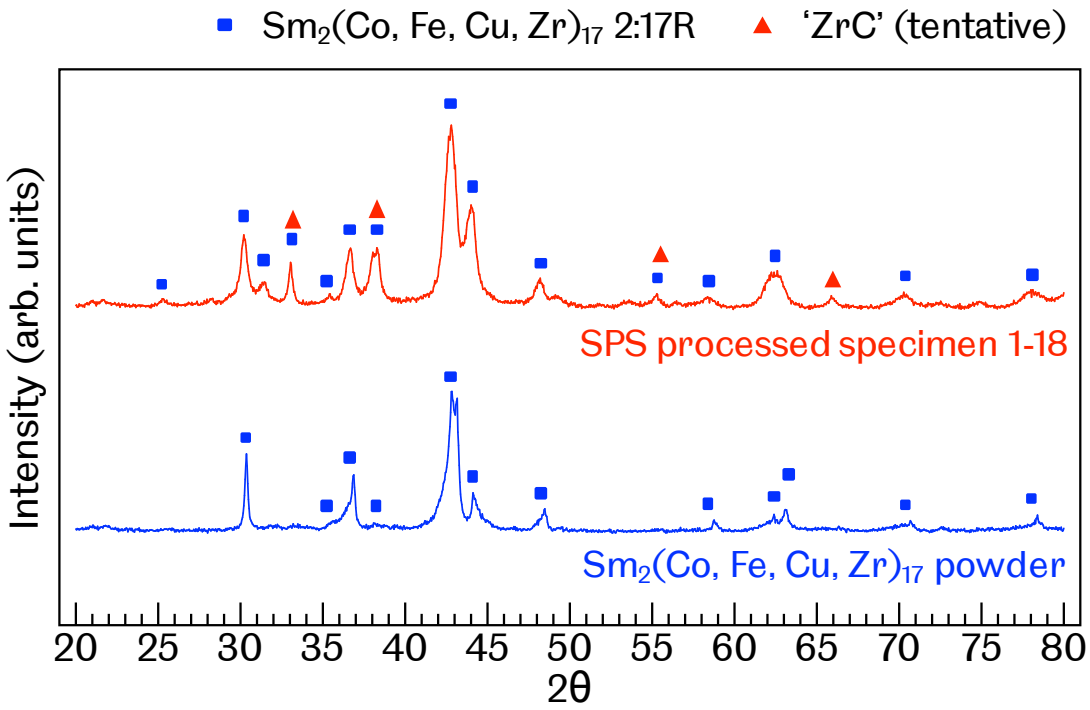

Figure 6.14: XRD 2θ analysis for $Sm_2(Co, Fe, Cu, Zr)_{17}$ pre-alloyed powder (blue) and after processing by SPS (red)

6.5.2 Electrical resistivity measurements

Electrical resistivity measurements were conducted using the VDP method outlined in chapter 5 with a purpose built rig designed for the 20 mm samples produced by SPS. The measurements serve as a general characterisation of $Sm_2(Co, Fe, Cu, Zr)_{17}$ magnets processed by SPS and can also indirectly detect changes in phase distribution and composition across the range of processing variables studied [132]. Resistivity measurements are also important for later studies, where comparison will be made after various heat treatments and in composite magnets produced by SPS with electrically insulating phases.

The measured current, I, and potential difference, V, values for all electric probe arrangements, along with the calculated bulk resistivity, ρ_{VDP}, using equations 5.5 to 5.7, are shown in table 6.2. The subscript on the potential difference values refers to the arrangement of current and potential difference probes around the sample. For example, V_1 refers to the current passing between contacts 1 and 2 ($I_{1,2}$), with the potential difference measured between 4 and 3 ($V_{3,4}$). Therefore, $V_2 = V_{4,3}/I_{2,1}$, $V_3 = V_{4,1}/I_{2,3}$, $V_4 = V_{1,4}/I_{3,2}$, etc. 8 measurements were made per sample with two repeats. The Q-value is the ratio between the horizontal and vertical potential difference measurements and used to derive the correction factor, f, for less than

ideal and non-symmetrical specimens. Q values < 1.5 require minimal correction (approximately 1-3% reduction in measured resistivity). ρ_H and ρ_V are the corrected horizontal and vertical resistivity values and ρ_{VDP} is the averaged bulk resistivity of the specimen. The uncertainty accounts for probe placement error (assuming all probes are 1 mm from the sample periphery) and fluctuations in the applied current and in the displayed potential difference values.

Sample ID	t (cm)	I (A)	V1 (μV)	V2 (μV)	V3 (μV)	V4 (μV)	V5 (μV)	V6 (μV)	V7 (μV)	V8 (μV)	Q	ρ_H (μΩ cm)	ρ_V (μΩ cm)	ρ_{VDP} (μΩ cm)
1-01	0.46	0.308	14.00	14.00	14.50	14.50	14.00	14.00	14.50	14.50	1.04	95.59	99.01	97.30 ± 6.91
1-04	0.48	0.297	11.50	11.50	12.83	13.00	11.67	11.50	13.00	13.00	1.12	83.47	93.71	88.59 ± 7.33
1-07	0.50	0.306	13.50	13.50	15.00	15.00	13.50	13.67	15.00	15.00	1.11	99.62	110.34	104.98 ± 7.47
1-08	0.49	0.304	12.83	13.00	14.67	14.50	13.00	13.00	14.67	14.50	1.13	94.48	106.33	100.41 ± 7.41
1-09	0.46	0.305	13.00	13.00	14.00	14.00	13.00	13.00	14.00	14.00	1.08	89.57	96.46	93.02 ± 6.97
1-11	0.44	0.298	13.00	13.00	15.00	15.00	13.00	13.00	15.00	15.00	1.15	85.28	98.40	91.84 ± 6.68
1-12	0.43	0.296	12.00	12.00	15.00	15.00	12.00	12.00	15.50	15.50	1.27	78.27	99.47	88.87 ± 6.87
1-16	0.37	0.304	16.50	16.50	16.50	16.50	16.50	16.50	16.50	16.50	1.00	91.68	91.68	91.68 ± 5.64
1-17	0.41	0.306	15.00	15.00	16.50	16.50	15.00	15.00	16.50	16.50	1.10	89.67	98.63	94.15 ± 6.08
1-18	0.40	0.400	19.33	19.67	21.17	21.50	19.33	19.33	21.33	21.17	1.10	87.49	95.94	91.71 ± 4.56
1-19	0.40	0.302	14.00	14.00	17.67	17.67	14.00	14.17	17.67	17.50	1.26	83.45	104.75	94.10 ± 6.14
1-20	0.47	0.298	12.00	12.00	13.00	13.00	12.00	12.00	13.00	13.17	1.09	86.39	93.89	90.14 ± 7.28
1-22	0.46	0.298	12.33	12.33	14.00	13.83	12.33	12.17	13.67	14.00	1.13	84.46	95.34	89.90 ± 6.98
1-23	0.43	0.298	13.83	13.50	14.17	14.33	13.83	13.67	13.83	14.00	1.03	90.49	92.96	91.72 ± 6.68
1-24	0.45	0.296	12.67	12.33	15.17	14.50	12.50	12.50	14.50	14.50	1.17	84.32	98.94	91.63 ± 6.89
1-25	0.45	0.295	12.33	12.83	13.83	13.83	13.00	12.50	14.00	14.00	1.10	88.35	97.07	92.71 ± 7.00
1-26	0.45	0.297	12.00	12.17	14.50	14.50	12.00	12.00	14.50	14.50	1.20	82.41	99.24	90.82 ± 7.00
1-27	0.45	0.296	12.50	12.50	13.83	14.50	12.50	12.50	14.50	14.50	1.15	84.32	96.69	90.50 ± 6.87
1-28	0.47	0.300	12.00	12.00	14.00	14.00	11.83	12.00	13.83	13.83	1.16	83.23	96.86	90.04 ± 7.09
1-29	0.46	0.300	12.50	12.50	14.00	14.00	12.50	12.50	14.00	14.00	1.12	85.88	96.18	91.03 ± 6.97
1-30	0.45	0.298	13.00	13.00	14.50	14.50	13.00	13.00	14.33	14.33	1.11	88.48	98.12	93.30 ± 6.91
1-32	0.53	0.298	20.00	20.00	23.75	24.00	20.25	20.25	24.00	23.75	1.19	161.61	191.73	176.67 ± 8.34
1-33	0.47	0.298	12.00	12.00	16.25	16.25	12.25	12.25	16.00	16.00	1.33	83.18	110.62	96.90 ± 7.15

Table 6.2: Measured current and potential difference values and calculated resistivity measurements by VDP method for $Sm_2(Co, Fe, Cu, Zr)_{17}$ samples processed by SPS. 't' refers to the thickness of the specimen, 'I' is the electric current, 'V' is the measured potential difference (subscript number refers to the direction of measurement in the VDP method, 'Q' is ratio of $\frac{V_{horizontal}}{V_{vertical}}$ used to derive the correction factor, *f*. Rows highlighted are specimens with relative densities $< 92\%$.

The reference resistivity values for $Sm_2(Co, Fe, Cu, Zr)_{17}$ magnets vary in the literature from 70 µΩ cm to 115 µΩ cm [131, 132, 134, 292, 294]. This is expected, as the ratio of alloying elements in $Sm_2(Co, Fe, Cu, Zr)_{17}$ magnets vary, depending on its application and desired performance. For this work, the solid resistivity of $Sm_2(Co, Fe, Cu, Zr)_{17}$ is taken as 90 µΩ cm, which has been referenced from the Arnold Magnetic Technologies Recoma 35E grade $Sm_2(Co, Fe, Cu, Zr)_{17}$ datasheet [295], which is designed for high coercivity at room temperature and likely similar in composition to the powders provided. It is assumed the reference value is after heat treatment, although no mention is made.

Nearly all of the SPS processed $Sm_2(Co, Fe, Cu, Zr)_{17}$ specimens studied by VDP method fall within uncertainty of the reference resistivity of 90 µΩ cm. The outliers to this are the specimens processed under sub-optimal SPS parameters and are of lower density. In table 6.2, the specimens with relative densities $< 92\%$ are highlighted.

Certain $Sm_2(Co, Fe, Cu, Zr)_{17}$ specimens show clear anisotropy in the resistivity measured in the horizontal and vertical directions and this is quantified with a large 'Q' value. Samples 1-12, 1-19, 1-26 and 1-33, all have relative densities approximately 99%, but some have been processed under slightly different sinter temperature and heating rates. The anisotropy was investigated with the samples rotated and remeasured and bearing the same results. A contributing factor may arise from a break-down in the measurement method due to slight damage at the periphery of the samples and uneven surfaces. The VDP method is useful for arbitrary shaped samples, however it works best if there is symmetry about the sample and the surface must be flat. A derived correction factor is used to address inhomogeneous and asymmetric issues. For the level of anisotropy in the SPS processed $Sm_2(Co, Fe, Cu, Zr)_{17}$ specimens, the correction factor is quite minor; ranging from 0.99 to 0.97.

The error associated with the electric probe displacement was shown to be quite minor in the methodology chapter. From analysis of the uncertainties in the measurement method, it was found that the variability in the potential difference readings from the Keithely 2000 multi-meter was the largest source of error. Practise of the methodology and repeat measurements reduced the level of uncertainty in reading the potential difference value. However, further improvements could be made if an automatic measurement system was implemented, which would make multiple measurements and average for a more accurate reading of the potential difference.

Figure 6.15 is able to compare the measured resistivity and relative density values for the SPS processed $Sm_2(Co, Fe, Cu, Zr)_{17}$ samples listed in table 6.2. The

data also includes information on the processing parameters: hold temperature is represented by colour and heating rate by symbol shape. Magnetically isotropic samples are represented by filled symbols and powder-aligned samples by un-filled symbols.

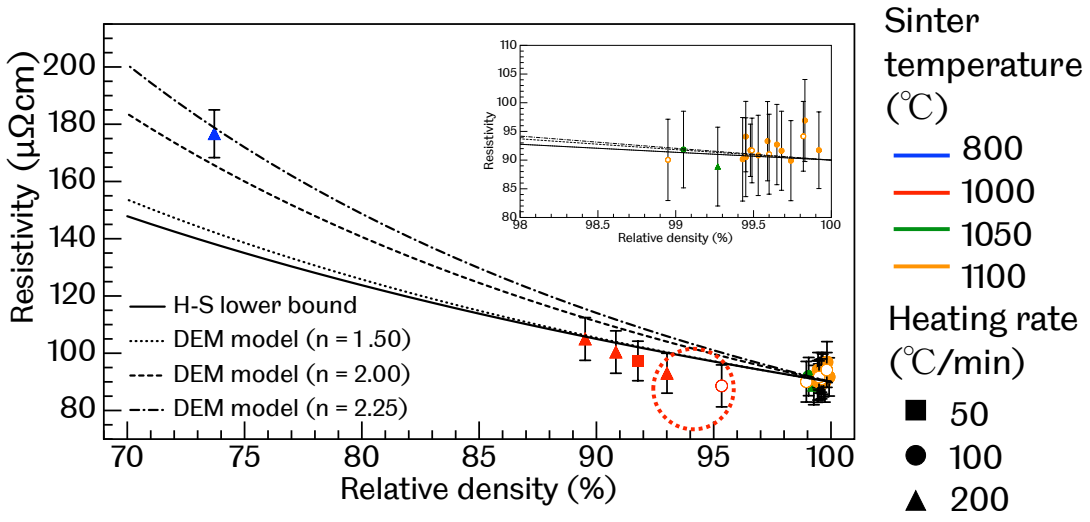

Figure 6.15: Measured resistivity values for SPS processed $Sm_2(Co, Fe, Cu, Zr)_{17}$ and their associated densities, relative to the theoretical value of $8.4\,g/cm^3$ [131, 292]. The colour of the symbol represents the sinter temperature and the symbol shape represents the heating rate. Filled symbols are isotropic, open symbols have received powder alignment via magnetic field before the SPS process. Inset shows magnification of data towards 100% relative density. Line and dashed data lines are resistivity models explained in section 6.5.2.

Magnetically anisotropic $Sm_2(Co, Fe, Cu, Zr)_{17}$ is expected to possess anisotropic resisivity if measurement is made either parallel to the basal plane or parallel to the c-axis [131, 132]. The data presented in figure 6.15 contains a mixture of isotropic, axial-aligned (samples 1-04, 1-28, 1-29) and transverse-aligned samples (samples 1-16, 1-17). As shown, the $Sm_2(Co, Fe, Cu, Zr)_{17}$ samples with (open symbols) and without powder alignment (filled symbols) possess the same resistivity within uncertainty ranges. This may indicate the powder alignment methods used have only resulted in partial alignment of the easy axes of the powders and thus there is only a negligible effect on the electrical anisotropy. The degree of alignment in the SPS processed samples is discussed in the following section 6.6.1. The VDP measurement system used may also not be sensitive enough to detect the subtle differences in the resistivity between aligned and isotropic samples, of which the relatively large uncertainties in our measurements are an indication of.

Comparison with resistivity models

The bulk resistivity and relative density values have been compared with two models, the Hashin-Shtrikman (H-S) upper bound for conductivity (which, in the discussion of resistivity will be a lower-bound value) and the Differential Effective Medium (DEM) model, which model the effect of secondary inclusions, which could be pores, on the conductivity of a material. For our results, we use the reciprocal of both equations to model the resistivity.

The H-S equation (equation 6.1) is a rigorous limit for the conductivity (or, resistivity in our study) of an isotropic material due to an isotropic distribution of uniform porosity [296, 297]. Comparison of this model with our experimental data can be useful to validate our measurement method and also provides context for the DEM model.

$$\rho_p = \rho_0 \left(\frac{3 - D_{rel}}{2D_{rel}} \right) \tag{6.1}$$

The DEM equation (equation 6.2) has been used to show good agreement with studies on the conductivity of materials with inclusions of different geometries [297, 298]. In this work, the primary phase is the $Sm_2(Co, Fe, Cu, Zr)_{17}$ and the secondary phases are pores with approximate spherical shape. The exponent in the equation, n, represents the shape of the inclusions, with n = 1.5 used to model spherical pores and values of greater than 1.5 used for non-equiaxed spheroids, which approach prolate spheroids as n becomes much larger than 1.5.

$$\rho_p = \frac{\rho_0}{D_{rel}^n} \tag{6.2}$$

Goodall et al. [296] provides an overview of the two theories and in their studies, they were able to show the H-S and DEM models were consistent with closed-cell foam data for different metals and varying volume fraction porosity. Analogously, we make the assumption that the relative densities measured in our samples are entirely due to an isotropic distribution of porosity between sintered particles. Therefore, $V_p = 1 - D_{rel}$, where V_p is the volume fraction of porosity and D_{rel} is the relative fractional density. In both equations ρ_p and ρ_0 represent the resistivity of porous $Sm_2(Co, Fe, Cu, Zr)_{17}$ and solid $Sm_2(Co, Fe, Cu, Zr)_{17}$ respectively. The solid resistivity of $Sm_2(Co, Fe, Cu, Zr)_{17}$ is taken as $90\,\mu\Omega\,cm$ [295] and the solid density as $8.4\,g/cm^3$ [131, 292].

The data in figure 6.15 generally lie just above the H-S lower bound (solid line), although for a couple of specimens (highlighted by red dashed circle), the experimental data is just lower than the predicted minimum resistivity. This is also the

true for the DEM model where n = 1.50, whereas for n > 1.50, the majority of porous specimens have lower resistivity than predicted by the model. The best fit for specimens with relative density between 88% and 90% is a DEM model which assumes spherical pores. Spherical pores could form in sub-optimal processing where the majority of mass-transfer during sintering occurs at the surface of the particles, resulting in spherical pores and low densities. For the single low-density data point, the best DEM model fit is one that assumes prolate spheroid pores (n > 1.5). In this scenario, very little sintering has occurred during the SPS process at 800 °C and has resulted in very irregular pore geometries.

Earlier in the chapter, SEM imaging showed the microstructure of a sample with relative density around 90% contained a large volume fraction of regions of un-sintered $Sm_2(Co, Fe, Cu, Zr)_{17}$ powders. The un-sintered regions contain powder particles in partial-contact with one another, which likely provide a path of electrical conduction, which is much different to the assumption in the H-S and DEM models, which assume ideal, electrically insulating pores or inclusions. Therefore, these model assumptions are not entirely representative of our experimental microstructure and could explain why the resistivity is lower than expected in the low density specimens. However, the overall data trend between resistivity and porosity in the experimental data was consistent with the overall trends of the studied models.

6.6 Magnetic characterisation and properties

6.6.1 Magnetic alignment

A significant aspect of permanent magnet processing is the alignment of individual magnetic grains such that their magneto-crystalline easy-axes (in the case of uniaxial systems; the c-axis) are orientated parallel to another. This has the effect of maximising the remanence and energy product of a permanent magnet material [28, 210, 299]. In powder sintered magnets; the conventional method is to align the powders while encased in a mould using a DC magnetic field (typically 2 T to 3 T) or a pulsed field (of the order 7 T to 10 T) [26]. Ideally, all magnetic grains are perfectly aligned within a hard magnetic material with coercivity, $H_c > 0.5J_r$, and the remanent polarisation, J_r, is thus equal to the saturation polarisation, J_s, ($J_r/J_s = 1$). Under this condition, the demagnetisation curve in the first and second quadrant of the hysteresis loop is a straight line, parallel to the horizontal axis until the coercivie field is reached [1]. Alternatively, If there is a random distribution of non-interacting magnetic grains, $J_r/J_s = 0.5$ [26, 299]. If a Gaussian distribution of easy c-axis is assumed with the material with respect to a texture axis, the projection of the polarisation vector can be expressed as an average deviation, $\bar{\theta}$, from the

texture axis, $J_r = J_s \cos\bar{\theta}$. Therefore, the degree of alignment can approximately be defined either as the ratio of the polarisation or as the average deviation angle [26, 299, 300].

$$\frac{J_r}{J_s} = \cos\bar{\theta} \tag{6.3}$$

For our study, several specimens received powder alignment of the c-axes in the axial direction either by a 2.5 T pulsed field or a 0.3 T DC electromagnetic field before SPS. To further explore the pulsed field method of powder alignment, the number of pulses applied was also investigated. Following alignment, the $Sm_2(Co, Fe, Cu, Zr)_{17}$ powders of average particle size of 5 µm were cold-pressed and sintered by SPS under standard processing parameters. Magnetic measurements were made using a Magnet-Physik DC hysteresisgraph and all specimens were magnetised before measurement using a 3.5 T pulsed field.

To quantify the alignment effect, the degree of alignment, J_r/J_{max} was calculated using equation 6.3. J_{max} is the maximum polarisation value reached in the first quadrant of the hysteresis loop. If a sufficiently large field is applied, then $J_{max} = J_s$. Due to changes in the standard operating procedure used for the hysteresisgraph equipment over the course of the project, the $Sm_2(Co, Fe, Cu, Zr)_{17}$ specimens either experienced an approximate maximum field of $300\,kA\,m^{-1}$ or $1200\,kA\,m^{-1}$. While the difference in the applied fields is quite large, this did not correspond to a significant difference in the J_{max} values measured in the SPS processed magnets in their current state. The difference in J_{max} was less than the 5% uncertainty associated with the hysteresisgraph measurement. It is noted that certain specimens included in table 6.3 have received a full $Sm_2(Co, Fe, Cu, Zr)_{17}$ heat treatment and are denoted with an asterisks. While the heat treatment affects the magnetic properties, it should not affect the degree of alignment, which is a ratio of the saturation and remanent polarisation. All magnets measured by hysteresisgraph received identical pulse magnetisation before measurement.

Table 6.3 lists the type of alignment method used for each sample, as well as the relative density, polarisation ratio and average deviation angle. Anisotropic and isotropic $Sm_2(Co, Fe, Cu, Zr)_{17}$ samples produced by conventional sinter methods are also included for comparison with commercial magnets. These specimens were provided by Arnold Magnetic technologies and are identified with the prefix 'ARN'.

The results in table 6.3 show pulsed or DC magnetic fields applied in the axial direction significantly align the powders of $Sm_2(Co, Fe, Cu, Zr)_{17}$ and induce texture

Sample ID	**Powder alignment**	J_r/J_{max}
Pulsed field (2.5 T)		
1-03	Axial (pulsed once)	0.75 ± 0.05
1-04	Axial (pulsed twice)	0.69 ± 0.05
1-28*	Axial (pulsed thrice)	0.83 ± 0.06
DC Electromagnetic field (0.3 T)		
1-29*	Axial	0.81 ± 0.06
ARN-R28*	Axial (>0.65 T)	0.99 ± 0.07
No powder alignment		
1-01	Isotropic	0.65 ± 0.05
1-05	Isotropic	0.61 ± 0.04
1-06	Isotropic	0.61 ± 0.04
1-07	Isotropic	0.60 ± 0.04
1-08	Isotropic	0.65 ± 0.05
1-09	Isotropic	0.66 ± 0.05
1-11	Isotropic	0.60 ± 0.04
1-12	Isotropic	0.61 ± 0.04
1-18	Isotropic	0.59 ± 0.04
1-19	Isotropic	0.57 ± 0.04
1-20	Isotropic	0.63 ± 0.05
1-30	Isotropic	0.58 ± 0.04
1-31	Isotropic	0.53 ± 0.04
1-32	Isotropic	0.54 ± 0.04
1-33	Isotropic	0.62 ± 0.04
ARN4*	Isotropic	0.52 ± 0.04
ARN5*	Isotropic	0.52 ± 0.04

Table 6.3: Quantification and comparison of the degree of alignment in $Sm_2(Co, Fe, Cu, Zr)_{17}$ samples that have undergone different methods of powder alignment before processing by SPS. Asterisks denotes samples which have also undergone a standard $Sm_2(Co, Fe, Cu, Zr)_{17}$ heat-treatment. Relative density is calculated using solid density $8.4\,g/cm^3$ [131, 292]

in the consolidated material. The best degree of alignment, approximately 0.82 and which corresponds to an average deviation angle of 35°, are observed in samples 1-28, which was pulsed with ≈2.5 T magnetic field three times, and sample 1-29, whose powders were aligned by 0.3 T of DC electromagnetic field over a minute. Repeated pulses show varying results, with the degree of alignment falling then increasing. This may due to how the powder was packed within the volume inside the graphite mould. Sample 1-04 may have been affected by a higher degree of powder packing, removing the freedom to allow reorientation of the particles, and the magnetic fields used were not large enough to overcome the frictional forces. Powder characterisation identified irregularly shaped larger particles, approximately 10 µm in size, surrounded by smaller, spherical 1 µm sized crystallites. During application of the magnetic field, the random orientation of the amalgamated large and small crystallites may mean not all crystallites can reorientate in the direction of the applied field, either through frictional forces or due to bonding with the larger crystallite, and this could affect the repeatability of the pulse alignment.

The inferred degree of alignment in the commercial ARN-R28 magnet was far superior to those achieved by the methods available in this project. The ARN-R28 magnet is aligned with a DC electromagnetic field of at least 0.65 T. As the ARN-R28 magnet has been produced from similar sized, jet milled $Sm_2(Co, Fe, Cu, Zr)_{17}$ powders, the only variable between our specimens and the comparison magnet is the strength of magnetic field applied. It is clear that to achieve the same degree of alignment in the SPS processed $Sm_2(Co, Fe, Cu, Zr)_{17}$ magnets, much larger magnetic fields are required in both pulsed and DC electromagnetic fields. Liu recommends DC magnetic fields of 2 T to 3 T or pulsed fields of 7 T to 10 T to ensure a high degree of alignment and are fields typically used within commercial magnet production [26].

The average degree of alignment in the SPS processed $Sm_2(Co, Fe, Cu, Zr)_{17}$ magnets which did not receive powder alignment was 0.60/pm0.04. Deemed 'isotropic', after processing by SPS there is evident some degree of alignment within these magnets as $J_r/J_{max} > 0.5$. Unexplanable by remanence enhancement as the powder/grains, measured between 5 µm to 10 µm, are too large for such effects, of which are associated with nanocrystalline grains [44]. The isotropic ARN magnets were processed by pressure-less sinter method and show a degree of alignment much closer to 0.5, as would be expected of an isotropic magnet. Deformation or rearrangement of the granular structure through the application of pressure may explain the observed texture in the isotropic powder and SPS processed $Sm_2(Co, Fe, Cu, Zr)_{17}$ magnets. Study of the SPS processed magnet microstructure

saw no clear evidence for grain deformation or elongation, which is the cause of texture in hot deformation techniques [49, 50]. The application of pressure to the powders before and during SPS process cause particle slide, rearrangement and rotation [153], which may favourably align the irregularly shaped particles and their c-axis with the pressing direction. Future study may provide more insight into the role of pressure on magnetic alignment in the SPS process, but for now it is evident from our study there is consistent texture, albeit slight, induced even within our 'isotropic' SPS processed $Sm_2(Co, Fe, Cu, Zr)_{17}$ magnets.

6.6.2 Magnetic characterisation

The state of the $Sm_2(Co, Fe, Cu, Zr)_{17}$ magnets presented in this chapter are after processing by SPS but before the multi-stage heat heat treatment. The material has been shown to primarily consist of the 2:17R phase and coercivity is expected to be under-developed without the precipitated cellular and lamellar nanostructure [19, 76, 82]. However, magnetic characterisation is still useful for comparison between low and full density specimens after processing by SPS and to document changes in the magnetic properties before and after heat treatment. A study of the coercivity mechanism of the magnets before and after heat treatment can also indirectly evidence of microstructure evolution.

Each SPS processed $Sm_2(Co, Fe, Cu, Zr)_{17}$ specimen has been characterised by their demagnetisation curve using a Magnet-Physik DC hysteresisgraph after magnetisation by a 3.5 T pulsed field. The remanent polarisation, J_r, coercive force, bH_c, intrinsic coercivity, iH_c and energy product, $(BH)_{max}$ are listed in table 6.4.

The reported data in table 6.4 confirms the coercivity, either the coercive force from a $\vec{B} - \vec{H}$ demagnetisation curve or the intrinsic coercivity from a $\vec{M} - \vec{H}$ demagnetisation curve, for the SPS processed magnets are under-developed compared to commercial $Sm_2(Co, Fe, Cu, Zr)_{17}$ magnets. Coey defines the lower bound of intrinsic coercivity for permanent magnet materials as $400\,kA\,m^{-1}$ [1] and all specimens listed in table 6.4 are below $100\,kA\,m^{-1}$. The $Sm_2(Co, Fe, Cu, Zr)_{17}$ magnets will develop into permanent magnets after an appropriate heat treatment [76].

The effect of powder alignment in the axial direction is seen in the remanence values of samples 1-03 and 1-04, with both samples measuring the largest J_r values. Sample 1-03, which only received powder alignment from a single 2.5 T pulsed magnetic field recorded the largest remanent polarisation of 0.58 T. The remanence values for the magnetically 'isotropic' samples in table 6.4 range approx-

Sample ID	Powder alignment	J_r (T)	bH_c (kA m^{-1})	iH_c (kA m^{-1})	$(BH)_{max}$ (kJ/m^3)	% relative density
1-03	Pulsed-axial (once) (2.5 T)	0.58 ± 0.03	46.66 ± 2.33	49.54 ± 2.48	10.70 ± 0.54	92.72
1-04	Pulsed-axial (twice) (2.5 T)	0.46 ± 0.02	54.27 ± 2.71	59.88 ±2.99	8.00 ± 0.40	95.34
1-01	Isotropic	0.35 ± 0.02	72.50 ± 3.63	87.10 ± 4.36	7.80 ± 0.39	91.77
1-05	Isotropic	0.37 ± 0.02	74.00 ± 3.70	89.92 ± 4.50	8.70 ± 0.44	87.93
1-06	Isotropic	0.36 ± 0.02	73.13 ± 3.66	89.52 ± 4.48	8.20 ± 0.41	87.68
1-07	Isotropic	0.35 ± 0.02	69.61 ± 3.48	84.49 ± 4.23	7.75 ± 0.39	89.52
1-08	Isotropic	0.33 ± 0.02	71.46 ± 3.57	86.74 ± 4.34	7.20 ± 0.36	90.83
1-09	Isotropic	0.34 ± 0.02	72.67 ± 3.63	88.27 ± 4.44	7.45 ± 0.45	93.01
1-11	Isotropic	0.40 ± 0.02	57.53 ± 2.88	65.04 ± 3.25	7.90 ± 0.40	99.05
1-12	Isotropic	0.41 ± 0.02	57.44 ± 2.88	64.86 ± 3.24	8.05 ± 0.41	99.27
1-18	Isotropic	0.39 ± 0.02	54.35 ± 2.92	61.62 ± 3.35	7.05 ± 0.43	99.48
1-19	Isotropic	0.31 ± 0.01	48.91 ± 2.45	57.30 ± 2.87	4.90 ± 0.25	99.45
1-20	Isotropic	0.37 ± 0.02	60.20 ± 3.01	68.80 ± 3.44	7.10 ± 0.36	99.43
1-30	Isotropic	0.39 ± 0.02	49.80 ± 2.49	55.70 ± 2.79	6.70 ± 0.34	99.59
1-31	Isotropic	0.22 ± 0.01	56.60 ± 2.83	76.70 ± 3.84	3.40 ± 0.17	72.50
1-32	Isotropic	0.19 ± 0.01	46.10 ± 2.31	61.60 ± 3.08	2.40 ± 0.12	73.71
1-33	Isotropic	0.36 ± 0.02	58.60 ± 2.93	66.80 ± 3.34	6.90 ± 0.35	99.83

Table 6.4: Magnetic properties of SPS processed $Sm_2(Co, Fe, Cu, Zr)_{17}$, as measured by Hysteresisgraph. Relative density is calculated using solid density 8.4 g/cm^3 [131, 292].

imately from 0.3 T to 0.4 T. Remanence is typically linked to the density of the specimen and this is most obvious when comparison is made with the lowest density samples (1-31 and 1-32) and the samples with near-theoretical densities (>98%).

Figure 6.16 plots the relationship between the remanent polarisation and the relative density of the SPS processed $Sm_2(Co, Fe, Cu, Zr)_{17}$ magnets. As indicated by the data in table 6.4, there is a trend of increasing remanent polarisation as density increases in the isotropic samples. Highlighted in figure 6.16 is an outlier to this trend. The inset shows the J_r values of specimens at near-theoretical density (>99% relative density).

The largest remanence, $J_r = 0.577$ T, is measured in sample 1-03, whose powders were aligned by a single pulse of 2.5 T. The two powder aligned specimens were processed by non-optimised parameters and, If the trend for increasing remanence with density was followed, the remanent polarisation of the axially aligned SPS processed could be even greater than that reported in figure 6.16.

The intrinsic coercivity and relative density relationship is shown in figure 6.17. The relationship between the coercive force and density is omitted because it is effectively the same trend as displayed for the intrinsic coercivity and density, albeit at slightly reduced values.

The intrinsic coercivities for the SPS processed $Sm_2(Co, Fe, Cu, Zr)_{17}$ magnets are comparable to those reported in 'as-cast' states [82, 90] and well below those

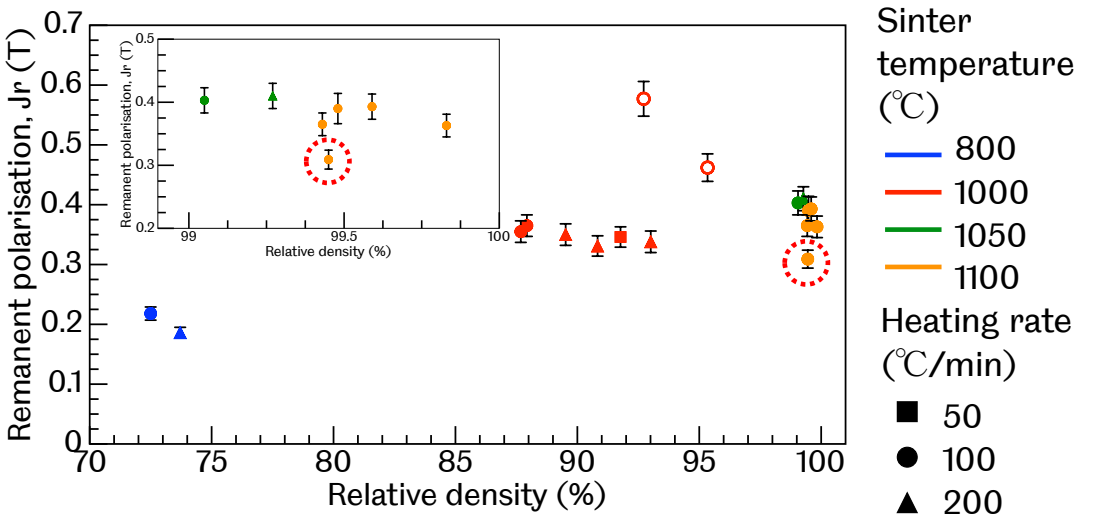

Figure 6.16: The relationship between polarisation and density for SPS processed $Sm_2(Co, Fe, Cu, Zr)_{17}$ in the as-processed state. Processing parameters used for each sample data point are represented by colour and shape as indicated in the key. Filled symbols represent samples with no powder alignment, open symbols have undergone powder alignment in the axial direction. Inset shows magnification of data points close to full density. Relative density is calculated using solid density $8.4\,g/cm^3$[131, 292].

observed for hard magnetic materials. In this state, figure 6.17 shows a trend of coercivity increasing as the density decreases down to 85% relative density in the 'isotropic' specimens. As density decreases, porosity increases within the magnet and these features can act as pinning sites for domain walls and increase the coercivity. However, this trend does not continue to the lowest density specimens and the intrinsic coercivity reduces back to values in the range of $60\,kA\,m^{-1}$ to $80\,kA\,m^{-1}$. The size and shape of defects in the microstructure are treated by a statistical description of domain wall pinning by Kronmüller and the greater volume fraction or size of pores in the lowest density specimens may be less effective at pinning domain walls than the porosity within the samples of relative density around 90%. There are also factors of increased self-demagnetising fields in the low density specimens, which provide an increased demagnetisation at lower applied fields compared to the high density specimens. Finally, the validity of the measurements for these low density specimens, which has not been verified, and how they hold up at low densities against the strong reversal fields of the hysteresisgraph.

The coercivity mechanism of a permanent magnet can indirectly be observed through the initial, or virgin, magnetisation curve of a thermally demagnetised magnet [21, 301]. Therefore, evidence for increased pinning sites in the higher

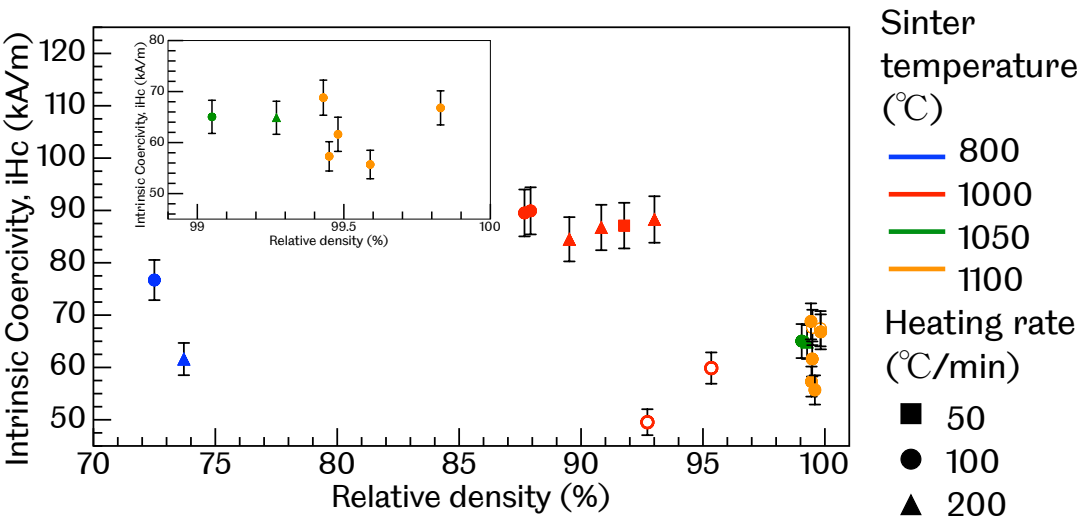

Figure 6.17: The relationship between the intrinsic coercivity for $Sm_2(Co, Fe, Cu, Zr)_{17}$ in the as-processed state. Processing parameters used for each sample data point are represented by colour and shape as indicated in the key. Filled symbols represent samples with no powder alignment, open symbols have undergone powder alignment in the axial direction. Inset shows magnification of data points close to full density. Relative density is calculated using solid density $8.4\,g/cm^3$ [131, 292].

porosity samples can be shown via changes in initial magnetisation of the magnets. Two samples (1-32 and 1-33) were magnetised by hysteresisgraph from their thermally demagnetised state after processing by SPS. Sample 1-32, one of the most porous samples produced by SPS, with a relative density of 73.71%, has comparable intrinsic coercivity to sample 1-33, has been produced under optimal processing parameters and has a measured relative density of 99.83%. Comparison of their initial magnetisation curve and gradients indicate whether the magnet's coercivity mechanism is nucleation-based (large gradient) or pinning-based (small gradient).

Figure 6.18 plots the measured initial magnetisation curves and, in the inset; the change in gradient of the two curves respectively. Here it is shown the porous sample 1-32 has a much lower gradient than the fully dense sample 1-33. Greater magnetic fields are required for sample 1-32 to reach the same level of magnetisation as 1-33, as domain walls are pinned during magnetisation. Conversely, the fully dense sample 1-33 is mostly free of porosity and magnetises relatively easily at much lower fields. The greater presence of porosity correlates with the increased pinning field within the low density $Sm_2(Co, Fe, Cu, Zr)_{17}$ magnet and if porosity is acting to pin domain walls, this could explain the higher coercivities of the magnets with relative densities 10% lower than the near-theoretical density magnets. However,

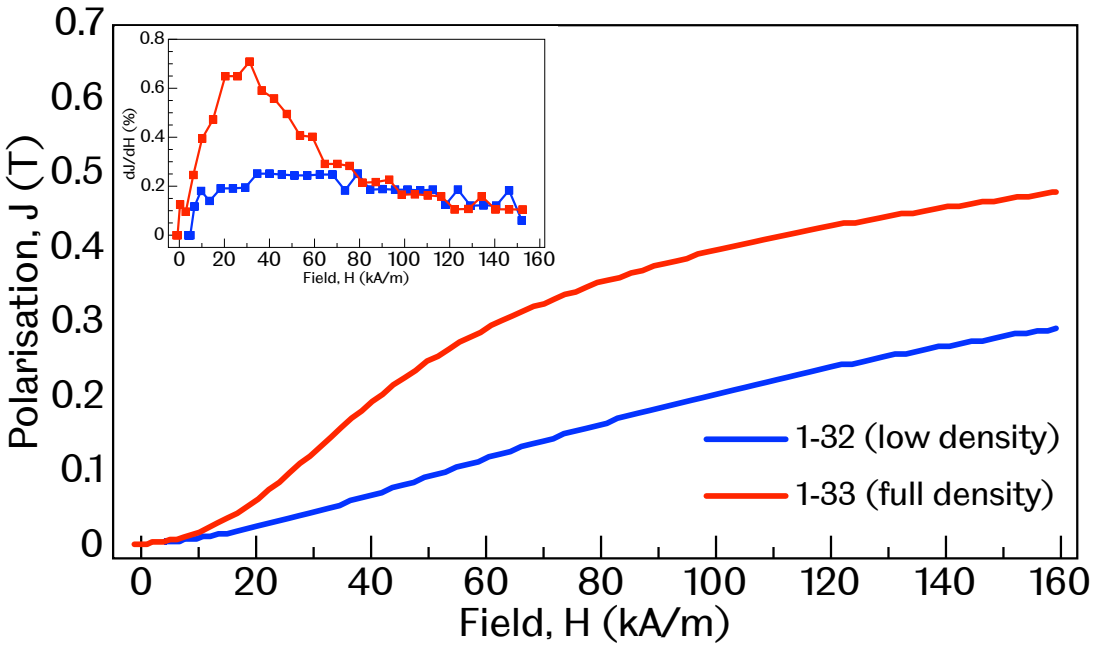

Figure 6.18: Initial magnetisation curves of as-processed $Sm_2(Co, Fe, Cu, Zr)_{17}$ samples 1-32 and 1-33. Inset show gradients of respective initial magnetisation curves.

the increased pinning effect does not always equate to higher coercivities, as is evident in the lowest density magnets, where other factors such as mechanical integrity and self-demagnetising fields also affect the measured coercivity.

The coercivites of the axial powder aligned $Sm_2(Co, Fe, Cu, Zr)_{17}$ samples are significantly lower than their 'isotropic' counterparts. The axial aligned magnets (red circles, unfilled) experience stronger self-demagnetising stray-fields than their isotropic counterparts [246, 302], which reduces the nucleation field.

The remanence and coercivity combine to produce the energy product, $(BH)_{max}$, which is the maximum product of the magnetic induction, $\vec{B}$, and the applied field, $\vec{H}$. Thus far, it has been shown in the 'isotropic' $Sm_2(Co, Fe, Cu, Zr)_{17}$ magnets that the remanence increased density, while the coercivity decreased as density approached theoretical. As a result, figure 6.19 shows the trend of the energy product with density to be mostly stable above 85% relative density, although a previously identified outlier (sample 1-19) is highlighted. The low density specimens, samples 1-31 and 1-32 had lowest remanence and average coercivity and thus have the lowest energy product. The largest energy product is reported in the axially aligned sample 1-03, which also had the biggest remanence. This shows the strong relationship between energy product and remanence, where sample 1-03 had a significantly lower coercivity than equivalently dense 'isotropic' magnets, but still

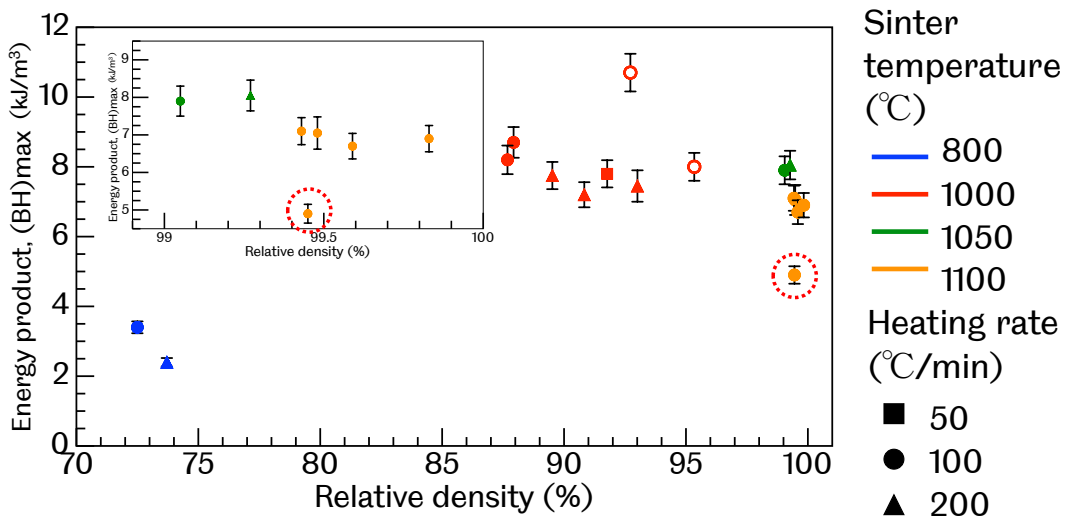

Figure 6.19: The relationship between the energy product for $Sm_2(Co, Fe, Cu, Zr)_{17}$ in the as-processed state. Processing parameters used for each sample data point are represented by colour and shape as indicated in the key. Filled symbols represent samples with no powder alignment, open symbols have undergone powder alignment in the axial direction. Inset shows magnification of data points close to full density. Relative density is calculated using solid density $8.4\,g/cm^3$ [131, 292].

has a much larger energy product.

Demagnetisation curves for selected SPS processed $Sm_2(Co, Fe, Cu, Zr)_{17}$ are shown in figure 6.20. The biggest effect on the demagnetisation curve shape is the alignment of powders in the axial direction before the SPS process. Sample 1-03 was aligned in the axial direction before the SPS process and shows a much more 'square' demagnetisation curve, compared to the other specimens which are either received no powder alignment. The demagnetisation curves for these specimens are described as approximately linear and characteristic of permanent magnets with zero or partial texture. While the differences in remanent polarisation and coercivity are evident in relation to their respective densities, between the 'isotropic' specimens there is no effect on the demagnetisation curve shape.

6.7 Carbon uptake in SPS process

The SPS technique has thus far been show as a successful method to consolidate $Sm_2(Co, Fe, Cu, Zr)_{17}$ powders to full density in preparation for heat treatment. However, due to the necessity for both the mould and punches to be electrically conductive and mechanically strong at high temperatures, the material most commonly used is graphite. Similarly, to prolong die usage, a liner material is used

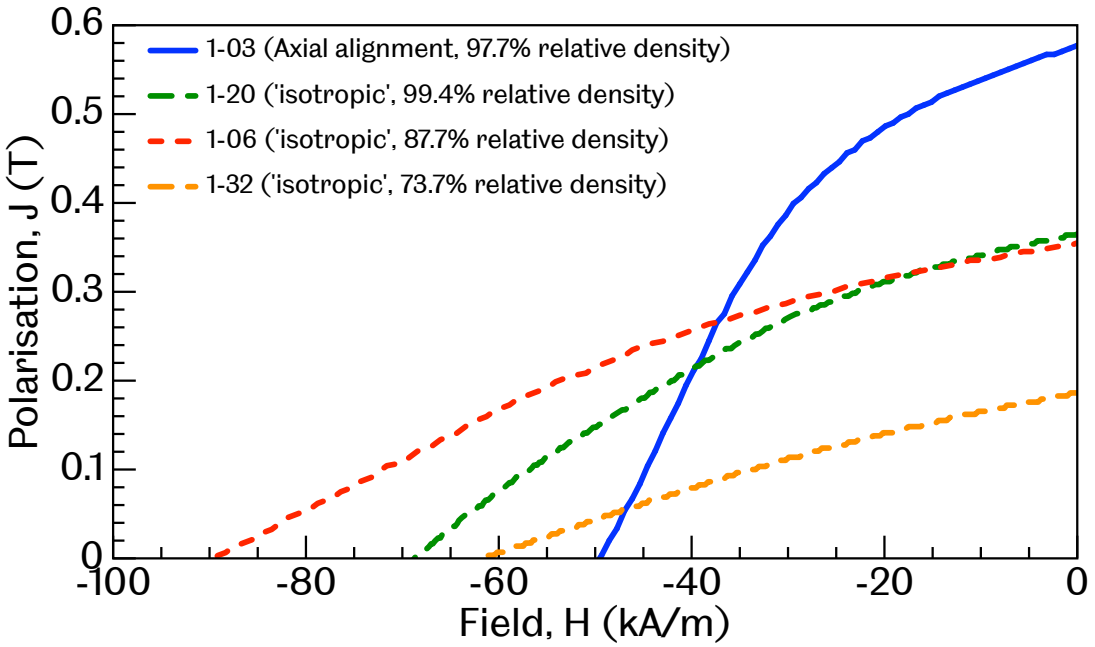

Figure 6.20: Second quadrant demagnetisation curves for as-SPS processed $Sm_2(Co, Fe, Cu, Zr)_{17}$ magnets, as measured by hysteresisgraph.

which is also a graphite material. Powders may therefore potentially uptake carbon through contact with the graphite foil/mould at high processing temperatures. For $Sm_2(Co, Fe, Cu, Zr)_{17}$, the hold temperature is optimised for density between 1050 °C to 1100 °C. However, the SPS process has a comparatively short processing cycle and the dwell time used in this study was 5 minutes. Therefore, it is not clear if carbon is taken up during the SPS process. If it is, then it raises further questions as to how much carbon may ingress and where the carbon is located/interacting within the microstructure of the $Sm_2(Co, Fe, Cu, Zr)_{17}$ material. The literature review in chapter 2 highlighted other studies of carbon uptake in SPS processed materials, in which carbon was detected at the material surfaces and in the form of carbides within the volume [45, 116–120]. For $Sm_2(Co, Fe, Cu, Zr)_{17}$ magnets processed by other sintering techniques, it was found for carbon concentrations of 0.2 wt.%, the magnetic properties were significantly affected; reducing the coercivity by half and disturbing the demagnetisation curve shape [121, 122].

To better understand the SPS process, the results of an investigation into carbon contamination of $Sm_2(Co, Fe, Cu, Zr)_{17}$ are presented. EPMA has been used to visualise, via elemental distribution maps, the spatial distribution of carbon at the surface of a SPS processed $Sm_2(Co, Fe, Cu, Zr)_{17}$ magnet and is compared with a corresponding map from a conventional sinter processed $Sm_2(Co, Fe, Cu, Zr)_{17}$ mag-

net. LECO-C has been used to quantify the weight concentration of carbon in the sample middle and edges of these two specimens.

The SPS magnet was processed using the following parameters: 1100 °C hold temperature, 100 °C heating rate, 51 MPa hold pressure and 5 minute dwell time. The processing of the conventional sinter processed $Sm_2(Co, Fe, Cu, Zr)_{17}$ specimen, provided by Arnold Magnetic technologies, was likely above 1200 °C and for approximately an hour. It has also not been in direct contact with graphite during the sinter process. Sectioned samples were mounted in Field's metal (32.5wt% Bi, 51wt% In and 16.5wt% Sn, Alfa Aesar, UK) rather than Bakelite to reduce ambiguity in carbon detected at the surface edges of the mounted specimen. A full description of the methodology used is described by Mackie et al. [303]. Imaging and elemental maps were performed by Dr. Gareth Hatton at Johnson-Matthey technology centre (Reading, England), using a Jeol JXA-8500F EPMA.

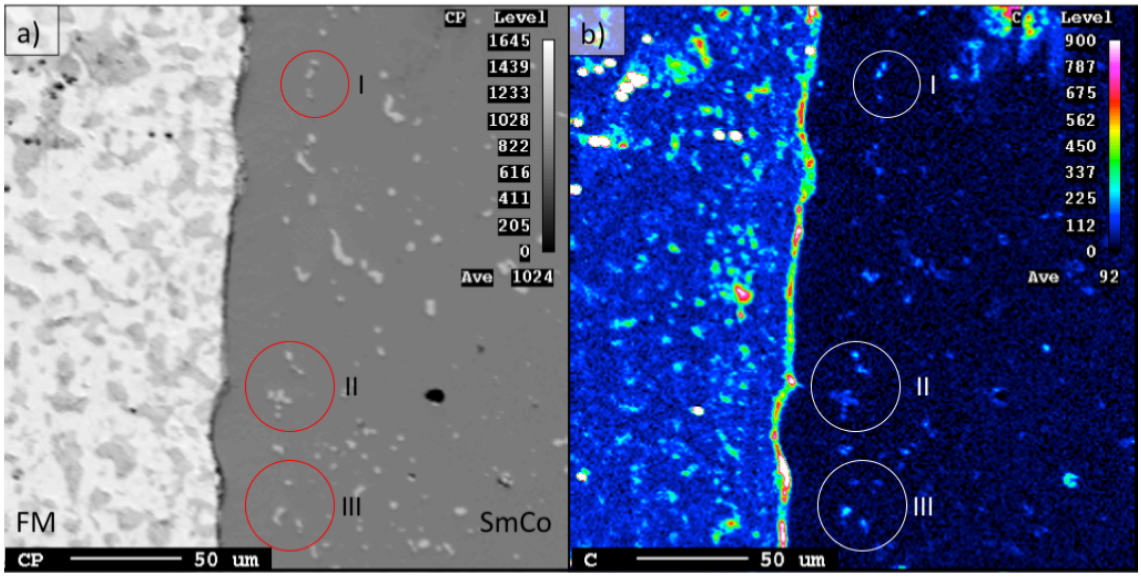

Figure 6.21: EPMA carbon map showing the spatial distribution of carbon in a SPS processed $Sm_2(Co, Fe, Cu, Zr)_{17}$ sample. 'SmCo' indicates the $Sm_2(Co, Fe, Cu, Zr)_{17}$ material, 'FM' indicates the Field's metal region. Also highlighted, in both the BS image and EPMA map, are features in the microstructure which have elevated carbon levels in comparison to the background and are possibly carbides of Sm.

Figure 6.21 a) shows the BS SEM image of the SPS processed $Sm_2(Co, Fe, Cu, Zr)_{17}$ at the edge of the specimen (dark grey region, labelled 'SmCo') and the Field's metal (lightest region, labelled 'FM'). Figure 6.21 b) shows the corresponding EPMA carbon map. The scale bar on the right of figure 6.21 b) relates the intensity of the carbon detected to colour: white and red are relatively high levels of carbon, dark blue and black are low levels of carbon.

The carbon map shows a continuous and mostly uniform distribution of carbon along the boundary between the Field's metal and $Sm_2(Co, Fe, Cu, Zr)_{17}$ specimen. The ingress of the carbon is approximately 10 µm. Comparative maps taken at different boundary locations around the sample showed similar distribution of carbon at the FM-SmCo boundary, although sometimes less uniform and, very rarely, discontinuous. Examples of inhomogeneity in the $Sm_2(Co, Fe, Cu, Zr)_{17}$ microstructure are highlighted as I, II and III in Figure 6.21, which show slightly elevated levels of carbon well beyond the material surface. The EPMA elemental maps are interpolated to give a smoother image, free of pixellation. While this is ideal for presentation, it also has the undesired effect of making small anomalies appear larger. There is correlation of these features with elevated Sm in corresponding element maps, which explain their light contrast in the BS figure 6.21. If these features are examples of samarium carbide (Sm_3C), carbon could remove both samarium and zirconium from the main phase, which would have a disruptive effect on the precipitation of the cellular nanostructure during the heat treatment process, and in turn significant effects on the magnetic properties [121]. Also seen in figure 6.21 b) is an irregular carbon feature at the top of the $Sm_2(Co, Fe, Cu, Zr)_{17}$ carbon map, which is attributed to be a remnant of dirt/grease. This feature does not correspond to anything within the comparative BS SEM image and similar anomalous features were not observed in other maps taken.

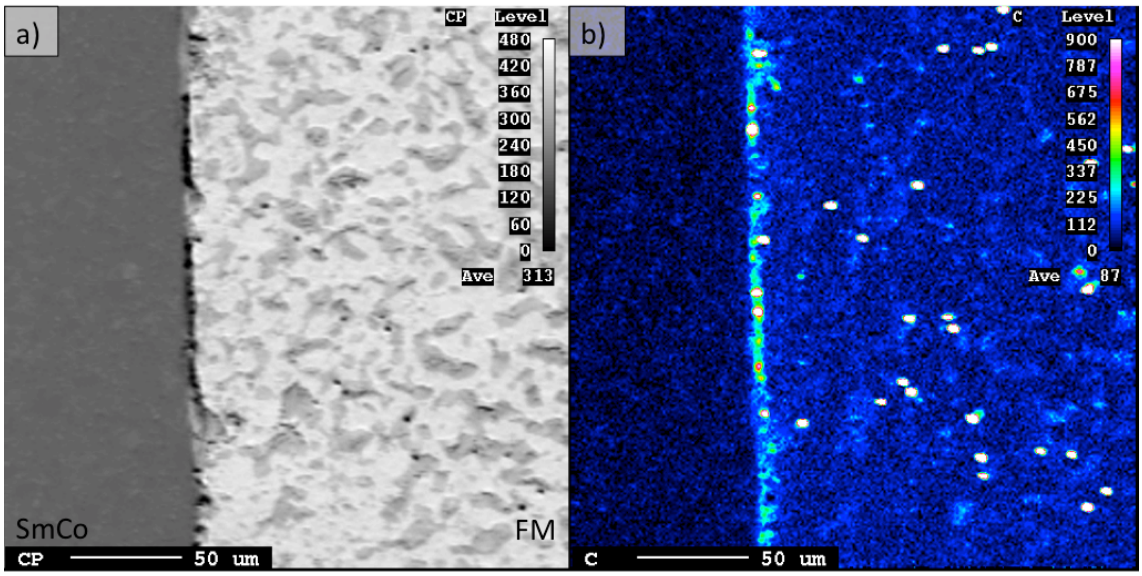

Figure 6.22: EPMA carbon map showing the spatial distribution of carbon in a conventional sinter processed $Sm_2(Co, Fe, Cu, Zr)_{17}$ sample. 'SmCo' indicates the $Sm_2(Co, Fe, Cu, Zr)_{17}$ material, 'FM' indicates the Field's metal region.

Figure 6.22 shows the BS SEM a) and EPMA carbon map b) for the con-

ventional sinter processed $Sm_2(Co, Fe, Cu, Zr)_{17}$ sample. Again, the Field's metal region is labelled 'FM' and the $Sm_2(Co, Fe, Cu, Zr)_{17}$ region 'SmCo'. Compared with the SPS processed sample, carbon is almost exclusively confined to the $Sm_2(Co, Fe, Cu, Zr)_{17}$/Field's metal boundary line and very little, if any, extends into the $Sm_2(Co, Fe, Cu, Zr)_{17}$ region. Beyond the surface, the $Sm_2(Co, Fe, Cu, Zr)_{17}$ microstructure appears more homogeneous than the SPS processed sample, with no features of elevated carbon observed in the 'SmCo' region in Figure 6.22 b).

Band profiles were taken to complement the EPMA carbon maps and quantify the depth of carbon uptake. 120 µm wide band scans, with 1 µm step size, were performed across the $Sm_2(Co, Fe, Cu, Zr)_{17}$ surface to a depth of 160 µm. Figure 6.23 shows the measured carbon levels for both samples up to a depth of 35 µm. The background carbon levels are approximately equal for both samples beyond 35 µm.

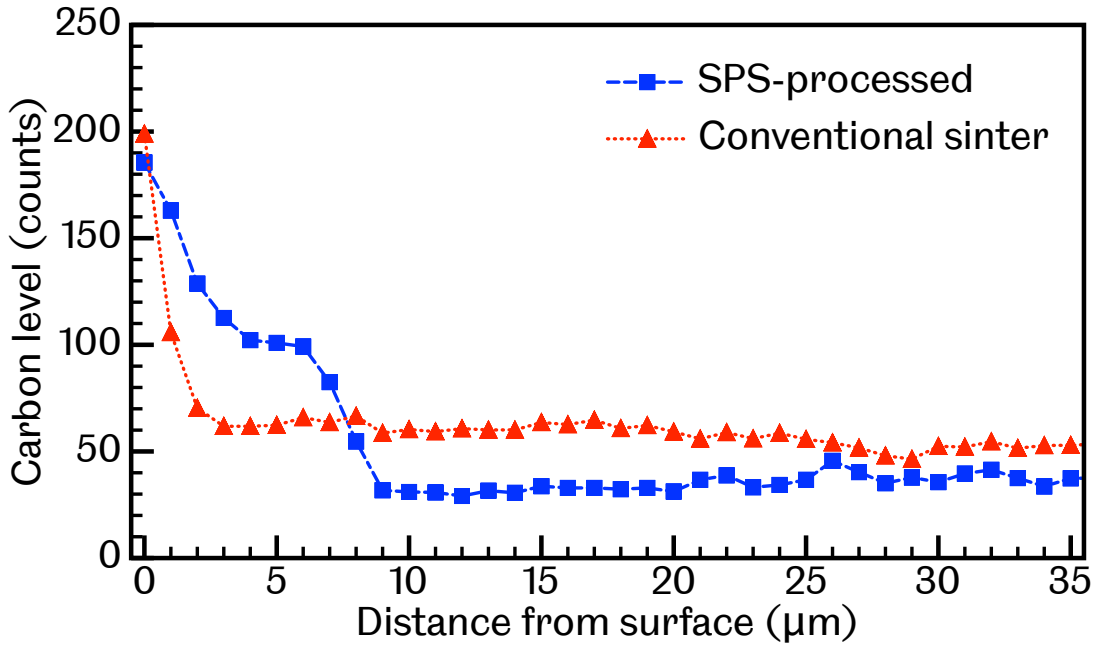

Figure 6.23: Band profile, with 1 µm step size across Field's metal and $Sm_2(Co, Fe, Cu, Zr)_{17}$ boundary for both SPS and conventional sinter processed samples.

Initially, the same levels of carbon are detected in both types of processed $Sm_2(Co, Fe, Cu, Zr)_{17}$ samples, which is a remnant of residual carbon along the FM-SmCo surface boundary. Beyond the boundary and into the sample, carbon in the SPS sample is at higher levels above the background to a depth of 9 µm (HWHM = 7 µm) from the surface. The small inhomogeneities of elevated carbon observed in the SPS sample microstructure are not evidenced in the band scan.

Comparatively, carbon reduces to background levels more rapidly (HWHM = 3 µm) in the conventional sinter processed $Sm_2(Co, Fe, Cu, Zr)_{17}$ sample. The powder material in pressure-less sinter method is not in direct contact with solid carbon during sintering, as is the case with the SPS processed material. The source of elevated surface carbon in the conventional sinter sample could be due to residual polishing material (SiC or diamond) or from oil-based lubricants used to remove the compact after pressing prior to sintering. The measured background level of carbon is marginally higher in the conventional sinter processed sample, but in both profiles, the background levels are consistent to the maximum examined depth of 160 µm.

To further quantify and compare the amount of carbon present at the surface and within the interior of the $Sm_2(Co, Fe, Cu, Zr)_{17}$ samples processed by SPS and by conventional sinter methods, a thermal decomposition carbon analysis technique was used. LECO-CS 844 (AMG-S, Rotherham, England), henceforth referred to as LECO-C, is a technique which relates the amount of carbon present in the sample by thermal decomposition and measurement of the CO_2 levels by infra-red absorption [282]. The inferred carbon content is provided as a weight percentage, allowing comparison to the studies of residual and added carbon in $Sm_2(Co, Fe, Cu, Zr)_{17}$ by Tien et al. [121] and Gong [122].

Segments from the SPS and conventional sinter processed $Sm_2(Co, Fe, Cu, Zr)_{17}$ samples were sectioned at the surface and in the centre of the specimens. The internal segments also underwent extra surface polishing on their top and bottom faces, removing approximately 0.5 mm of material from each surface, to remove all surfaces with contact to the graphite foil or mould wall. The results of the LECO-C analysis for this initial study are shown in figure 6.24.

The level of carbon in the SPS processed $Sm_2(Co, Fe, Cu, Zr)_{17}$ sample show higher concentrations in the surface segment compared to the internal segment, although with the uncertainties of the measurement taken into account they are not significantly different. For the conventional sinter processed $Sm_2(Co, Fe, Cu, Zr)_{17}$ sample segments, the concentration of carbon present in both the surface and interior segments are lower than the surface segment of the SPS processed sample. There is slight overlap with the uncertainties of the interior segment of the SPS sample, but combining all the evidence presented thus far; it is evident that the concentration of carbon in the SPS processed $Sm_2(Co, Fe, Cu, Zr)_{17}$ sample, especially at the surface, is higher than in the conventional sinter processed $Sm_2(Co, Fe, Cu, Zr)_{17}$ material. However, the measured carbon concentrations are in all the specimens are much smaller than 0.2 wt%, which was the concentration level

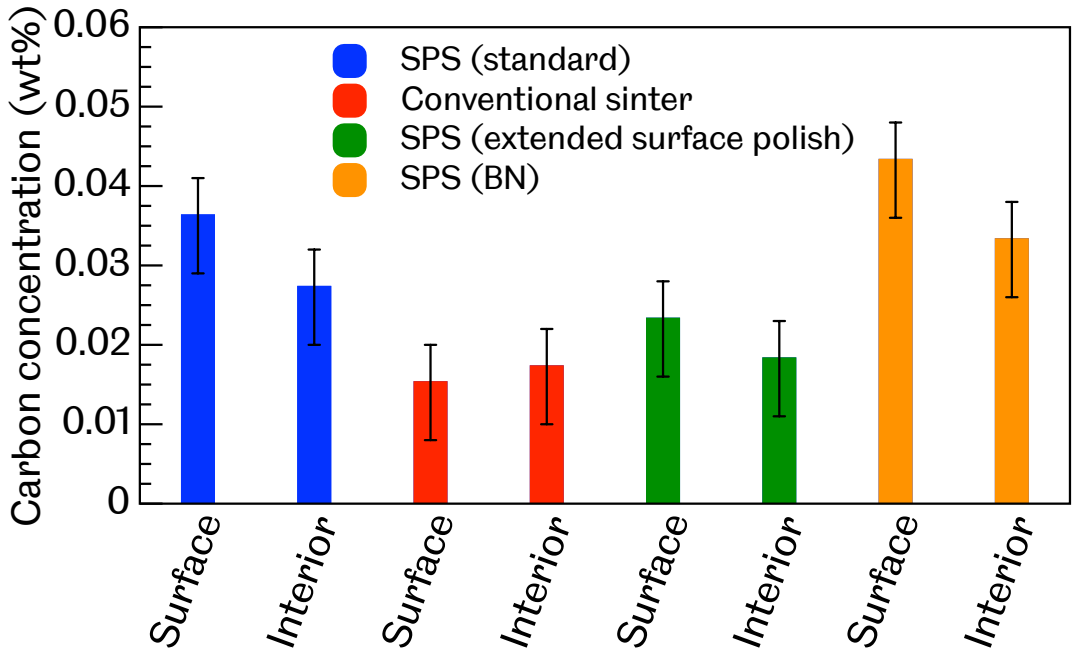

Figure 6.24: LECO-C analysis of surface and centre regions in SPS and conventional sinter processed $Sm_2(Co, Fe, Cu, Zr)_{17}$ samples. SPS (extended surface polish) has 100 µm of surface material removed. BN refers to Boron Nitride, which was applied to the inside of the graphite die mould. All SPS processed $Sm_2(Co, Fe, Cu, Zr)_{17}$ samples were produced under identical processing parameters.

reported to significantly affect the cellular nanostructure and magnetic properties of $Sm_2(Co, Fe, Cu, Zr)_{17}$ [121, 122]. The SPS processed $Sm_2(Co, Fe, Cu, Zr)_{17}$ magnets do measure elevated levels of carbon at their surfaces, however from the techniques used; the concentration of carbon is not expected to be severe enough to have a noticeable affect on the phase composition or magnetic properties over the processing cycle times studied. An extension of this work would require the utilisation of Transmission Electron Microscopy (TEM) to confirm any destructive effect on the cellular nanostructure at the surface of the SPS processed $Sm_2(Co, Fe, Cu, Zr)_{17}$ magnet.

A study of two different methods that could be incorporated into the SPS processing route to reduce or remove carbon contamination if elevated levels of surface carbon are undesired. One method explored is to remove the affected surface material. A standard SPS processed sample (1-18) was subjected to an extended surface polish on all faces, removing approximately 250 µm of material. This value was estimated via measurement of the specimen thickness before and after surface polish using digital callipers. An alternative method looked at creating a buffer between the $Sm_2(Co, Fe, Cu, Zr)_{17}$ powders and the graphite foil/mould.

Boron Nitride (BN) is used in the ceramics industry to coat moulds and is used as a lubricant due to its 'anti-stick' properties. It is also thermally and chemically resistant making it a potential 'buffer' material. Boron Nitride aerosol spray CC-18 (Combat, Saint-Gobain Ceramic Material, France) was applied to the outer and internal surfaces of the graphite foil, which was then added to line the interior of the graphite mould. $Sm_2(Co, Fe, Cu, Zr)_{17}$ powder was then processed under standard SPS conditions and subjected to a standard surface polish. As before, segmentations were taken at the surface and centres of the extended surface polish and BN samples and prepared in the same manner was previously reported.

The measured carbon concentrations by LECO-C technique are reported in figure 6.24. The extended surface polish of 250 µm of the SPS processed $Sm_2(Co, Fe, Cu, Zr)_{17}$ material removes the ingress of carbon and reduces the concentration of carbon to levels measured in conventionally processed magnets. If the SPS processed magnets were required to match the tolerances as those produced by conventional sinter methods, further work could investigate precisely how much material requires removal to match the carbon concentration of conventional sinter processed $Sm_2(Co, Fe, Cu, Zr)_{17}$.

A different outcome was obtained for the sample which explored BN as a buffer material to carbon uptake. The LECO-C analysis shows the carbon concentrations increased within the surface segments, or were at least comparable to the standard SPS processed material, which shows the 'buffer' effect was not effective at inhibiting carbon uptake into the $Sm_2(Co, Fe, Cu, Zr)_{17}$ surface material. A explanation for observed increase in carbon in these samples could be because BN spray is a powder material dispersed in an acetone carrier. Therefore, the application of the material by aerosol spray unintentionally contaminated the interior of the mould with organics material. Application of a buffer material to reduce carbon uptake in the SPS process could be further investigated, but this would require a different method to aerosol application.

6.8 Chapter summary

In this chapter, the SPS technique has successfully been shown to produce fully dense $Sm_2(Co, Fe, Cu, Zr)_{17}$ specimens from powder under optimal processing parameters: 1050 °C to 1100 °C hold temperature, 100 °C/ min to 200 °C/ min heating rate, 51 MPa hold pressure and 5 minute hold time. Under these parameters, the microstructure was shown to be free of significant porosity and un-sintered powder regions. The microstructure was shown to comprise of a matrix 2:17R $Sm_2(Co, Fe, Cu, Zr)_{17}$ phase, with a grain boundary precipitate phase rich in samarium and oxygen.

Methods of aligning the powders before the SPS process were explored, showing near identical levels of alignment achieved by 2.5 T pulsed field and 0.3 T in the axial direction of the graphite mould. The enhanced alignment was significant in measurement of the remanence and energy products of the studied magnets. However, the available magnetic fields failed to achieve a similar level of alignment as those achieved in commercial magnets and the methods used were susceptible to variability in the degree of alignment induced when repeated. It has therefore been chosen for the majority of specimens produced in the remainder of this project to not receive powder alignment, to remove an aspect of variability when characterising the magnetic properties.

The $Sm_2(Co, Fe, Cu, Zr)_{17}$ specimens processed under different SPS processing parameters have shown porosity to increase the resistivity. Comparison of the resistivity profile with the DEM model of conductivity indicates a change in pore morphology as the density decreases.

Characterisation of the magnetic properties showed the remanent polarisation, J_r, increased with density for the 'isotropic' $Sm_2(Co, Fe, Cu, Zr)_{17}$ magnets. The relationship with coercivity was more complex, with peak values measured for 'isotropic' specimens with relative densities between 85% and 92%. $Sm_2(Co, Fe, Cu, Zr)_{17}$ magnets with higher and lower densities measured lower coercivities. Analysis and comparison of the initial magnetisation curves for the lowest and highest density $Sm_2(Co, Fe, Cu, Zr)_{17}$ samples showed the higher volume fraction of porosity correlated with a smaller gradient in the initial magnetisation, which is characteristic of pinning based coercivity. This effect may explain the increased coercivity seen in the specimens with relative densities spanning between 85% and 92%. However, this beneficial effect is not seen in the lowest density specimens, where the powder material is barely consolidated due to ineffective sintering conditions.

A study of carbon uptake into $Sm_2(Co, Fe, Cu, Zr)_{17}$ from the graphite foil/moulds during the SPS process found carbon contamination occurred at the surface to a depth of approximately 10 µm for a hold temperature of 1100 °C, heating rate of 100 °C and a hold time of 5 minutes. However, in comparison to literature values of 0.2 wt.% carbon concentration; shown to be significantly detrimental to the microstructure and magnetic properties of $Sm_2(Co, Fe, Cu, Zr)_{17}$, the concentration of carbon measured at the surface due to SPS processing was much lower at 0.04 wt.% and not believed to be significant. However, If surface carbon was to be removed to maintain tolerances and/or reduce potential microstructure inhomogeneity in other magnetic materials, it is recommended that removal of approximately 250 µm of surface material is sufficient to reduce the concentration of carbon to background levels comparable with conventional sinter processed $Sm_2(Co, Fe, Cu, Zr)_{17}$ material.

Chapter 7

Heat treatment of SPS processed SmCoFeCuZr magnets

7.1 Introduction

In this chapter, the production of SPS processed $Sm_2(Co, Fe, Cu, Zr)_{17}$ permanent magnets is developed further with a study and application of heat treatments. Chapter 2 provided a detailed description of the theory and literature related to the heat treatments for sintered $Sm_2(Co, Fe, Cu, Zr)_{17}$ magnets. As a general summary; the $Sm_2(Co, Fe, Cu, Zr)_{17}$ material is first homogenised into a 1:7H or 2:17H structure [75] and quenched to room temperature. The material is then aged, where nanostructured 2:17R cell and 1:5H cell boundaries are precipitated, crossed with a 1:3 lamellar phase [54]. After ageing, the material is slowly cooled and subtle microstructural changes coincide with elemental redistribution which enrich the 2:17R cells with Co and Fe, the 1:5H cell boundaries with Sm and Cu and the 1:3 lamellar phase rich with Zr [66, 67]. Sharp gradients in the intrinsic magnetic properties, and equivalent domain wall energies, across the 2:17R cell and 1:5H cell boundary phases pin or trap domain walls which give $Sm_2(Co, Fe, Cu, Zr)_{17}$ permanent magnets their large coercivities [54, 74, 90].

The morphology of the cellular nanostructure and the elemental composition of the respective phases are strongly linked to the magnet alloying composition, heat treatment parameters and processing methodology [19, 22, 73, 80, 304, 305]. A general summary, as well as a visual aid, showing the three main stages which define the typical heat treatment used for $Sm_2(Co, Fe, Cu, Zr)_{17}$ follows:

- Homogenisation - typically at 1150 °C to 1220 °C for 0.5 h to 2 h, followed by quench to room temperature [54, 78–82]
- Ageing - typically at 800 °C to 850 °C for times ranging from 2 h to 40 h [19,

23, 52, 75, 76, 78, 79]

- Slow cooling, at a rate of 0.5 °C/min to 1.0 °C/min, from the ageing temperature to 400 °C, followed by quench to room temperature [74, 75, 78, 79, 83, 84].

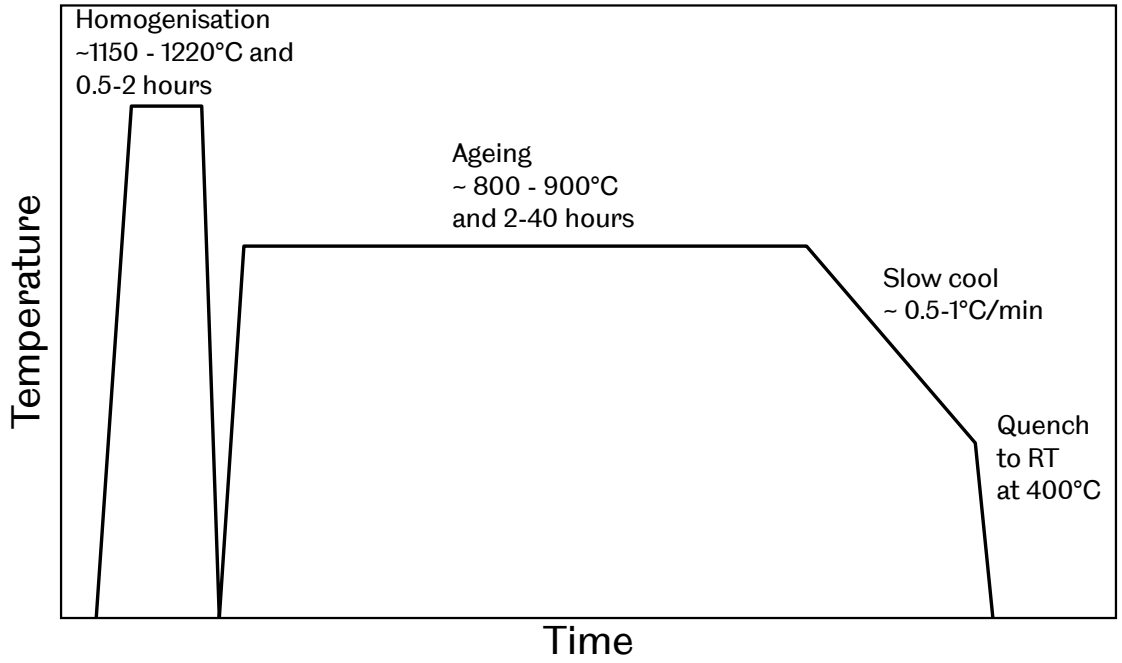

Figure 7.1: General scheme of the heat treatment used for $Sm_2(Co, Fe, Cu, Zr)_{17}$ magnets.

The SPS technique has primarily been used to produce fine structured $Sm_2(Co, Fe, Cu, Zr)_{17}$ magnets, which achieve relatively large coercivities without heat treatment through their nanoscale grain structure [36, 223]. SPS processed $Sm_2(Co, Fe, Cu, Zr)_{17}$ permanent magnets which require heat treatment have not been reported. Therefore, just as the processing parameters of the SPS technique were investigated systematically for this material and alloying composition, so too must the heat treatment structure and parameters for $Sm_2(Co, Fe, Cu, Zr)_{17}$ magnets processed by the SPS technique be studied. A general investigation into the material properties after heat treatment are made, with particular focus on identifying phase changes and grain growth, with direct comparison of the SPS processed magnets with conventional sinter processed material. Naturally, the magnetic properties are also investigated for the purpose of maximising the coercivity and energy product and exploring the viability of $Sm_2(Co, Fe, Cu, Zr)_{17}$ magnets through the SPS technique.

7.2 Investigation of the heat treatment process

7.2.1 Study of heat treatment stages

There are multiple processing variables across the three stages that make up the $Sm_2(Co, Fe, Cu, Zr)_{17}$ heat treatment process. To limit the scale of the investigation, table 7.1 lists the heat treatment parameters selected to remain consistent.

Homogenisation temperature	**(°C)**	1170
Homogenisation time	**(hours)**	2
Ageing temperature	**(°C)**	850
Post ageing cooling rate	**(°C/min)**	1
Quenching temperature	**(°C)**	400

Table 7.1: List of fixed variables in heat treatment study for $Sm_2(Co, Fe, Cu, Zr)_{17}$ permanent magnets processed by SPS technique. Parameters are separated by stage of the heat treatment they fall within: Homogenisation, Ageing or Slow Cooling.

The temperatures selected fall within the narrow range of reported temperatures within the literature studies of conventional sinter processed $Sm_2(Co, Fe, Cu, Zr)_{17}$ and for a range of alloying compositions [13, 19, 21, 60, 76–80, 259]. The cooling rate selected was the slowest available. A description of the heat treatment methodology and equipment used is found in chapter 5 section 5.2.3. All processes were conducted within a furnace under an inert argon atmosphere, unless otherwise stated. After heat treatment, the specimens were mechanically surface polished until any visible discolouration was removed.

The breadth of the study involves discussion of multiple specimens, sometimes processed under different parameters, which have undergone different stages of the heat treatment and under different heat treatment parameters. Therefore, the study has been split into sub sections, which attempt to simplify the number of samples and variables under discussion. The three stages of heat treatment are labelled with shorthand letters: Homogenisation (H), Ageing (A) and Slow Cooling (SC), and reference to specific stages of the heat treatment are described by the heat treatment parameters in table 7.1. Variables, such as ageing time are specified after the corresponding heat treatment stage. For example; a full heat treatment where the specimen was aged for 8 hours is labelled 'H-A8-SC'.

All $Sm_2(Co, Fe, Cu, Zr)_{17}$ specimens used within this study were not powder aligned (defined 'isotropic') and were processed by SPS using the following param-

eters, unless stated otherwise: 1100 °C hold temperature, 100 °C/min heating rate, 51 MPa and 5 minute hold time.

Homogenisation stage

Ideally, the $Sm_2(Co, Fe, Cu, Zr)_{17}$ material is quenched after the homogenisation stage to room temperature to retain the high temperature phase [75]. However, the first run of heat treated SPS processed $Sm_2(Co, Fe, Cu, Zr)_{17}$ specimens experienced significant cracking and damage through thermal shock, rendering them unreliable for further testing and use. A decision was made to allow the specimens to air cool, which provided a faster cooling rate than if allowed to cool within the furnace. Slow cooling after homogenisation initiates nucleation of the 2:17R and 1:5H cellular nanostructure [75] and as such, the phase composition will be heterogeneous once the ageing stage begins.

For this study, two SPS processed $Sm_2(Co, Fe, Cu, Zr)_{17}$ samples were used for comparison. Sample 1-33 has received no homogenisation and is used as reference to the as-processed state. Sample 1-22 has been characterised after the homogenisation stage only (1-22 (a), 'H') and after full heat treatment (1-22 (b), 'H-A4-SC'). Magnetic characterisation was performed by hysteresisgraph after magnetisation of the specimens by 3.5 T pulsed magnetic field.

Sample ID	Powder alignment	Heat treatment	Jr (T)	iH_c (kA/m)	(BH)max (kJ/m^3)
1-33	Isotropic	None	0.36 ± 0.02	66.80 ± 3.34	6.90 ± 0.35
1-22 (a)	Isotropic	H	0.30 ± 0.03	36.90 ± 3.19	3.13 ± 0.37
1-22 (b)	Isotropic	H-A4-SC	0.53 ± 0.03	553.00 ± 27.65	35.00 ± 1.75

Table 7.2: Magnetic properties measured for SPS processed $Sm_2(Co, Fe, Cu, Zr)_{17}$ magnets as-processed (sample 1-33), with homogenisation stage only (1-22 (a)) and after a full heat treatment (1-22 (b)).

Table 7.2 reports the magnetic properties measured for sample 1-33 and sample 1-22 after a partial and full heat treatment. After homogenisation, the magnetic properties of sample 1-22 (a) are reduced compared to the reference as-processed magnet. An explanation for this difference could be due to the relatively slow air cooling used from homogenisation, rather than quenching in water and rapidly cooling into a meta-stable state. The main phase identified in the $Sm_2(Co, Fe, Cu, Zr)_{17}$ specimens after processing by SPS was the 2:17R structure. After quenching from the homogenisation temperature, the high temperature phase is expected to be of 1:7R structure, as identified by Maury et al. [75]. However, Maury et al. [75] also identified that if cooled slowly from homogenisation ('slowly' defined as 30 °C/min), the main phase was predominantly a 2:17R structure via XRD analysis, although

EPMA analysis also showed compositional segregation within the grains, implying partial precipitation of the 2:17R cell and 1:5H cell boundary phases. The magnet being in this heterogeneous state may explain the reduction in coercivity, especially if the high temperature phase has a lower magneto-crystalline anisotropy than the 2:17R and 1:5H phases, which is indicated by the analysis of homogenised $Sm_2(Co, Fe, Cu, Zr)_{17}$ magnets by Arinicheva et al. [82]. Oxidation could also be a factor with air cooling from high temperature.

After a full heat treatment involving a 4 hour age, sample 1-22 (b) improved on all magnetic properties measured. The coercivity increased significantly, showing the effectiveness of the heat treatment towards $Sm_2(Co, Fe, Cu, Zr)_{17}$ permanent magnets. The remanence also increased, which is likely due to the 2:17R precipitated cell phase enriching in Fe [84].

XRD phase analysis

XRD 2θ phase analysis of a reference SPS processed $Sm_2(Co, Fe, Cu, Zr)_{17}$ magnet before heat treatment (1-18), after homogenisation stage only (1-22 (a), 'H') and after full heat treatment (1-22 (b), 'H-A4-SC') was conducted to identify the phase changes that occur during these stages of heat treatment. A conventional sinter processed $Sm_2(Co, Fe, Cu, Zr)_{17}$ magnet (labelled ARN), which has undergone a full heat treatment similar to that performed in 1-22 (b) (although the specifics are not known), has also been analysed. Figure 7.2 shows the XRD 2θ spectra for the above magnets.

The results of the XRD 2θ phase analysis show the predominant phase that exits throughout the heat treatment process is the 2:17R $Sm_2(Co, Fe, Cu, Zr)_{17}$ phase. Sample 1-22 (a) ('H') was air cooled after homogenisation and the presence of the 2:17R phase is consistent with the observations reported by Maury et al. in their homogenised and slowly cooled $Sm_2(Co, Fe, Cu, Zr)_{17}$ samples [75]. In their studies, further analysis by EPMA showed compositional variation, suggesting a state comprised of partially nucleated 2:17R cells and 1:5H cell boundaries, although phase analysis by XRD failed to evidence the boundary phase. Strong peaks relating to a Co-Fe phase are also identified in the post homogenisation spectra. Co-Fe is a soft magnetic phase which can form in $Sm_2(Co, Fe, Cu, Zr)_{17}$ magnets due to an excess of Fe or the removal of Sm [66]. Oxidation studies of $Sm_2(Co, Fe, Cu, Zr)_{17}$ permanent magnets identify the Co-Fe phase when Sm_2O_3 is formed [110, 111]. Both the Co-Fe and Sm_2O_3 phase are identified in the 1-22 (a) $Sm_2(Co, Fe, Cu, Zr)_{17}$ magnet after homogenisation and air cool to room temperature.

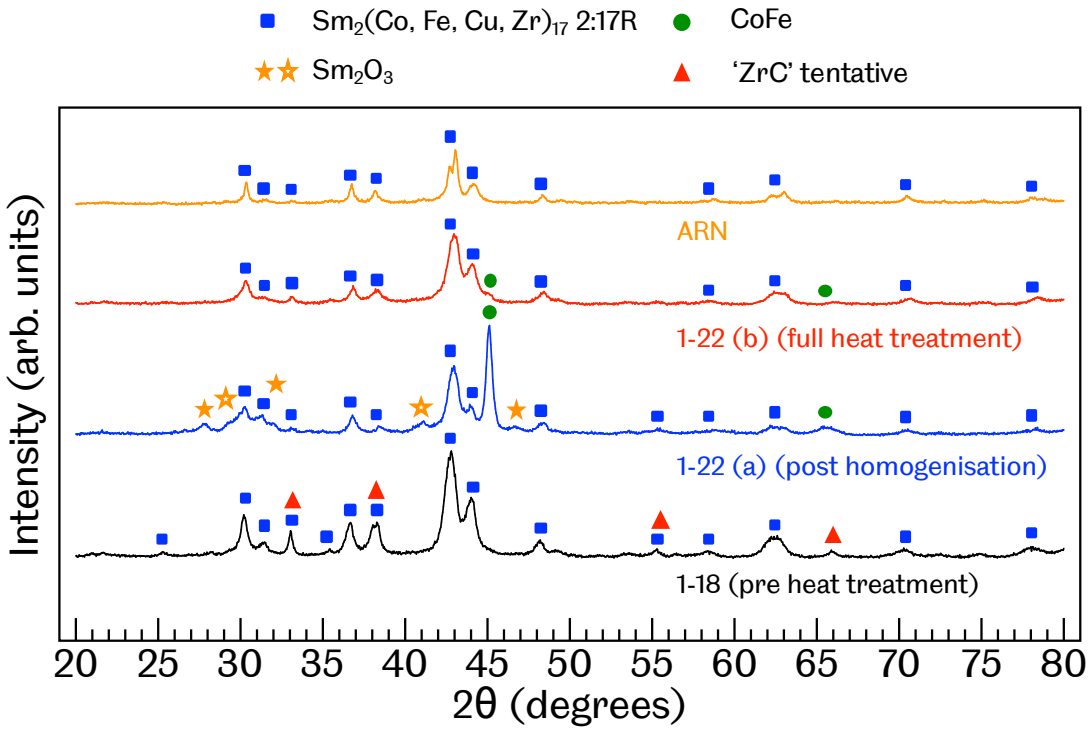

Figure 7.2: XRD 2θ analysis of SPS processed $Sm_2(Co, Fe, Cu, Zr)_{17}$ in the pre-heat treatment state (sample 1-18, black), after homogenisation only (1-22 (a), 'H', blue) and after a full heat treatment (1-22 (b), 'H-A4-SC', red). The conventional sinter processed and fully heat treated $Sm_2(Co, Fe, Cu, Zr)_{17}$ permanent magnet is labelled ARN (orange data)

1-22 (b) (red data) shows the XRD 2θ spectrum after a full heat treatment ('H-A4-SC'). Strong peaks are again identified corresponding to the 2:17R phase, however now there is only a subtle indication for the presence of Co-Fe phase, and no presence of the Sm_2O_3 phase. Why the oxidation phases have disappeared after ageing and slow cooling stages of the heat treatment can be explained by surface preparation after the heat treatment process. As the sample has undergone a full heat treatment effectively in two parts, the sample has twice been subjected to mechanical surface polishing and the surface oxidation phases have been removed during this second process. If oxidation is occurring during the air cooling after homogenisation, then the exposure period is relatively short. In oxidation studies of $Sm_2(Co, Fe, Cu, Zr)_{17}$ by Wang et al., an oxidation zone depth, where the Co-Fe phase and Sm_2O_3 featured, was 11.8 ± 1.5µm after 1 hour of exposure to air at 600 °C [114].

The orange data in figure 7.2 shows the spectra for a controlled conventionally

sinter processed and heat treated commercial $Sm_2(Co, Fe, Cu, Zr)_{17}$ magnet, again displaying the peaks relating to the 2:17R phase, which is the only phase identified.

Ageing and slow cooling stage

SPS processed $Sm_2(Co, Fe, Cu, Zr)_{17}$ magnets have also been studied omitting the homogenisation stage. The powder aligned sample 1-03, processed under sub-optimal SPS parameters and possessing a relative density of 93%, was aged for 8 hours and slowly cooled. For comparison, another specimen (1-23) received a full heat treatment, also with an 8 hour age.

Sample ID	Powder alignment	Heat treatment	Jr (T)	iH_c (kA/m)	(BH)max (kJ/m^3)
1-03	Pulsed-axial (once)(2.5 T)	None	0.58 ± 0.03	49.54 ± 2.48	10.70 ± 0.54
1-03 (a)	Pulsed-axial (once)(2.5 T)	A8-SC	0.63 ± 0.03	94.30 ± 4.72	16.00 ± 0.80
1-23	Isotropic	H-A8-SC	0.53 ± 0.03	592.50 ± 29.63	42.00 ± 2.10

Table 7.3: Magnetic properties measured for SPS processed $Sm_2(Co, Fe, Cu, Zr)_{17}$ magnets as-processed (sample 1-03), ageing and slow cooling (1-03 (a)) and after a full heat treatment (1-23).

Table 7.3 displays the measured magnetic properties when the homogenisation stage is omitted. Sample 1-03 (a), with an 'A8-SC' heat treatment improves its magnetic properties after the partial heat treatment, compared to its magnetic properties before heat treatment. The material has become magnetically harder via a noticeable increase in coercivity, which during the ageing stage is likely due to an partial precipitation of an inhomogeneous cellular nanostructure. The remanence also increased, albeit marginally. As established in the literature, the ageing and slow cooling stages of the heat treatment are where the magnetic properties improve, which is directly related to the microstructure changes and element redistribution [66, 67]. However, this study shows the importance of the homogenisation stage, and in general a full heat treatment (sample 1-23 with 'H-A8-SC'), is still required to properly precipitate the cellular nanostructure to pin domain walls and significantly enhance the coercivity.

7.2.2 Initial magnetisation curve study

In chapter 6, initial magnetisation curves were used to show an increase in porosity acted to pin domain walls and increase the coercivity. Here, initial magnetisation curves are again used to emphasise the change in coercivity mechanism from nucleation to domain wall pinning, and explain the increase in coercivity in a fully heat treated sample (1-33, 'H-A2-SC'). As such, this provides indirect evidence for the precipitated cellular nanostructure within the $Sm_2(Co, Fe, Cu, Zr)_{17}$ grains

during the heat treatment.

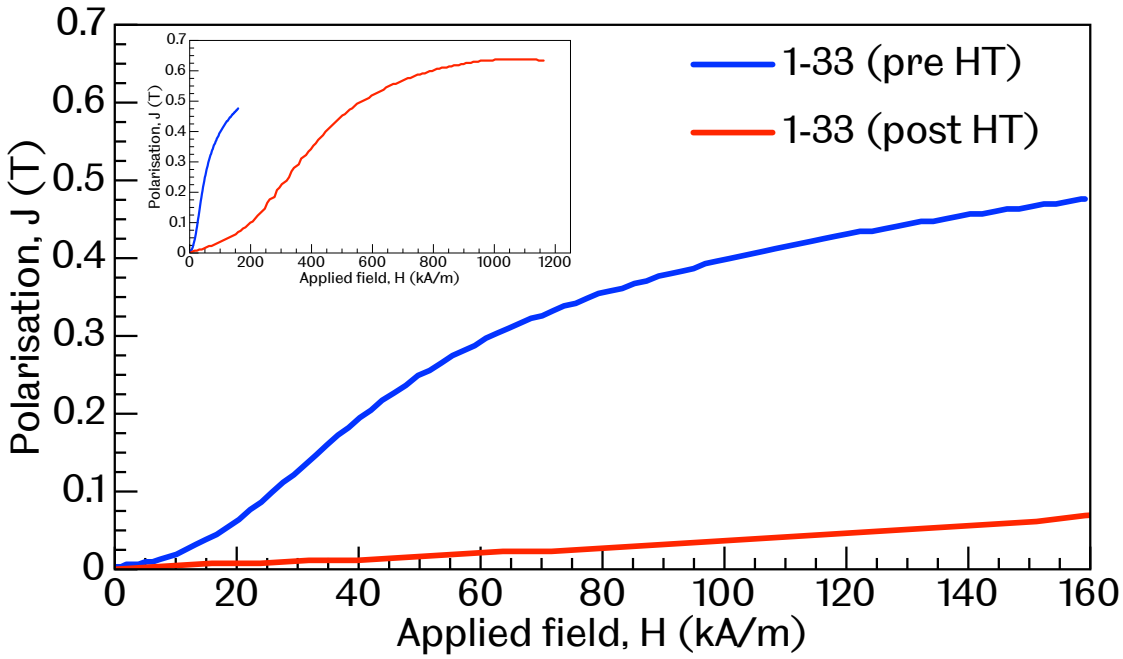

Figure 7.3: Initial magnetisation curves for sample 1-33 before (blue) and after (red) full heat treatment ('H-A2-SC'). The inset shows the full data range of the same initial magnetisation curves.

The two initial magnetisation curves reported in figure 7.3 are for the sample 1-33 before and after full heat treatment. In both cases, the sample was magnetised from a thermally demagnetised state using the hysteresisgraph to a field of at least 160 kA/m, which was found to be sufficient in showing the differences between the initial magnetisation curves.

Before heat treatment (blue curve), sample 1-33 magnetises more readily at comparatively lower fields than after heat treatment (red curve). This is even more evident in the inset in figure 7.3, which shows sample 1-33 after heat treatment only reaches saturation with around 1200 kA/m of applied field, whereas before heat treatment the specimen is approaching saturation with an applied magnetic field of 160 kA/m.

Figure 7.4 further emphasises these results, showing the percentage gradient change of the respective initial magnetisation curves. The much larger gradient of the pre-heat treatment sample is characteristic of a nucleation-based coercivity mechanism, whereas post-heat treatment, the very low rate-of-change of the polarisation with respect to the applied field is indicative of a developed cellular nanostructure pinning domain walls as the applied field attempts to saturate the

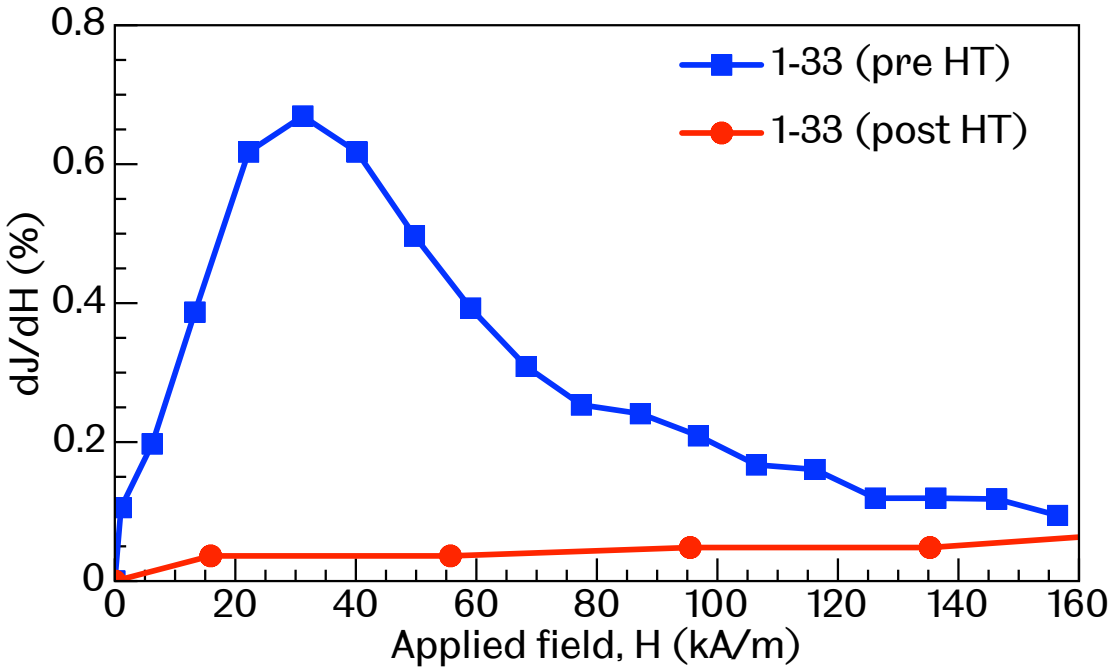

Figure 7.4: The change in polarisation with respect to the applied external field (dJ/dH) for the initial magnetisation of sample 1-33 before (blue) and after (red) full heat treatment ('H-A2-SC').

magnet [20]. As a result, after heat treatment; significantly more field is required to saturate the $Sm_2(Co, Fe, Cu, Zr)_{17}$ magnet.

Sample 1-33 has been processed under optimal SPS processing parameters and has a relative density of 99.45%. Therefore, the observed results are not affected by porosity, as was concluded in chapter 6, and are entirely due to the microstructural and phase changes onset by the full heat treatment of $Sm_2(Co, Fe, Cu, Zr)_{17}$ permanent magnets.

7.2.3 The effect of ageing time on the magnetic properties

Having confirmed a full heat treatment (homogenisation, ageing and slow cooling) as a requirement for improving the magnetic properties of the SPS processed $Sm_2(Co, Fe, Cu, Zr)_{17}$ magnets. To further develop an understanding of the heat treatment parameters, the duration of the ageing stage is investigated in this subsection.

For our investigation, five identically SPS processed $Sm_2(Co, Fe, Cu, Zr)_{17}$ samples underwent heat treatment. They differed only in the time spent aged at 850 °C: 2, 4, 8, 16 and 24 hours respectively. A reference specimen, also processed under identical SPS parameters, but without heat treatment, was included for comparison within the study to show the evolution of the magnetic properties.

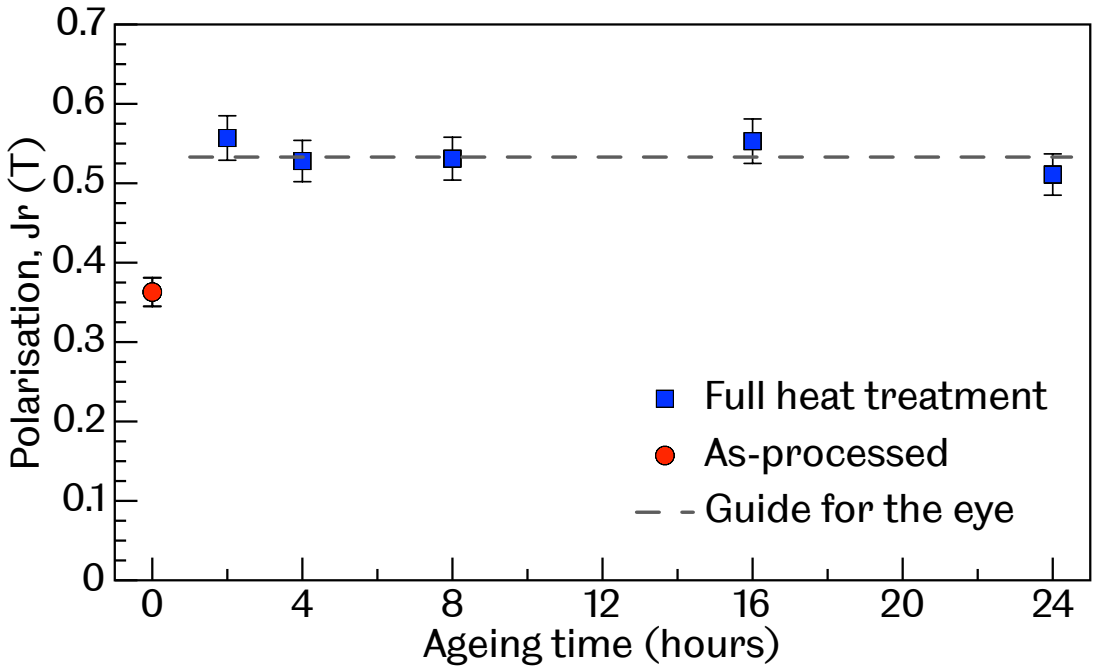

Figure 7.5: The measured remanent polarisation values for SPS processed $Sm_2(Co, Fe, Cu, Zr)_{17}$ magnet specimens before heat treatment (red data) and after full heat treatment ('H-A-SC', blue data) with varying ageing times as indicated on the horizontal axis.

Figure 7.5 shows the measured remanent polarisation values for the ageing times studied. As previously reported; a general increase in the remanence is observed after the full heat treatment, which is attributed to Fe enriching the $Sm_2(Co, Fe)_{17}$ cells during the slow cooling stage and increasing the saturation polarisation compared to the pre-heat treatment $Sm_2(Co, Fe, Cu, Zr)_{17}$ 2:17R matrix phase [13, 84]. A dashed guideline is added to show the uniformity of J_r across the ageing times studied.

Figure 7.6 plots the measured intrinsic coercivity and coercive force values for the pre-heat treatment magnet (1-33) and the post-heat treatment ('H-A-SC') magnets, of varying ageing times. After heat treatment, the coercive fields for all ageing times studied are much greater than the coercivities measured in the pre-heat treatment reference magnet. The intrinsic coercivity of the pre-heat treatment $Sm_2(Co, Fe, Cu, Zr)_{17}$ magnet was $iH_c = 67\,kA/m$. After a full heat treatment involving the shortest ageing time of 2 hours, the intrinsic coercivity increased to 428 kA/m; above the 400 kA/m 'hard magnetic material' definition by Coey [1]. The intrinsic coercivity continued to increase with ageing time up to a maximum at 8 hours, where $iH_c = 592\,kA/m$. Beyond 8 hours ageing, iH_c decreased

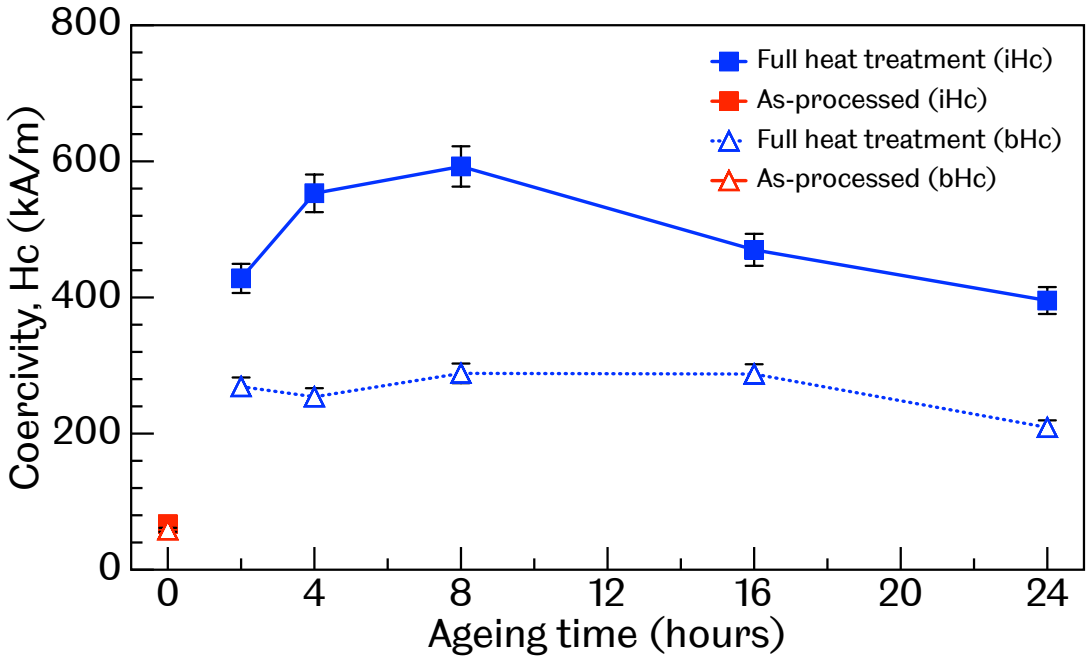

Figure 7.6: Measured intrinsic coercivity, iH_c, (filled squares) and coercive force, bH_c, (unfilled triangles) values for SPS processed $Sm_2(Co, Fe, Cu, Zr)_{17}$ magnet specimens before heat treatment (red data) and after full heat treatment ('H-A-SC', blue data) with varying ageing times as indicated on the horizontal axis.

as the ageing time extended, with the minimum intrinsic coercivity, 395 kA/m, measured after 24 hours. The coercive force, bH_c, displayed a more stable trend with the ageing time, only showing significant degradation for the longest ageing time of 24 hours.

Figure 7.7: The cellular nanostructure of $Sm(Co_{bal}, Fe_{0.224}, Cu_{0.08}, Zr_{0.033})_z$ permanent magnets, with (a) z = 7.0 and iH_c = 1500 kA/m, (b) z = 8.5 and iH_c = 2800 kA/m and (c) z = 9.1 and iH_c = 636 kA/m [77]. ©2000 IEEE.

To optimise the pinning strength of the precipitated cellular nanostructure of heat treated $Sm_2(Co, Fe, Cu, Zr)_{17}$ permanent magnets, a large energy barrier/well needs to created across the cell-boundary phase. This is facilitated during the slow cooling process with Fe enriching the 2:17R $Sm_2(Co, Fe)_{17}$cells and Cu enriching the 1:5H $Sm(Co, Cu)_5$ cell walls, creating a magneto-crystalline anisotropy gradient

across the boundary [75]. Furthermore, a uniform cellular nanostructure must be generated such that the cells are fully encompased by domain walls and the latter have sufficient thickness to contain domain walls [55]. The largest room temperature coercivities are achieved when uniform cells are preceipitated, which are approximately 100 nm in diameter, and cell boundary thickness around 10 nm [19, 76, 87, 92]. When the cellular structure is irregular and the average cell size much greater than ≈100 nm, the coercivities are comparatively much lower [77]. Figure 7.7 shows Transmission Electron Microscopy (TEM) imaging of $Sm_2(Co, Fe, Cu, Zr)_{17}$ magnets with different alloying compositions. For the same heat treatment applied, the resulting cellular nanostructure is very different across the studied materials and directly affects the measured coercivity. While it cannot be confirmed without TEM imaging, it is proposed that the decreasing coercivity for the longest duration aged SPS processed $Sm_2(Co, Fe, Cu, Zr)_{17}$ magnets is due to the cellular structure coarsening.

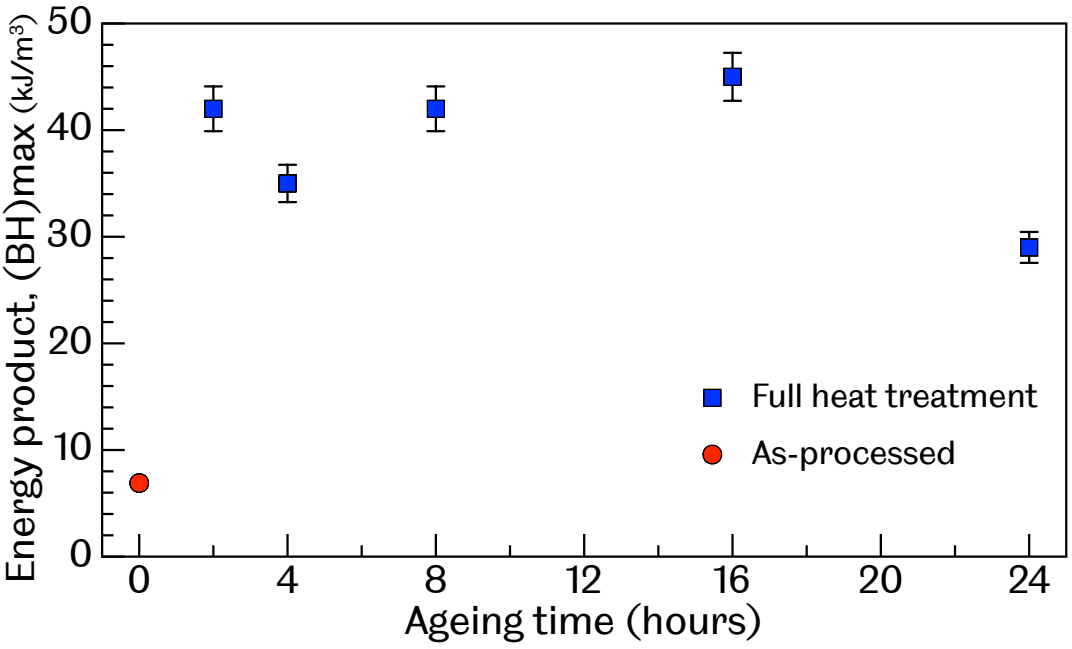

Figure 7.8: The measured $(BH)_{max}$ values for SPS processed $Sm_2(Co, Fe, Cu, Zr)_{17}$ magnet specimens before heat treatment (red data) and after full heat treatment ('H-A-SC', blue data) with varying ageing times as indicated on the horizontal axis.

Figure 7.8 displays the trend for the energy product with ageing time, which is mostly stable until the ageing time reaches 24 hours. The observed trend correlates with those reported for the remanence and coercive force, bH_c, with the ageing time.

7.2.4 Investigation of modified homogenisation stage

In the phase analysis of the homogenised and fully heat treated ('H-A4-SC') $Sm_2(Co, Fe, Cu, Zr)_{17}$ sample (1-22), the Co-Fe and Sm_2O_3 phases were identified, which were associated with the oxidation of $Sm_2(Co, Fe, Cu, Zr)_{17}$. These phases were not identified in $Sm_2(Co, Fe, Cu, Zr)_{17}$ magnets before heat treatment. This is evidence that oxidation occurs during the heat treatment process; with the likely exposure arising when allowing the samples to air cool after homogenisation. To investigate whether oxidation could be avoided, the heat treatment was modified, such that the air cool is replaced with a straight transition from the homogenisation stage to the ageing stage ('H*-A-SC'). This allows the entire heat treatment process to occur under an inert Ar atmosphere. A similar modification to the heat treatment was investigated my Maury et al. [75]. They found their $Sm_2(Co, Fe, Cu, Zr)_{17}$ specimen cooled from the homogenisation temperature to the ageing temperature had a similar cellular nanostructure to those which had been quenched and heated up, with comparable cell sizes of 200 nm and 2:17R, 1:5H and 1:3R phases identified. To perform our study, two $Sm_2(Co, Fe, Cu, Zr)_{17}$ magnets processed using the same parameters by SPS technique and were put through heat treatments which only differed in how the were cooled from the homogenisation temperature. Sample 1-27 transitioned straight from the homogenisation to ageing temperature ('H*-A16-SC'), while sample 1-24 air cooled from homogenisation to room temperature ('H-A16-SC').

Sample ID	Powder alignment	Heat treatment	Jr (T)	iH_c (kA/m)	(BH)max (kJ/m^3)
1-24	Isotropic	H-A16-SC	0.55 ± 0.03	470.00 ± 23.50	45.00 ± 2.25
1-27	Isotropic	H*-A16-SC	0.52 ± 0.03	462.00 ± 23.10	31.00 ± 1.55

Table 7.4: Magnetic properties measured for isotropic SPS processed $Sm_2(Co, Fe, Cu, Zr)_{17}$ magnets with standard air cooled from homogenisation (1-24) and modified transition under argon atmosphere from homogenisation temperature (1-27) heat treatments.

Table 7.4 displays the magnetic properties of the two $Sm_2(Co, Fe, Cu, Zr)_{17}$ samples. It is noted that sample 1-27 was partially cracked after quenching in water from 400 °C to room temperature and repaired using a small amount of Loctite x648 glue so magnetic characterisation could be carried out by hysteresisgraph. With this taken into account, the magnetic properties of the two specimens are approximately the same, sharing comparable J_r and iH_c values. Only the energy product, $(BH)_{max}$ shows significant deviation between the two samples, which is because sample 1-24 has a larger coercive force ($bH_c^{1-24} = 287.50 \pm 14.38$ kA/m) compared to sample 1-27 ($bH_c^{1-27} = 228.00 \pm 11.40$ kA/m). This deviation could be due to the crack running through the sample and glue used to bond the material, creating an inhomogeneous

material and affecting the magnetic results. With the ageing time kept constant between the two samples, these results show transitioning the $Sm_2(Co, Fe, Cu, Zr)_{17}$ sample from the homogenisation temperature to the ageing temperature under argon atmosphere achieves roughly the same magnetic properties as when allowed to air cool, before reheating and ageing.

XRD phase analysis

XRD 2θ phase analysis was performed on the surface of sample 1-27 to see if the oxidation related phases were present after allowing the heat treatment to occur entirely under argon atmosphere.

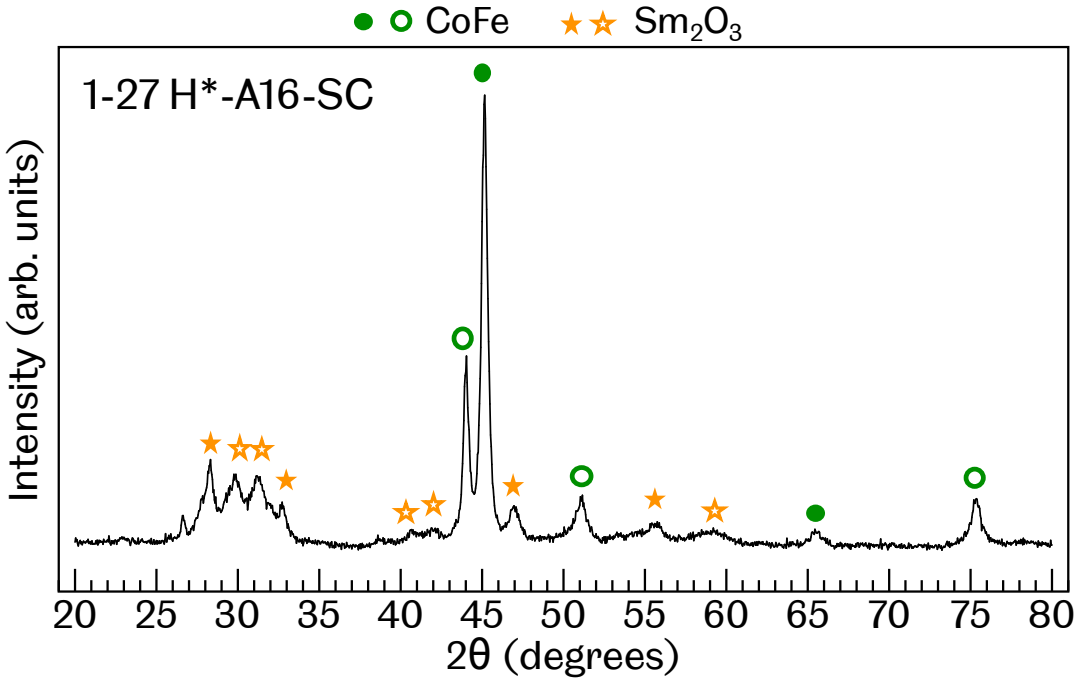

Figure 7.9: XRD 2θ analysis of modified heat treatment $Sm_2(Co, Fe, Cu, Zr)_{17}$ sample 1-27.

Figure 7.9 shows the XRD 2θ spectrum for sample 1-27 does not contain any peaks relating to the 2:17R phase, which is usually present in the $Sm_2(Co, Fe, Cu, Zr)_{17}$ magnets thus far studied. The peaks that are present instead correspond to structures relating to different Co-Fe phases, which are either face-centred-cubic (fcc) γ Co-Fe and body-centred-cubic (bcc) α Co-Fe [114]. Separate phases of Sm_2O_3 are also identified. The magnetic properties of sample 1-27 were shown to be comparable to 1-24, so there must exist a hard magnetic $Sm_2(Co, Fe, Cu, Zr)_{17}$ material below the surface oxidation layer. The modified heat treatment was expected to reduce the extent of oxidation, however from the analysis of a single specimen (sample 1-27), the oxidation

effects were at least the same as when the $Sm_2(Co, Fe, Cu, Zr)_{17}$ sample is allowed to cool in air to room temperature after homogenisation. These results warrants further investigation as to the source of the oxidation. It is possible that oxygen may be prevalent within the material before the heat treatment, as the powders used throughout the project gradually become more exposed to oxygen.

Summary of heat treatment study

Having studied the effect of specific stages and parameters of the required heat treatment for SPS processed $Sm_2(Co, Fe, Cu, Zr)_{17}$ magnets, the following was found to provide the best magnetic properties:

1. Homogenisation - 1170 °C for 2 hours in Ar atmosphere, followed by air cool to room temperature.

2. Ageing - 850 °C for 8 hours (for best coercivity) or 16 hours (for best $(BH)_{max}$) in Ar atmosphere.

3. Slow cool (1 °C/min) from 850 °C to 400 °C in Ar atmosphere. Quench in oil to room temperature.

Using a water quench from 400 °C resulted in cracking due to thermal shock in a couple of $Sm_2(Co, Fe, Cu, Zr)_{17}$ samples studied. It is recommended that oil is used instead, as it is less harsh due to oil having a cooling rate less than in water and minimising the thermal shock effect.

The maximum coercivity achieved for the SPS processed and heat treated ('H-A8-SC') $Sm_2(Co, Fe, Cu, Zr)_{17}$ permanent magnets was 592 kA/m. This value sets a benchmark for future studies, which could develop the investigation into other aspects and parameters of the heat treatment to further increase the magnetic properties. Conventionally sintered $Sm_2(Co, Fe, Cu, Zr)_{17}$ magnets with optimised alloying compositions and established heat treatments can achieve room temperature coercivities as high as iH_c =3100 kA/m [80].

7.3 Oxidation investigation

In this section, the investigation of oxidation after heat treatment was expanded over several SPS processed and conventional sinter processed $Sm_2(Co, Fe, Cu, Zr)_{17}$

to confirm the extent of the oxidation effect. Once established, FEM micromagnetic models were used to simulate the debilitating effect based on the phases and microstructures identified and inferred. The simulated demagnetisation curves and magnetic properties measured were compared with literature studies of oxidation effects in $Sm_2(Co, Fe, Cu, Zr)_{17}$ permanent magnets. Finally, methods to remove the oxidation-related phases to improve the magnetic properties were explored.

7.3.1 XRD phase analysis

Figure 7.10 collectively shows the XRD 2θ analysis for several SPS processed and heat treated $Sm_2(Co, Fe, Cu, Zr)_{17}$ magnets, detailing the range in oxidation effects. All samples analysed have undergone a full heat treatment with a 16 hour age, except for sample 1-23, which was aged for 8 hours. Sample 1-27 also differs; transitioning directly from the homogenisation to ageing stage under argon atmosphere, as described in section 7.2.4.

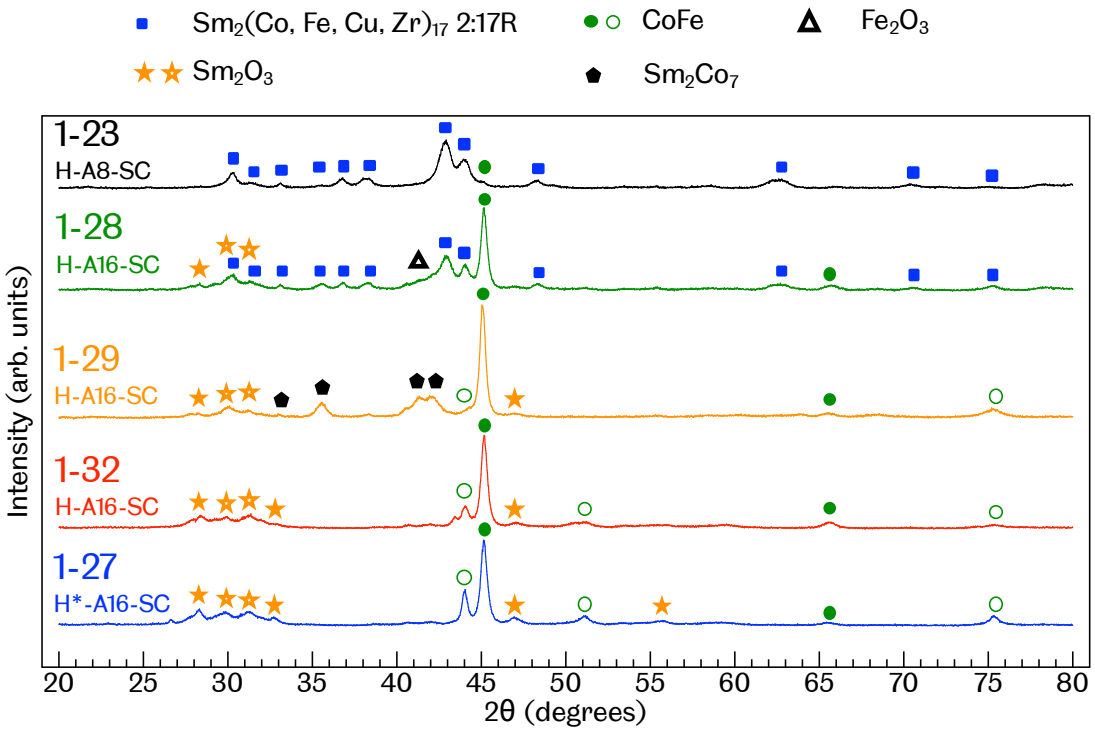

Figure 7.10: XRD 2θ analysis of several SPS processed and heat treated $Sm_2(Co, Fe, Cu, Zr)_{17}$ magnets. Heat treatment used for each specimen noted under sample ID. Multiple symbols used for Co-Fe and Sm_2O_3 phases refer either to different stoichiometry or structure of the phase.

Over the range of XRD 2θ spectra analysed, a range of phases relating to oxidation effects are identified, as well as the $Sm_2(Co, Fe, Cu, Zr)_{17}$ 2:17R phase. The

extent of surface oxidation is most severe in the spectra at the bottom of figure 7.10 for the 1-27 and 1-32 samples. Sample 1-32 was allowed to air cool after homogenisation, while 1-27 remained under Ar atmosphere, yet both show significant peaks relating to the Co-Fe and Sm_2O_3 phases and no evidence of the 2:17R $Sm_2(Co, Fe, Cu, Zr)_{17}$ phase.

Moving up the the spectra in figure 7.10, the extent of oxidation diminishes as phases relating to $Sm_2(Co, Fe, Cu, Zr)_{17}$ become prominent and the intensities of certain Co-Fe and Sm_2O_3 phases reduce, or even disappear altogether. Interestingly, for sample 1-29, a 2:7R Sm-Co phase is identified, which is unusual for $Sm_2(Co, Fe, Cu, Zr)_{17}$ type magnets. Xu et al. have used SPS to produce Sm_2Co_7 type magnets from amorphous powders of Sm and Co exclusively [217]. With the effects of oxidation in the $Sm_2(Co, Fe, Cu, Zr)_{17}$ material removing Co, Fe, Cu and Sm at the surface, it is feasible that outside of the typical oxides and Co-Fe phases forming, a predominant stoichiometry of Sm and Co in the ratio of 2:7 exists.

The previous reported 2:17R phase is, however, clearly evident in the 1-28 and 1-23 samples, whose spectra are shown at the top of figure 7.10. The Co-Fe and Sm_2O_3 phases are identified in the 1-28 specimen, but at lower intensities to the spectra displayed below. Sample 1-23 displays little evidence for the oxidation-induced phases, with the only indication via a minor Co-Fe identified peak at 45°, which normally dominates in the other heat treated samples.

The extent of oxidation-related effects do not correlate with the heat treatment method used. It is more likely to assume oxidation is prevalent for all heat treated $Sm_2(Co, Fe, Cu, Zr)_{17}$ magnets, but the variation in the oxidation phases identified and their respective intensities are due to differences in the material preparation after heat treatment. Post-heat treatment, the $Sm_2(Co, Fe, Cu, Zr)_{17}$ sample surfaces are 'cleaned' by a mechanical surface polish in preparation for material and magnetic characterisation. This process is performed manually and the time spent polishing each face on each specimen can differ greatly; either due to difficulty in removing surface graphite/discolouration, human error or in difficulty maintaining flat surfaces, which are necessary for optimal characterisation by techniques such as XRD and hysteresisgraph.

FEM modelling and simulation of oxidation affected magnets

The literature review in chapter 2 discussed the state of $Sm_2(Co, Fe, Cu, Zr)_{17}$ oxidation studies and it was shown short exposure to oxidising environments can noticeably affect the demagnetisation curve and thus magnetic properties of $Sm_2(Co, Fe, Cu, Zr)_{17}$ permanent magnets. The debilitating effect worsens as the

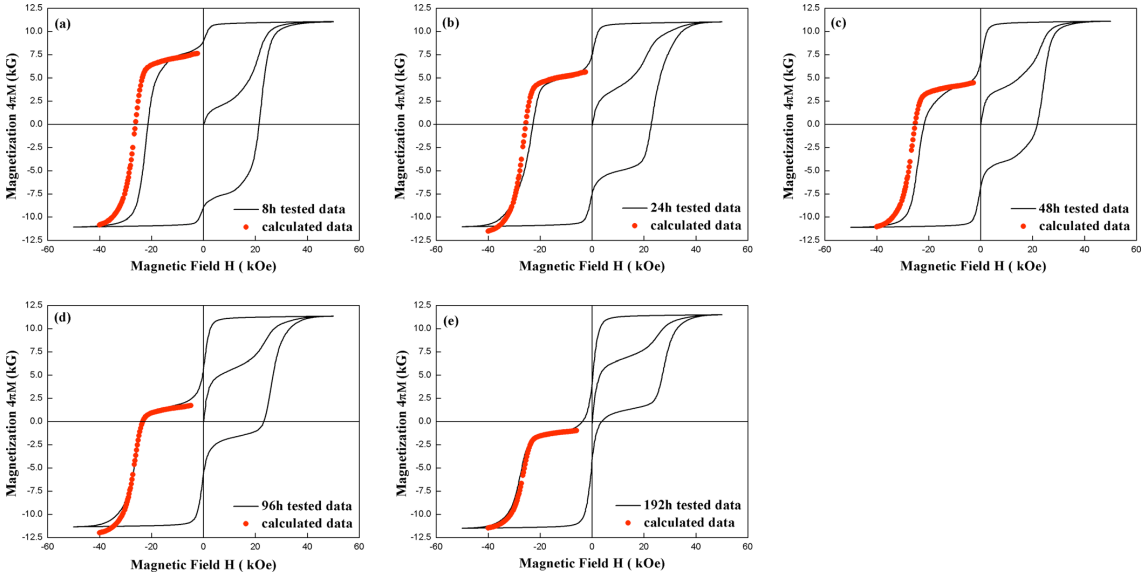

Figure 7.11: Demagnetisation curves for $Sm_2(Co, Fe, Cu, Zr)_{17}$ magnets isothermally aged in air at 500 °C for different times (black lines) and analytically derived results (red symbols) [306] ©2014 AIP Publishing LLC, licence granted for reuse in thesis (licence number 4197581257576).

exposure to oxygen increases and this correlates with the increasing volume fraction and penetration depth of the oxidation regions. Mao et al. [306] attempted to use analytical equations to correlate the volume fraction of soft and hard magnetic phase present after different exposure times to calculate partial demagnetisation curves of oxidised $Sm_2(Co, Fe, Cu, Zr)_{17}$. Their calculated partial demagnetisation curves, shown in figure 7.11, compared well with the experimental data in the second and third quadrants of the hysteresis loops, showing that the degradation of magnetic properties in oxidised $Sm_2(Co, Fe, Cu, Zr)_{17}$ magnets was proportional to the thickness of the oxidation region.

An understanding of the effect of the oxidation layers on the $Sm_2(Co, Fe, Cu, Zr)_{17}$ microstructure and magnetic properties can be developed with the use of FEM to simulate the demagnetisation curves for $Sm_2(Co, Fe, Cu, Zr)_{17}$ models with a defined volume fractions of soft magnetic phase and irregular structure. An 8 grain cubic $(2 \times 2 \times 2)$ $Sm_2(Co, Fe, Cu, Zr)_{17}$ model, with each 'grain' comprised of a single 2:17R core/cell and 1:5H shell/cell boundary. Figure 7.12 shows the structure of four grains on one face of the model. The core-shell structure is created by shrinking each grain surface to its centroid by a defined fraction to create a separate volume. The core-shell volumes can each be assigned unique magnetic properties.

In the FEM models of the $Sm_2(Co, Fe, Cu, Zr)_{17}$ cellular nanostructure, the

core-shell structure is created by shrinking the the grain by 0.05. This results in each 100 nm 'grain', made up of a 90 nm 2:17R cell and 5 nm 1:5H cell boundaries, replicating a typical $Sm_2(Co, Fe, Cu, Zr)_{17}$ cellular nanostructure [19, 76, 87, 92]. Figure 7.12 b) shows the surface mesh structure of the model. The average mesh size, 3.86 nm, is smaller than the domain wall width for the 2:17R cells (5.25 nm) and 1:5H cell boundaries (3.92 nm). The intrinsic magnetic properties assigned to each phase in the model, and which have been used to calculate the domain wall widths, are specified in table 7.5.

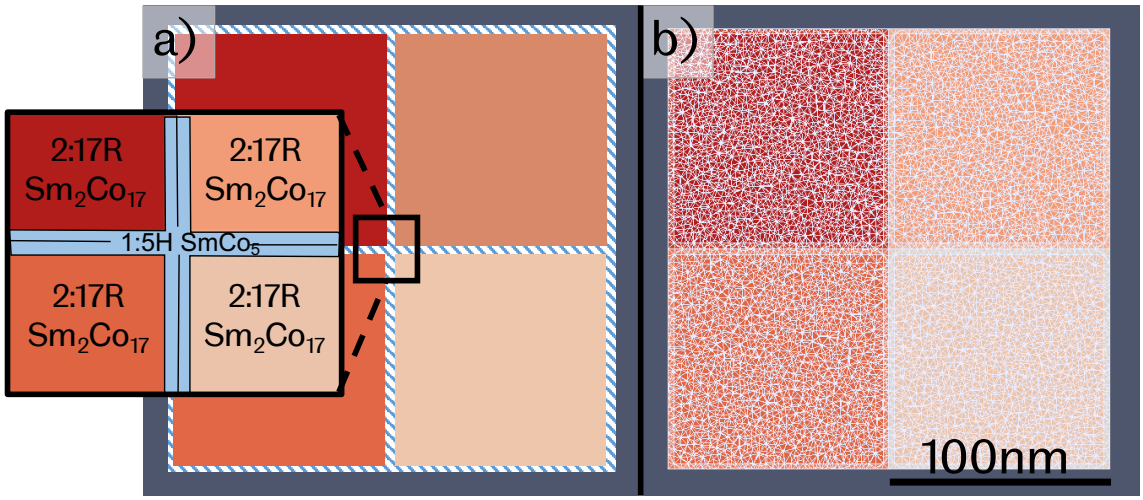

Figure 7.12: a) Face on image of 8 uniform $Sm_2(Co, Fe, Cu, Zr)_{17}$ 'grain' ($2 \times 2 \times 2$) model. Inset shows close up of 'grain' core-shell structure comprised of 2:17R Sm_2Co_{17} cell phase and 1:5H $SmCo_5$ cell wall phase. b) shows the surface mesh structure of the corresponding model.

The structure of an oxidation affected $Sm_2(Co, Fe, Cu, Zr)_{17}$ material was modelled by modifying the granular model described above with a quarter of the model volume comprised of the soft magnetic Co-Fe phase. This phase was used because it dominates the largest oxidation region in oxidised $Sm_2(Co, Fe, Cu, Zr)_{17}$ [111, 114]. Figure 7.13 a) shows the $Sm_2(Co, Fe, Cu, Zr)_{17}$/Co-Fe granular model, with the red 'grains' identifying the soft magnetic Co-Fe phase and the blue 'grains' the 2:17R cells and 1:5H cell boundaries. The inset shows the three-dimensional structure of the model. The intrinsic magnetic properties used for the Co-Fe phase are given in table 7.5. Comparison of the simulated demagnetisation curves between the standard $Sm_2(Co, Fe, Cu, Zr)_{17}$ and oxidised $Sm_2(Co, Fe, Cu, Zr)_{17}$/Co-Fe granular models aims to show the effect on the curve shape and magnetic properties due to the presence of the soft magnetic phase, and also provide validation and extention to the comparable analytical model used by Mao et al. [306].

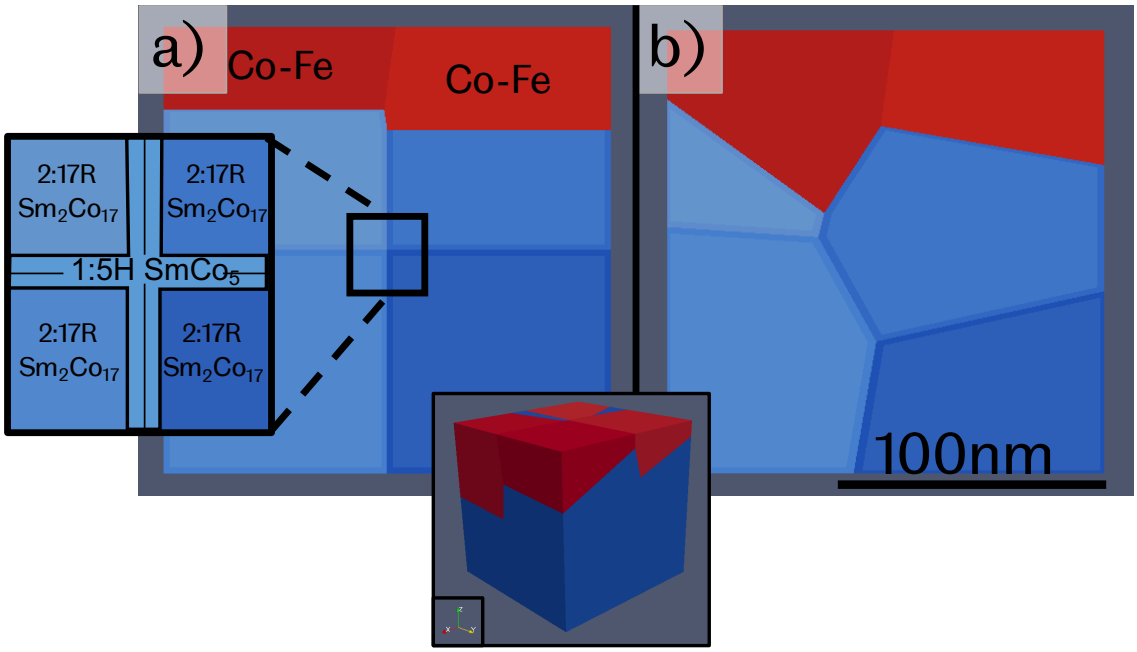

Figure 7.13: a) Face on image of 8 uniform $Sm_2(Co, Fe, Cu, Zr)_{17}$/Co-Fe 8 'grain' $(2 \times 2 \times 2)$ generated model. Left inset shows core-shell structure of $Sm_2(Co, Fe, Cu, Zr)_{17}$ grains (blue), comprised of a core 2:17R Sm_2Co_{17} cell phase and 1:5H $SmCo_5$ cell wall phase. Soft magnetic Co-Fe phase grains are red. b) Face on image of the equivalent model, with an irregular and disordered grain structure. Bottom inset shows three-dimensional representation of model.

The final set of models generated in this study are again an $Sm_2(Co, Fe, Cu, Zr)_{17}$/Co-Fe model, but with an irregular and disordered granular structure. The purpose of these models are to replicate the debilitating effect on the $Sm_2(Co, Fe, Cu, Zr)_{17}$ cellular nanostructure due to the removal of vital stabilising elements due to oxidation. This type of model is novel with respect to previous oxidation studies of $Sm_2(Co, Fe, Cu, Zr)_{17}$ permanent magnets. The models are created in the same manner as in the previously described $Sm_2(Co, Fe, Cu, Zr)_{17}$/Co-Fe models, however the 'grain' shapes are heavily distorted. An example is given in figure 7.13 b) and the bottom inset shows a three-dimensional representation.

For each model type, three unique models of the same structure were run to show the variation in the demagnetisation process, which can be affected by the mesh structure or the distribution of grain easy axes. The granular models were set-up to be magnetically anisotropic for better comparison to the literature studies. The easy axis direction of the grains were centred around the positive x-axis, with a normal distribution between $-90°$and$+90°$ (average standard deviation, $\sigma = 11.2 \pm 0.3°$) of possible orientations, relative to the y and z axis.

Intrinsic magnetic property		**2:17R Sm_2Co_{17}** [54, 55]	**1:5H $SmCo_5$** [54, 55]	**Co-Fe** [285–287]
$\mathbf{J_s}$	**(T)**	1.32	0.8	2.20
$\mathbf{K_1}$	**(MJ/m³)**	5.0	9.0	-7.0×10^{-3}
$\mathbf{K_2}$	**(MJ/m³)**	0	0	0
$\mathbf{A_{ex}}$	**(pJ/m)**	14	14	25
$\boldsymbol{\alpha}$		0.2	0.2	0.2

Table 7.5: Intrinsic magnetic properties used for 2:17R Sm_2Co_{17}, 1:5H $SmCo_5$ and Co-Fe phases in FEM micromagnetic models.

The demagnetisation simulations were performed using the MagPar software [288]. The models were initially magnetised to saturation in the positive x-axis, before being allowed to relax with gradual removal of the applied field. Application of the external magnetic field in the negative x-axis demagnetises the magnetic volume until reaching saturation at 10 T (8000 kA/m).

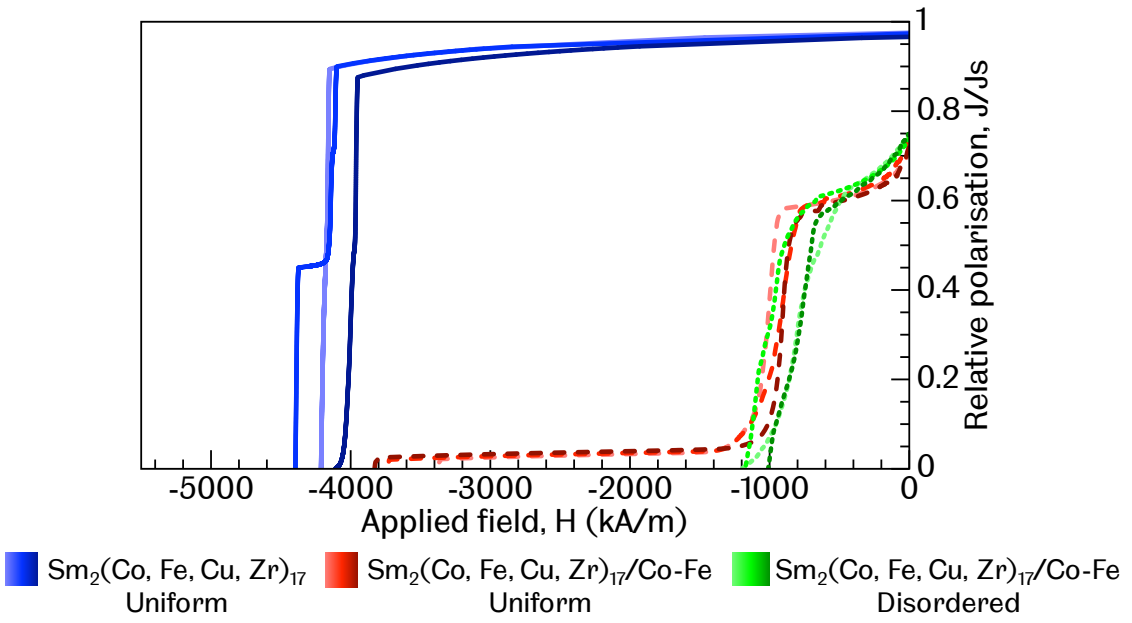

Figure 7.14: Simulated and repeated demagnetisation curves for our uniform $Sm_2(Co, Fe, Cu, Zr)_{17}$ (blue), uniform $Sm_2(Co, Fe, Cu, Zr)_{17}$/Co-Fe (red) and disordered $Sm_2(Co, Fe, Cu, Zr)_{17}$/Co-Fe models (green).

The demagnetisation curves from the simulations of the three sets of models are displayed in figure 7.14. The blue line data is the three $Sm_2(Co, Fe, Cu, Zr)_{17}$ only models, and the red and green data lines are for the uniform and irregular $Sm_2(Co, Fe, Cu, Zr)_{17}$/Co-Fe models respectively. The data shows, expectedly, that the $Sm_2(Co, Fe, Cu, Zr)_{17}$ models without any soft magnetic phases have the

largest coercivity, with the three repeats showing the variance with respect to the mesh structure and easy axis orientations. The blue demagnetisation curves are approximately square, bar one of the simulations which shows an inflection around $J/J_s = 0.45$, where the magnetisation reversal is momentarily pinned. The blue line with the lowest coercivity also appears to be in the process of being pinned just as it crosses the x-axis.

In the first set of simulations where the soft magnetic Co-Fe material is introduced into the model, a significant change in the shape of the demagnetisation curves is observed. The $Sm_2(Co, Fe, Cu, Zr)_{17}$/Co-Fe models with a uniform granular structure (red data) show the soft magnetic Co-Fe phase completely reverse its magnetisation at around 1000 kA/m. The hard magnetic $Sm_2(Co, Fe, Cu, Zr)_{17}$ 'grains' hold their magnetisation until they finally reverse between 3400 kA/m to 3800 kA/m, which are slightly lower than the coercivities in the blue data, for the $Sm_2(Co, Fe, Cu, Zr)_{17}$ only models. In addition to the externally applied magnetic field, inter-granular interactions between the reversed Co-Fe and $Sm_2(Co, Fe, Cu, Zr)_{17}$ 'grains' also contribute to magnetic reversal.

The shape of the simulated demagnetisation curves compare very well with the experimental and analytically derived demagnetisation curves produced by Mao et al., shown in figure 7.11, which show the incremental effect on the demagnetisation curve and magnetic properties as the volume fraction of the oxidation region increases with oxidation exposure time [306]. Both the FEM micromagnetic simulations and the analytical models show the debilitating effect on the demagnetisation of oxidised $Sm_2(Co, Fe, Cu, Zr)_{17}$ and how it is proportional to the presence and volume fraction of the magnetically soft phases present at the surface of the material.

In the final set of models, disorder is introduced into the granular structure of the $Sm_2(Co, Fe, Cu, Zr)_{17}$/Co-Fe models. The simulated demagnetisation curves (green data) again show the volume fraction of soft magnetic Co-Fe phase has a significant and detrimental effect on the magnetic properties and shape of the demagnetisation curves. In comparison to the uniform structured $Sm_2(Co, Fe, Cu, Zr)_{17}$/Co-Fe, the irregular model has a considerably lower coercivity (ranging from 1011 kA/m to 1202 kA/m compared to 3401 kA/m to 3828 kA/m) as the inflection point, where the soft and hard magnetic phases are anti-ferromagnetically aligned, is now well below the x-axis. The volume fraction of the Co-Fe phase is approximately the same between models, so the effect is due to irregularity in the grain shape. Similar disparity between uniform and irregular shaped grains in FEM micromagnetic models of composite hard and soft magnetic materials show similar results to those reported here [241, 242]. Inter-granular interactions between reversed Co-Fe and

$Sm_2(Co, Fe, Cu, Zr)_{17}$ 'grains' were used to explain the reduction in coercivity in the uniform 'grain' $Sm_2(Co, Fe, Cu, Zr)_{17}$/Co-Fe models. With an irregular granular structure, the contact area between the $Sm_2(Co, Fe, Cu, Zr)_{17}$ and Co-Fe 'grains' is greater. The granular volumes in these models are $<$100 nm and at this scale, inter-granular interactions such as exchange are influential. Therefore, there is a greater influence from the soft magnetic Co-Fe phase in the irregular shaped granular $Sm_2(Co, Fe, Cu, Zr)_{17}$/Co-Fe models, compared to the uniform models. It is also expected that there is a greater influence from the self-demagnetising field within the irregular $Sm_2(Co, Fe, Cu, Zr)_{17}$ 'grains'. The irregular shaped 'grains' will more likely have a greater number of sharp edges and corners, which are sources of 'magnetic charges' [241]. Irregularity also leads to a distribution of volumes and larger grains posses greater magnetic inhogeneity at the corners of grains, where the magnetisation is more greatly influenced by self-demagnetising field effects [32, 243].

In summary, the FEM micromagnetic models comprised of $Sm_2(Co, Fe, Cu, Zr)_{17}$ and Co-Fe phases successfully show the debilitating effect of soft magnetic oxidation-related phases on the demagnetisation curves of permanent magnets and are in agreement with the analytical models of Mao et al. [306]. Disruption to a uniform precipitated $Sm_2(Co, Fe, Cu, Zr)_{17}$ cellular nanostructure close to the oxidation regions will also reduce the coercivity, which will be irreversible if the disorder extends well into the $Sm_2(Co, Fe, Cu, Zr)_{17}$ material.

7.3.2 Oxidation phase removal and effect on magnetic properties

Studies have shown removal of oxidation affected material at the surface allows recovery of most of the magnetic properties and shape of the demagnetisation curve of $Sm_2(Co, Fe, Cu, Zr)_{17}$ permanent magnets [114, 306]. Accordingly, the coercivities measured for the oxidised SPS processed $Sm_2(Co, Fe, Cu, Zr)_{17}$ magnets may be able to be improved with the removal of the soft-magnetic oxide and Co-Fe phases.

Two identically SPS processed and heat treated ('H-A16-SC') $Sm_2(Co, Fe, Cu, Zr)_{17}$ specimens (1-28 and 1-29) were studied before and after removal of at least 200 µm of surface material by mechanical surface polish using 120 grit SiC abrasive paper. These value was estimated via measurement of the specimen thickness before and after surface polish using digital callipers.

Before surface material removal (blue spectra), both specimen 1-28 in figure 7.15 and 1-29 in figure 7.16, show peaks relating to Co-Fe and Sm_2O_3 phases, as have

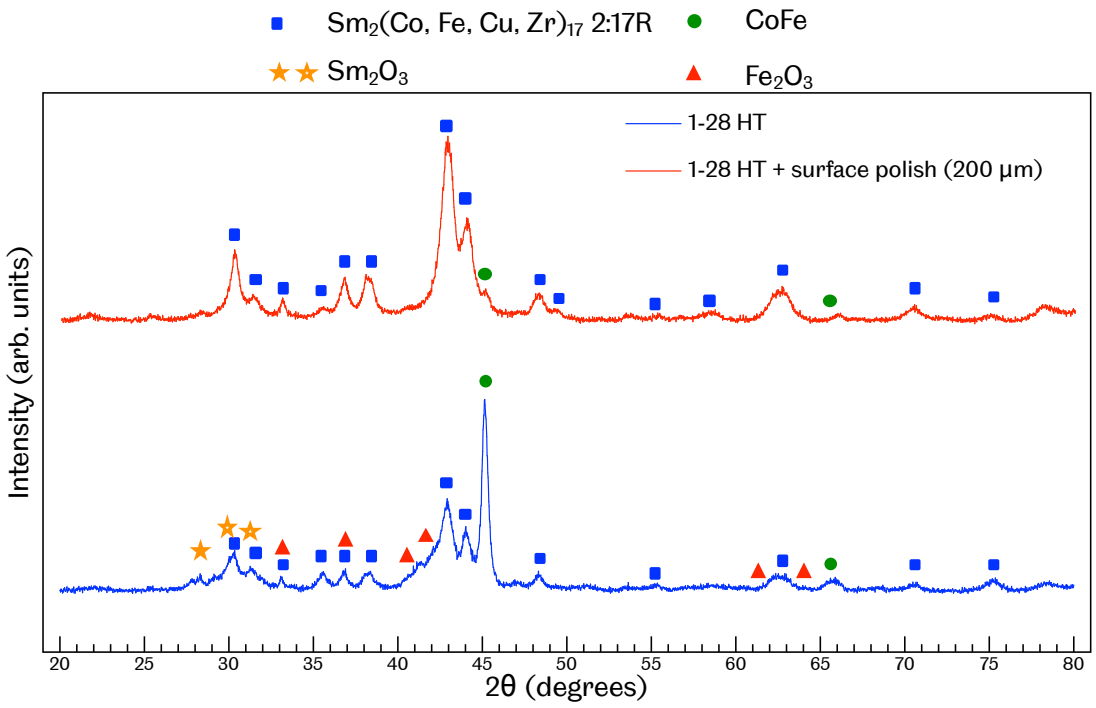

Figure 7.15: XRD 2θ phase analysis of SPS processed and heat treated ('H-A16-SC') $Sm_2(Co, Fe, Cu, Zr)_{17}$ sample 1-28 before (blue spectrum) and after (red spectrum) removal of 200 µm of surface material by mechanical surface polish.

been identified before in other SPS processed and heat treated $Sm_2(Co, Fe, Cu, Zr)_{17}$ samples. Sample 1-28 also shows evidence for another oxide phase, Fe_2O_3, which share peaks positions with the 2:17R $Sm_2(Co, Fe, Cu, Zr)_{17}$ phase between 30° and 45° 2θ angles. Iron-oxide phases are expected to from outwards from the surface in the EOS layer [111, 114]. The $Sm_2(Co, Fe, Cu, Zr)_{17}$ 2:17R phase is also observed in sample 1-28, although in sample 1-29 we identify Sm_2Co_7 phase, which we proposed earlier may form in the absence of the other alloying elements.

After removal of approximately 200 µm of surface material (red spectra in figures 7.15 and 7.16), both samples 1-28 and 1-29 unambiguously show the 2:17R phase. The oxidation-related phases are absent after the surface polish, although sample 1-28 shows subtle peaks relating to the Co-Fe phase.

For comparison, a conventional sinter processed and heat treated $Sm_2(Co, Fe, Cu, Zr)_{17}$ magnet ('ARN') was also analysed. Figure 7.17 shows the XRD 2θ spectrum before surface material has been removed (blue spectrum) and it is clear that the material is entirely comprised of the 2:17R $Sm_2(Co, Fe, Cu, Zr)_{17}$ phase, with no indication of peaks relating to the Co-Fe or metal oxide phases are present. It is not known the exact heat treatment process or parameters used in the heat treatment of the commercial ARN $Sm_2(Co, Fe, Cu, Zr)_{17}$ magnet,

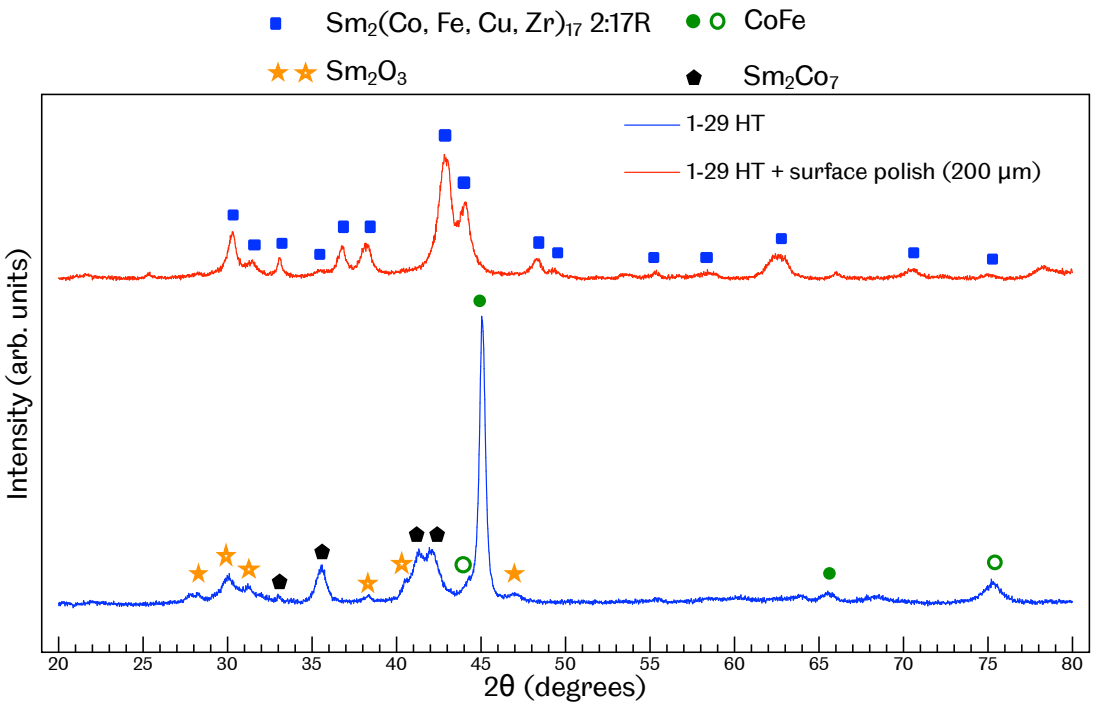

Figure 7.16: XRD 2θ phase analysis of SPS processed and heat treated ('H-A16-SC') $Sm_2(Co, Fe, Cu, Zr)_{17}$ sample 1-29 before (blue spectrum) and after (red spectrum) removal of 200 µm of surface material by mechanical surface polish.

however it would follow a similar structure, albeit optimised, to the one used for the SPS processed $Sm_2(Co, Fe, Cu, Zr)_{17}$ magnets. After removal of 200 µm of surface material, the XRD spectrum (red) in figure 7.17 is, again, entirely comprised of the 2:17R $Sm_2(Co, Fe, Cu, Zr)_{17}$ phase and the peak profile is near identical to that of the blue spectrum.

The phase comparisons have shown, after heat treatment, the commercial $Sm_2(Co, Fe, Cu, Zr)_{17}$ magnet to be more homogeneous from the surface than those processed by the developing SPS technique. The commercial production of the $Sm_2(Co, Fe, Cu, Zr)_{17}$ permanent magnets evidently has greater control of oxidation effects during the heat treatment process. As such, we believe there is no need to remove surface material when characterising the magnetic properties of the ARN $Sm_2(Co, Fe, Cu, Zr)_{17}$ magnets.

Magnetic characterisation after surface material removal

The magnetic properties of samples 1-28 and 1-29 before and after the removal of approximately 200 µm of surface material, as well two conventional sinter processed and heat treated $Sm_2(Co, Fe, Cu, Zr)_{17}$ magnets (ARN-4 and ARN-5), which have not had any surface material removed for this study are given in table 7.6.

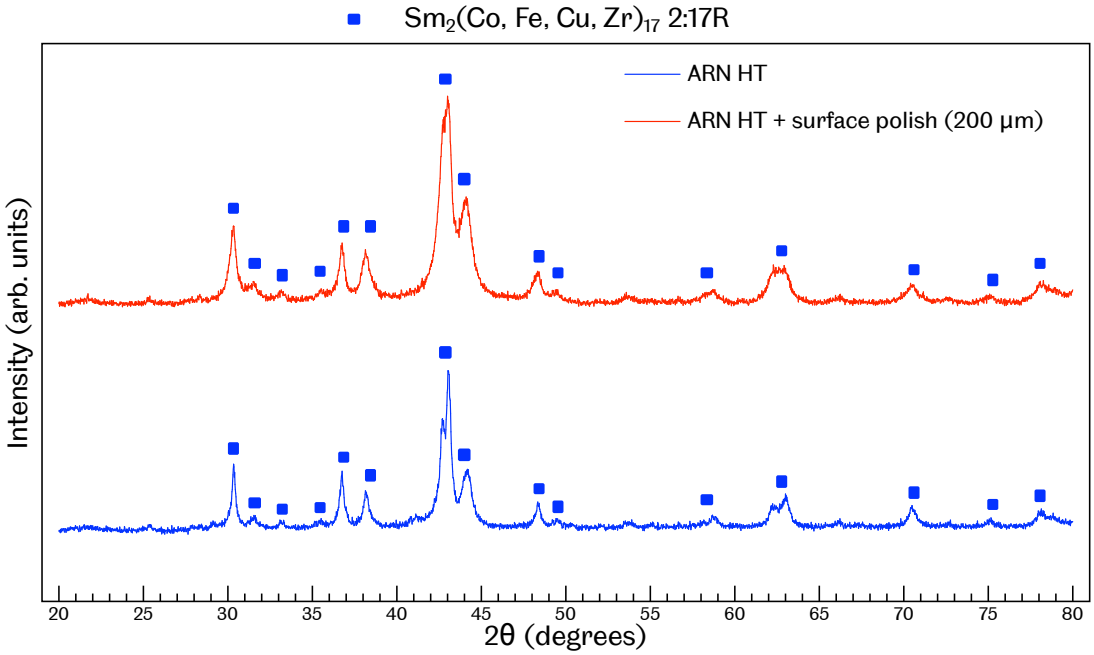

Figure 7.17: XRD 2θ phase analysis of conventional sinter processed and heat treated $Sm_2(Co, Fe, Cu, Zr)_{17}$ sample ARN before (blue spectrum) and after (red spectrum) removal of 200 µm of surface material by mechanical surface polish.

The reported data shows that there is no change in the remanent polarisation after the removal of surface material in either sample 1-28 and 1-29. Significantly oxidised specimens studied by Mao et al. [306] showed both experimentally, and through analytical models, that the soft magnetic regions can reverse their magnetisation close to the y-axis in the first quadrant of the hysteresis loop, leading to a stepped demagnetisation curve in the second quadrant. FEM micromagnetic models in section 7.3.1, where the volume fraction of soft-magnetic phase was 0.25, also showed this step feature. With no noticeable change in the remanent

Specimen ID	Powder alignment	$\mathbf{J_r}$ **(T)**	$\mathbf{iH_c}$ **(kA/m)**	$\mathbf{(BH)_{max}}$ **(kA/m^3)**
1-28	Axial pulsed field ≈2.5 T	0.63 ± 0.03	446.00 ± 22.30	42.00 ± 2.10
1-28 + 200 µm SP	Axial pulsed field ≈2.5 T	0.64 ± 0.03	497.00 ± 24.85	47.00 ± 2.35
1-29	Axial DCEM ≈0.3 T	0.62 ± 0.03	366.00 ± 18.30	37.00 ± 1.85
1-29 + 200 µm SP	Axial DCEM ≈0.3 T	0.62 ± 0.03	434.00 ± 21.70	41.00 ± 2.05
ARN-4	Isotropic	0.56 ± 0.03	>1214.00 ± 60.70	56.00 ± 2.80
ARN-5	Isotropic	0.56 ± 0.03	>1078.00 ± 53.90	56.65 ± 2.80

Table 7.6: Measured magnetic properties for SPS processed and heat treated ('H-A16-SC') $Sm_2(Co, Fe, Cu, Zr)_{17}$ magnets, 1-28 and 1-29, before and after approximately 200 µm of surface material removal. Conventional sinter processed and heat treated $Sm_2(Co, Fe, Cu, Zr)_{17}$ magnets, ARN-4 and ARN-5 provided for reference without surface material removed.

polarisation post surface polish, and because phase analysis showed the oxidation phases were absent after 200 µm surface material removal, it is in-directly inferred that the volume fraction of the oxidation phases, relative to the hard-magnetic $Sm_2(Co, Fe, Cu, Zr)_{17}$ material, are significantly smaller than those studied in the FEM micromagnetic model. If the surface oxidation in the SPS processed magnets is due to the cooling in air from the homogenisation, the exposure time is relatively short and the resulting effect on J_r is negligible. Samples 1-28 and 1-29 have had powder alignment before processing by SPS and so their J_r values are, as expected, larger than the two ARN magnets.

The coercivities show noticeable improvement after surface material was removed in samples 1-28 and 1-29. Near full recovery of coercivity was reported after the removal of oxidation affected surfaces in similar studies of $Sm_2(Co, Fe, Cu, Zr)_{17}$ magnets [114, 306], although it is not specified how much material was removed. Accordingly, if the surface polish removed the oxidation phases, as was indicated by XRD phase analysis, then the recovered coercivities in table 7.6 must be close to the 'true' coercivity of the SPS processed $Sm_2(Co, Fe, Cu, Zr)_{17}$ magnets for the heat treatment applied. Beyond controlling the heat treatment process to avoid oxidation effects, there is still much room for optimisation of the SPS processing method to improve the coercivity of the SPS processed $Sm_2(Co, Fe, Cu, Zr)_{17}$ magnets to comparable levels as measured in the conventional sinter processed commercial $Sm_2(Co, Fe, Cu, Zr)_{17}$ magnets, ARN-4 and ARN-5. Similarly, it warrants examining the bulk oxygen content in the $Sm_2(Co, Fe, Cu, Zr)_{17}$ powder and again after SPS processing and heat treatment.

7.3.3 LECO-O bulk oxygen analysis

Quantification of the bulk oxygen concentration was measured using LECO-O analysis. This method infers the concentration of oxygen within the sample from the release of carbon monoxide when heated to extreme temperatures (3000 °C) while in contact with a graphite crucible. Using this technique, $Sm_2(Co, Fe, Cu, Zr)_{17}$ samples in the form of the powders used throughout the project, and sections taken approximately 5 mm from the edge of the specimen of SPS processed material after heat treatment and a conventional sinter processed and heat treated specimen provided by Arnold Magnetic Technologies (Sheffield, England) were analysed.

Figure 7.18 shows the results of the measured concentrations in the samples analysed. All measurements have an associated experimental uncertainty of 0.006%, while the SPS samples also show a statistical uncertainty from the analysis of three different samples. The ARN sample, produced in a controlled environment by an

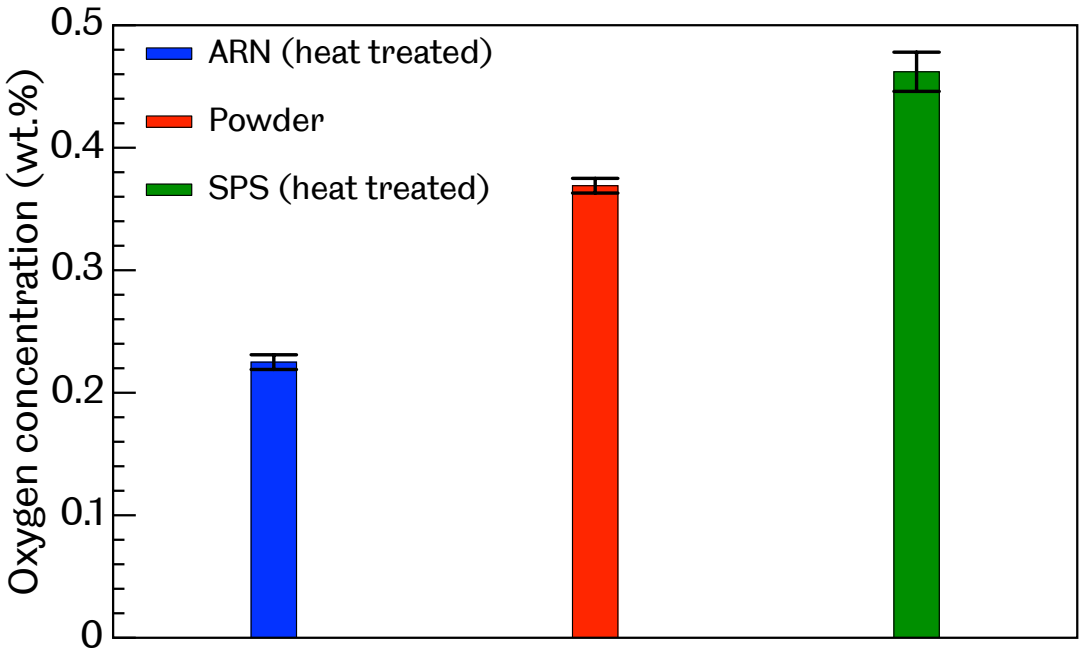

Figure 7.18: Bulk measurement of oxygen concentrations within $Sm_2(Co, Fe, Cu, Zr)_{17}$ powders used in project and sample sections of SPS and conventional sinter ('ARN') processed $Sm_2(Co, Fe, Cu, Zr)_{17}$, both after full heat treatment

optimised and conventional processing route, measured 0.225 wt.%; the lowest level of oxygen. Comparatively, the precursor powders used in this project measured at 0.369 wt.%, showing over the course of the project oxygen was prevalent in the $Sm_2(Co, Fe, Cu, Zr)_{17}$ material and at higher levels than in a commercial magnet after conventional sinter processing and heat treatment. The SPS processed and heat treated samples measured an average (from three specimens) of 0.462 wt.%. The lack of data point from the measurement of sample after SPS processing and before heat treatment means it cannot be said if any oxidation arises from the SPS process. However, it is evident from the LECO-O analysis that oxygen has contaminated the precursor powder and bulk concentration has been escalated after the heat treatment.

$Sm_2(Co, Fe, Cu, Zr)_{17}$ sintered magnets show evidence for oxides in the form of grain boundary Sm_2O_3 precipitates [75], and these features were observed in chapter 6 with the SEM and EDS analysis of conventional sinter processed $Sm_2(Co, Fe, Cu, Zr)_{17}$ magnets. Taking the ARN sample data as a reference for the background levels of oxygen in a controlled processing route, if comparison is made to the other data a threshold for severe and significant oxidation effects may be estimated. The $Sm_2(Co, Fe, Cu, Zr)_{17}$ powder measured significantly higher oxygen

levels, although XRD 2θ phase analysis showed no evidence of any oxidation related phases. After processing by SPS, a similar microstructure to the conventional sinter processed magnet; featuring Sm_2O_3 precipitates was observed, but again XRD 2θ phase analysis showed no evidence of oxidation related phases. While LECO-O measurement is lacking for the pre-heat treatment SPS processed magnet, for a minimum oxygen concentration equivalent to that measured in the powder, there does not appear to be any evidence of severe microstructural change at the surface of the material for this level of oxygen concentration. After heat treatment, the concentration of oxygen within the bulk increased further and it is in these samples that notable oxidation effects at the surface occurred. XRD 2θ phase analysis in section 7.3.1 showed the numerous phases present at the surface of the material and related to oxidation [106, 107, 110–113]. Removal of surface material in the SPS processed $Sm_2(Co, Fe, Cu, Zr)_{17}$ magnets reduced, or completely removed, the presence of these phases and the underlying phases were the same dominant phases identified in the $Sm_2(Co, Fe, Cu, Zr)_{17}$ powders, and in the SPS processed and conventional sinter processed $Sm_2(Co, Fe, Cu, Zr)_{17}$ samples. From the oxidation studies of [114], when the oxidation layers were removed, the magnetic properties were recovered. When this was performed on the SPS processed and heat treated $Sm_2(Co, Fe, Cu, Zr)_{17}$ magnets, an enhancement of the coercivity was measured, but not to comparable levels of the conventional sinter processed $Sm_2(Co, Fe, Cu, Zr)_{17}$ magnets. Therefore, it is hypothesised that the during the heat treatment, oxidation occurs primarily at the surface of the SPS processed $Sm_2(Co, Fe, Cu, Zr)_{17}$ sample, most likely as a result of the cooling in air from the homogenisation stage. However, as a result of the high oxygen content in the precursor $Sm_2(Co, Fe, Cu, Zr)_{17}$ powder, the bulk of the material has already been affected by elevated oxidation. As a result, samarium may be at lower bulk levels if there are more grain boundary Sm_2O_3 precipitates and this negatively affect the cellular nanostructure generated from the heat treatment and thus adversely affect the coercivity achievable.

7.4 Material characterisation after heat treatment

So far our study of the heat treatment process for SPS processed $Sm_2(Co, Fe, Cu, Zr)_{17}$ magnets has focussed on understanding and optimisation towards achieving the best magnetic properties, specifically the coercivity and energy product, for high performance permanent magnet applications. Accepting the limitations in the heat treatment developed, we can still apply this form of heat treatment to all SPS processed $Sm_2(Co, Fe, Cu, Zr)_{17}$ magnets and reassess the material properties studied in the previous chapter, namely grain size and resistivity. The resistivity of the material after heat treatment will become a significant benchmark for

the final chapter of this thesis. The broad range of SPS processing parameters studied in chapter 6 also allows a basis for whether the heat treatment used is dependent on the SPS processing parameters and/or the density of $Sm_2(Co, Fe, Cu, Zr)_{17}$.

7.4.1 Grain size measurement

One of the touted benefits of SPS technique is a minimisation of grain growth during the sinter process, which is often attributed to the high heating rates and short processing times at lower sintering temperatures, in comparison to conventional sinter techniques [36, 153, 171, 173, 175, 185, 191, 195, 209, 215, 307]. The average grain diameter by linear intercept method for pre-heat treatment $Sm_2(Co, Fe, Cu, Zr)_{17}$ magnets in chapter 6 was 8.5 ± 0.6µm. This value was larger than $\bar{a} = 5.9 \pm 0.8$µm; the averaged long-axis measurement of $Sm_2(Co, Fe, Cu, Zr)_{17}$ powder crystallites, showing some grain coarsening had occurred during the SPS processing cycle.

Here, we are able to make comparison of the grain sizes after heat treatment in both SPS and conventionally sintered $Sm_2(Co, Fe, Cu, Zr)_{17}$ magnets. Measurement of the grain diameters after heat treatment is also a better representation of the material properties in the work-ready state for $Sm_2(Co, Fe, Cu, Zr)_{17}$ magnets.

A citric acid solution was again used as an etchant to emphasise the grain boundary structure for a SPS processed and heat treated ('H-A8-SC') $Sm_2(Co, Fe, Cu, Zr)_{17}$ sample, 1-23. A full description of the process used is described in the methodology chapter 5. Figure 7.19 shows an example light microscopy image of the etched granular microstructure in sample 1-23.

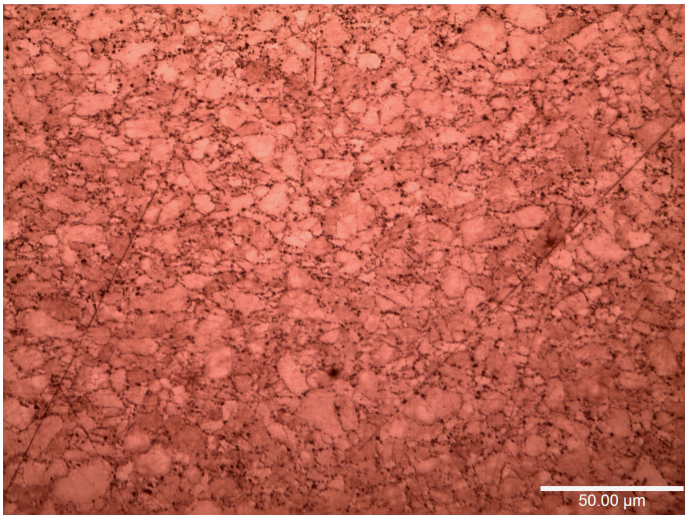

Figure 7.19: Light microscopy image of citric acid 10% solution etched SPS processed and heat treated ('H-A8-SC') $Sm_2(Co, Fe, Cu, Zr)_{17}$ sample 1-23.

Using the linear intercept method, the average grain diameter was measured in

the horizontal and vertical directions in two different regions of the material. By this method, with 95% confidence values calculated using a t-value of 2, the mean horizontal grain diameter for the SPS processed and heat treated sample 1-23 are 6.8 ± 0.3µm and the mean vertical grain diameter is 6.3 ± 0.3µm. The calculated average of these two measurements is 6.6 ± 0.4µm. Both measurements are slightly smaller than the equivalent measurements made in $Sm_2(Co, Fe, Cu, Zr)_{17}$ material before heat treatment, but approximately the same size as the averaged powder crystallite long axis.

The grain size measurements before and after heat treatment were made analysing different $Sm_2(Co, Fe, Cu, Zr)_{17}$ samples, although they share identical processing parameters by the SPS technique. It is also noted that approximately 50% more grains were measured in the post-heat treatment sample, so it is possible that the discrepancy in the grain size before and after heat treatment is due to minor sampling bias. Irrespective of this, from the study it can said that the grain diameters measured in our SPS processed $Sm_2(Co, Fe, Cu, Zr)_{17}$ magnets are, on average, less than 10 µm, even after heat treatment. Thus, very little, if any, grain coarsening occurs within the SPS processed and heat treated $Sm_2(Co, Fe, Cu, Zr)_{17}$ magnets using the processing parameters studied.

Grain size measurements were also made for a conventional sinter processed and heat treated $Sm_2(Co, Fe, Cu, Zr)_{17}$ sample ('ARN'), provided by Arnold Magnetic Technologies. The exact details of the heat treatment structure and parameters used for the ARN sample were not disclosed, but would follow a typical heat treatment used for $Sm_2(Co, Fe, Cu, Zr)_{17}$ permanent magnets, and thus, is similar to the one used in sample 1-23. The ARN sample was also etched using a citric acid solution and performed identically to the method used for the SPS processed $Sm_2(Co, Fe, Cu, Zr)_{17}$ specimens before and after heat treatment.

Figure 7.20 shows a light microscopy image taken of the etched granular structure of the ARN sample. The microscopy image was taken in dark-field viewing mode using cross-polarised light and manipulated using imageJ software, which significantly emphasised the grain boundary structure. Using the linear intercept method again, the mean grain diameter was measured to be 61.2 ± 3.3µm in the horizontal direction and 47.4 ± 3.4µm in the vertical direction of the image. The calculated average of these two measurements is 54.3 ± 4.9µm. A t-value of 2.15 was used to calculate the 95% confidence value. A relatively large variance in the horizontal and vertical grain size measurements is possibly a result of the irregularly shaped grains. The grains in the SPS processed $Sm_2(Co, Fe, Cu, Zr)_{17}$ magnets became more equiaxed with the pressure-assisted sinter process. Both the mean horizontal and vertical grain diameters measured in the ARN $Sm_2(Co, Fe, Cu, Zr)_{17}$

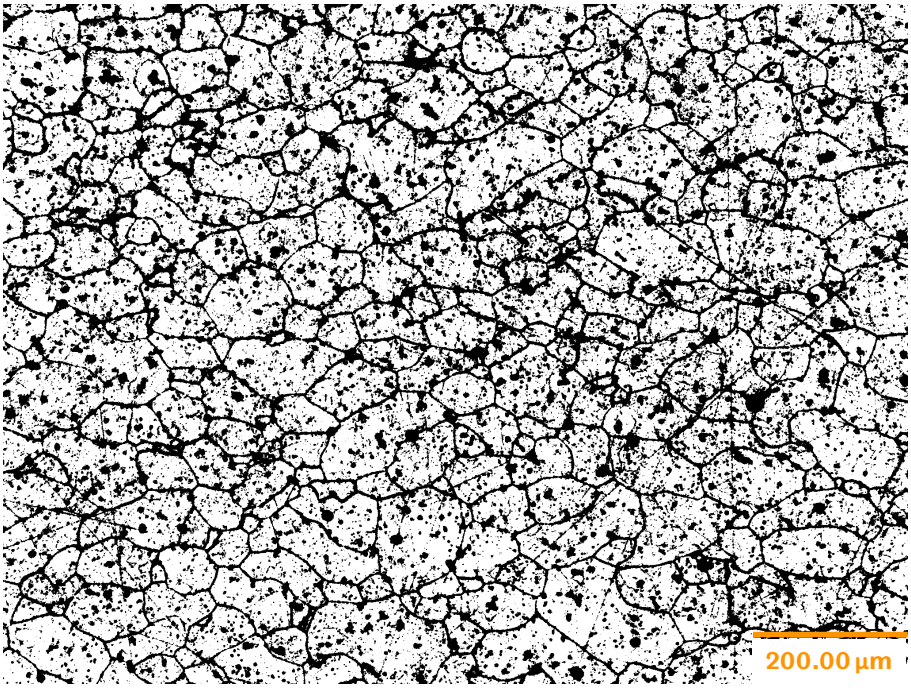

Figure 7.20: Dark-field and cross-polarised light image of conventional sinter processed and heat-treated $Sm_2(Co, Fe, Cu, Zr)_{17}$ sample 'ARN' after a surface etching using 10% concentration citric acid and water solution at 80 °C. Image processed in imageJ to highlight grain boundaries.

sample are significantly larger than the equivalent grain size measurements in the SPS processed and heat treated $Sm_2(Co, Fe, Cu, Zr)_{17}$ specimen, and also the averaged powder crystallite long axis diameter. Similar observations were reported in SPS processed $Sm_2(Co, Fe, Cu, Zr)_{17}$ magnets by Matsumoto et al. [223].

These results support the claim for suppressed grain growth when powders are consolidated using the SPS technique under optimised processing parameters. Assuming the ARN $Sm_2(Co, Fe, Cu, Zr)_{17}$ specimen has been produced using identical powders to those used in this project, the conventional sinter processing method also shows an order of magnitude grain growth after sintering and full heat treatment process.

7.4.2 Electrical resistivity measurements

The heat treatment of $Sm_2(Co, Fe, Cu, Zr)_{17}$ magnets changes the phase structure within the grains and this change may be evidenced in the electrical resistivity measurements. The results of the study for all measurable specimens are collected in table 7.7. Samples marked with †, and highlighted, were noticeably damage or cracked, but still in a measurable state and therefore their data was

recorded for completeness. As noted previously, sample 1-22 (a) refers to the magnet after homogenisation stage only and 1-22 (b) after a full heat treatment ('H-A4-SC').

There are a few obvious outliers in table 7.7 that warrant explanation. Samples 1-03, 1-25, 1-26 and 1-27, highlighted and denoted with a †, all measure considerably larger resistivity values compared to the rest of the specimens listed. These samples, from early heat treatment studies, were damaged from thermal shock when water quenched from 400 °C. The damage to the samples ranged from partial cracking, evident at the surface, to complete separation of the specimen. The latter occurred in samples 1-26 and 1-27 and were repaired using a minimal application of Loctite x648 glue to become measurable using the four probe VDP resistivity rig, as well as magnetic characterisation by hysteresisgraph. Acknowledging this, it is clear that these material defects have a significant effect on the electrical resistivity anisotropy (quantified by the 'Q' value) and resultant bulk resistivity measurement. Thermal shock damage was not observed in specimens once the quenching medium was changed to oil.

The relationship between electrical resistivity and density for the $Sm_2(Co, Fe, Cu, Zr)_{17}$ magnets which have received full heat treatments are shown in figure 7.21. Colour is used to denote the difference in the ageing time of the heat treatment. Filled symbols are magnetically 'isotropic', while unfilled symbols are magnetically anisotropic magnets, receiving powder alignment by magnetic field before the SPS process.

Sample ID	Heat treatment	t (cm)	I (A)	V1 (µV)	V2 (µV)	V3 (µV)	V4 (µV)	V5 (µV)	V6 (µV)	V7 (µV)	V8 (µV)	Q	ρ_H (µΩ cm)	ρ_V (µΩ cm)	ρ_{VDP} (µΩ cm)
1-01	H-A16-SC	0.43	0.302	12.00	12.00	14.00	14.00	12.00	12.00	14.00	14.00	1.17	76.84	89.65	83.25 ± 9.22
1-03†	A8-SC	0.50	0.298	38.17	38.17	14.33	14.00	38.00	38.00	14.00	14.00	2.70	275.86	102.01	188.94 ± 14.60
1-04	H-A16-SC	0.44	0.303	10.50	10.50	13.00	13.00	10.50	10.50	12.75	13.00	1.23	69.09	85.13	77.11 ± 9.53
1-05	H-A16-SC	0.51	0.302	10.33	10.50	11.50	11.33	10.33	10.50	11.67	11.67	1.11	79.40	87.97	83.68 ± 10.90
1-06	H-A16-SC	0.50	0.300	11.17	11.33	12.00	12.00	11.50	11.00	12.00	12.00	1.07	84.25	89.86	87.05 ± 10.69
1-07	H-A16-SC	0.43	0.302	13.00	13.00	14.50	14.50	13.00	13.00	14.75	14.75	1.13	83.76	94.23	89.00 ± 9.26
1-08	H-A16-SC	0.46	0.303	11.50	11.50	12.50	12.50	11.50	11.50	12.50	12.50	1.09	79.82	86.76	83.29 ± 9.92
1-09	H-A16-SC	0.45	0.302	11.00	11.00	12.50	12.75	11.00	11.00	12.50	12.50	1.14	72.78	83.12	77.95 ± 9.49
1-10	H-A16-SC	0.43	0.302	12.00	12.00	13.00	13.00	12.00	12.00	13.00	13.00	1.08	78.28	84.80	81.54 ± 9.33
1-11	H-A16-SC	0.43	0.304	10.50	10.50	12.00	12.00	10.50	10.50	12.25	12.00	1.15	65.97	75.79	70.88 ± 9.01
1-12	H-A16-SC	0.40	0.304	11.25	11.00	13.75	13.75	11.25	11.25	13.50	13.50	1.22	66.22	80.64	73.43 ± 8.57
1-16	H-A16-SC	0.32	0.302	14.00	14.00	17.75	18.00	14.00	14.00	18.00	18.00	1.28	66.22	84.84	75.53 ± 6.94
1-17	H-A16-SC	0.37	0.302	12.50	13.00	14.00	14.00	12.50	12.75	14.00	14.00	1.10	70.56	77.86	74.21 ± 7.98
1-19	H-A16-SC	0.38	0.300	13.50	13.50	12.00	12.00	13.50	13.50	12.00	12.00	1.13	76.26	67.78	72.02 ± 8.10
1-20	H-A8-SC	0.47	0.302	9.50	9.50	11.00	11.00	9.50	9.75	11.00	11.00	1.15	66.44	76.43	71.44 ± 9.96
1-22 (a)	H	0.44	0.302	13.25	13.50	14.50	14.50	13.50	13.25	14.50	14.50	1.08	88.99	96.48	92.73 ± 9.54
1-22 (b)	H-A4-SC	0.43	0.306	11.00	11.00	12.75	12.75	11.50	11.50	12.75	12.75	1.13	70.19	79.55	74.87 ± 8.95
1-23	H-A8-SC	0.42	0.300	12.00	12.00	12.50	12.50	12.00	12.00	12.50	12.50	1.04	76.39	79.57	77.98 ± 9.09
1-24	H-A16-SC	0.44	0.298	11.50	11.50	12.50	12.50	11.50	11.50	12.75	12.75	1.10	76.67	84.17	80.42 ± 9.49
1-25†	H-A24-SC	0.45	0.300	12.50	12.50	31.75	31.75	12.50	12.50	31.00	31.25	2.52	81.58	205.18	143.38 ± 12.34
1-26†	H-A16-SC	0.46	0.928	73.00	75.00	98.50	98.50	120.25	121.25	98.00	98.00	1.01	217.82	219.77	218.79 ± 3.54
1-27†	H-A16-SC	0.44	0.300	33.75	33.75	34.75	34.75	33.75	33.75	35.00	35.00	1.03	226.39	233.94	230.16 ± 10.12
1-28	H-A16-SC	0.46	0.298	9.00	9.00	11.00	11.00	9.00	9.00	11.00	11.00	1.22	61.75	75.47	68.61 ± 9.91
1-29	H-A16-SC	0.45	0.299	9.50	9.50	11.00	11.00	9.50	9.50	11.00	11.00	1.16	64.01	74.12	69.07 ± 9.66
1-32	H-A16-SC	0.42	0.307	6.00	6.00	7.00	7.00	6.00	6.00	7.00	7.00	1.17	37.07	43.24	40.15 ± 8.83
1-33	H-A2-SC	0.45	0.302	13.50	13.50	11.83	11.67	13.50	13.50	11.67	11.67	1.15	90.06	78.11	84.08 ± 9.59

Table 7.7: Measured current and potential difference values and calculated resistivity measurements by VDP method for $Sm_2(Co, Fe, Cu, Zr)_{17}$ samples processed by SPS. 't' refers to the thickness of the specimen, 'I' is the electric current, 'V' is the measured potential difference (subscript number refers to the direction of measurement in the VDP method, 'Q' is ratio of $\frac{V_{horizontal}}{V_{vertical}}$ used to derive the correction factor, *f*. Rows highlighted and denoted† are noticeably damaged/cracked.

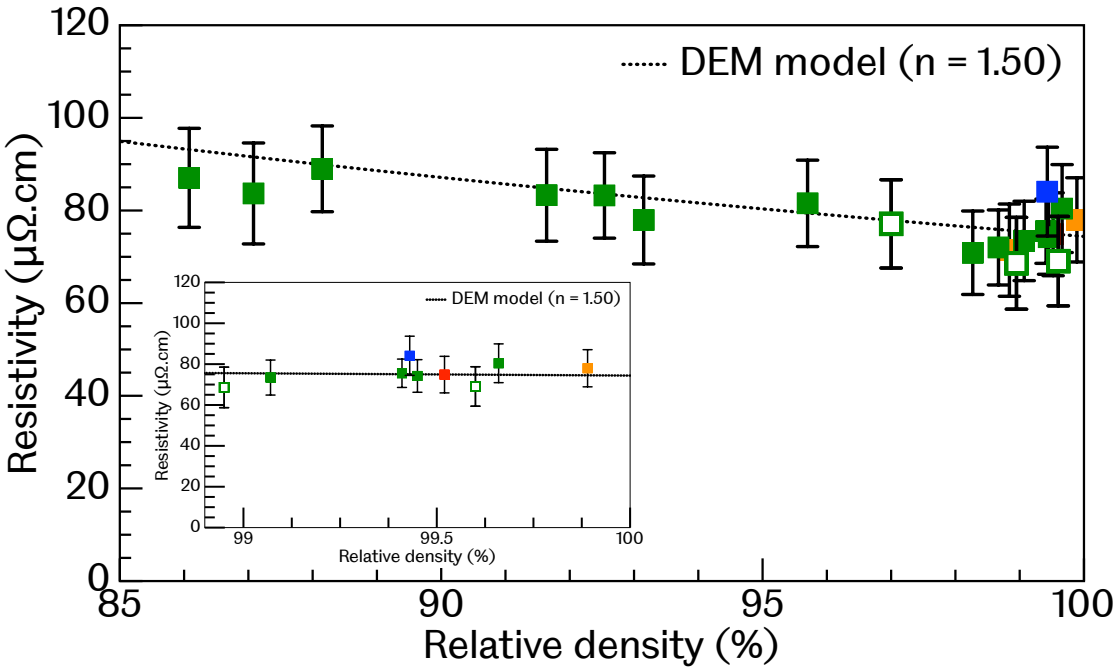

Figure 7.21: Resistivity measurements plot against relative density for SPS processed and heat treated $Sm_2(Co, Fe, Cu, Zr)_{17}$ magnets. Colour indicates the ageing time used in the heat treatment. Unfilled symbols have axial powder alignment before SPS process. Sample 1-32 data ommited from plot as outlier. Inset shows specimens with relative densities >99%. Relative density is calculated using solid density $8.4\,g/cm^3$ [131, 292]

Before heat treatment, the resistivity of the SPS processed $Sm_2(Co, Fe, Cu, Zr)_{17}$ magnets increased as density decreased (or porosity increased). The trend was well replicated, for relative densities ranging between 85% and 100%, by the reciprocal of the Differential Effective Medium (DEM) model for conductivity, where the exponent of the equation, $n = 1.50$, represented roughly spherical pores. After heat treatment, figure 7.21 shows the same relationship and the DEM model for $n = 1.50$ is in good agreement with the data. To calculate the DEM model for the $Sm_2(Co, Fe, Cu, Zr)_{17}$ material, a theoretical density of $8.4\,g/cm^3$ [131, 292] is used and the electrical resistivity at this density is assumed as $74.4\,\mu\Omega \cdot cm$, which is the average resistivity for the specimens in the inset of figure 7.21 with relative densities >98% and in agreement with literature values for full heat treated $Sm_2(Co, Fe, Cu, Zr)_{17}$ magnets [131, 132]. In general, the measured resistivities for the $Sm_2(Co, Fe, Cu, Zr)_{17}$ specimens after heat treatment are lower than when measured before heat treatment. Before heat treatment, the averaged electrical resistivity for the SPS processed $Sm_2(Co, Fe, Cu, Zr)_{17}$ specimens with relative densities greater than 98% is $91.8\,\mu\Omega\,cm$, while after heat treatment the averaged resistivity is $74.4\,\mu\Omega\,cm$. The change in bulk resistivity measurement is seen in

all full heat treatment specimens and is a consequence of the precipitation of the Fe rich 2:17R cells, Cu rich 1:5H cell walls and Zr rich lamellar structure during the heat treatment [67], specifically the ageing and slow cooling stage, and the values reported here are comparable to the resistivities measured in studies of the heat treatment stages of $Sm_2(Co, Fe, Cu, Zr)_{17}$ magnets [131, 132]. Sample 1-22 (a) is an example of a sample which only underwent the homogenisation stage of the heat treatment process and table 7.7 shows the resistivity of this specimen is comparable to those of pre-heat treatment specimens. Sample 1-32 is highlighted by the dashed circle and has seen an abnormal decrease in the resistivity.

Samples 1-28 and 1-29, which were used in the study of the magnetic properties before and after removal of surface oxidation material, have received identical processing and heat treatment ('H-A16-SC') and were measured by VDP method before and after removal of 200 µm of surface material by mechanical polishing methods. XRD phase analysis showed the most abundant phase present in the oxidised $Sm_2(Co, Fe, Cu, Zr)_{17}$ specimens after heat treatment was the Co-Fe phase, which also has a lower resistivity than the $Sm_2(Co, Fe, Cu, Zr)_{17}$ bulk material [308]. Table 7.8 shows the results of the study.

Sample ID	**t (cm)**	**I (A)**	**Q**	ρ_H **(µΩ cm)**	ρ_V **(µΩ cm)**	ρ_{VDP} **(µΩ cm)**
1-28	0.46	0.298	1.22	61.75	75.47	68.61 ± 9.91
1-28 + 200 µm SP	0.40	0.300	1.18	66.30	78.36	72.33 ± 8.68
1-29	0.45	0.299	1.16	64.01	74.12	69.07 ± 9.66
1-29 + 200 µm SP	0.41	0.300	1.18	66.96	79.14	73.05 ± 8.77

Table 7.8: Electrical resistivity values for SPS processed and heat treated $Sm_2(Co, Fe, Cu, Zr)_{17}$ samples by VDP method before and after an extended and controlled mechanical surface polish, removing at least 200 µm of surface material.'t' refers to the thickness of the specimen, 'I' is the electric current, 'Q' is the ratio of the horizontal and vertical resistivity measures and is used to calculate the correction factor, *f*, for the VDP resistivity calculation, and 'ρ' is the resistivity where the subscripts 'H', 'V' and 'VDP' refer to the horizontal, vertical and bulk VDP resistivity respectively.

After removal of 200 µm of surface material, the resistivity did not significantly change in the $Sm_2(Co, Fe, Cu, Zr)_{17}$ specimens 1-28 and 1-29. Thus, removal of the Co-Fe phase has not changed the measured resistivity, reaffirming the original results as representative of the bulk material. These results further emphasise that, while the oxidation phases are present at the surface after the heat treatment, they evidently do not ingress significantly into the material surface, with respect to the overall thickness of the samples.

However, while these results are fairly conclusive for full density

$Sm_2(Co, Fe, Cu, Zr)_{17}$ specimens, an outlier exists in the form of sample 1-32. Sample 1-32 recorded the largest resistivity ($176.67 \pm 11.80 \mu\Omega\,cm$) before heat treatment, which fit the trend of resistivity increasing as density decreased. After a full heat treatment ('H-A16-SC'), the resistivity dropped considerably to $40.15 \pm 8.83\ \mu\Omega\,cm$. Sample 1-32 was processed using sub-optimal SPS parameters and possess the lowest density of all SPS produced $Sm_2(Co, Fe, Cu, Zr)_{17}$ magnets. As a result of being low density, the standard mechanical surface polish after the heat treatment removed significantly more material in sample 1-32 (estimated at 1 mm), compared to full density specimens (typically around 100 µm to 200 µm). Even with so much more surface material removed in sample 1-32, the XRD 2θ phase analysis (figure 7.10) still showed prevalent oxidation phases. The unusually low resistivity of the high porosity specimen 1-32 must have had much more oxidation occur throughout the bulk of the material and as a result, the lower resistivity Co-Fe phase [308], is influencing the bulk resistivity. This suggests a correlation between the density, or volume fraction of porosity within the volume, and the extent of oxidation, which is either confined to the surface or prevalent within the bulk due to the oxidation of the precursor powders. However, for oxygen to permeate through the volume via porosity, a network of open celled pores must exist within the $Sm_2(Co, Fe, Cu, Zr)_{17}$ volume, which would be unusual even for relative densities of 72%.

7.5 Magnetic characterisation after heat treatment

Applying the general form of the heat treatment to all SPS processed $Sm_2(Co, Fe, Cu, Zr)_{17}$ magnets allows us to investigate any trends in their magnetic performance with respect to their heat treatment and the SPS processing parameters, which are strongly linked to the specimen density. The study also allows us to test the reproducibility of the magnetic properties reported in the heat treatment and ageing time study (section 7.2.3). These results will help confirm the optimal heat treatment to use for the isotropic SPS processed $Sm_2(Co, Fe, Cu, Zr)_{17}$ magnets if the desired applications require high room temperature coercivities or high energy products.

Following heat treatment, all SPS processed $Sm_2(Co, Fe, Cu, Zr)_{17}$ samples were mechanically surface polished until the surface was again visibly clear of discolouration and clean. Magnetic characterisation was performed using hysteresisgraph after magnetisation of the specimens by 3.5 T pulsed magnetic field. Table 7.9 collects the magnetic properties measured from the demagnetisation curves, as well as detailing the heat treatment used and the relative density, measured

Sample ID	Powder alignment	Heat treatment	J_r (T)	bH_c (kA/m)	iH_c (kA/m)	$(BH)_{max}$ (kJ/m^3)	% relative density
1-03 †	Pulsed-axial (once)(2.5 T)	A8-SC	0.63 ± 0.03	79.23 ± 3.96	94.30 ± 4.72	16.00 ± 0.80	91.40
1-04	Pulsed-axial (twice) (2.5 T)	H-A16-SC	0.67 ± 0.03	265.00 ± 13.25	533.00 ± 26.65	50.00 ± 2.50	97.00
1-28	Pulsed-axial (thrice) (2.5 T)	H-A16-SC	0.63 ± 0.03	238.00 ± 11.90	446.00 ± 22.30	42.00 ± 2.10	98.95
1-29	DCEM-axial (0.23 T)	H-A16-SC	0.62 ± 0.03	213.00 ± 10.65	366.00 ± 18.30	37.00 ± 1.85	99.60
1-01	Isotropic	H-A16-SC	0.43 ± 0.02	138.00 ± 6.90	204.00 ± 10.20	16.00 ± 0.80	92.54
1-07	Isotropic	H-A16-SC	0.32 ± 0.02	57.90 ± 2.90	69.20 ± 3.46	5.30 ± 0.27	88.15
1-08	Isotropic	H-A16-SC	0.43 ± 0.02	136.00 ± 6.80	202.00 ± 10.10	17.00 ± 0.85	91.64
1-09	Isotropic	H-A16-SC	0.48 ± 0.03	200.00 ± 10.00	388.00 ± 19.41	26.00 ± 1.32	93.15
1-10	Isotropic	H-A16-SC	0.50 ± 0.03	226.00 ± 11.30	515.00 ± 25.75	30.00 ± 1.50	95.70
1-11	Isotropic	H-A16-SC	0.52 ± 0.03	229.00 ± 11.45	507.00 ± 25.35	31.00 ± 1.55	98.27
1-12	Isotropic	H-A16-SC	0.51 ± 0.03	228.00 ± 11.40	507.00 ± 25.35	30.00 ± 1.50	99.07
1-20	Isotropic	H-A8-SC	0.54 ± 0.03	269.00 ± 13.45	649.00 ± 32.45	39.00 ± 1.95	98.84
1-22 (a)	Isotropic	H	0.30 ± 0.03	34.13 ± 2.31	36.90 ± 3.19	3.13 ± 0.37	99.41
1-22 (b)	Isotropic	H-A4-SC	0.53 ± 0.03	254.00 ± 12.70	553.00 ± 27.65	35.00 ± 1.75	99.52
1-23	Isotropic	H-A8-SC	0.53 ± 0.03	288.50 ± 14.43	592.50 ± 29.63	42.00 ± 2.10	99.89
1-24	Isotropic	H-A16-SC	0.55 ± 0.03	287.50 ± 14.38	470.00 ± 23.50	45.00 ± 2.25	99.66
1-25 †	Isotropic	H-A24-SC	0.51 ± 0.03	209.00 ± 10.45	395.50 ± 19.78	29.00 ± 1.45	98.77
1-26 †	Isotropic	H-A16-SC	0.49 ± 0.03	208.00 ± 10.40	421.00 ± 21.07	26.00 ± 1.30	95.86
1-27 †	Isotropic	H*-A16-SC	0.52 ± 0.03	228.00 ± 11.40	462.00 ± 23.10	31.00 ± 1.55	97.57
1-32	Isotropic	H-A16-SC	0.21 ± 0.01	11.30 ± 0.57	12.10 ± 0.61	0.53 ± 0.03	71.77
1-33	Isotropic	H-A2-SC	0.56 ± 0.03	269.00 ± 13.45	428.00 ± 21.40	42.00 ± 2.10	99.43
ARN-4	Isotropic	H-A-SC	0.56 ± 0.03	>211.00 ± 10.55	>1214.00 ± 60.70	56.07 ± 2.80	98.89
ARN-5	Isotropic	H-A-SC	0.56 ± 0.03	>211.00 ± 10.55	>1078.00 ± 53.90	56.65 ± 2.83	99.87

Table 7.9: Magnetic properties of SPS processed and heat treated $Sm_2(Co, Fe, Cu, Zr)_{17}$ magnets, as measured by hysteresisgraph. Highlighted rows and † symbol indicate cracked/damaged specimens. 'ARN' specimens are comparative $Sm_2(Co, Fe, Cu, Zr)_{17}$ magnets processed by conventional sinter methods and their coercivities represent lower bound measurements which exceed to capabilities of the hysteresisgraph. Relative density is calculated using solid density 8.4 g/cm^3 [131, 292].

after heat treatment. To repeat the nomenclature used; the three stages of heat treatment are labelled with shorthand letters: Homogenisation (H), Ageing (A) and Slow Cooling (SC), and reference to specific stages of the heat treatment are described by the heat treatment parameters in table 7.1. Sample 1-27 transitioned from the homogenisation to ageing stage under argon atmosphere and thus its heat treatment is labelled 'H*-A16-SC'. Samples 1-03, 1-25, 1-26 and 1-27 have previously been noted as being damaged/cracked as a result of thermal shock from water quenching from 400 °C at the end of the heat treatment process. Samples 1-26 and 1-27 were repaired using minimal application of glue (Loctite x648) to make measurable. These samples are highlighted in table 7.9 and denoted with a † symbol. Isotropic conventional sinter processed $Sm_2(Co, Fe, Cu, Zr)_{17}$ provide a comparison to fully optimised commercial permanent magnet properties. The exact details of the heat treatment applied to the 'ARN' $Sm_2(Co, Fe, Cu, Zr)_{17}$ magnets are not known, but it is expected to be typical of this type of magnet and similar to that used in our study, albeit optimised to maximise room temperature coercivity.

The data reported in table 7.9 show that, when processed under optimal SPS parameters and relative densities are in excess of 95%, the fully heat treated $Sm_2(Co, Fe, Cu, Zr)_{17}$ magnets achieve intrinsic coercivities, iH_c >400 kA/m. The largest coercivities are achieved in two specimens, 1-20 and 1-23, both of which have been fully heat treated and aged for 8 hours. For applications which require the largest room temperature coercivities, the 'H-A8-SC' heat treatment is best suited for the SPS processed $Sm_2(Co, Fe, Cu, Zr)_{17}$ permanent magnets in our study.

The majority of the heat treated specimens have been aged for 16 hours and there is strong consistency in the measured values in specimens with relative densities in excess of 95%. The damaged/cracked specimens, highlighted in table 7.9 and denoted † symbol, do not show any significant negative effects on their magnetic properties as a result of their damage. Sub-optimally SPS processed $Sm_2(Co, Fe, Cu, Zr)_{17}$ magnets with relative densities lower than 95% measure noticeably lower coercivities. This is most obvious in samples 1-07 and 1-32, which measure lower intrinsic coercivities than when measured before heat treatment (1-07 $iH_c = 84.49 \pm 4.23$ kA/m and 1-32 $iH_c = 61.60 \pm 3.08$ kA/m). Sample 1-32 showed similar deleterious effects in resistivity measurements after heat treatment, which was attributed to significant oxidation throughout the bulk material linked to the large volume fraction of porosity in the magnet. The Co-Fe phase is soft-magnetic and, if prevalent throughout the material volume, would have a negative effect on the coercivity. It is possible significant oxidation also effects sample 1-07, which has a relative density of 88%. If oxidation effects are not thought to be as significant when restricted to the surface, as appears to be the case from the studies in section 7.3.2, then it is recommended the minimum allowable relative density of the SPS processed magnets is 95%, where above this value the magnetic properties are most stable with respect to the heat treatment used.

To better visualise the data in table 7.9, figures 7.22 to 7.24 show the relationships between the remanent polarisation, intrinsic coercivity and energy product with respect to the relative density. The plots only include data for $Sm_2(Co, Fe, Cu, Zr)_{17}$ magnets that have received full heat treatments. This includes both the SPS processed magnets (square symbols) and the conventional sinter method processed magnets (diamond symbols) and colour is used to depict the length of the ageing stage in hours. Filled symbols are for data where no powder alignment has been used before processing, while unfilled symbols have received axial alignment, either through pulsed or DCEM field. The low density SPS processed specimens 1-32 and 1-07 have been omitted from figures 7.22 to 7.24, as their magnetic properties are believed to be significantly affected by oxidation effects and are outliers.

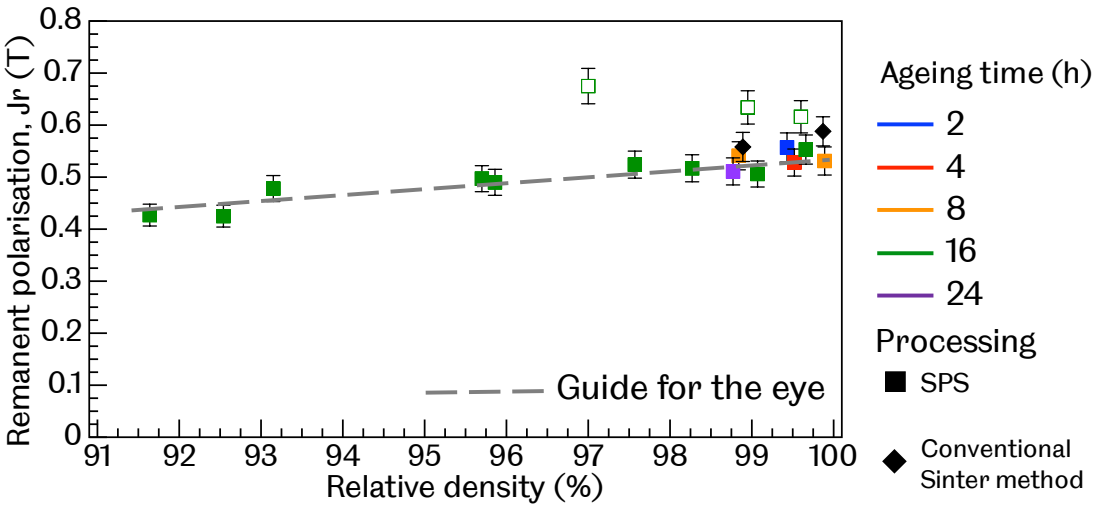

Figure 7.22: Remanent polarisation, J_r, measured against density for fully heat treated SPS processed (square symbols) and conventional sinter method processed (diamond symbols) $Sm_2(Co, Fe, Cu, Zr)_{17}$ magnets. Relative density is calculated using solid density $8.4\,g/cm^3$ [131, 292]

Figure 7.22 shows a general trend for the isotropic magnets, where J_r increases with the density. A dashed line used as a guide for the eye and the remanence appears largely independent of the ageing time used in the heat treatment. The conventional sinter processed 'ARN' magnets (diamond symbols) also fit the trend for similarly isotropic $Sm_2(Co, Fe, Cu, Zr)_{17}$ magnets. The outliers in figure 7.22 are the $Sm_2(Co, Fe, Cu, Zr)_{17}$ magnets which received partial powder alignment before the SPS process (unfilled symbols) and have noticeably larger J_r values in comparison to their non-powder aligned counterparts. With optimised powder alignment, a similarly alloyed $Sm_2(Co, Fe, Cu, Zr)_{17}$ permanent magnet can achieve a $J_r = 1.07\,T$ [309]. Overall, the remanent polarisation values have increased for all SPS processed $Sm_2(Co, Fe, Cu, Zr)_{17}$ magnets after heat treatment, an effect alluded to phase changes and elemental redistribution during the ageing and slow cooling stages. This effect is most strongly felt at higher densities, as the observed trend in figure 7.22 is different to the equivalent plot before heat treatment, which showed J_r was approximately constant for the isotropic magnets above 95% relative density.

The primary motivation for the heat treatment of the SPS processed $Sm_2(Co, Fe, Cu, Zr)_{17}$ magnets was to increase the coercive field. Before heat treatment, the intrinsic coercivity measured for the SPS processed $Sm_2(Co, Fe, Cu, Zr)_{17}$ magnets was consistently below $100\,kA/m$. There was also a general trend where

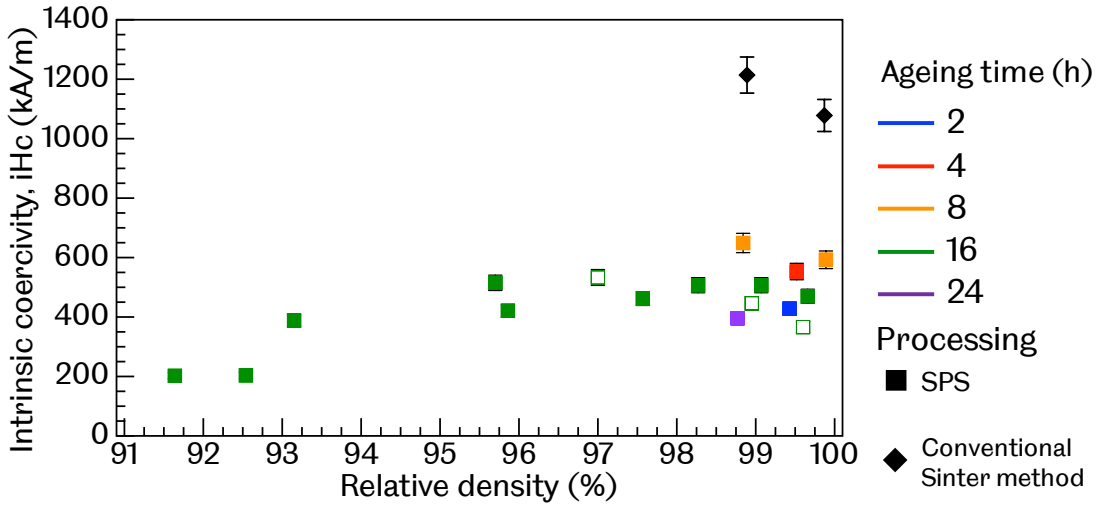

Figure 7.23: Intrinsic coercivity, iH_c, measured against density for fully heat treated SPS processed (square symbols) and conventional sinter method processed (diamond symbols) $Sm_2(Co, Fe, Cu, Zr)_{17}$ magnets. Colour represents ageing time used. Relative density is calculated using solid density $8.4\,g/cm^3$ [131, 292]

the coercivity increased as density decreased, which was shown to be due to an increase in porosity increasing the pinning field of the as-processed magnets. Figure 7.6 shows the data for the same SPS processed $Sm_2(Co, Fe, Cu, Zr)_{17}$ magnets after heat treatment. Here, the trend is much different and now the coercivity generally increases with density up to 95% relative density, where the data plateaus and remains approximately constant with increasing density. The effect of porosity is clearly now detrimental to the coercivity of the heat treated $Sm_2(Co, Fe, Cu, Zr)_{17}$ magnets. Increasing volume fraction of pores may either interfere with the pinning mechanism of the cellular nanostructure within the grains or be linked to the increasing oxidation effects in lower density specimens.

Figure 7.23 also shows the ageing time of the heat treatment has an influence on the coercivity for the $Sm_2(Co, Fe, Cu, Zr)_{17}$ magnets. The largest coercivities are reported for the 4 and 8 hour aged samples (red and orange squares respectively), reaffirming the conclusions of the initial ageing time study in section 7.2. There is also strong consistency in the coercivities for specimens near full density which were aged for 16 hours (green squares). The lowest coercivities recorded in isotropic samples at full density are for the 2 hour and 24 hour aged $Sm_2(Co, Fe, Cu, Zr)_{17}$ magnets. It is inferred that these forms of heat treatment under and over-develop the 2:17R cells and 1:5H cell walls, leading to lower pinning effects and coercivities. Powder alignment only has a minor effect on the coercivity, slightly reducing the coercivity at full density. Stronger self-demagnetising fields are experienced in

aligned magnets [302].

The ARN magnets (black diamonds) show the potential coercivity that could be achieved with an optimised heat treatment process and better control over oxidation in the SPS processed $Sm_2(Co, Fe, Cu, Zr)_{17}$ magnets. This is further emphasised by the fact that the measured coercivities for the ARN permanent magnets are a lower bound value, as the hysteresisgraph is limited in measurement high coercivity permanent magnets. While the study of the magnetic properties after an estimated 200 µm of surface material removal showed no significant recovery of the coercivity, oxidation effects may still penetrate into the bulk material and, through removal of crucial alloying elements such as Cu, disrupt the formation of an uniform and well formed cellular nanostructure [114, 306]. FEM micromagnetic simulations showed this effect to reduce the coercivity in models replicating the $Sm_2(Co, Fe, Cu, Zr)_{17}$ 2:17R cell and 1:5H cell wall structure.

Grain size effects may also negatively affect the achievable coercivity in the SPS processed $Sm_2(Co, Fe, Cu, Zr)_{17}$ magnets, which are an order of magnitude smaller than the ARN magnets. Generally, the grain size is not thought to be significant to the magnetic properties of conventional, heat treated $Sm_2(Co, Fe, Cu, Zr)_{17}$ magnets, as it is the cellular structure within the grains that are most integral to the coercivity. However, the grain boundaries, which are rich in Zr and Sm-oxides, remove these elements from regions in the grain close to the grain boundaries. This has been shown to affect the formation of a uniform cellular nanostructure at the grain peripheries [310]. The greater volume fraction of grain boundaries in the finer grained SPS processed $Sm_2(Co, Fe, Cu, Zr)_{17}$ magnets may therefore have greater regions of inhomogeneity, affecting the pinning potential of the $Sm_2(Co, Fe, Cu, Zr)_{17}$ material.

The energy product, $(BH)_{max}$, in figure 7.24 naturally follows the same positive linear relationship seen with the remanent polarisation and coercivity (albeit coercive force, which has approximately the same trend as intrinsic coercivity) with density in full heat treatment $Sm_2(Co, Fe, Cu, Zr)_{17}$ permanent magnets. The largest energy product was measured in the powder aligned sample 1-04, which after a full heat treatment ('H-A16-SC') recorded $(BH)_{max} = 50.0 \pm 2.5 kJ/m^3$. The other partially powder aligned (unfilled symbols) SPS processed $Sm_2(Co, Fe, Cu, Zr)_{17}$ magnets measure energy products comparable to non-powder aligned magnets. Of the isotropic SPS processed $Sm_2(Co, Fe, Cu, Zr)_{17}$ magnets, the energy products at full density are approximately the same for the specimens aged between 2 and 16 hours.

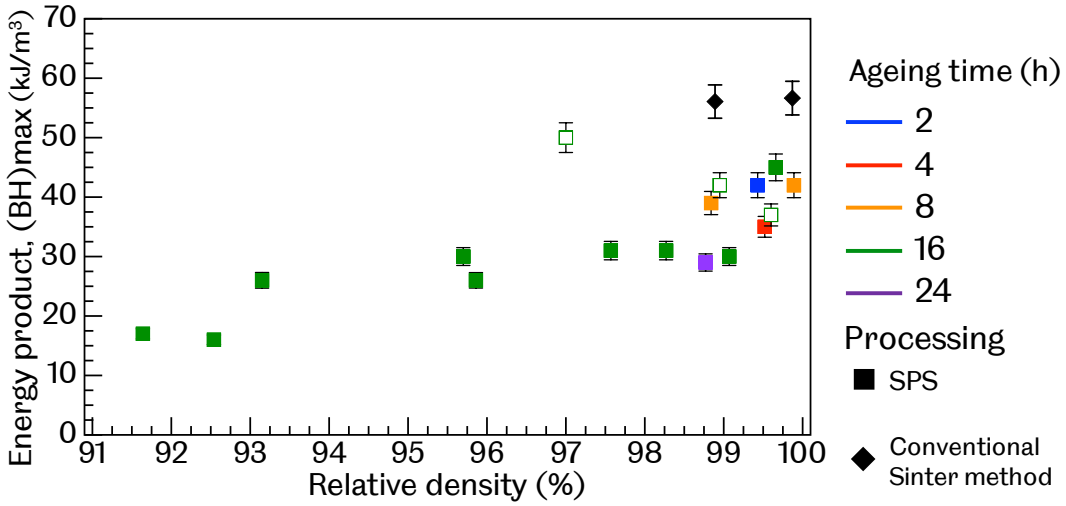

Figure 7.24: Energy product, $(BH)_{max}$, measured against density for fully heat treated SPS processed (square symbols) and conventional sinter method processed (diamond symbols) $Sm_2(Co, Fe, Cu, Zr)_{17}$ magnets. Colour represents ageing time used. Relative density is calculated using solid density $8.4\,g/cm^3$ [131, 292]

7.6 Chapter summary

This chapter has dealt with the study of the heat treatment necessary for SPS processed $Sm_2(Co, Fe, Cu, Zr)_{17}$ magnets designed for high room temperature coercivity. Specific stages of the heat treatment were investigated with respect to their effect on the material and magnetic properties and it was confirmed that a full heat treatment; consisting of a homogenisation stage, an ageing stage and slow cooling to quench, was essential to enhance the coercivity of the SPS processed $Sm_2(Co, Fe, Cu, Zr)_{17}$ magnets.

A systematic study of the ageing time followed, which again focussed on maximising the coercivity and energy product of the permanent magnet for high performance applications. The following heat treatment was found to produce the best performing SPS processed, isotropic $Sm_2(Co, Fe, Cu, Zr)_{17}$ magnet.

1. Homogenisation - 1170 °C for 2 hours in an argon atmosphere. Cooled slowly in air to room temperature.

2. Ageing - 850 °C for 8 hours (for largest coercivity) or 16 hours (for largest $(BH)_{max}$) in argon atmosphere.

3. Slow cool (1 °C/min) from 850 °C to 400 °C in argon atmosphere. Quench in oil to room temperature.

The maximum intrinsic coercivity was measured in an isotropic SPS processed $Sm_2(Co, Fe, Cu, Zr)_{17}$ magnet aged for 8 hours, where $iH_c = 649kA/m$, and the max-

imum energy product was measured in a partially powder aligned specimen aged for 16 hours, where $(BH)_{max} = 50 kJ/m^3$. The maximum energy product in non-powder aligned SPS processed $Sm_2(Co, Fe, Cu, Zr)_{17}$ magnets was $(BH)_{max} = 45 kJ/m^3$, which was measured in two specimens aged either 8 or 16 hours. Future study would look to improve on the aforementioned magnetic properties through optimisation of the heat treatment process and parameters. The SPS technique is well suited to this type of study, with high-reproducibility, rapid batch processing able to produce full density specimens for systematic study.

The heat treatment study has been affected by oxidation which has likely come from two sources: Higher concentrations of oxygen were measured in the bulk of the $Sm_2(Co, Fe, Cu, Zr)_{17}$ powders and SPS processed and heat treated samples than in the commercial and conventional sinter processed $Sm_2(Co, Fe, Cu, Zr)_{17}$ magnet. It is expected that the handling and storage of the $Sm_2(Co, Fe, Cu, Zr)_{17}$ powders has resulted in elevated oxygen levels from the beginning of processing. Secondly, allowing the samples to air cool from homogenisation stage of the heat treatment has also seen significant oxidation occur at the surface of the SPS processed $Sm_2(Co, Fe, Cu, Zr)_{17}$ magnets. Further study may look to investigate using the SPS to not only consolidate the powders but also perform the homogenisation stage (2 hours at 1170 °C) and rapid cool to room temperature, which was not available in this study.

The effect of oxidation on the magnetic and material properties can be significant in the removal of samarium and a disruption to the cellular precipitation nanostructure, as well as forming soft magnetic phases at the surface. FEM micromagnetic models complemented analytical studies within the literature, showing the soft magnetic Co-Fe phase can strongly influence the demagnetisation curve and coercivity of oxidation affected $Sm_2(Co, Fe, Cu, Zr)_{17}$ magnets. However, for $Sm_2(Co, Fe, Cu, Zr)_{17}$ magnets processed under optimal SPS processing parameters, the oxidation-related phases are mostly confined to the surface and depths of 200 µm. Removal of this surface material showed a slight improvement in the coercivity and no effect on the resistivity. The higher concentration of oxygen in the bulk of the material may be affecting the formation of the 2:17R cells and 1:5H cell boundaries during the heat treatment in the removal of samarium and the formation of Sm_2O_3.

Therefore, it is believed that with improved storage and handling of the $Sm_2(Co, Fe, Cu, Zr)_{17}$ powders and better control of the heat treatment process, in combination with optimisation of the heat treatment parameters, would further improve the magnetic properties, specifically the coercivity, of the SPS processed $Sm_2(Co, Fe, Cu, Zr)_{17}$ magnets and become comparable to magnets processed by conventional sinter method. For optimal powder aligned and heat treated $Sm_2(Co, Fe, Cu, Zr)_{17}$ magnets of a similar alloyed composition used in our stud-

ies, the energy product achievable is between 195 kJ/m^3 to 225 kJ/m^3 [309].

Chapter 8

Increased resistivity SmCoFeCuZr magnets

8.1 Introduction

The SPS technique as a rapid batch processing tool is well suited to prototyping and reproducing specimens for systematic study. This has been used to study both the optimal processing parameters for full density $Sm_2(Co, Fe, Cu, Zr)_{17}$ and the necessary heat treatment to enhance the coercivity significantly. Here, we use this feature of the SPS technique, as well as the information and knowledge developed thus far for SPS processed $Sm_2(Co, Fe, Cu, Zr)_{17}$ permanent magnets, to study high resistivity composite permanent magnets. In chapter 2, eddy current effects were introduced as one form of losses in electrical machines and drives [123, 124]. While rotor eddy current losses are generally not the largest losses experienced, it is the generation of heat from the circulating electrons in the REPM that causes irreversible demagnetisation and reduced performance [6, 97, 108].

Chapter 2 detailed the methods used to minimise the eddy current effects. Segmentation, which can be axial or circumferential, involves cutting the magnet and applying an electrically insulating layer before reassembly [6, 126, 128]. While this is a successful method in reducing eddy current effects, by limiting their circulating area, it is a costly, wasteful and time consuming production method. Studies investigating efficient, low-cost methods to reduce eddy current effects, which can be added into the current processing route for sintered rare earth permanent magnets have increased over the last decade. These have generally revolved around increasing the bulk resistance of the REPM, as the eddy currents are resistance limited and losses are inversely proportional to the resistivity of the magnet [6, 7, 130]. The literature review covered the different methods studied; powder coatings, blended powders and laminated structures. Blended powders of $Sm_2(Co, Fe, Cu, Zr)_{17}$ and electri-

cally insulating material offer the simplest, most efficient and practical method to increase the resistivity of $Sm_2(Co, Fe, Cu, Zr)_{17}$ magnets produced by the SPS technique. Layered structures are very effective at increasing the resistivity, albeit in one direction. The blended method offers an isotropic increase in the electrical resistivity, which is a property important for potential applications of lower cost, high performance and versatile $Sm_2(Co, Fe, Cu, Zr)_{17}$ magnets.

The literature review also summarised the different insulating materials studied in relation to increasing the resistivity of rare-earth permanent magnets and their effect on the magnetic properties [7, 130, 135, 140, 142, 143, 147, 311–313]. Of the non-rare earth fluorides studied, CaF_2 has been shown to have the least disruptive effect on the coercivity [8, 128, 133, 138, 144, 146]. The financial cost of CaF_2 is also considerably much less than the rare-earth containing fluorides. Based on these reasons, CaF_2 has been selected as the electrically insulating material for the study of blended powder composite permanent magnets.

8.2 Calcium fluoride powder analysis

Characterisation of the CaF_2 99.99% powder (Fischer Scientific, UK) was made using SEM to identify shape and measure crystallite size, much in the same way that was performed for the $Sm_2(Co, Fe, Cu, Zr)_{17}$ alloyed powders. Figure 8.1 shows secondary electron SEM images of CaF_2 powder crystallites and it is immediately clear that the powder crystallites are roughly cubic in shape. This is different to the irregular, prolate spheroid shape of $Sm_2(Co, Fe, Cu, Zr)_{17}$ powders, which were produced by jet milling method. The cubic shape of the CaF_2 suggests a different method of crystallite synthesis, for example; precipitation.

Measurement and distribution of CaF_2 crystallite size was performed for a sample of 130 random crystallites across the four images displayed in figure 8.1. For each crystallite, an estimation of the long axis diameter, a, of the crystallite was made and the axis perpendicular to this was then measured as the short axis diameter, b. The long and short axis diameters was also used to calculate the aspect ratio (a/b) for each crystallite, providing a quantification of crystallite geometry. It is noted that measurement of crystallite dimensions via microscopy image is of a two-dimensional projection for each crystallite and therefore prone to an under-estimate relative to their actual, three-dimensional profiles.

The average long axis diameter, $\bar{a} = 0.5 \pm 0.1\mu m$ and the average short axis diameter, $\bar{b} = 0.4 \pm 0.1\mu m$. 95% confidence limits were calculated using a t-distribution value of 1.96. While the SEM images show a wide range of crystallite sizes, Figure

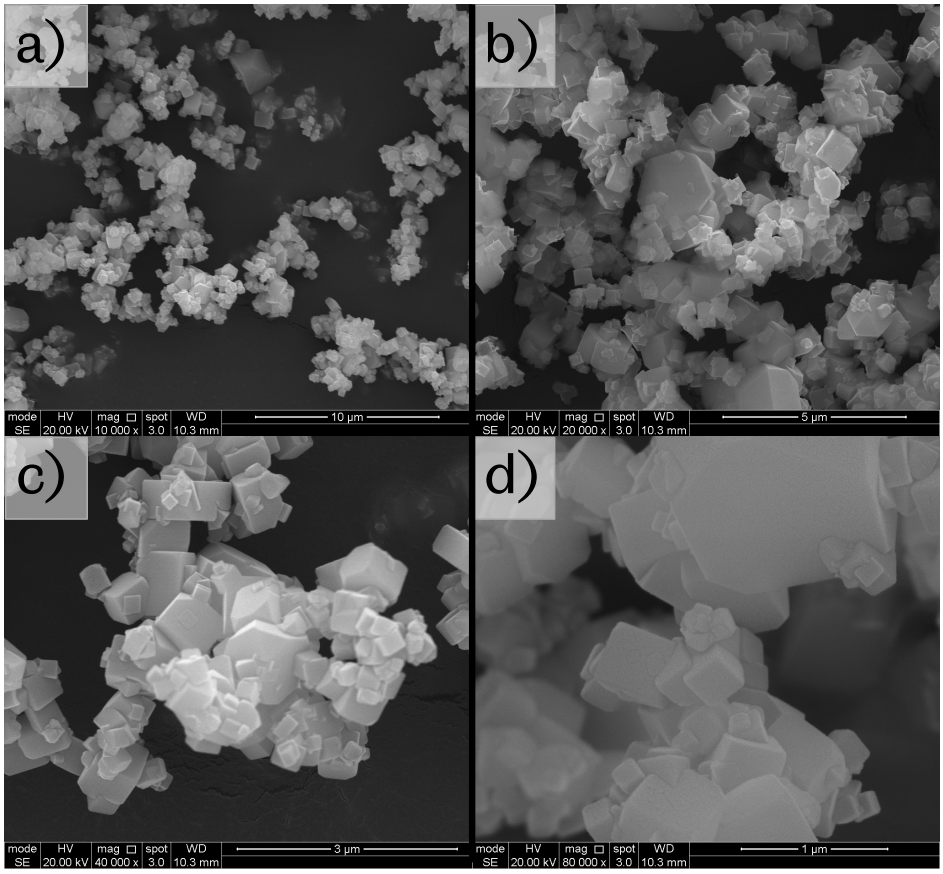

Figure 8.1: Secondary electron SEM images of CaF_2 powders at different magnifications a) 10,000×, b) 20,000×, c) 40,000×, d) 80,000×.

8.2 shows the distribution of crystallite sizes is strongly weighted diameters <1 µm. Compared to the same measurements of $Sm_2(Co, Fe, Cu, Zr)_{17}$, this represents the majority of CaF_2 crystallite diameters an order of magnitude smaller than the magnetic powders. The noticeable difference in crystallite size could aid mixing of the powders, which will benefit the distribution of the insulating phases throughout the composite material and reduce agglomeration [133, 145, 313].

The distribution of aspect ratios calculated from each crystallite sampled is collected in figure 8.3 and shows the majority of crystallites measure an aspect ratio <1.5. This result is non-surprising, as the distributions of long and short axis diameters in figure 8.2 were identical and this result is confirmation that the crystallites are approximately equiaxed and cubic. In comparison, the $Sm_2(Co, Fe, Cu, Zr)_{17}$ powders, which are produced by jet milling, had a much larger distribution of aspect ratio, which the majority of crystallites measured <4.

EDS analysis in figure 8.4 of the CaF_2 powder confirmed the elemental composition of the CaF_2 powders. Spot measurements were repeated on several crystallites,

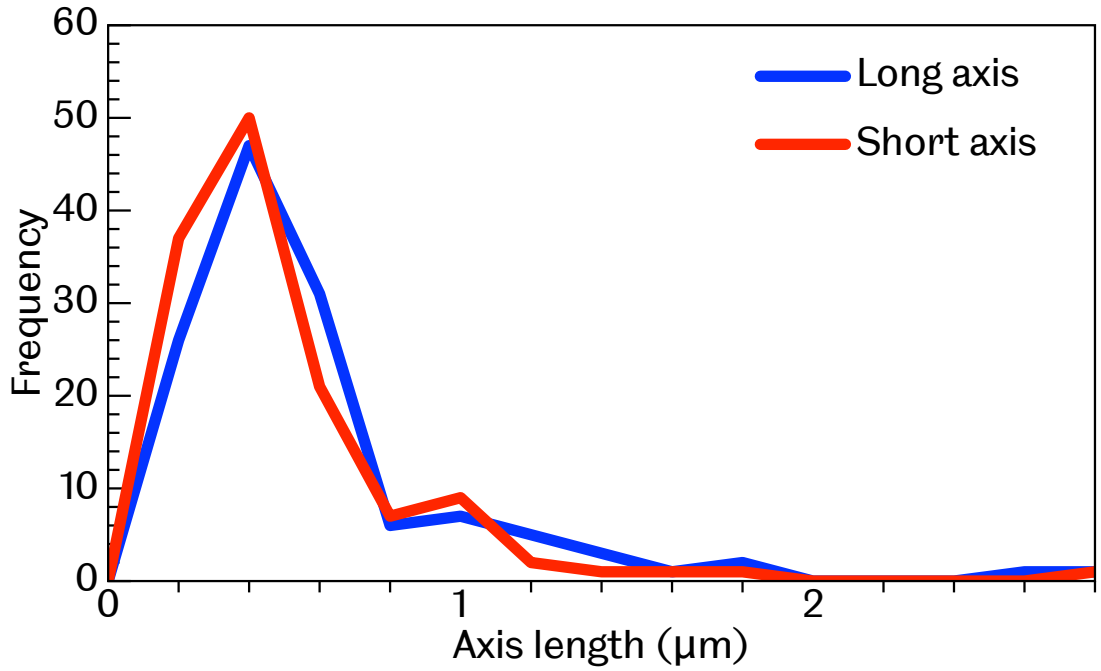

Figure 8.2: Distribution of long axis and short axis diameters, measured for 130 CaF_2 powder crystallites imaged by SEM.

which all verified the powders as predominantly calcium and fluoride, with trace concentration of oxygen. Gold is also identified, although its presence is intentional as the sputter coating material for the electrically insulating CaF_2 powders.

8.3 Blended powder composite magnet materials

For this study, multiple powder mixtures were blended with the weight addition of CaF_2 weighed out ranging from 2.5 wt.% to 35 wt.%. The blending of $Sm_2(Co, Fe, Cu, Zr)_{17}$ and CaF_2 powders was performed by centrifugal powder mixing using a SpeedMixer DAC 800 (FlakTek Inc, USA). The methodology used is covered in chapter 5 and was consistent across all powder mixtures.

The SPS processing parameters used for the composite specimens were as follows: 200 °C/min heating rate, 1050 °C holding temperature, 51 MPa hold pressure and 5 minute hold time. The hold temperature and heating rate differ slightly to those used in the previous chapters to produce full density $Sm_2(Co, Fe, Cu, Zr)_{17}$ specimens for study of the heat treatment. However, these modified SPS parameters also produce full density $Sm_2(Co, Fe, Cu, Zr)_{17}$ samples and therefore are not expected to significantly affect the potential magnetic properties after heat treatment. The first test batch of composite magnet samples used these processing parameters and

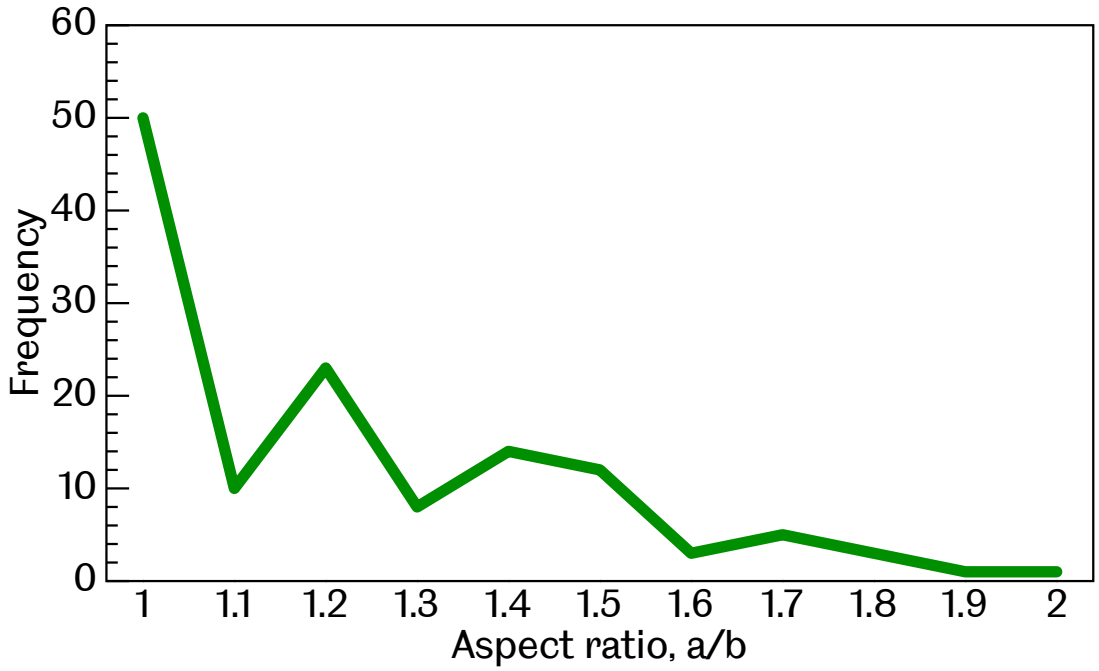

Figure 8.3: Distribution of aspect ratio, which is the ratio of the long axis (a) and the short axis (b), measured for 130 CaF_2 powder crystallites imaged by SEM.

for consistency were retained for all future specimens. In this chapter, where comparison is made to a reference SPS processed $Sm_2(Co, Fe, Cu, Zr)_{17}$ sample (1-12), it is a specimen which has also been processed using the aforementioned parameters.

Analysis has been performed on the composite magnet specimens before and after heat treatment and is made clear when reporting the data. Characterisation of the composite magnets in the as-processed, pre-heat treatment state is to initially identify any effect the electrically insulating material may have on the consolidation of the powder using the SPS technique. After heat treatment, the coercivity of the $Sm_2(Co, Fe, Cu, Zr)_{17}$ magnet is strongly dependent on the precipitation structure of the 2:17R cells and 1:5H cell walls within grains. Our analysis of the $Sm_2(Co, Fe, Cu, Zr)_{17}$ and CaF_2 after heat treatment will help identify whether the insulating phases have any influence on the generation of the cellular nanostructure through changes in the coercive field.

The heat treatment used for all $Sm_2(Co, Fe, Cu, Zr)_{17}$ and CaF_2 composite specimens in this study:

1. Homogenisation at 1170 °C in an argon atmosphere for 2 hours. Allowed to cool in air to room temperature.

2. Age at 850 °C in an argon atmosphere for 16 hours.

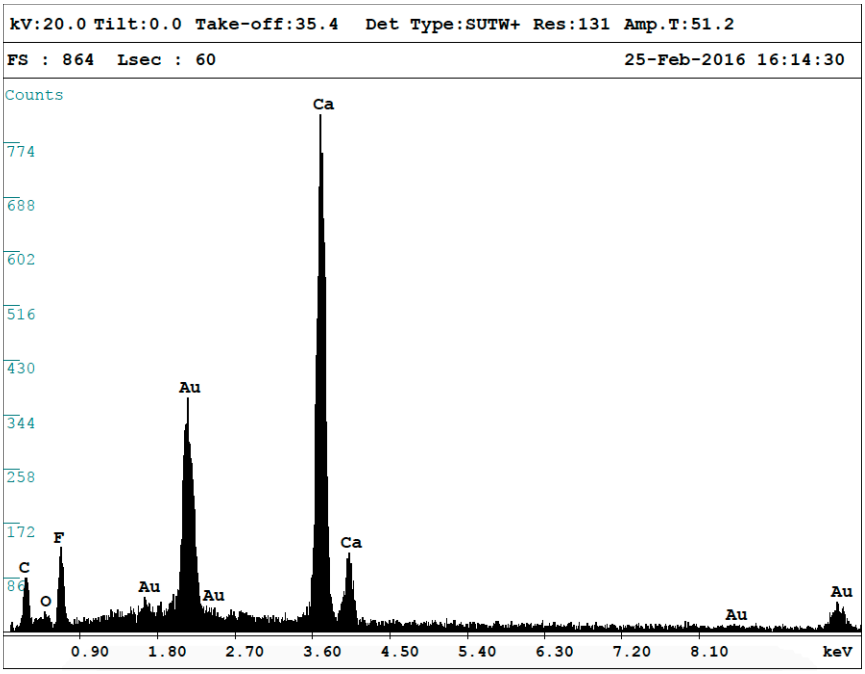

Figure 8.4: Spot measurement for CaF_2 showing EDS spectrum. Elements identified through corresponding peak energy. The presence of gold (Au) is due to its use as sputter coating material for the electrically insulating CaF_2.

3. Slow cool at 1 °C/min in an argon atmosphere to 400 °C and immediately quench in oil to room temperature.

Post-heat treatment the specimens were mechanically surface polished on all surfaces using 120 grit/grade SiC abrasive paper to remove all visible discolouration.

8.3.1 Density study of composite specimens

The measured densities of $Sm_2(Co, Fe, Cu, Zr)_{17}$ and CaF_2 composite magnets are plot as a function of CaF_2 weight percentage in figure 8.5. The relative densities for the composite magnets were calculated by multiplying the theoretical densities of $Sm_2(Co, Fe, Cu, Zr)_{17}$ and CaF_2, 8.40 g/cm^3 [131, 292] and 3.18 g/cm^3 [128] respectively, by the weight fraction of each phase present in the material and summing. The presented data is for the composite magnets after heat treatment, with very little change in the density before and after heat treatment.

As the density of CaF_2 is less than half of $Sm_2(Co, Fe, Cu, Zr)_{17}$, there is an expected decrease in the density of the composite samples relative to $Sm_2(Co, Fe, Cu, Zr)_{17}$, as the weight percentage (or equivalent volume fraction) of CaF_2 increases. The theoretical relationship between the composite density and

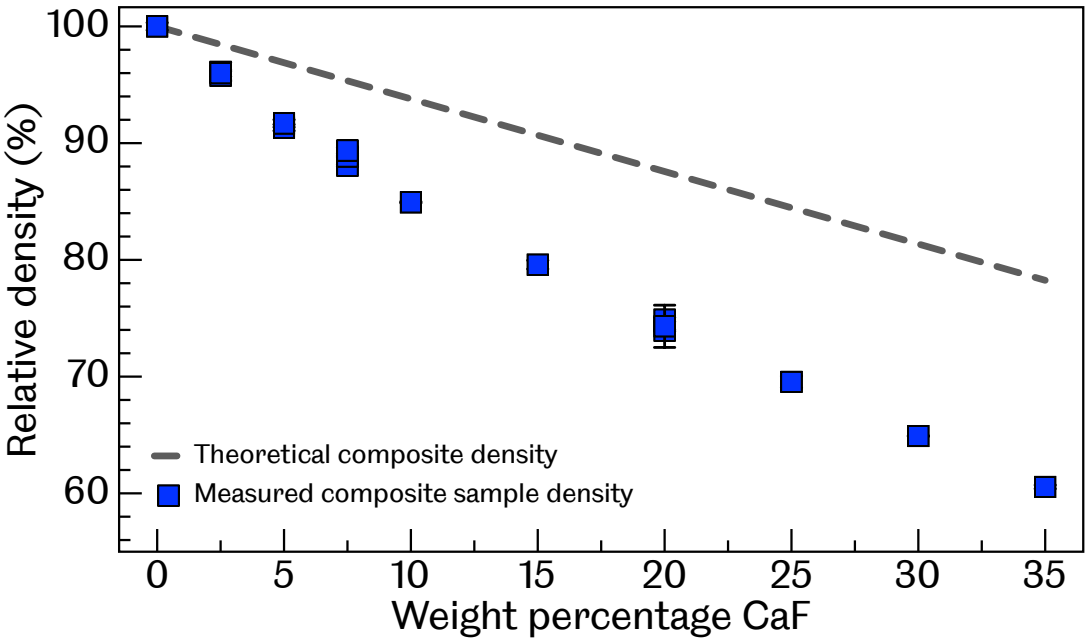

Figure 8.5: Calculated and measured relative densities for SPS processed and heat treated $Sm_2(Co, Fe, Cu, Zr)_{17}$ and CaF_2 composite magnets. Theoretical composite densities calculated using theoretical densities for $Sm_2(Co, Fe, Cu, Zr)_{17}$ and CaF_2 as $8.40\,g/cm^3$ [131, 292] and $3.18\,g/cm^3$ [128] respectively.

weight percentage of CaF_2 is represented by a dashed line in figure 8.5. However, the experimental data shows the density of the SPS processed $Sm_2(Co, Fe, Cu, Zr)_{17}$ and CaF_2 composite magnets decreases more rapidly than predicted. There is also a widening gap between the theoretical composite density (dashed line) and the experimental data points as the weight percentage CaF_2 increases within the composite magnets. This implies the composite magnets are gradually getting more porous and the SPS processing parameters become less effective at consolidating the blended powder with increasing amounts of CaF_2. The melting temperature of CaF_2 is just over 1400 °C, while experience has shown the $Sm_2(Co, Fe, Cu, Zr)_{17}$ material powders to melt during the pressure assisted SPS process at temperatures around 1200 °C. The higher melting temperature of CaF_2 can have a significant effect on the densification by SPS [153]. Within the literature, a similar decrease in the density was observed in Nd-Fe-B segmented with increasing amounts of NdF_3 additions [147]. However in $SmCo_5$ type magnets with CaF_2, the addition of the insulating material slightly increased the relative density, albeit to a maximum of 94% with 10 wt.% addition CaF_2.

From this analysis, specific SPS processing parameters are required for $Sm_2(Co, Fe, Cu, Zr)_{17}$ composite magnets of different weight additions of CaF_2. Limitations are set in the hold temperature, due to the melting of $Sm_2(Co, Fe, Cu, Zr)_{17}$

material powders at 1200 °C, and hold pressure, which is limited to 51 MPa due to material properties of graphite mould. However, future study and optimisation of the SPS processing parameters for $Sm_2(Co, Fe, Cu, Zr)_{17}$ and CaF_2 composite magnets could investigate the hold time, extending beyond 5 minutes to allow the removal of porosity in all composite specimens.

8.4 Composite magnet microstructure analysis

8.4.1 Backscattered SEM imaging of pre-heat treatment composite magnets

BS SEM has been used to clearly identify the distribution of the $Sm_2(Co, Fe, Cu, Zr)_{17}$ and CaF_2 phases within the microstructure. All specimens studied in the following SEM images and EDS analysis are before heat treatment. Figures 8.6 and 8.7 show the $Sm_2(Co, Fe, Cu, Zr)_{17}$ phase (light grey) and the CaF_2 phase (black) in composite magnet specimens containing increasing concentrations of CaF_2. EDS area analysis was used to confirmed the elemental composition of the phases.

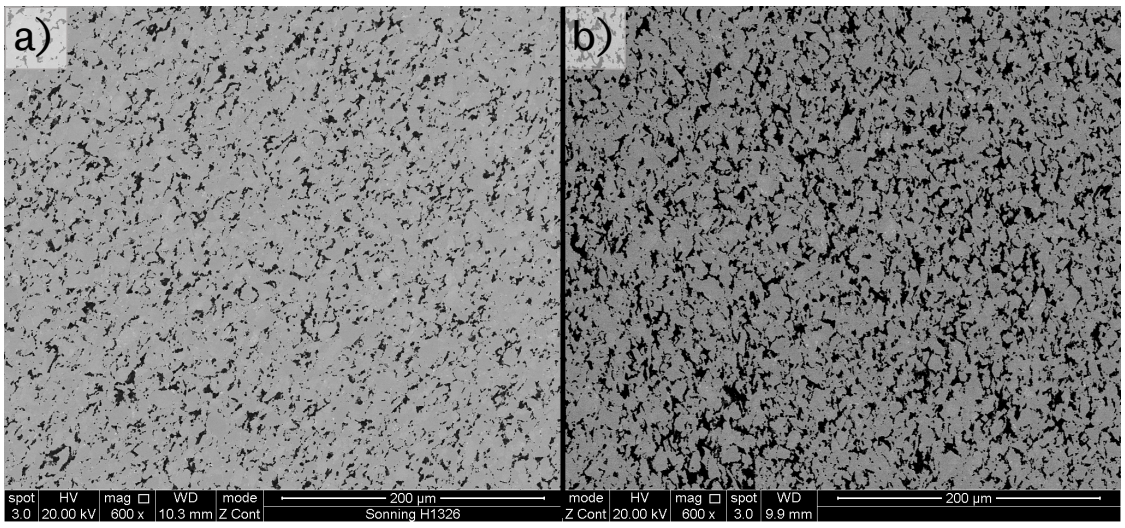

Figure 8.6: BS SEM images showing microstructures for $Sm_2(Co, Fe, Cu, Zr)_{17}$ (grey phase) and CaF_2 (black phase) composite magnets. a) shows typical microstructure for composite specimen containing 5 wt.% CaF_2. b) shows typical microstructure for composite specimen containing 10 wt.% CaF_2.

In general, the CaF_2 phase is well distributed throughout all the imaged specimens, showing a good mixture of the powders was achieved, although, as the concentration of the CaF_2 increases, there is increasing agglomeration of the insulating phase. The insulating phase begins to dominate the microstructure in figure 8.7

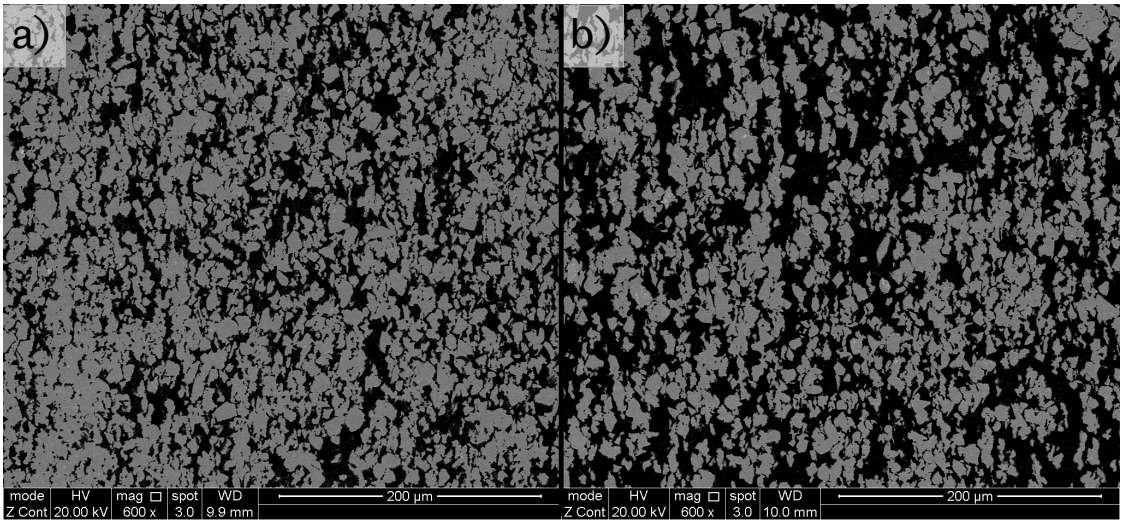

Figure 8.7: BS SEM images showing microstructures for $Sm_2(Co, Fe, Cu, Zr)_{17}$ (grey phase) and CaF_2 (black phase) composite magnets. a) shows typical microstructure for composite specimen containing 20 wt.% CaF_2. b) shows typical microstructure for composite specimen containing 30 wt.% CaF_2.

for the composite magnets containing 20 and 30 wt.% . At these volume fractions of insulating material; 0.40 and 0.53 respectively, the distribution of the insulating material begins to resemble percolation. In two-dimensions, the percolation threshold is averaged at 0.44 ± 0.02 for different lattice shapes [314] and this effect should be characterised in the composite magnets by a significant enhancement in the resistivity.

Volume fraction analysis

Analysis of the insulating phase volume fraction in the BS SEM images was performed using ImageJ image analysis software [280]. This was performed using colour thresholds to isolate the black CaF_2 phase and the volume fraction was measured three times in three different microscopy images for each $Sm_2(Co, Fe, Cu, Zr)_{17}$ and CaF_2 composite specimen with 5, 10, 20 and 30 wt.% addition CaF_2. All microscopy images were taken in pre-heat treatment composite specimens, unless otherwise stated. The theoretical volume fractions were calculated based on the theoretical solid densities of the the $Sm_2(Co, Fe, Cu, Zr)_{17}$ and CaF_2 phases and the measured weight fraction of CaF_2.

Table 8.1 shows the results of the insulating phase volume fraction analysis in several BS SEM images of $Sm_2(Co, Fe, Cu, Zr)_{17}$ and CaF_2 composite magnet samples. Across all composite magnets analysed, the measured volume fraction of insulating material matches the calculated theoretical volume fractions. Therefore, from this analysis, the concentration of CaF_2 present in the composite materials is same as

Wt. % CaF_2	Theoretical vol. frac. CaF_2	imageJ vol. frac. CaF_2 1	imageJ vol. frac. CaF_2 2	imageJ vol. frac. CaF_2 3	Mean
5	0.12	0.14	0.11	0.13	0.13 ± 0.03
10	0.23	0.26	0.22	0.24	0.24 ± 0.05
10 (heat treated)	0.23	0.23	0.24	0.24	0.24 ± 0.02
20	0.40	0.41	0.39	0.40	0.40 ± 0.02
30	0.53	0.52	0.50	0.55	0.53 ± 0.05

Table 8.1: Volume fraction analysis of insulating phase in BS SEM images for $Sm_2(Co, Fe, Cu, Zr)_{17}$ and CaF_2 composite magnets. Theoretical volume fraction calculated from known weight fraction using theoretical densities for $Sm_2(Co, Fe, Cu, Zr)_{17}$ and CaF_2 as $8.40\,g/cm^3$ [131, 292] and $3.18\,g/cm^3$ [128] respectively. Uncertainty quoted as 95% confidence value, using a t-value of 4.

the weight percentages measured during preparation.

It is also noted that the measured CaF_2 volume fraction in the composite magnet containing 10 wt.% CaF_2 did not change after heat treatment.

8.4.2 EDS elemental analysis

EDS elemental distribution maps

To complement the BS SEM images of the composite magnet microstructure, EDS elemental distribution maps were made to identify the spatial distribution of the elements. The $Sm_2(Co, Fe, Cu, Zr)_{17}$ and CaF_2 composite magnet specimen studied contained 10 wt.% of CaF_2. Figure 8.8 shows EDS elemental distribution maps, which were created through multiple raster scans over a 45 minute period on the backscattered SEM image labelled SE1. The corresponding EDS energy spectrum and identified elements are shown in figure 8.9.

The elemental distribution maps confirm the grey regions in the BS SEM images are comprised entirely of the elements within $Sm_2(Co, Fe, Cu, Zr)_{17}$, while the black regions are strongly associated with calcium (yellow map). Samarium (purple map) is primarily distributed in the grey regions of the SE1 map, although there is a noticeable distribution in the black CaF_2 region. Similar studies of increased resistivity permanent magnets reported CaF_2 to remain inert within the blended composite magnet microstructure [8, 133], and was a factor in using CaF_2 as the insulating material within the study. Fluorine is not identified or profiled in these maps, as its primary, alpha energy peak (seen previously in the EDS analysis of CaF_2 powder crystallites in figure 8.4) is located at around 0.9 eV and is obscured by larger energy peaks for the elements cobalt, copper and samarium. This approximate position for the fluorine peak is highlighted in figure 8.9. The X-ray detectors used in energy dispersive spectroscopy have difficulty distinguishing between closely located energy peaks, especially at low energies and for light elements. This energy

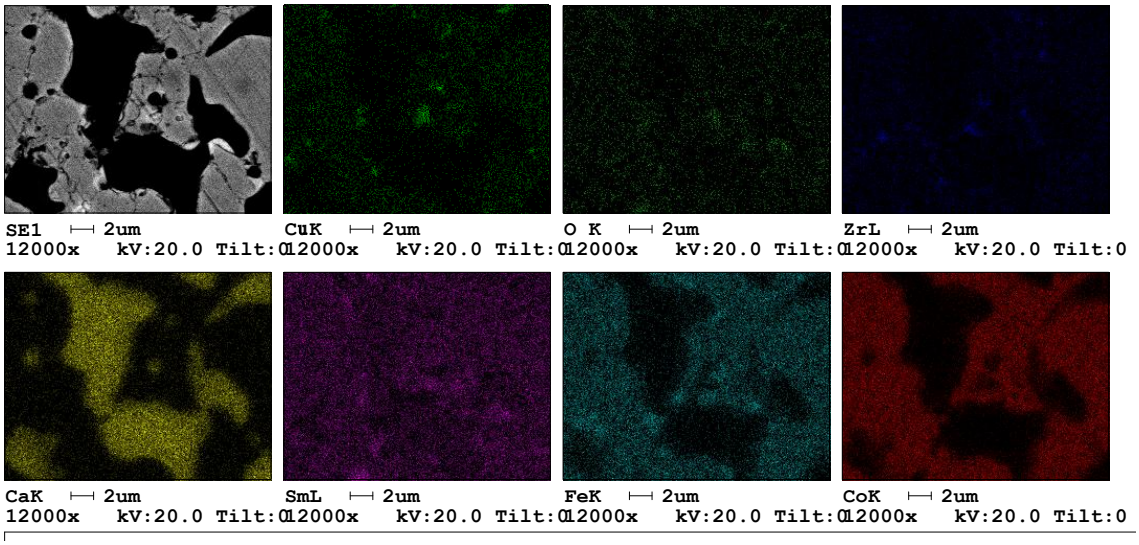

Figure 8.8: EDS elemental map showing spatial distribution in the corresponding BS SEM image (labelled SE1) for a $Sm_2(Co, Fe, Cu, Zr)_{17}$ and 10 wt.% CaF_2 composite magnet. Elements measured are labelled below each map.

overlap could explain why samarium is misidentified in the black CaF_2 regions. The other corresponding $Sm_2(Co, Fe, Cu, Zr)_{17}$ elements are not detected at similar levels in the black regions, ruling out the detection of the $Sm_2(Co, Fe, Cu, Zr)_{17}$ phase in the interaction volume below the imaging plane.

The clearest map profiles are from the calcium (yellow) and cobalt (red) maps, which record the highest concentrations with regards to the EDS energy spectrum and is because these elements are largest in abundance within the composite magnets. A few distinct regions, high in concentration of copper, are clearly visible and coincide with relatively low concentrations of the other alloying elements, suggesting some elemental segregation in the $Sm_2(Co, Fe, Cu, Zr)_{17}$ regions of the composite magnet. The highest concentrations of samarium are detected at the periphery of the grey $Sm_2(Co, Fe, Cu, Zr)_{17}$ regions, which coincide with higher concentrations of oxygen, which samarium has a strong affinity for [113, 114].

EDS line scan analysis

While most literature studies of REPMs with CaF_2 show the insulating phase to be non-interacting with the magnetic material phase, the laminated structures studied by Gabay et al. [128] showed evidence for the existence of Nd-Ca-O-F-type phase close to the boundary between the two regions. To investigate whether Sm and CaF_2 may be interacting, EDS line scans were performed on a $Sm_2(Co, Fe, Cu, Zr)_{17}$ and 20 wt.% CaF_2 sample across the boundary between the two phases. This will

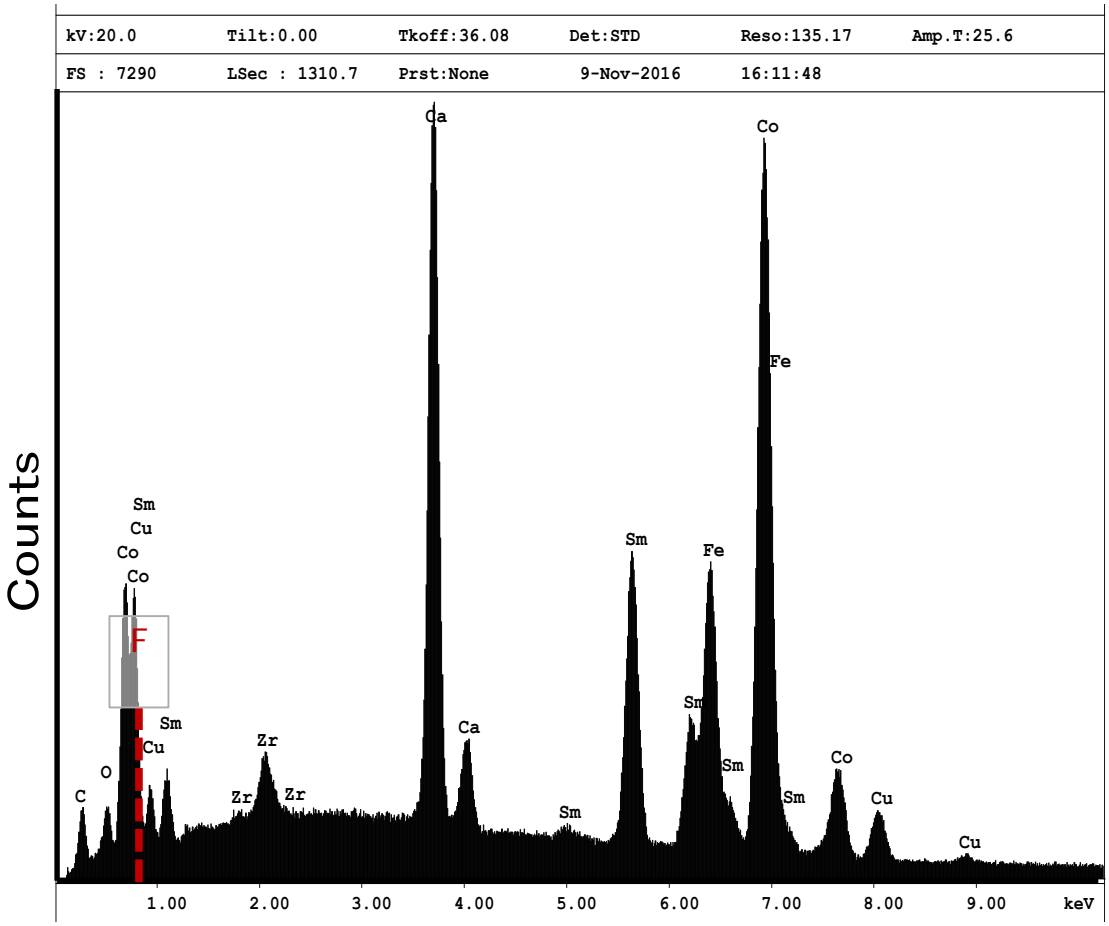

Figure 8.9: EDS spectrum measured over the entire SE1 image. Approximate fluorine alpha peak position is labelled.

allow quantification of the elemental concentrations with distance and may provide a correlation, suggesting potential elemental interaction, close to and across the phase boundary [8].

Figure 8.10 shows on the left the BS SEM image and the white line shows the path of the line scan, beginning at the red zero. The corresponding elemental detection levels are shown on the right. The EDS line scan measurements were repeated three times and averaged. Across the black CaF_2 region, the levels of the elements associated with $Sm_2(Co, Fe, Cu, Zr)_{17}$ drop considerably, and this is most evidenced with the concentration of cobalt (red data line). Samarium (blue) and iron (orange) also drop to similar minimum counts, but comparably, the drop is less severe. Low counts for Cu and Zr are measured within the $Sm_2(Co, Fe, Cu, Zr)_{17}$ phase and no significant changes are detectable across the CaF_2 phase regions. Calcium expectedly peaks across the CaF_2 region.

Measurement and comparison of the peak widths across the CaF_2 region using half-width at half-maximum (HWHM) for the elements calcium, cobalt and samarium could show how distinct the elemental concentration is across the phase

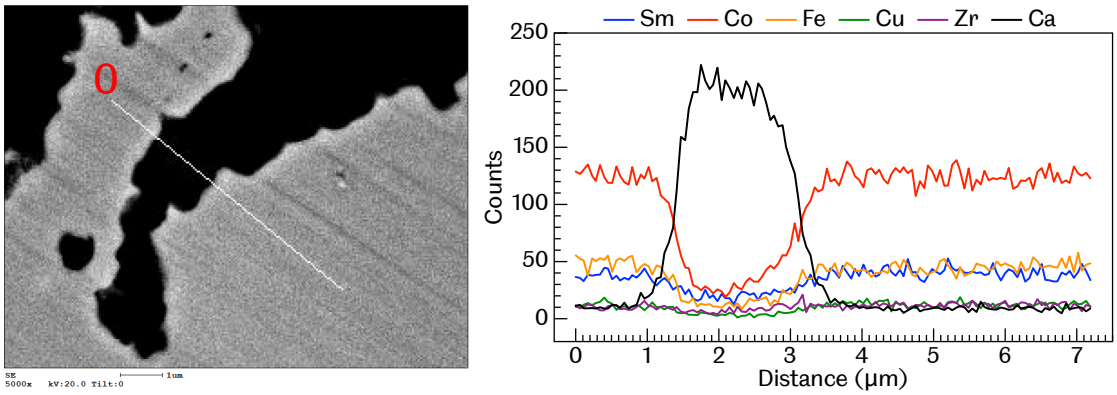

Figure 8.10: Left: BS SEM image of $Sm_2(Co, Fe, Cu, Zr)_{17}$ and 20 wt.% CaF_2 composite magnet. EDS line scan follows white line, which begins at the red zero. Grey region is $Sm_2(Co, Fe, Cu, Zr)_{17}$ phase, black region is CaF_2. Right: Corresponding EDS elemental analysis along line scan.

boundaries or whether elemental mixing is detected through a gradual change. The HWHM are measured as 0.96 ± 0.30 µm, 0.96 ± 0.30 µm and 1.41 ± 0.30 µm for calcium, cobalt and samarium respectively. The errors have been taken from the difference between maximum and minimum measured values relative to the mean value in a distance of 1 µm.

Relatively large uncertainties are associated with the HWHM due to the noise in the measurement data and in the estimation of the peak maximum values. Therefore, the measured HWHMs for Ca, Co and Sm are not significantly different from each other and the elemental compositions of the $Sm_2(Co, Fe, Cu, Zr)_{17}$ and CaF_2 phases appear distinct. In other words, the method of measuring elemental concentrations from the presented EDS line scans is not able to clearly identify whether mixing of elements close to the boundaries of the two different phases occurs. However, beyond 1 µm, there is no evidence of elemental mixing and the $Sm_2(Co, Fe, Cu, Zr)_{17}$ and CaF_2 phases are distinct and non-interacting.

Grain size analysis

Grain size measurements of the $Sm_2(Co, Fe, Cu, Zr)_{17}$ phase were made using a modified linear intercept method, commonly used for duplex structures, accounting for the CaF_2 phase in the microstructure. Measurements were made in the horizontal and vertical axes of two light microscopy images taken in pre-heat treatment $Sm_2(Co, Fe, Cu, Zr)_{17}$ and CaF_2 composite magnet specimens, each containing 5, 10 and 20wt.% CaF_2. The granular structure of the $Sm_2(Co, Fe, Cu, Zr)_{17}$ phase was emphasised using a 10% concentration citric acid and water solution at 80 °C as an etchant.

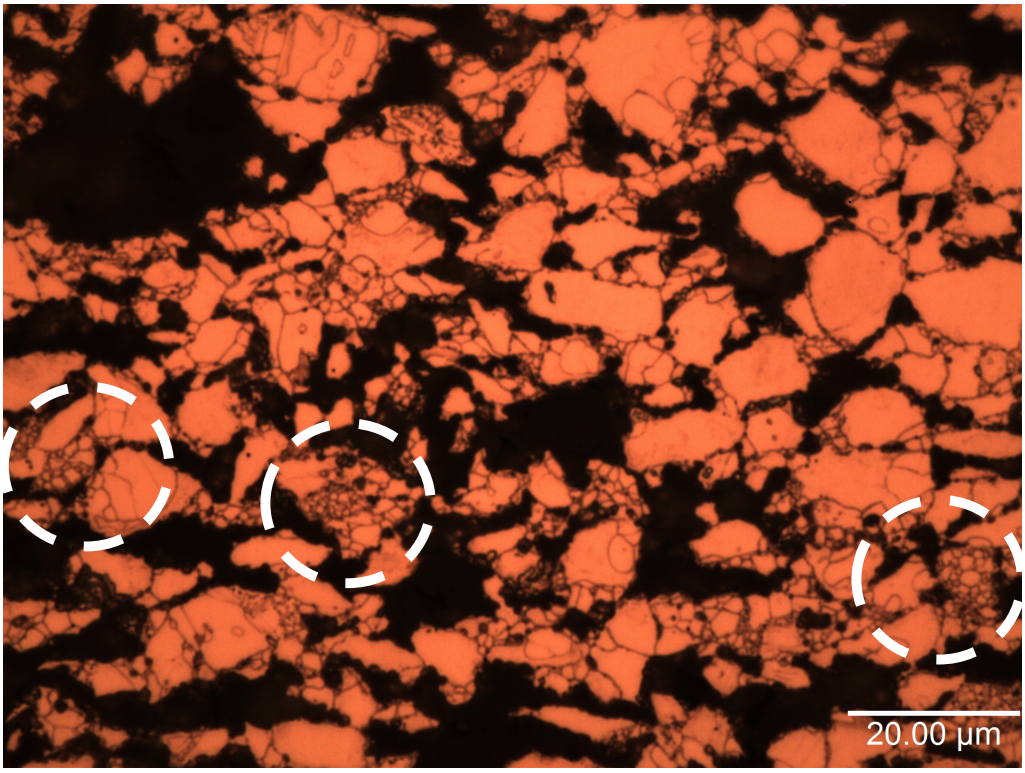

Figure 8.11: 100× magnification light microscopy image of citric acid etched $Sm_2(Co, Fe, Cu, Zr)_{17}$ and 20 wt.% CaF_2 composite magnet. White dashed circles highlight increasingly frequent regions of grain size inhomogeneity.

An example of the etched microstructure for the composite specimen containing 20 wt.% CaF_2 is shown in figure 8.11. Measurements were not made in the composite specimens after heat treatment as results in previous chapters showed no significant change occurred in the grain size after heat treatment in the SPS processed $Sm_2(Co, Fe, Cu, Zr)_{17}$ magnets.

The average grain diameters measured in the horizontal and vertical axes for the $Sm_2(Co, Fe, Cu, Zr)_{17}$ and CaF_2 composite magnets are displayed in figure 8.12. Also included for comparison are equivalent measurements made in SPS processed $Sm_2(Co, Fe, Cu, Zr)_{17}$ magnets before heat treatment, as well as the precursor powder diameters.

Overall, the horizontal and vertical measurements are very similar across all SPS processed $Sm_2(Co, Fe, Cu, Zr)_{17}$ and CaF_2 magnets, suggesting approximately equiaxed $Sm_2(Co, Fe, Cu, Zr)_{17}$ grains based on the two directional measurements. Figure 8.12 also shows the addition of CaF_2 correlates with a decrease in the average $Sm_2(Co, Fe, Cu, Zr)_{17}$ grain size. After processing by SPS, there is some indication of grain growth through the difference in the powder crystallite and grain size measurements (although this difference was less severe in another SPS processed $Sm_2(Co, Fe, Cu, Zr)_{17}$ magnet analysed after heat treatment). The addition of

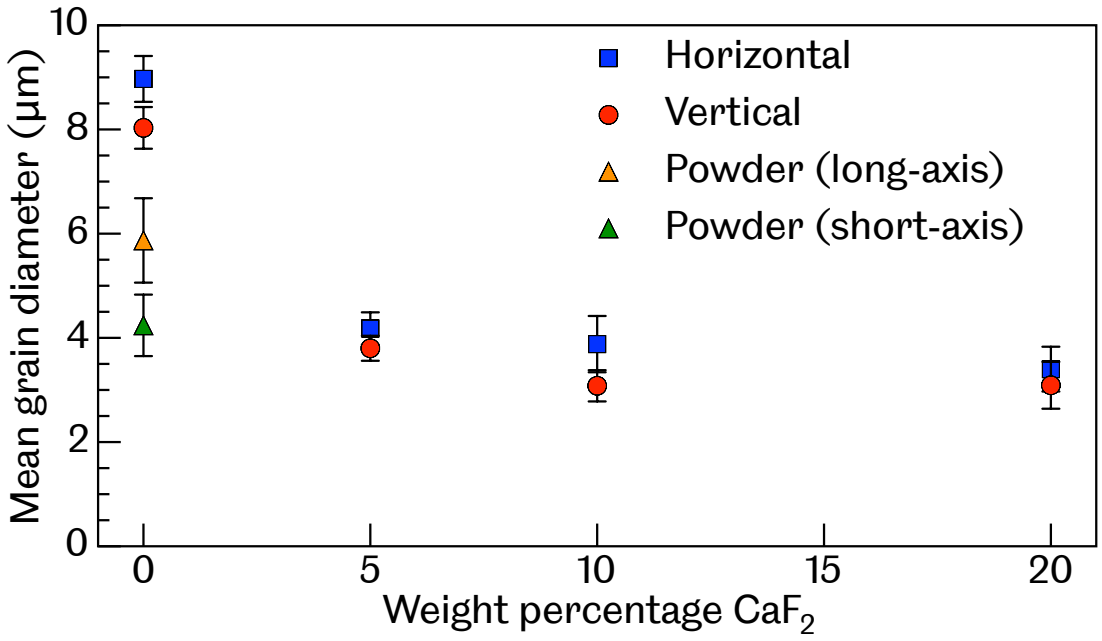

Figure 8.12: Average grain diameter measurements using linear intercept method for etched $Sm_2(Co, Fe, Cu, Zr)_{17}$ and CaF_2 composite magnets (square and circle symbols). Colours help to denote measurement made either in horizontal or vertical direction of the image. Average long and short-axis measurement for $Sm_2(Co, Fe, Cu, Zr)_{17}$ powder crystallites are also provided (triangle symbols) for reference.

CaF_2 appears to suppress the observed grain growth, and in the composite magnet specimens the average grain diameter is comparable to the short-axis of the powder crystallites. The grain diameters of the composite magnets remain constant, within statistical uncertainty, as the CaF_2 concentration increases. This type of behaviour has been reported in the literature, where CaF_2 was also added to Nd-Fe-B-type magnets and inhibited grain growth during sintering [133].

While the uncertainty associated with the data in figure 8.12 is derived from the standard deviation and is thus some indication of the range of measured data, linear intercept methods do not provide sufficient detail on the distribution of the grain sizes. From performing these measurements, regions of significant grain inhomogeneity were noticeable within the $Sm_2(Co, Fe, Cu, Zr)_{17}$ material. The frequency of these regions within the microstructure also appeared to increase with the weight percentage of CaF_2 in the composite. Figure 8.11 highlights some of these observed features.

To better understand these features, a study using high resolution SEM was performed on pre-heat treated composite magnets which had been etched. Figure

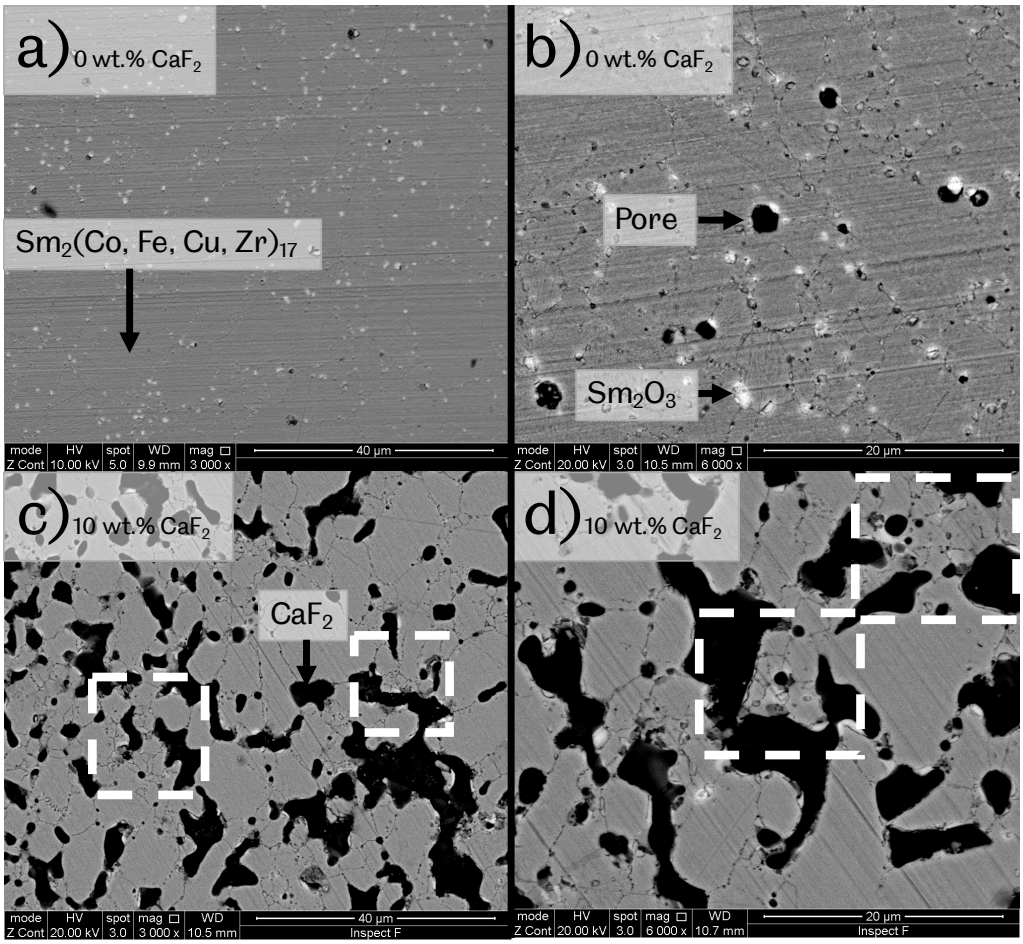

Figure 8.13: (a) and (b) show BS SEM images of etched $Sm_2(Co, Fe, Cu, Zr)_{17}$ magnet sample at different magnifications. (c) and (d) are BS SEM images of etched $Sm_2(Co, Fe, Cu, Zr)_{17}$ and 10 wt.% CaF_2 composite magnet sample at different magnifications. Microstructure features are labelled and highlighted by dashed boxes are regions of noticeably smaller grains in the composite magnet specimens.

8.13 a) and b) shows BS SEM images of a $Sm_2(Co, Fe, Cu, Zr)_{17}$ sample, accompanied with identification of typical microstructural features of this material processed by the SPS technique. The grain boundaries are just about visible Figure 8.13 b) and the microstructure features mostly homogeneous grains, with a small fraction of pores (black features) and Sm_2Co_3 grain boundary precipitates.

Figure 8.13 c) and d) show the BS SEM images of a $Sm_2(Co, Fe, Cu, Zr)_{17}$ and 10 wt.% CaF_2 composite sample. Highlighted within the $Sm_2(Co, Fe, Cu, Zr)_{17}$ phase are the inhomogeneous grain size regions, which are significantly smaller than the majority of grains in the $Sm_2(Co, Fe, Cu, Zr)_{17}$ matrix. These features appear to be found close to the CaF_2 phase.

As the CaF_2 weight percentage is increased to 20 wt.%, the inhomogeneous

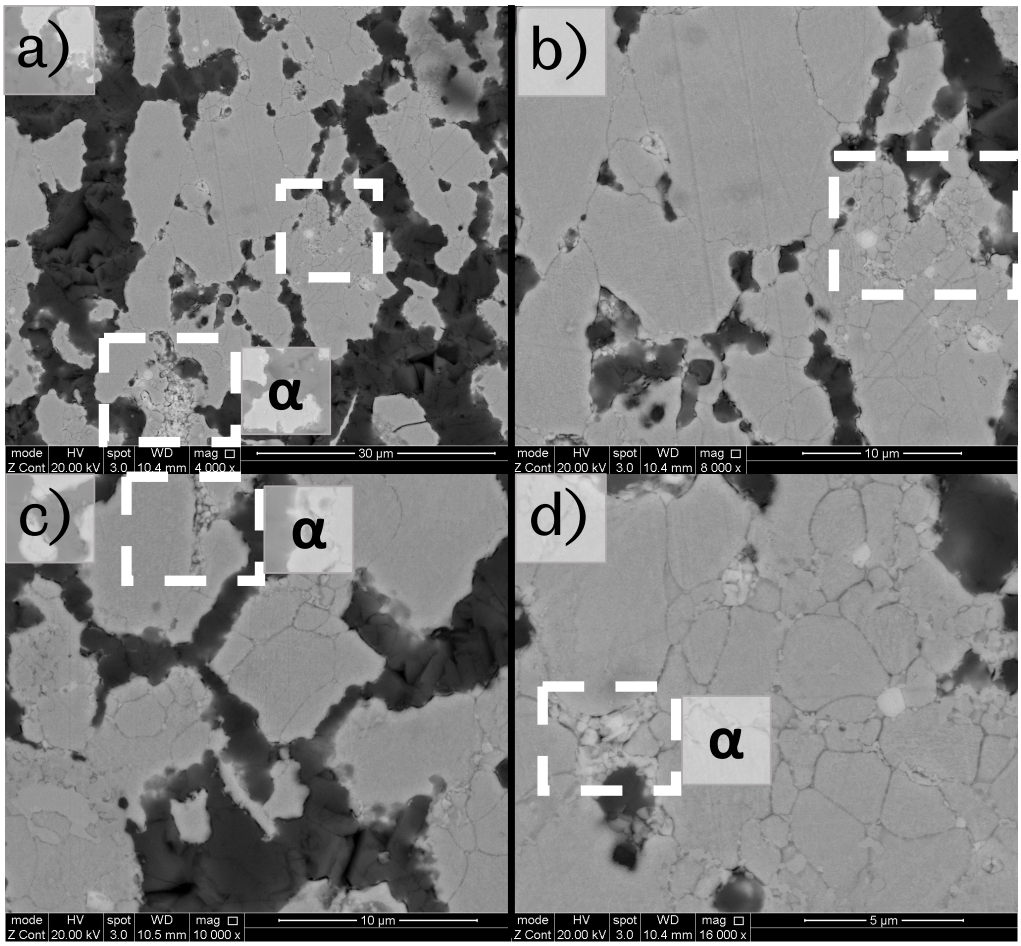

Figure 8.14: (a) - (d) BS microscopy SEM images of a $Sm_2(Co, Fe, Cu, Zr)_{17}$ and 20 wt.% CaF_2 composite magnet sample at various magnifications. Highlighted by dashed boxes are the regions of noticeably smaller grains, with further emphasis on areas denoted with α, which closely resemble un-sintered grains, a feature previously observed in low relative density SPS processed $Sm_2(Co, Fe, Cu, Zr)_{17}$ samples.

grain regions become more prevalent within the microstructure. Figure 8.14 (a) - (d) is made up of four BS SEM images taken at different magnifications of the same $Sm_2(Co, Fe, Cu, Zr)_{17}$ and 20 wt.% CaF_2 composite magnet specimen. The inhomogeneous features are highlighted and at the highest magnifications, the small 'grains' resemble un-sintered $Sm_2(Co, Fe, Cu, Zr)_{17}$ powder. These features are emphasised with α in figure 8.14). Similar un-sintered regions were observed in SEM images of sub-optimally SPS processed $Sm_2(Co, Fe, Cu, Zr)_{17}$ magnets in chapter 6.

Section 8.3.1 showed the relative density of the $Sm_2(Co, Fe, Cu, Zr)_{17}$ and CaF_2 composite magnets decreased as the content of CaF_2 increases. Here, evidence is shown of un-sintered powder regions due to sub-optimal SPS processing parameters used for the composite magnet specimens and the effect appears more widespread as the CaF_2 weight percentage increases. CaF_2 inhibits the sinter process and as

the concentration of the insulating material changes within the composite magnet, refined processing parameters are required to achieve full densification and sintering of the powders.

8.5 X-Ray Diffraction phase analysis

EDS analysis identified the elements present in the $Sm_2(Co, Fe, Cu, Zr)_{17}$ and CaF_2 composite microstructure and their spatial distribution was shown to be distinct from one another. XRD 2θ phase analysis can be used to compliment the elemental study and identify the main phases present in the composite magnets before and after heat treatment and complement the EDS analysis as to whether we there is any interaction between the insulating phase material and the hard magnetic phase.

All materials were analysed as solid specimens and had no powder alignment before consolidation by the SPS technique. After processing by SPS, a gentle mechanical surface polish, using 120 grit/grade SiC abrasive paper, was performed to visibly remove adhered graphite foil on all surfaces. Similarly, after heat treatment an identical mechanical surface polish was performed to remove discoloured surfaces. For both processes, the exact amount of material removed varied from sample to sample, but it is estimated that a minimum of ≈100 µm to 200 µm of surface material was removed from each specimen per mechanical surface polish.

Pre-heat treatment

Figure 8.15 shows the XRD 2θ for several $Sm_2(Co, Fe, Cu, Zr)_{17}$ and CaF_2 composite specimens with varying weight additions of CaF_2, as well as providing a comparative reference 2θ spectra for a standard SPS processed $Sm_2(Co, Fe, Cu, Zr)_{17}$ specimen (1-18). The $Sm_2(Co, Fe, Cu, Zr)_{17}$ and CaF_2 composite magnets analysed in this study were comprised of 5 wt.% CaF_2 (sample 2-01), 10 wt.% CaF_2 (sample 2-05) and 15 wt.% CaF_2 (sample 2-06).

Figure 8.15 shows that as the CaF_2 concentration increases (spectra going upwards in the figure), there is a clear consistency throughout, with the main phases identified as the 2:17R $Sm_2(Co, Fe, Cu, Zr)_{17}$ and, in the composite magnets the CaF_2 phases. The 2:17R $Sm_2(Co, Fe, Cu, Zr)_{17}$ phase was the main phase consistently identified in SPS processed and conventional sinter method magnets, as well as the precursor powders. Blending powders of $Sm_2(Co, Fe, Cu, Zr)_{17}$ and CaF_2 and processing by SPS shows no disruption to main powder component phases and no interaction between the phases. As the concentration of CaF_2 increases up the image in figure 8.15, the prominence and intensity of the CaF_2 phase peaks also increases,

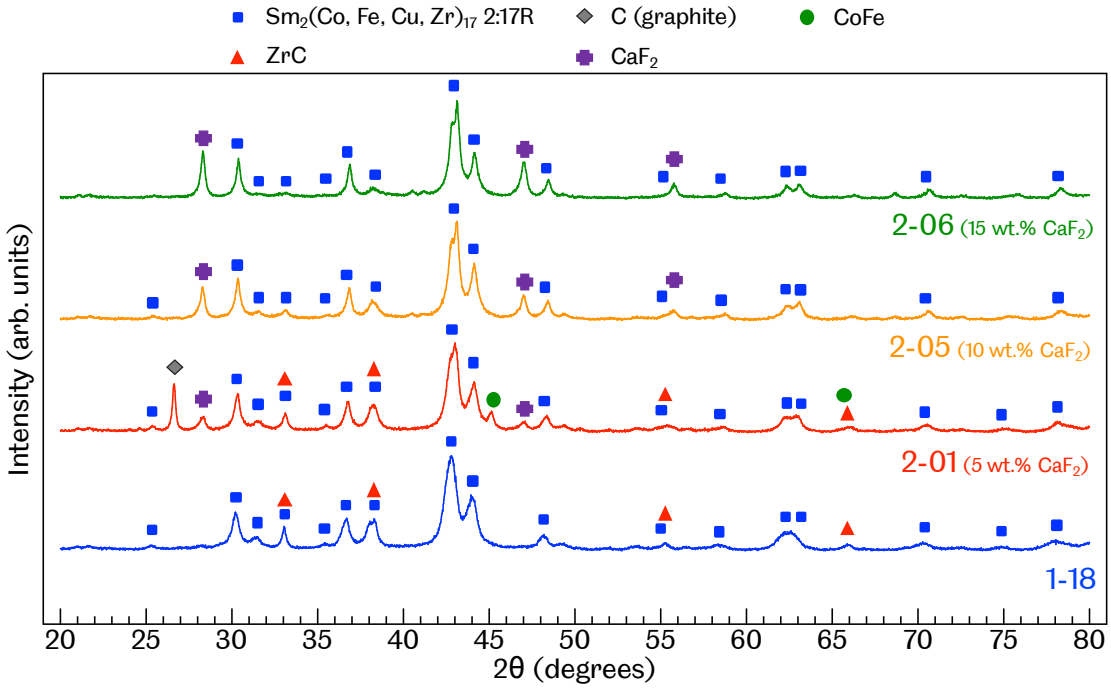

Figure 8.15: XRD 2θ spectra and phase analysis for pre-heat treatment SPS processed $Sm_2(Co, Fe, Cu, Zr)_{17}$ magnet (1-18) and $Sm_2(Co, Fe, Cu, Zr)_{17}$ and CaF_2 composite magnet specimens with 5 wt.% (2-01), 10 wt.% (2-05) and 15 wt.% (2-06) CaF_2. Main phases identified through peak analysis are marked with associated symbols.

which is most evident in the main peak at 2θ angle 28.2°.

The spectra of the composite magnets 2-05 and 2-06 (10 wt.% and 15 wt.% CaF_2 respectively) are near identical, however sample 2-01 (5 wt.% CaF_2) clearly shows presence of other phases, with the clearest peak identified as carbon (graphite) at 2θ angle 30.2°. Graphite foil adheres to the surface of the consolidated specimens after processing by SPS and the dull material is removed from all surfaces by a mechanical surface polish until visibly gone and the underlying $Sm_2(Co, Fe, Cu, Zr)_{17}$ material revealed. Remnants of graphite foil possibly remained on sample 2-01 and the presence of the graphite peak in the 2-01 spectra attributed to sub-optimal surface polish. There is also evidence for ZrC, which is also identified in the standard $Sm_2(Co, Fe, Cu, Zr)_{17}$ reference sample 1-18, and this phase is related to carbon contamination at the surface of specimens during the SPS process.

The soft magnetic Co-Fe phase, which had previously only been identified in $Sm_2(Co, Fe, Cu, Zr)_{17}$ magnets after heat treatment as a result of oxidation, is also identified in sample 2-01. Sintering during SPS occurs under an argon atmosphere and if contamination of the gas-feed was the cause, similar peaks would be expected to be identified in the other SPS processed specimens. Instead, an external uncontrollable factor, such as some variation in the powder handling or the blending

process for the $Sm_2(Co, Fe, Cu, Zr)_{17}$ and 10 wt.% CaF_2 powder mixture, are more likely an explanation for the oxidation-related phases.

Post-heat treatment

The same composite magnet specimens underwent the multi-stage heat treatment and their XRD 2θ spectra are reported in figure 8.16, along with a different reference $Sm_2(Co, Fe, Cu, Zr)_{17}$ (sample 1-28) after heat treatment.

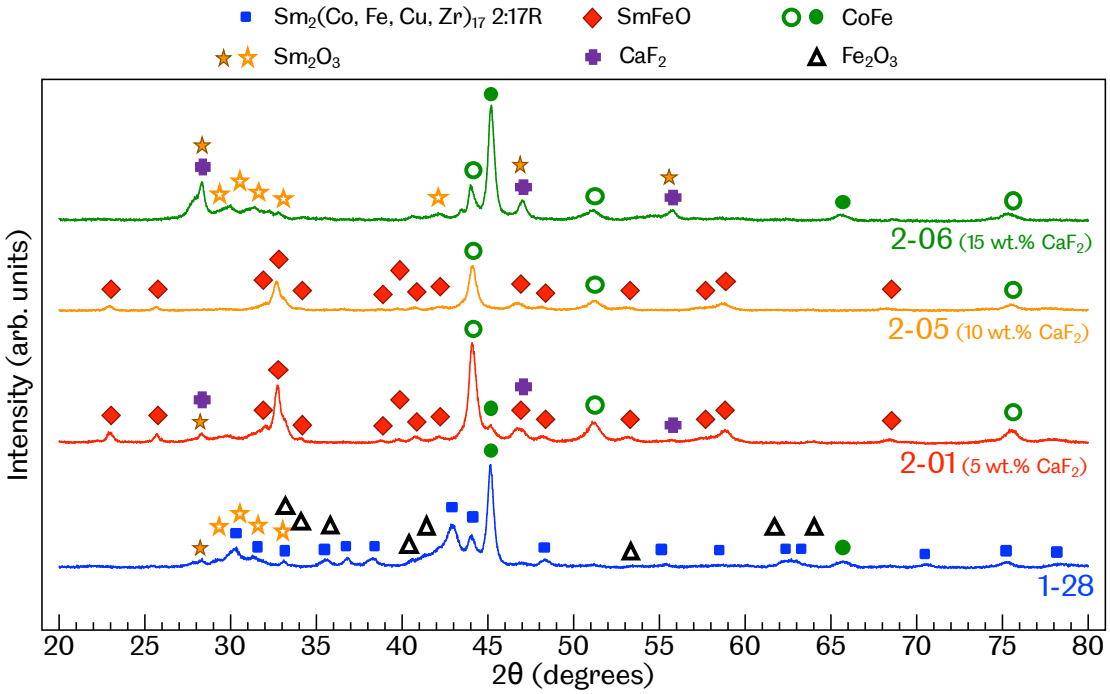

Figure 8.16: XRD 2θ spectra and phase analysis for post-heat treatment SPS processed $Sm_2(Co, Fe, Cu, Zr)_{17}$ magnet (1-28) and $Sm_2(Co, Fe, Cu, Zr)_{17}$ and CaF_2 composite magnet specimens with 5 wt.% (2-01), 10 wt.% (2-05) and 15 wt.% (2-06) CaF_2. Main phases identified through peak analysis are marked with associated symbols.

The XRD 2θ spectra in figure 8.16 show the changes in the surface phase composition after heat treatment. From the previous chapters, oxidation of the $Sm_2(Co, Fe, Cu, Zr)_{17}$ surface material occurred during the heat treatment and the resulting phases; Co-Fe, Sm_2O_3 and Fe_2O_3, are shown in the reference $Sm_2(Co, Fe, Cu, Zr)_{17}$ sample 1-28 spectra. Elevated oxygen levels were also prevalent in the $Sm_2(Co, Fe, Cu, Zr)_{17}$ powders and thus also inherent to the bulk material. The characteristic 2:17R $Sm_2(Co, Fe, Cu, Zr)_{17}$ phase is still identified however. In all the composite specimens; 2-01, 2-05 and 2-06, variants of the Co-Fe phase are also identified and dominate the spectra. In 2-01 and 2-05, the stoichiometry of the main

Co-Fe phase (unfilled green circle symbol) present is believed to be $Co_{0.92}Fe_{0.08}$ and $Co_{0.82}Fe_{0.18}$ respectively. In sample 2-06, $Co_{0.92}Fe_{0.08}$ was identified (green unfilled circle symbol), but this is the minor Co-Fe phase in the material. Instead, the primary Co-Fe phase (filled green circle symbol) stoichiometry is Co_7Fe_3, which is also identified as a minor phase in 2-01. The preference in the formation of the different stoichiometries of the soft magnetic CoFe phase is related to the abundance of the cobalt and iron in the internal oxidation zone, the largest region of the oxidation affected region at the surface of $Sm_2(Co, Fe, Cu, Zr)_{17}$ magnets [110, 111, 114], which is directly related to the decomposition of the 2:17R phase by removal of samarium and the formation of Sm_2O_3 [114]. In the 1-28 and 2-06 samples, the Co_7Fe_3 phase appears to be associated with stronger concentrations of Sm_2O_3 type phases. In the 2-01 and 2-05 samples, the $Co_{0.92}Fe_{0.08}$ and $Co_{0.82}Fe_{0.18}$ phases are instead favoured. These composite magnet specimens show large concentrations of SmFeO, which has previously been unidentified in relation to oxidation affected $Sm_2(Co, Fe, Cu, Zr)_{17}$, and this phase removes iron from the matrix, altering the stoichiometry of the main Co-Fe phase towards cobalt-heavy variants.

In all composite magnets, the 2:17R $Sm_2(Co, Fe, Cu, Zr)_{17}$ phase is not identified. This indicates the extent of the oxidation at the surfaces of the composite magnets is quite severe and the presence of the Co-Fe and SmFeO phase also suggest the 2:17R phase has decomposed through removal of Sm [113, 114].

Due to oxidation in the $Sm_2(Co, Fe, Cu, Zr)_{17}$ and CaF_2 composite specimens, there is uncertainty in the presence of the CaF_2 phase, with the main peaks obscured by overlapping peaks relating to the Sm_2O_3 and SmFeO phases. If we assume CaF_2 does not interact with the $Sm_2(Co, Fe, Cu, Zr)_{17}$ phase, as no new phases containing Ca or F have been identified, then its disappearance from the spectra is explained by the formation of the external oxide scale during the oxidation of $Sm_2(Co, Fe, Cu, Zr)_{17}$, which grows outwards from the surface [110, 111, 114].

Surface material removal

To further our understanding of the extent of the oxidation, a study the phase composition after removal of a controlled amount of surface material allows analysis of the phase composition below the surface after heat treatment. Sample 2-05, a composite magnet containing 10 wt.% CaF_2, underwent a mechanical surface polish, using 120 grit/grade SiC abrasive paper to approximately remove a further 500 µm of surface material. This value was estimated via measurement of the specimen thickness before and after surface polish using digital callipers. Figure 8.17 shows the XRD 2θ spectra for sample 2-05 after heat treatment (blue spectrum), after

removal of 500 µm of surface material (red spectrum) and before heat treatment (orange spectrum). For further comparison, an XRD 2θ spectrum for a standard $Sm_2(Co, Fe, Cu, Zr)_{17}$ magnet (1-28) after it had approximately 200 µm of surface material removed is also included.

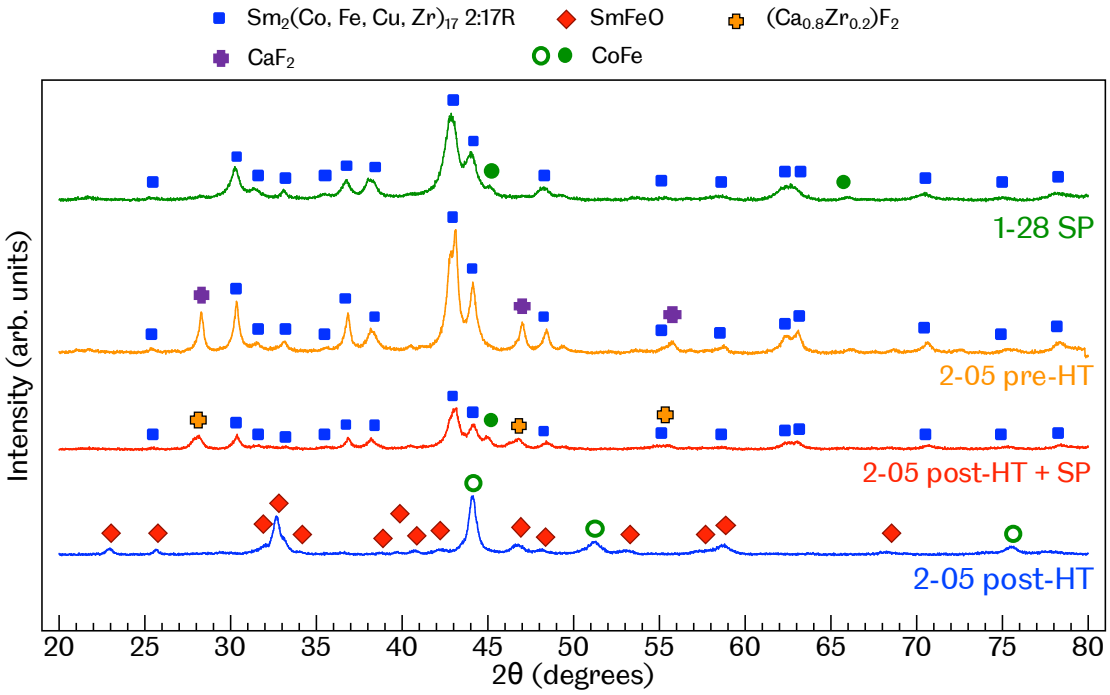

Figure 8.17: XRD 2θ spectra and phase analysis for $Sm_2(Co, Fe, Cu, Zr)_{17}$ and 10 wt.% CaF_2 composite magnet specimen after heat treatment (2-05 post-HT, blue spectrum), after 500 µm of surface material removed (2-05 post-HT + SP, red spectrum), before heat treatment (2-05 pre-HT, orange spectrum) and post-heat treatment SPS processed $Sm_2(Co, Fe, Cu, Zr)_{17}$ magnet after 200 µm of surface material removed (1-28 SP, green spectrum). Main phases identified through peak analysis are marked with associated symbols.

Working from the bottom spectrum upwards in figure 8.17, sample 2-05 after heat treatment shows the only phases identified as the Co-Fe type ($Co_{0.82}Fe_{0.18}$) and SmFeO. After removal of approximately 500 µm of surface material, the spectrum labelled '2-05 post-HT SP' shows a strong presence of the characteristic 2:17R $Sm_2(Co, Fe, Cu, Zr)_{17}$ phase. However, even after removal of a significant amount of surface material, there is still evidence for the oxidation-related soft magnetic Co-Fe phase, albeit now identified under a different stoichiometry - $Co_{0.5}Fe_{0.5}$. These two phases are also identified as the only significant phases in the $Sm_2(Co, Fe, Cu, Zr)_{17}$ 1-28 sample after removal of 200 µm surface material (top spectra, labelled 1-28 SP). The heat treatment of the 2-05 and 1-28 specimens was identical. The identification of the Co-Fe phase in sample 2-05 after removal of approximately 500 µm of

surface material shows oxidation may be more severe than expected in the composite magnet samples. Earlier, sample 2-01 showed evidence of the Co-Fe phase before heat treatment and this was attributed to uncontrollable external factors, such as oxygen contamination during the powder handling or blending stage. The $Sm_2(Co, Fe, Cu, Zr)_{17}$ and CaF_2 composite magnets may therefore contain more oxygen throughout the material.

It was hypothesised that the absence of the CaF2 phase in the '2-05 post-HT' spectrum was due to a large, outward growth of the oxidation region at the surface in the composite magnet. However, after the removal of approximately 500 µm, figure 8.17 shows, instead of the CaF_2 phase, a match is made for the $(Ca_{0.8}Zr_{0.2})F_2$ phase. This is indication, at least in the 2-05 specimen, that zirconium interacted with CaF_2 during the heat treatment. Removal of zirconium from the $Sm_2(Co, Fe, Cu, Zr)_{17}$ matrix would inhibit the formation of a homogeneous and well structured 2:17R cells and 1:5H cell wall structure within the $Sm_2(Co, Fe, Cu, Zr)_{17}$ grains during the heat treatment [60, 69, 92]. Further study of other $Sm_2(Co, Fe, Cu, Zr)_{17}$ and CaF_2 composite specimens after heat treatment and surface material removal is required to confirm the $(Ca_{0.8}Zr_{0.2})F_2$ phase is consistently observed. However, if this is true indication of an interaction between the $Sm_2(Co, Fe, Cu, Zr)_{17}$ and CaF_2 phases, it would have a strong and negative impact on the hard magnetic properties of these type of high resistivity composite permanent magnets.

8.6 Resistivity measurements

The addition of CaF_2 to $Sm_2(Co, Fe, Cu, Zr)_{17}$ powders to form higher resistivity composite magnets which minimise eddy current effects [7, 8]. The relationship between the bulk resistivity of the composite magnets, as measured by the VDP method, and the weight percentage addition of CaF_2 is studied. Figure 8.18 shows the resistivity data for all composite magnet specimens before and after heat treatment. All samples in figure 8.18 were 'isotropic' with regards to their powder-alignment.

Focussing on the pre-heat treatment data (blue data), there is a clear increase in the resistivity with the weight percentage of insulating material. The resistivity increases even with the smallest additions of CaF_2 and from 10 wt.% addition CaF_2 begins to increase rapidly. The resistivity profile in the pre-heat treatment composite samples follows the form characteristic of a percolation effect, which appeared in the BS SEM image of the 20 wt.% CaF_2 composite magnet (figure 8.7 b)). At 10 wt.% addition CaF_2, the composite sample has a resistivity 1.68× greater than the reference $Sm_2(Co, Fe, Cu, Zr)_{17}$ sample (1-12, processed under identical SPS pa-

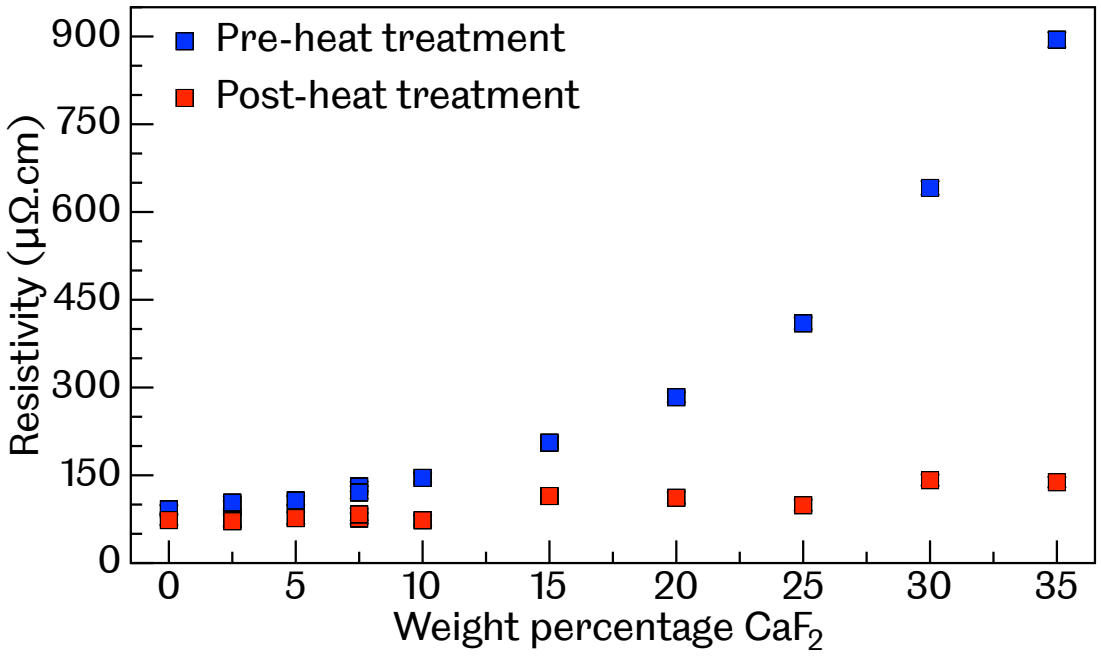

Figure 8.18: VDP four probe resistivity measurements for all $Sm_2(Co, Fe, Cu, Zr)_{17}$ and CaF_2 composite magnets before (blue data) and after heat treatment (red data).

rameters as composites). For the maximum weight addition of insulating material, 35 wt.%, the resistivity reaches the maximum measured value of $894.6 \pm 12.7 \mu\Omega\,\text{cm}$, which is nearly a factor of ten greater than the reference magnet.

After heat treatment, a much different relationship is observed and there is an obvious change in the impact of CaF_2 on the bulk resistivity in the composite material. While there is an overall increase in the resistivity, the trend is much more gradual compared to the data before heat treatment and significantly higher concentrations of insulating material are required to achieve comparable levels of resistivity enhancement. For example, before heat treatment, 10 wt.% weight addition of CaF_2 increased the resistivity by a factor 1.68 compared to the reference specimen. After heat treatment, between 15 wt% and 20 wt% weight percentage of CaF_2 is required increase the resistivity to comparable levels ($1.56\times$ and $1.52\times$ the reference specimen). At 35 wt.% CaF_2, the measured resistivity post-heat treatment is a more modest $138.3 \pm 8.8 \mu\Omega\,\text{cm}$.

In the previous chapter, it was shown the resistivity of the $Sm_2(Co, Fe, Cu, Zr)_{17}$ decreased after heat treatment, as a result of the phase structure changes and elemental redistribution during the heat treatment process [67, 74, 79, 132]. The resistivity of the reference $Sm_2(Co, Fe, Cu, Zr)_{17}$ magnet, 1-12, before heat treatment was $91.7 \pm 7.1 \mu\Omega\,\text{cm}$, and after heat treatment was $73.4 \pm 8.6 \mu\Omega\,\text{cm}$. It would be

expected for this effect to apply to all $Sm_2(Co, Fe, Cu, Zr)_{17}$ and CaF_2 composite magnets but cannot explain the change in the resistivity profile after heat treatment.

Phase analysis of the composite magnets after heat treatment showed significant phase composition changes. On the surface, SmFeO and Sm_2O_3 oxides, as well as the relatively conductive Co-Fe phase, emerged from the decomposition of the 2:17R $Sm_2(Co, Fe, Cu, Zr)_{17}$ phase, which was observed predominantly before heat treatment. Below the surface (500 µm), the 2:17R $Sm_2(Co, Fe, Cu, Zr)_{17}$ phase became evident but the electrically insulating CaF_2 phase also appeared to change to $(Ca_{0.8}Zr_{0.2})F_2$. These changes, observed to depths of 500 µm from the surface may explain the significantly modified resistivity profile in the $Sm_2(Co, Fe, Cu, Zr)_{17}$ and CaF_2 composite magnets after heat treatment and is therefore a result of oxidation. Within the literature, it has been reported that partial disintegration of rare-earth fluorides were found at grain boundaries in high resistivity Nd-Fe-B-type composite magnets [140, 142, 312]. Generally, CaF_2 has been reported as a stable insulating material addition [8, 138, 144], although in the studies of milled powders/flakes which where exposed to oxygen, a type of Nd-Ca-O-F phase formed in Nd-Fe-B/CaF_2 composite magnets [128].

8.7 Magnetic property characterisation

Having investigated the material properties and phase composition of the $Sm_2(Co, Fe, Cu, Zr)_{17}$ and CaF_2 composite magnets, a noticeable change in the phase composition coincided with a significant change in the resistivity of the composites magnets after heat treatment. The resistivity profile change after heat treatment was such that large concentrations of CaF_2 required to achieve comparable resistivity enhancement observed in much lower insulating material weight addition composite magnets before heat treatment and also within the literature for similarly blended insulating material composite magnets [8, 143, 144]. However, conclusions on the viability of the $Sm_2(Co, Fe, Cu, Zr)_{17}$ and CaF_2 composite magnets cannot be made until the demagnetisation curves and magnetic properties are also investigated.

8.7.1 Pre-heat treatment

Measurement of the magnetic properties were made through analysis of demagnetisation curves for the SPS processed $Sm_2(Co, Fe, Cu, Zr)_{17}$ and CaF_2 composite magnets, as well as a reference standard SPS processed $Sm_2(Co, Fe, Cu, Zr)_{17}$

magnet (1-12). All specimens received no powder alignment before SPS processing and therefore designated 'isotropic' with regards to their magnetic alignment. Their demagnetisation was measured by hysteresisgraph (Magnet-Physik, Germany) after magnetisation by pulse magnetisation (Hirst Magnetics, UK) in a pulsed field of around 3.5 T.

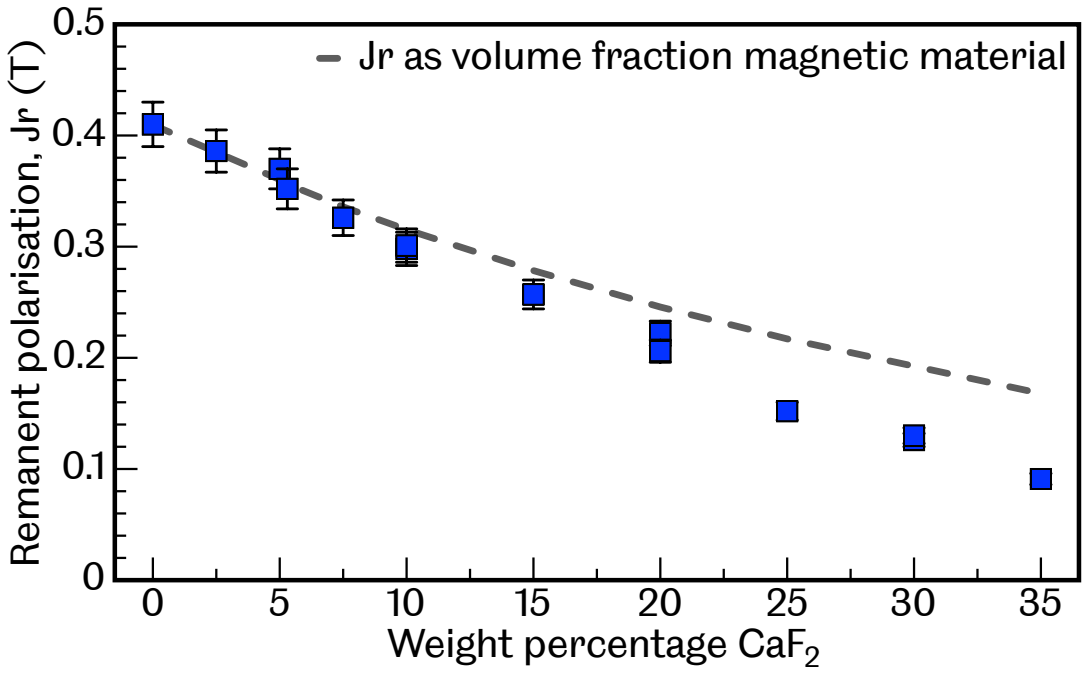

Figure 8.19: Remanent polarisation, J_r, as a function of CaF_2 weight percentage for SPS processed and pre-heat treatment $Sm_2(Co, Fe, Cu, Zr)_{17}$ and CaF_2 composite magnets.

Figure 8.19 shows the relationship between the remanent polarisation, J_r and the concentration of CaF_2 in the composite magnets. Expectedly, as the weight percentage (or equivalent volume fraction) of non-magnetic CaF_2 increases within the composite magnets, the remanence (either J_r or B_r), decreases. The relationship between J_r and weight percentage CaF_2 is a approximately negative linear relationship and the red dashed line in figure 8.19 used a guide for the eye to emphasise this.

The decrease of J_r as a function of weight percentage CaF_2 decreases more rapidly when compared to the theoretical J_r trend as a function of the volume fraction of the magnetic $Sm_2(Co, Fe, Cu, Zr)_{17}$ material within the composite magnet. On figure 8.19 this is shown with the grey dashed line. The largest divergence between the theoretical values and the experimental data is seen in the composite magnets with the highest concentrations of insulating material. This

correlates with a similar divergence between the theoretical density and measured density in the $Sm_2(Co, Fe, Cu, Zr)_{17}$ and CaF_2 composite magnets. In chapter 6, a study of the relationship between the remanent polarisation and density in pre-heat treatment $Sm_2(Co, Fe, Cu, Zr)_{17}$ magnets found, for specimens with relative densities below 85%, the remanence was negatively affected and significantly lower than comparative, full density $Sm_2(Co, Fe, Cu, Zr)_{17}$ magnets. Similarly, with an increasing addition of CaF_2, the remanence begins to noticeably diverge from the theoretical trend when the relative density of the composite magnet reaches around 80% and below, which equates to composite magnets with weight additions of CaF_2 15 wt.% and above.

Similar deviations in the remanent magnetisation and volume fraction of insulating material are reported within the literature [7, 134, 144]. The introduction of the insulating material also reduced the degree of alignment in powder aligned or hot deformed high-resistivity permanent magnets [128, 147]. While the composite magnets have received no powder alignment, a study of the degree of alignment in SPS processed $Sm_2(Co, Fe, Cu, Zr)_{17}$ in chapter 6 reported $J_r/J_s > 0.5$, indicating some texture in the material. This was believed to be due to the application of pressure during the SPS process, which can reorientate and rearrange the powder particles [153] or induce texture through hot plastic deformation, although investigation of the latter for the 2:17R-type crystal structure in Sm-Co type multiphase alloys showed little susceptibility to deformation induced texture [49]. The pressure-less sinter method produced commercial $Sm_2(Co, Fe, Cu, Zr)_{17}$ magnet that comparison was made with measured $J_r/J_s \approx 0.5$. In the SPS processed composite magnet containing 5 wt.% CaF_2 $J_r/J_s = 0.61$, while in the composite magnet containing 20 wt.% CaF_2 $J_r/J_s = 0.50$. Therefore, there is also some influence in a reduced degree of alignment within the SPS processed $Sm_2(Co, Fe, Cu, Zr)_{17}$ and CaF_2 composite magnets as the concentration of insulating material increases that also is detrimental to the remanence of the composite magnet.

Figure 8.20 displays the measure of coercivity and weight percentage CaF_2. Intrinsic coercivity, iH_c, is represented the blue data and coercive force, bH_c, by the red data.

An interesting effect on the coercivity through the addition of the insulating material is observed. In the region denoted 'i', coercivity is enhanced by the addition of CaF_2 and this trend continues up to around 10 wt.% CaF_2. In region 'ii', the trend changes to a subtle increases in both the intrinsic coercivity and coercive force with the CaF_2. A maximum intrinsic coercivity of 120 kA/m is measured in the composite magnet with a 20 wt.% addition of CaF_2, nearly double the intrinsic

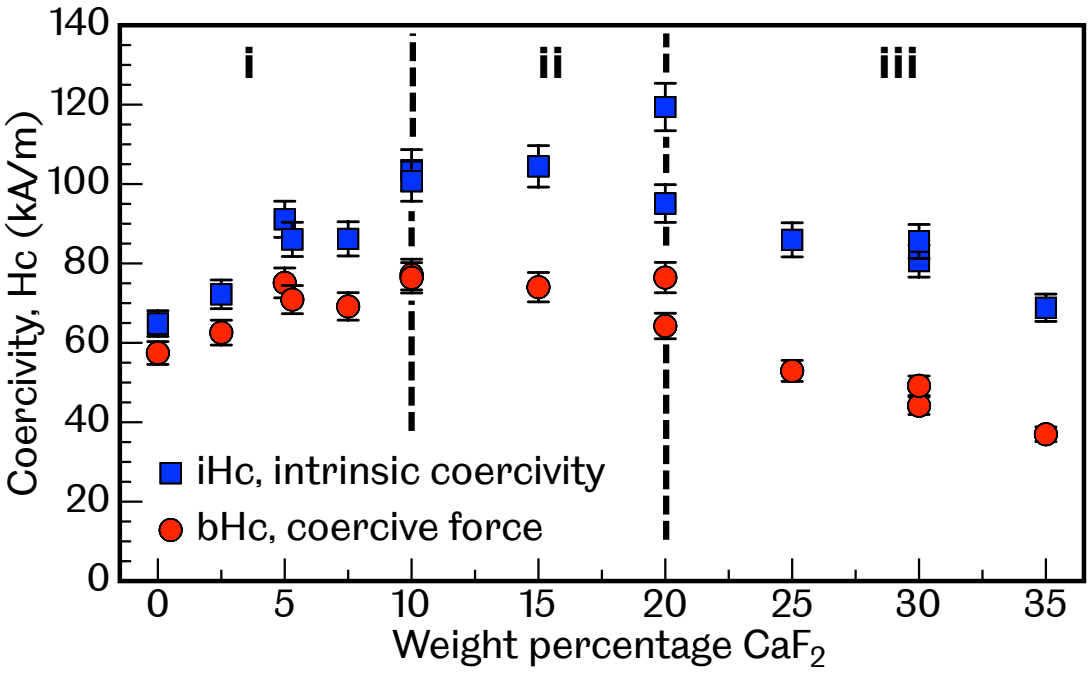

Figure 8.20: Intrinsic coercivity, iH_c, and coercive force, bH_c, as a function of CaF_2 weight percentage for SPS processed and pre-heat treatment $Sm_2(Co, Fe, Cu, Zr)_{17}$ and CaF_2 composite magnets, with regions denoted i, ii and iii showing different trends.

coercivity of the reference $Sm_2(Co, Fe, Cu, Zr)_{17}$ magnet; 65 kA/m.

In region 'iii', further addition of CaF_2 from 20 wt.% results in a decrease in the coercivity. However, even at the highest weight addition (35 wt.%) of CaF_2, the coercivity is still comparable to the coercivity of the reference $Sm_2(Co, Fe, Cu, Zr)_{17}$ magnet. These results show that, with regards to the coercivity of the composite permanent magnet before heat treatment, the addition of CaF_2 even up to 35 wt.% has a beneficial effect.

The relationship between the energy product, $(BH)_{max}$ and CaF_2 concentration is displayed in figure 8.21. At low weight additions of CaF_2 (up to 5 wt.%, region 'i'), the positive effect by the insulating material on the coercivity is able to maintain, or even slightly enhance the energy product, in spite of the reduction in the remanence. A maximum energy product, $(BH)_{max} = 8.9 \pm 0.4 kJ/m^3$, is achieved in the $Sm_2(Co, Fe, Cu, Zr)_{17}$ and 5 wt.% CaF_2 composite magnet. However, in region 'ii', the deleterious effect on the polarisation (or flux density) and the relative density with increasing additions of insulating material dominates over the coercivity enhancement and beyond 5 wt.% addition of CaF_2, a negative linear relationship is observed.

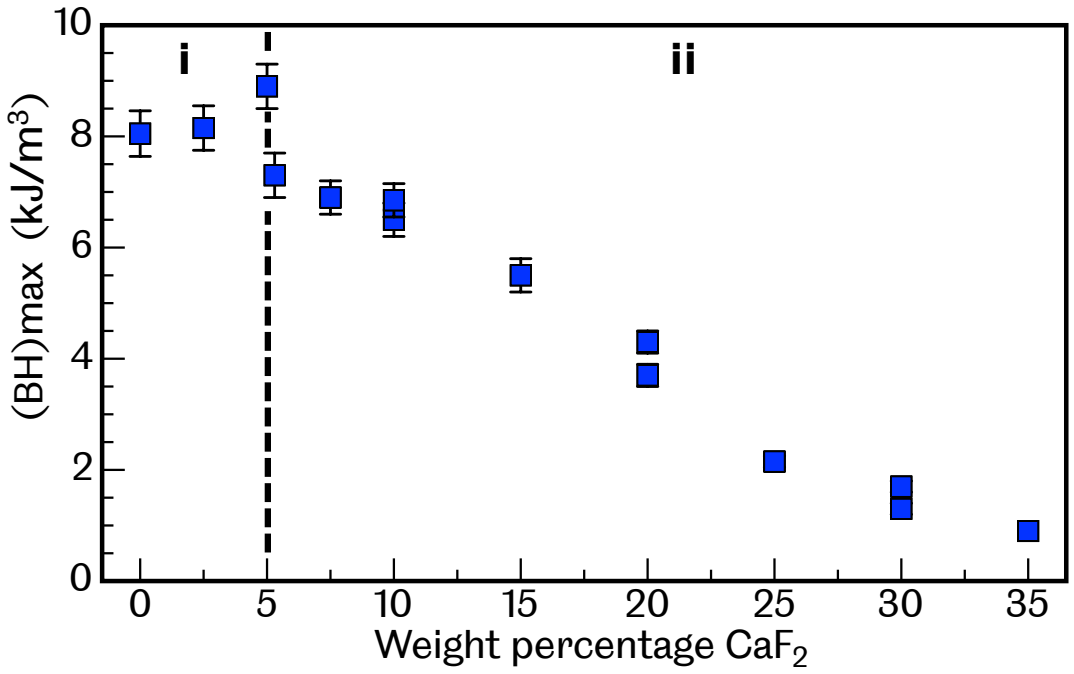

Figure 8.21: Energy product, $(BH)_{max}$, as a function of CaF_2 weight percentage for SPS processed and pre-heat treatment $Sm_2(Co, Fe, Cu, Zr)_{17}$ and CaF_2 composite magnets. Region i shows energy product unaffected by insulating material addition, while region ii shows negative relationship.

Investigation of initial magnetisation curves

The trend of coercivity enhancement through the addition of the CaF_2 insulating phase could be explained by the adding features to the microstructure which act as pinning sites for domain walls [13]. This effect would bear similarity to the coercivity enhancement with an increase in porosity, which was observed in the study of pre-heat treatment SPS processed $Sm_2(Co, Fe, Cu, Zr)_{17}$ magnets in chapter 6. BS SEM images showed the CaF_2 was well distributed throughout the composite microstructure and agglomerate features increased with the weight percentage of CaF_2. This type of study is repeated for the $Sm_2(Co, Fe, Cu, Zr)_{17}$ and CaF_2 composite magnets with increasing concentration of insulating material.

Figure 8.22 shows how the gradient of the initial magnetisation curves (which is the susceptibility of the magnet) decreases as the weight percentage CaF_2 increases. This is an indication of increasing pinning fields within the composite magnets. The initial magnetisation curve for the full density $Sm_2(Co, Fe, Cu, Zr)_{17}$ sample 1-33 (relative density 99.8%) provides comparison as increasingly more insulating phase is added to the composite magnet microstructure. A similar effect on the initial magnetisation curve gradient was observed in low density (high porosity)

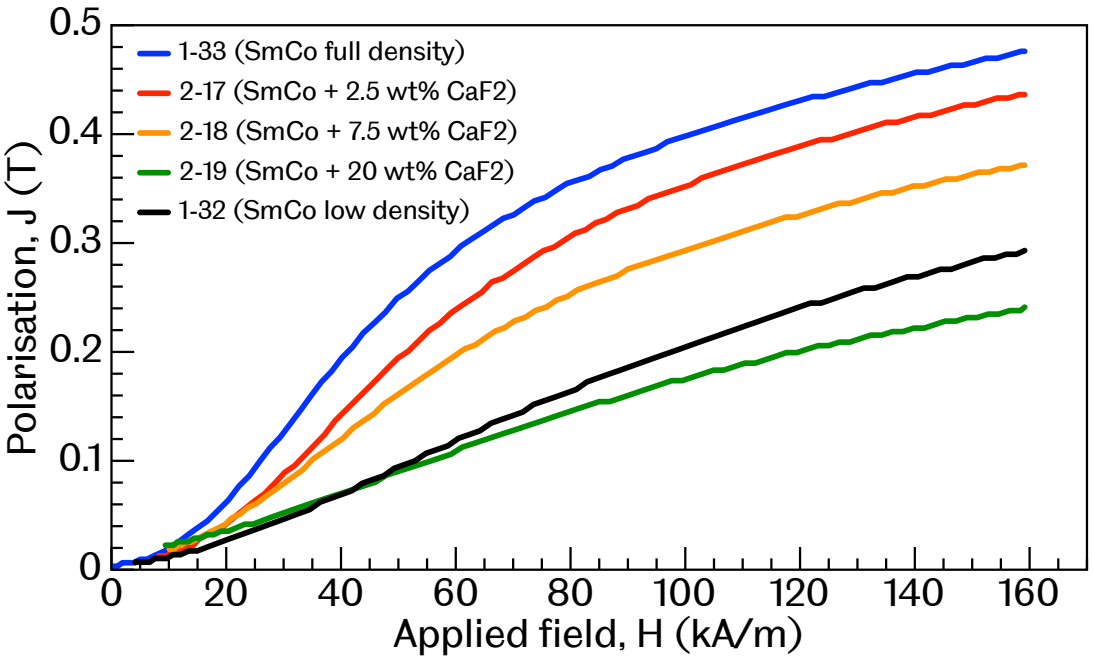

Figure 8.22: Initial magnetisation curves for SPS processed and pre-heat treatment $Sm_2(Co, Fe, Cu, Zr)_{17}$ and CaF_2 composite magnets. Also included are initial magnetisation curves for standard SPS processed $Sm_2(Co, Fe, Cu, Zr)_{17}$ magnets before heat treatment with full density (Sample 1-33, relative density 99.8%) and low density (sample 1-32, relative density 73.7%).

sample $Sm_2(Co, Fe, Cu, Zr)_{17}$ 1-32 (relative density 73.7%).

Investigation of demagnetisation curves

Examination of the composite magnet demagnetisation curves also highlights a change in in the magnetic reversal as the concentration of CaF_2 increases. Figure 8.23 shows the demagnetisation curves for the reference $Sm_2(Co, Fe, Cu, Zr)_{17}$ specimen, as well as several $Sm_2(Co, Fe, Cu, Zr)_{17}$ and CaF_2 composite magnets with varying insulating material.

The $Sm_2(Co, Fe, Cu, Zr)_{17}$ demagnetisation curve (blue data) has an inflection point at around H =25 kA/m, which defines the change from gradual to critical demagnetisation within the magnetic material. Addition of CaF_2 into the material changes the form of the demagnetisation curve and become progressively more linear with weight addition of CaF_2. This effect also coincides with an increase in the coercivity. The change of behaviour in the demagnetisation of the composite magnetic material is indicative of magnetic decoupling of the magnetic grains [142]. BS SEM imaging showed that as the volume fraction of the non-magnetic CaF_2 phase became quite large (>25%) and dominates the microstructure, the magnetic

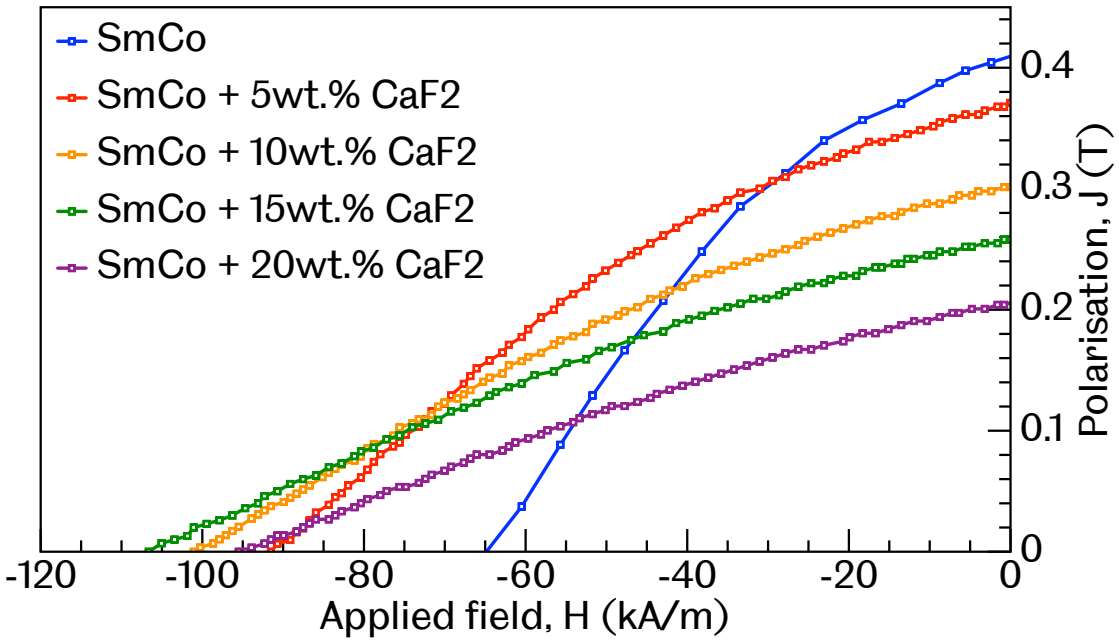

Figure 8.23: Demagnetisation curves for selected SPS processed and pre-heat treatment $Sm_2(Co, Fe, Cu, Zr)_{17}$ and CaF_2 composite magnets

$Sm_2(Co, Fe, Cu, Zr)_{17}$ phases are isolated. At the highest concentrations of CaF_2 this reaches the extreme situation where very few magnetic grains are 'connected'. During demagnetisation in a multi-domain, coupled granular system, the point of cascading domain wall motion is defined by an inflection point in the demagnetisation curve. At this point, reversed magnetic grains, coupled to adjacent grains through the exchange interaction, cause further grains to reverse their magnetisation instantly. However, decoupled grains will reverse individually without influence of neighbouring, reversed magnetic grains and only when nucleation is achieved within the individual grains. As the magnetic grains reverse individually at different fields, the result is a linear demagnetisation curve.

8.7.2 Modelling of pre-heat treatment coercivity mechanism

The hypothesis of the CaF_2 phase decoupling the magnetic grains and affecting the demagnetisation curves can be tested using FEM micromagnetic models. In the following, the decoupling effect is tested in granular $Sm_2(Co, Fe, Cu, Zr)_{17}$ models and simulating demagnetisation. A second set of models investigates the effect of the CaF_2 phase within a granular $Sm_2(Co, Fe, Cu, Zr)_{17}$ model.

Decoupling

FEM models comprised of 14 grains were created by Voronoi tessellation method and meshed using the methodology outlined in chapter 5. Figure 8.24 a) shows the arrangement of 14 tetradecahedron shaped $Sm_2(Co, Fe, Cu, Zr)_{17}$ grain volumes, which are approximately $100 \times 150 \times 150$ nm in size. At this size, the volumes are below the single domain limit and multi-domain states, and by effect domain walls, within the grains are not energetically favourable to exist. The size of these volumes are also orders of magnitude smaller than the grains observed in SPS processed $Sm_2(Co, Fe, Cu, Zr)_{17}$ magnets. Limitations in the granular volume are set by the computational cost of maintaining a fine mesh structure. However, as this study is modelling the decoupling effect, rather than inherent magnetic phenomena within grains, it is not believed that the size of the granular volumes will be significant.

Replicating the effect of the non-magnetic CaF_2 has been done by decreasing the exchange energy between grains, going from a coupled to fully decoupled system, rather than directly modelling the increasing volume fraction of the non-magnetic CaF_2 phase between the magnetic grains. This method saves computing cost as fewer mesh elements require generation and the scale of the model and grains is maintained throughout the different models. The magnetic grains are created as a core-shell type structure, but the 'shell' is not meshed and a fixed distance ranging from 1 nm to 1.5 nm is maintained between the meshed 'core' $Sm_2(Co, Fe, Cu, Zr)_{17}$ grains. The exchange energy between connected nodes in the FEM model is gradually reduced to replicate magnetic decoupling as the non-magnetic CaF_2 concentration increases in the composite magnet. A schematic, figure 8.24 b), shows a slice through the model and displays the magnetic grains, with the yellow arrows representing connected nodes, connected over the inter-granular region at a maximum distance 1.5 nm.

Each $Sm_2(Co, Fe, Cu, Zr)_{17}$ grain was assigned the following intrinsic magnetic properties, which are for the Sm_2Co_{17} phase [55]: $K_1 = 5\,MJ/m^3$, $K_2 = 0$, $J_s = 1.32\,T$, $A_{ex} = 14\,pJ/m$. A magnetic damping coefficient, $\alpha = 0.2$, was used in all models. Each grain volume was assigned a random easy-magnetisation axis within a cone centred on the positive x-axis within a range of $-90°$ and $+90°$. The only variation between models was the exchange stiffness parameter, A_{ex}. The average mesh cell size in the model was 5 nm.

Figure 8.25 shows the simulated demagnetisation curves for the several models, where A_{ex} is gradually reduced from 1.4×10^{-11} J/m (the intrinsic A_{ex} value for Sm_2Co_{17} [55]) to 1.4×10^{-15} J/m. Each data curve shows the demagnetisation as a

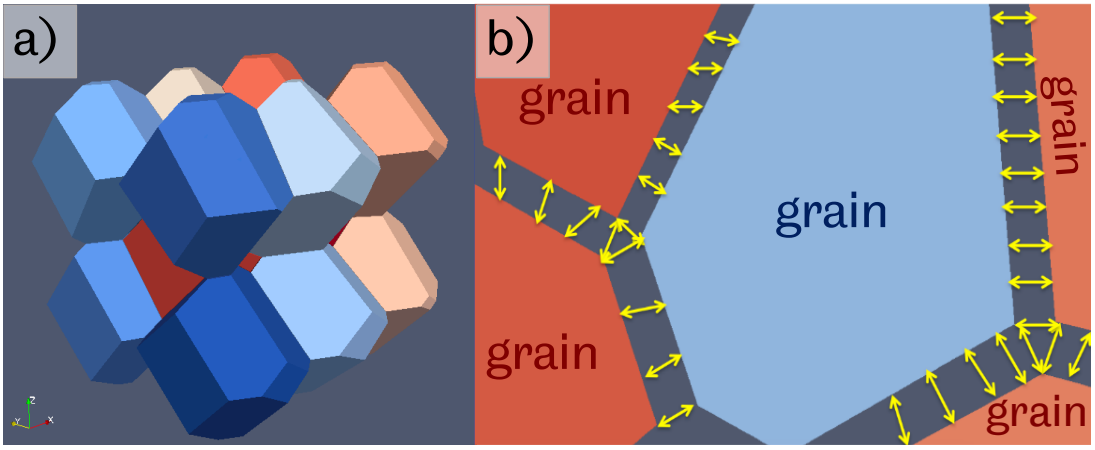

Figure 8.24: a) FEM 14 tetradecahedron shaped $Sm_2(Co, Fe, Cu, Zr)_{17}$ grain volumes with dimensions which are approximately $100 \times 150 \times 150$ nm. b) displays a slice through the magnetic model showing the non-meshed, inter-granular region (maximum 1.5 nm thickness). Yellow arrows represent connected nodes between grain surfaces.

function of the exchange energy between adjacent grains. As the exchange energy is decreased, the coercivity of the magnetic models increases. The chosen values used for the exchange stiffness/energy are arbitrary but represent a gradual decoupling of the system. Eventually, the magnetic grains are completely decoupled for the model with $A_{ex} = 1.4 \times 10^{-14}$ J/m and further reduction of the exchange stiffness does not increase the coercivity.

The cause for the coercivity enhancement in the decoupled state is due to maximising the nucleation field, H_N. A modified form of Brown's expression (equation 8.1), accounts for non-ideal microstructures of real permanent magnets, can be used to estimate the coercivity of an ideal set of homogeneously magnetised particles [315, 316].

$$\mu_0 H_c = \alpha_K \alpha_{ex} \alpha_\Psi H_N^{min} - \mathcal{N}_{eff} J_s \tag{8.1}$$

α_K accounts for the influence of imperfect grain surfaces on the magneto-crystalline anisotropy. Ψ is added to handle the reduction in coercivity due to misalignment of grains and their easy axis with respect to the applied magnetic field and is 0.5 for isotropic magnets [264]. The effective demagnetisation factor, $\mathcal{N}_{\uparrow\{\{}$, is added to attribute the demagnetisation field effects, which are significant at sharp corners and edges of grains. α_{ex} describes the detrimental effects of exchange coupling of adjacent magnetic grains on the coercive field. Exchange coupling between neighbouring grains can exacerbate magnetic inhomogeneity when the coupling rotates the dipoles away from the easy axis within the grain volumes and across

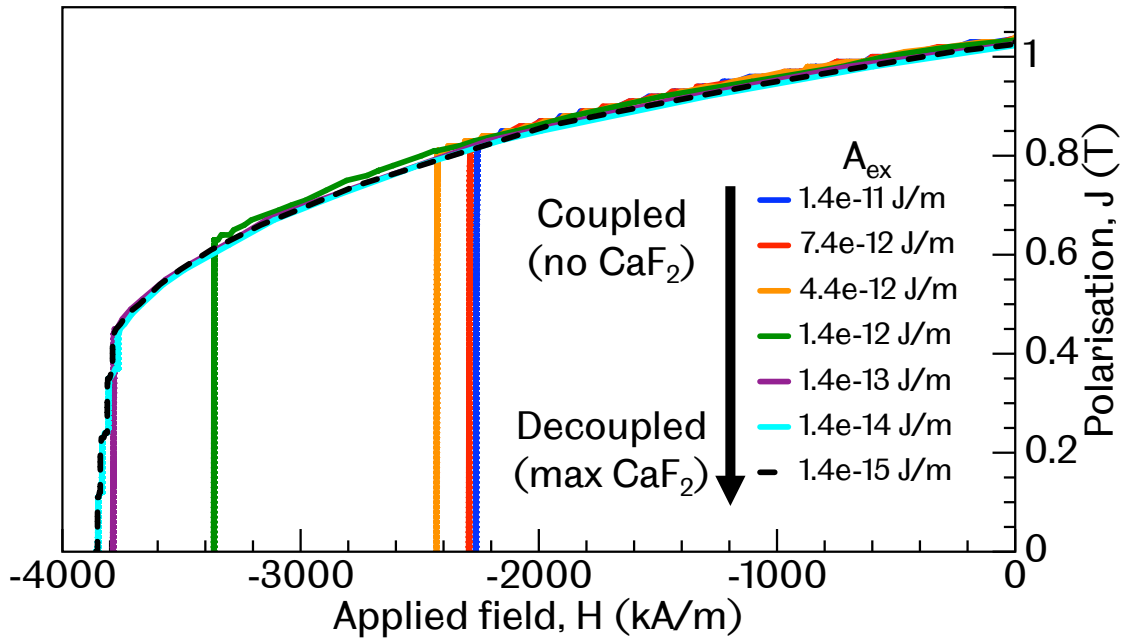

Figure 8.25: Simulated demagnetisation curves for various 14 $Sm_2(Co, Fe, Cu, Zr)_{17}$ grain models. The exchange stiffness, A_{ex}, is decreased from the intrinsic value of the Sm_2Co_{17} phase, (1.4×10^{-11} J/m [55], which is a magnetically coupled system), to 1.4×10^{-15} J/m (magnetically decoupled system).

grain boundaries. In exchange coupled magnets, α_{ex} is significantly less than 1 [264, 315], while in exchange decoupled magnets it is equal to 1 [264, 316]. Therefore, as features and parameters within the FEM micromagnetic models, other than A_{ex}, are kept consistent, the only variable in equation 8.1 is α_{ex}, which approaches unity as the magnetic grains are gradually decoupled.

Due to random distribution of easy axes (within a cone spanning $-90°$ and $+90°$ centred on the positive x-axis) with the 14 grain models, there exists a strong angular relationship between the applied demagnetising field and the easy axes. This affects the 'squareness' of all demagnetising curve, with results much alike those produced by Stoner-Wohlfarth [226]. As the easy-axes for each grain was kept constant in every model, the general shape of the demagnetisation curve to the point of inflection is identical. In the magnetically coupled models (models with $A_{ex} > 1.4 \times 10^{-14}$ J/m), the reversal of the magnetisation is instantaneous at the inflection point and all magnetic grains reverse their magnetisation. However, in the magnetically decoupled models (models with $A_{ex} < 1.4 \times 10^{-14}$ J/m), the shape of the demagnetisation curve after the point of inflection show the magnetic reversal of individual grains. The two models that are fully decoupled possess demagnetisation curves that lie atop of each other, as they are effectively the same

model. This step-like magnetic reversal is indicative of the behaviour observed in the linear demagnetisation curves of the $Sm_2(Co, Fe, Cu, Zr)_{17}$ and CaF_2 composite magnets with large weight additions of insulating material, albeit the latter is on a much larger scale.

Insulating material volume fraction

The previous models simulated the magnetic decoupling effect of the CaF_2 material, which in combination of an increasing pinning effect, contributes to the increase in resistivity and change in the demagnetisation curve of the $Sm_2(Co, Fe, Cu, Zr)_{17}$ and CaF_2 composite magnets. The decoupling effect has a maximum effect on the coercivity when full decoupling is reached, which can be used to explain the peak coercivity value achieved in the composite magnets. However, with increasing concentration of the insulating material, the coercivity begins to decrease again. Here, we present new models, which replicate the volume fraction of non-magnetic material within a granular magnetic system and simulate the effect on demagnetisation.

The same method of model generation by Voronoi tessellation was used to populate our models. The base model is made up of 9 tetradecahedron shaped $Sm_2(Co, Fe, Cu, Zr)_{17}$ grain, approximately $100 \times 100 \times 100$ nm in dimensions and the average cell size of the mesh was 5 nm. Again, for these grain sizes, the $Sm_2(Co, Fe, Cu, Zr)_{17}$ grains act as single-domain magnetic volumes. To model the $Sm_2(Co, Fe, Cu, Zr)_{17}$ and CaF_2 composite models, random seed points were used to populate the CaF_2 phase volume(s). The volume fraction of the CaF_2 phase was matched to calculated volume fractions of the composite magnets with 5, 10 and 20 wt.% addition of CaF_2 (volume fractions equal to 0.12, 0.23 and 0.40 respectively). The intrinsic magnetic properties assigned to the respective phases are presented in table 8.2. The CaF_2 phase is assumed to be diamagnetic and to model this the magnetic properties are set to zero. However, the simulations require a minimum saturation polarisation of 2×10^{-8} T to run without error. The magnetic damping coefficient, $\alpha = 0.2$ in all models.

Phase	J_s **(T)**	K_1 **(MJ/m³)**	K_2 **(MJ/m³)**	A_{ex} **(pJ/m)**
Sm_2Co_{17} [55]	1.32	5.00	0	14
CaF_2	2×10^{-8}	0	0	0

Table 8.2: Intrinsic magnetic properties of the material phases in the $Sm_2(Co, Fe, Cu, Zr)_{17}$ and CaF_2 composite models.

A normal distribution of granular easy axes were generated within cone centred

on the positive x-axis within a range of $-10°$ and $+10°$. This was designed to produce 'square' demagnetisation curves. The granular easy axes were kept consistent throughout each model as the volume fraction of CaF_2 increased. This methodology was repeated three times to produce three different sets of insulating phase models for the purpose of investigating variation in the easy axes distribution, mesh structure and random placement of the insulating phase within the system.

The simulated demagnetisation curves for the three sets of $Sm_2(Co, Fe, Cu, Zr)_{17}$ and CaF_2 composite models of various volume fraction of 'diamagnetic', insulating material are shown in figure 8.26. Different shades of colour are used to represent the sets of data for each composite model type. Dark shades represent the first sets of models, with the second set being a lighter shade, and so forth.

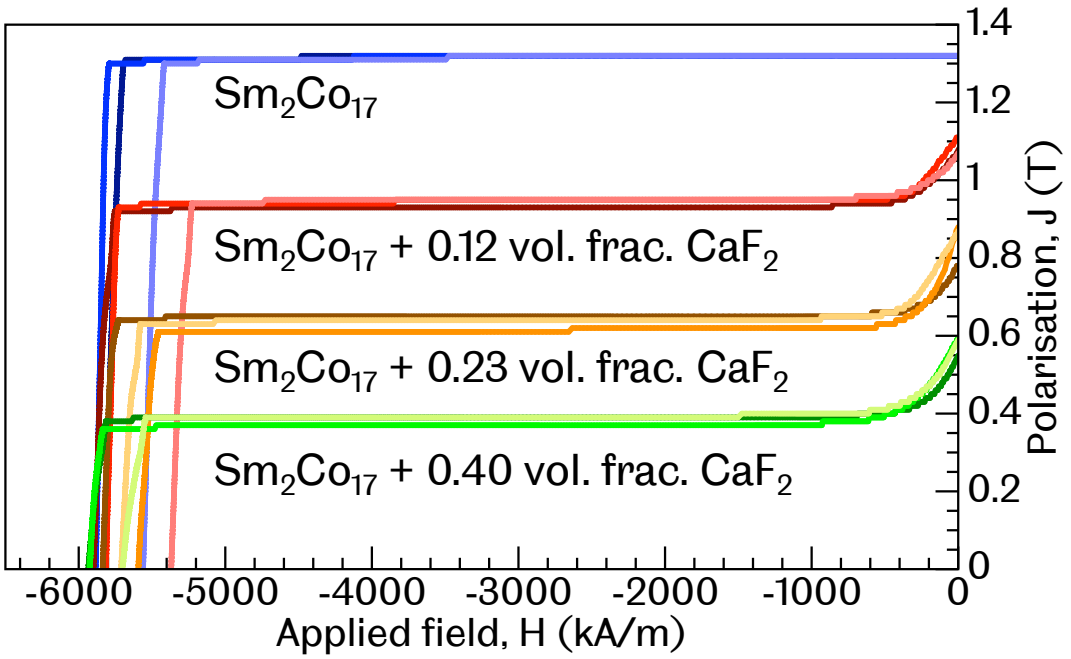

Figure 8.26: Simulated demagnetisation curves for three sets FEM micromagnetic models of $Sm_2(Co, Fe, Cu, Zr)_{17}$ (labelled Sm_2Co_{17}, blue data) and $Sm_2(Co, Fe, Cu, Zr)_{17}$ and CaF_2 composite models with 0.12, 0.23 and 0.40 volume fraction CaF_2 (red, orange and green data curves respectively).

These models show that the replacement of the $Sm_2(Co, Fe, Cu, Zr)_{17}$ magnetic material within the composite material leads to a decrease in the remanence. The simulated demagnetisation curves for the composite magnet models differ in shape from the $Sm_2(Co, Fe, Cu, Zr)_{17}$ only model as they feature a gradual decrease from J_r to a plateau at an applied field of around -500 kA/m. This appears to show a non-instantaneous reversal of the magnetisation in the 'diamagnetic' CaF_2 grains,

which is not expected for phases with assigned zero magneto-crystalline anisotropy. It is suggested that this feature may be as a result of magnetic hardening from the magnetic $Sm_2(Co, Fe, Cu, Zr)_{17}$ grains, as the exchange interaction (present only in the $Sm_2(Co, Fe, Cu, Zr)_{17}$ grains) couples within a few cell lengths (cell size = 5 nm) of the adjacent CaF_2 grains. The CaF_2 phase is treated as 'diamagnetic', but does posses a minimum magnetisation as per requirement of the FEMME (SuessCo, Austria) micromagnetics package. If the magnetically hard $Sm_2(Co, Fe, Cu, Zr)_{17}$ grains exert influence on the smaller fraction CaF_2 grains, a small field is required to overcome this hardening effect, which we see in the demagnetisation curves. Once plateaued, only the $Sm_2(Co, Fe, Cu, Zr)_{17}$ grains are still magnetised in the positive x-axis.

No significant effect is observed on the coercivity in the composite magnet models with increasing volume fraction of CaF_2. Near instantaneous reversal occurs when the critical field is reached, which varies between 5500 kA/m to 6000 kA/m in all composite models. This is approximately the same as the $Sm_2(Co, Fe, Cu, Zr)_{17}$-only models.

The CaF_2 grains within the composite models is modelled as non-interacting, 'diamagnetic' feature within the microstructure. Micromagnetic theory states the presence of such features within the magnetic material should lead to a build up of magnetic 'charge' at the edges/boundaries of the $Sm_2(Co, Fe, Cu, Zr)_{17}$ and CaF_2 phases [1, 227]. The magnetic 'charges' within the volume or at surfaces are a sources of self-demagnetising fields [236, 317]. Based on the modified Brown's expression stated previously (equation 8.1), the self-demagnetisation field is represented by the second term in the formula and therefore, a build up or the magnetic 'charge' leads to a reduction of the field required to nucleate magnetic reversal. In theory, an increase in volume fraction of the CaF_2 should lead to a build up of self-demagnetisation field and explain why a decrease in the coercivity is observed in the experimental data for the composite magnets with large concentrations of insulating material.

To investigate why this effect is not observed in the FEM micromagnetic simulations, the strength and spatial distribution of the demagnetising energy in the models can be visualised at their saturated state, where the self-demagnetising field is at its strongest, and make comparison with the location of magnetic reversal at the onset of nucleation.

Figure 8.27 a) shows the normalised magnetisation (M/M_s) within the grain volumes at the onset of reversal in the $Sm_2(Co, Fe, Cu, Zr)_{17}$-only magnetic model.

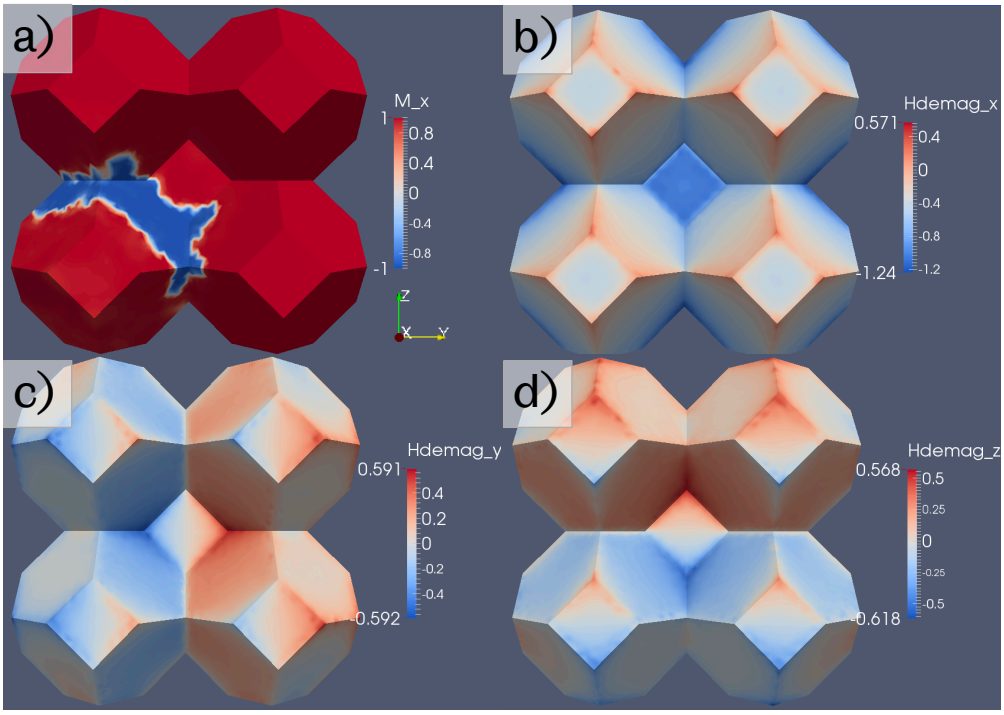

Figure 8.27: $Sm_2(Co, Fe, Cu, Zr)_{17}$ magnetic grains a) magnetisation in the x-axis at the onset of magnetic reversal at -5500 kA/m as viewed down the negative x-axis. Demagnetising field energy at 8000 kA/m as viewed down the negative x-axis b) in the x-axis c) in the y-axis d) in the z-axis. Magnetisation unit-less (J/J_s. Units of demagnetising field energy are in J/m^3.

Red denotes the magnetisation vector in the positive x-axis, while blue is in the negative x-axis. The applied field at the onset of magnetic reversal in figure 8.27 a) is around -5500 kA/m. Looking down the negative x-axis, reversal has nucleated around the edge of the bottom left grain and around the boundary of the adjacent grains. From the same orientation, figure 8.27 b), c) and d) show the demagnetisation field energy at magnetic saturation with respect to the x, y and z axes. The strongest demagnetisation field energies are expectedly in the x-axis, as result of magnetic saturation applied in the positive x-axis. The peak energies are located at the surface edges, which is expected from micromagnetic theory [13]. In this model, the grains and model structure are identical and symmetric about the model centre, so there is symmetry too in the spatial distribution of the demagnetisation energy. Nucleation is favoured in the region shown in figure 8.27 a), when the critical field is reached. Exactly why this particular region nucleates first is not completely understood at this time, but is believed to be due to the easy axis of this magnetic grain lying mostly out of plane, in comparison to the other magnetic grain volumes. Magnetic nucleation occurs in different grains in the second and third sets of models. Again, the grains in which nucleation occurs have

the greatest out of plane easy axis and therefore the nucleation field is lowest for these volumes.

Figures 8.28 and 8.29 show the same composite model with 0.12 volume fraction CaF_2 looking along the negative x and negative y axes respectively. In both figures, a) highlights the distinct material phases: $Sm_2(Co, Fe, Cu, Zr)_{17}$ in orange, CaF_2 in green, b) shows the normalised magnetisation along the negative x-axis at the onset of magnetisation reversal at -5800 kA/m (≈7.25 T). c) shows the demagnetisation energy profile at magnetic saturation in the x axis.

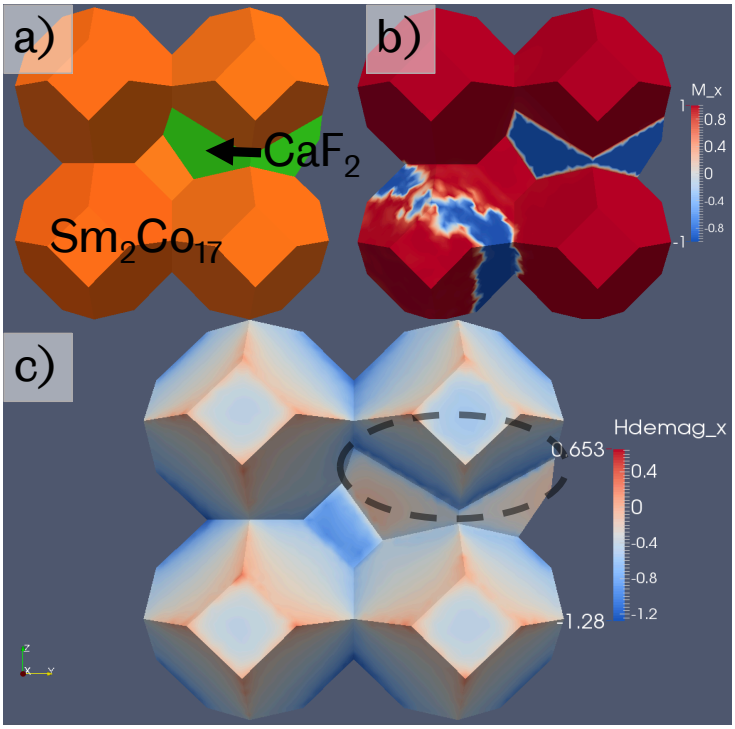

Figure 8.28: FEM composite magnet model containing 0.12 volume fraction of non-magnetic material as viewed along the negative x-axis. a) highlights the distinct material phases: $Sm_2(Co, Fe, Cu, Zr)_{17}$ in orange, CaF_2 in green, b) the ratio of polarisation to saturation polarisation along the negative x-axis at the onset of magnetisation reversal at -5800 kA/m (≈7.25 T). c) shows the demagnetisation energy profile at magnetic saturation in the x axis.

As previously seen, the edges created at the boundary between the $Sm_2(Co, Fe, Cu, Zr)_{17}$ and CaF_2 phase give rise to high demagnetisation energy. Dark blue regions are large negative energies which imply strong self-demagnetising fields in the negative x-axis. This is shown in figure 8.28 c), where the area highlighted shows an increase in the demagnetisation energy in the x-axis. Figure 8.28 c) is the composite magnet model at magnetic saturation and well before nucleation occurs.

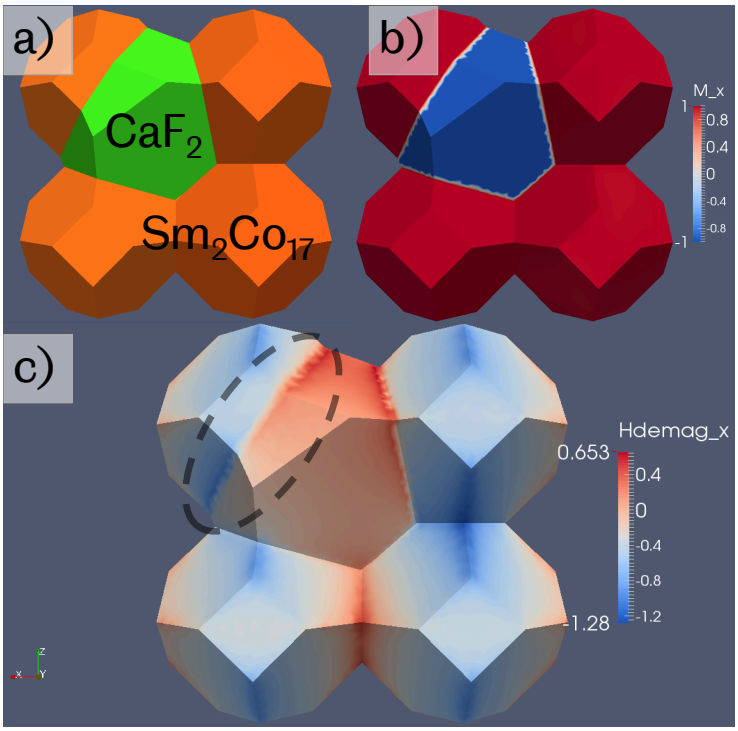

Figure 8.29: FEM composite magnet model containing 0.12 volume fraction of non-magnetic material as viewed along the negative y-axis. a) highlights the distinct material phases: $Sm_2(Co, Fe, Cu, Zr)_{17}$ in orange, CaF_2 in green, b) the ratio of polarisation to saturation polarisation along the negative x-axis at the onset of magnetisation reversal at -5800 kA/m (≈7.25 T). c) shows the demagnetisation energy profile at magnetic saturation in the x axis.

Figure 8.28 b) shows the composite magnet model after it has been subjected to an applied field in the negative x-axis which has nucleated magnetic reversal (blue regions) in the bottom left $Sm_2(Co, Fe, Cu, Zr)_{17}$ grain volume. This is the same magnetic grain in which magnetic reversal nucleated in the $Sm_2(Co, Fe, Cu, Zr)_{17}$-only model and was shown in figure 8.27 a). Nucleation in this grain was believed to occur because the easy axis of this grain volume deviated the most out of plane with respect to the positive x-axis. This relates to a large magneto-crystalline energy term in micromagnetic theory and clearly is more significant to magnetic reversal in the composite magnetic models than the elevated demagnetisation energy experienced at the boundary of the adjacent $Sm_2(Co, Fe, Cu, Zr)_{17}$ and CaF_2 grains. Shown from another angle, figure 8.29 shows the same model as viewed from the negative y-axis. Again, high demagnetisation field energies are shown in figure 8.29 c), however at the onset of magnetic reversal, the magnetisation is maintained in the highlighted grain.

In summary, FEM micromagnetic composite magnet models are not able to

show the volume fraction of diamagnetic CaF_2 to have an effect on the coercivity. It was hypothesised that a build up of demagnetisation energy at the boundary of the $Sm_2(Co, Fe, Cu, Zr)_{17}$ and CaF_2 grains would initiate nucleation of magnetic reversal. However, the large magneto-crystalline energy (models run at 0 K) of the Sm_2Co_{17} dominates and magnetic reversal of the $Sm_2(Co, Fe, Cu, Zr)_{17}$ phase first occurs in grains with the largest deviation angle of the easy axis to the magnetisation vector (positive x-axis).

The assumption of the 'diamagnetic' properties of the CaF_2 may require re-assessment as what best represents the CaF_2 material within the composite magnet model. Size effects may also have a strong influence on the magnetic reversal in the composite models. The dimensions of the granular volumes in the composite magnet models are of the order of 100 nm, while the real magnetic grains range from approximately 1 µm to 20 µm. The dipolar field interaction between grains becomes most effective in larger grains, well beyond the dimension of the grains in the composite magnet models studied [32, 240]. Limitations in the grain dimensions due to computational costs mean the demagnetisation energy effects and dipolar fields may not be truly representative. However, with current methods, it may still be possible to improve on the models through the introduction of grain size and shape inhomogeneity, which would be more representative of the actual microstructure. Inhomogeneity would increase the demagnetisation energy further. Similarly, stress effects are not accounted for in the current FEM micromagnetic models, and would be another boundary energy between the two phases and may initiate nucleation.

8.7.3 Post heat treatment

The study performed on the $Sm_2(Co, Fe, Cu, Zr)_{17}$ and CaF_2 composite magnets before heat treatment is able to show the initial effects on the magnetic and material properties after processing by SPS and showed the addition of the insulating material phase into the microstructure can add magnetic hardness through of domain wall pinning sites, as well as decouple magnetic grains and improve coercivity. However, an understanding of the magnetic properties of the composite materials after heat treatment is a true indication of the SPS processed high-resistivity $Sm_2(Co, Fe, Cu, Zr)_{17}$-based magnets as processed in preparation for application. The $Sm_2(Co, Fe, Cu, Zr)_{17}$ magnet undergoes a change in coercivity mechanism after heat treatment and so the effect of the insulating CaF_2 material into the microstructure may have a different effect.

Polarisation after heat treatment

The measured remanence against CaF_2 concentration for the heat treated composite magnets is displayed in figure 8.30.

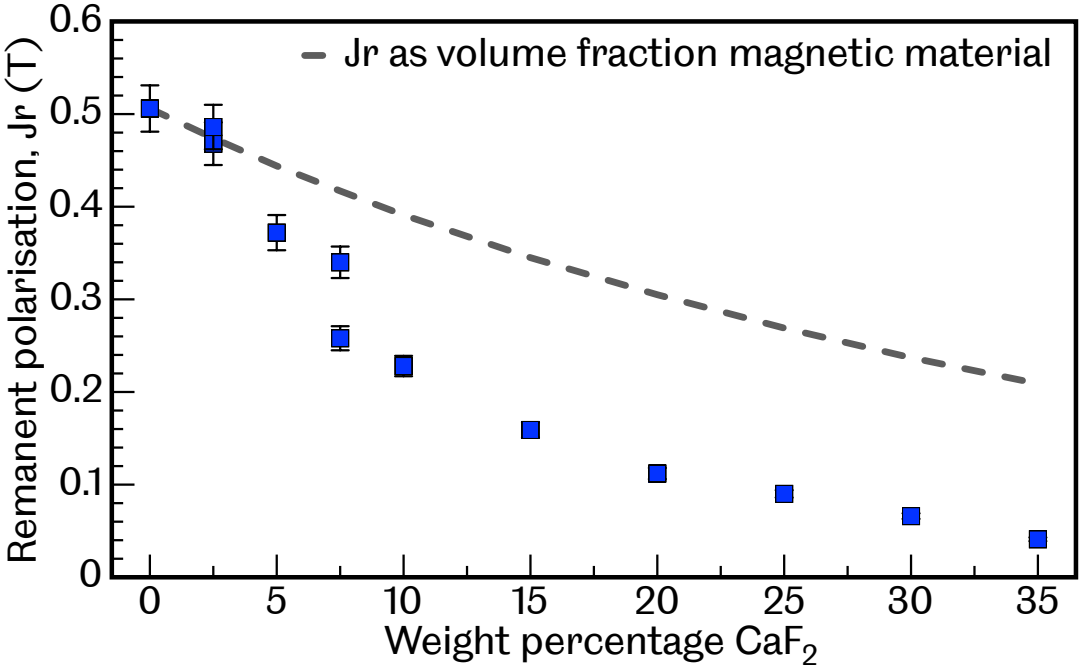

Figure 8.30: Remanent polarisation, J_r, measured in $Sm_2(Co, Fe, Cu, Zr)_{17}$ and CaF_2 composite magnets after heat treatment, against weight percentage of CaF_2.

After heat treatment, the general form of the remanent polarisation as a function of the CaF_2 weight percentage is a negative one, as was the trend observed before heat treatment. The addition of the electrically insulating and 'non-magnetic' CaF_2 phase in increasing volume fractions, as well as the relative density decreasing, has the effect of reducing the remanence. In terms of absolute values, the heat treatment induced increase in the remanence is observed in the $Sm_2(Co, Fe, Cu, Zr)_{17}$ only specimen and in low weight addition CaF_2 (<5 wt.%) composite magnets. However, the deleterious effect of the CaF_2 is significantly more severe in the post-heat treatment composite magnets and very rapidly the remanence falls off to smaller absolute values than the pre-heat treatment equivalents. The theoretical calculation of the remanence as a function of the volume fraction of $Sm_2(Co, Fe, Cu, Zr)_{17}$ magnetic material is represented in figure 8.30 by the dashed line. The experimental data falls off from this theoretical trend much more rapidly compared to the pre-heat treatment study and this most evident in the composite magnets containing 5 wt.% CaF_2 and greater. Phase analysis identified significant oxidation-related phases after heat treatment, which exists at the surface and penetrate to a depth of at least 500 µm. These phases, notably oxides, appear to have a much more significant effect

on the remanent polarisation in the composite magnets when compared to effects observed in post-heat treatment and oxidised $Sm_2(Co, Fe, Cu, Zr)_{17}$. Changes in the resistivity profile were also observed after heat treatment.

Coercivity and initial magnetisation curves

The measured intrinsic coercivity and coercive force values with the concentration of CaF_2 are shown in figure 8.31.

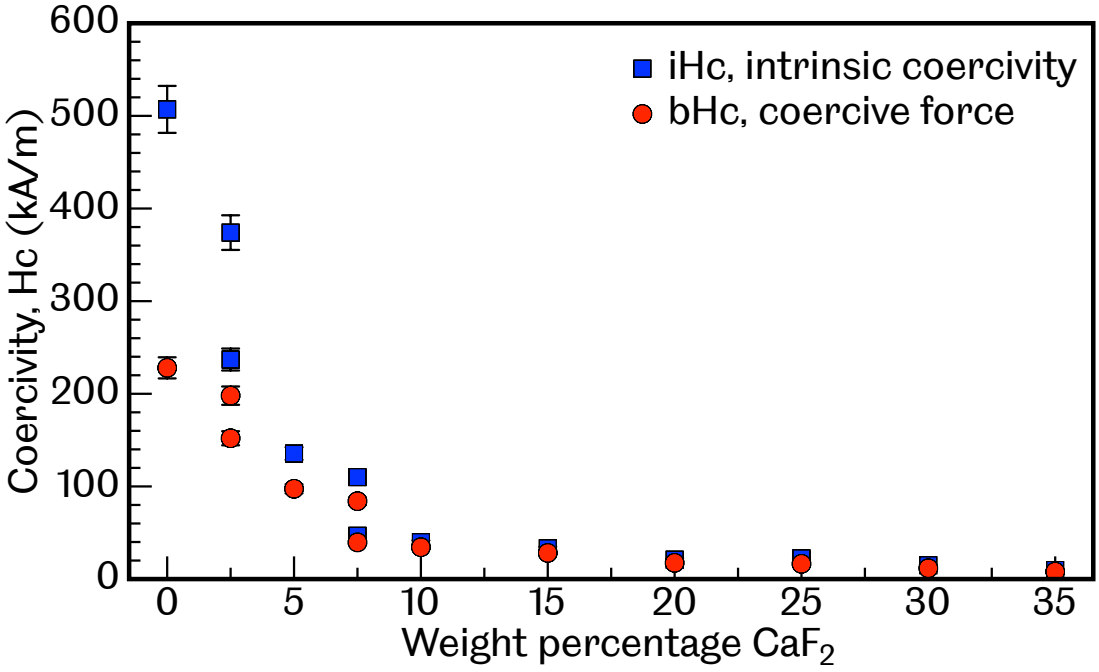

Figure 8.31: Intrinsic coercivity, iH_c, and coercive force, bH_c, measured in post-heat treatment $Sm_2(Co, Fe, Cu, Zr)_{17}$ and CaF_2 composite magnets and plot against weight percentage of CaF_2.

There is a significant change in relationship between the coercivity and weight percentage of insulating material before and after heat treatment in the $Sm_2(Co, Fe, Cu, Zr)_{17}$ and CaF_2 composite magnets. Before heat treatment, the trend saw an initial increase in coercivity, attributed to increased domain wall pinning effects and decoupling of the magnetic grains, before decreasing at the highest insulating material concentrations to coercivity values comparable with the reference magnet. After heat treatment, these effects are not observed and there is an entirely negative influence on the coercivity with the introduction of CaF_2. The heat treatment did improve the absolute coercivities values in the composite magnets with weight addition CaF_2 equal to and below 10 wt.%. However, thereafter the coercivities dropped rapidly towards zero. The composite magnets with CaF_2 weight addition above 5 wt.% are soft magnetic materials and would not

be suitable for permanent magnet applications.

In terms of the overall trend, the addition of CaF_2 is detrimental and volatile to the coercivity of the heat treated $Sm_2(Co, Fe, Cu, Zr)_{17}$. Our study of the heat treatment process and coercivity development in $Sm_2(Co, Fe, Cu, Zr)_{17}$ magnets as shown this to be a delicate process. It is clear the addition of a new material phase into the microsturcture, even though shown to be non-interacting after processing by SPS, further complicates the coercivity generating mechanism. This is further complicated by oxidation effects. All composite specimens analysed by XRD after heat treatment failed to show the 2:17R $Sm_2(Co, Fe, Cu, Zr)_{17}$ phase. In all but one specimen analysed, the the SmFeO phase was dominant and variants of the soft magnetic Co-Fe phase were also prevalent to depths at least 500 µm. After removal of approximately 500 µm of surface material, these oxidation-related phases were not identified. Beneath the surface, the characteristic 2:17 $Sm_2(Co, Fe, Cu, Zr)_{17}$ phase was present, but another new phase was also identified; $(Ca_{0.8}Zr_{0.2})F_2$. The CaF_2 material in the composite magnets may, through the heat treatment or as an effect of oxidation, react with Zr and remove it from the $Sm_2(Co, Fe, Cu, Zr)_{17}$ matrix. Removal of zirconium in $Sm_2(Co, Fe, Cu, Zr)_{17}$ magnets has a significant effect as to disrupt the phase equilibria and the formation the 2:17R cell and 1:5H cell-boundary nanostructured phases [60, 86]. As the concentration of CaF_2 increases, more zirconium would be removed, making the precipitation and formation of the cellular nanostructure during heat treatment more difficult and heterogeneous, resulting in a complete reduction of coercivity for this type of REPM. This could explain why such trends are observed after heat treatment. Future work would seek to confirm the relationship between $(Ca_{0.8}Zr_{0.2})F_2$ within the $Sm_2(Co, Fe, Cu, Zr)_{17}$ and CaF_2 composite magnet material and the morphology of the cellular nanosructure via TEM. No published literature on $Sm_2(Co, Fe, Cu, Zr)_{17}$ and CaF_2 exists as comparison.

Figure 8.32 shows the initial magnetisation curves for several $Sm_2(Co, Fe, Cu, Zr)_{17}$ and CaF_2 composite samples, as well as a reference $Sm_2(Co, Fe, Cu, Zr)_{17}$-only magnet. The reference $Sm_2(Co, Fe, Cu, Zr)_{17}$ sample (1-33) underwent a slightly different heat treatment, in that it was aged for 2 hours, rather than the 16 hours used for the composite magnets. However, this is not expected to affect the initial magnetisation curves.

The $Sm_2(Co, Fe, Cu, Zr)_{17}$ specimen (blue data) has the lowest gradient (susceptibility) of all the initial magnetisation curves and as a result requires the largest field on approach to magnetic saturation. There is a point of inflection at around 250 kA/m, which is an indication of the applied field surpassing the

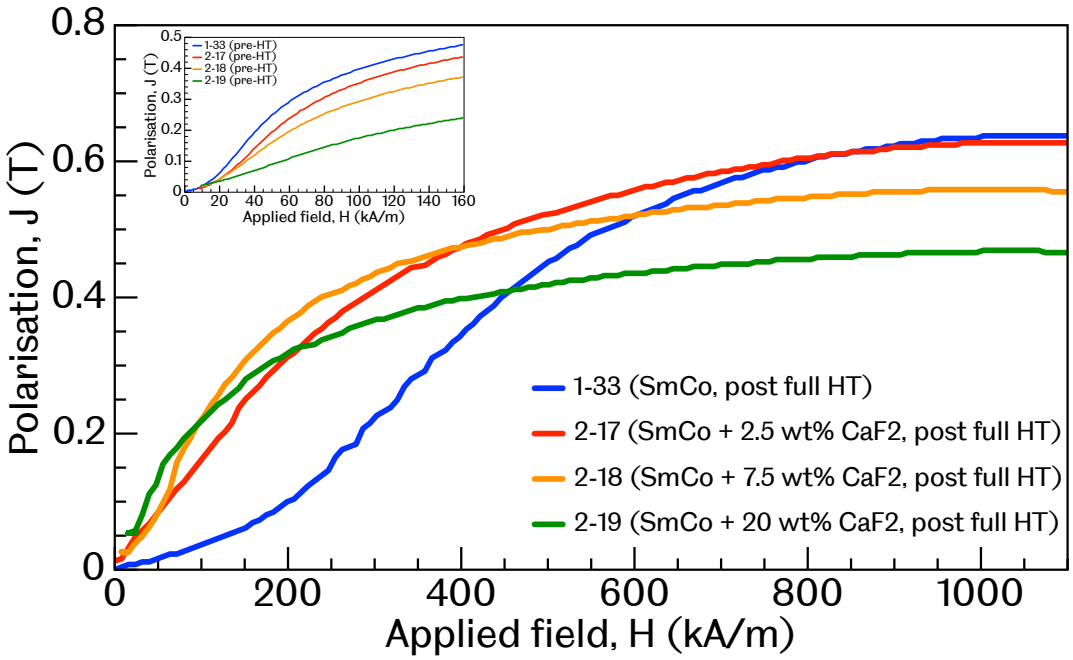

Figure 8.32: Initial magnetisation curves for post-heat treatment $Sm_2(Co, Fe, Cu, Zr)_{17}$ magnet (1-33) and $Sm_2(Co, Fe, Cu, Zr)_{17}$ and CaF_2 composite magnets with varying concentration of insulating material. Inset shows the initial magnetisation curves for the same samples before heat treatment.

pinning field of the magnet. This inflection point is comparable to the coercivity (iH_c =428 kA/m) of sample 1-33 and this shape of the initial magnetisation curve is characteristic of the pinning-based coercivity. As CaF_2 is added, the gradient of the initial magnetisation changes and increases. The initial magnetisation curves of all the composite magnets studied become nearly identical in their shape and appears independent of the CaF_2 weight percentage, although the saturation polarisation decreases as the volume fraction of magnetic material decreases.

Figure 8.33 is another way of presenting the this information and shows the rate of change in the gradient with the applied field and evidences the similar gradients of the composite magnets. The large initial susceptibility of the composite magnets is characteristic of magnets with a nucleation-based coercivity mechanism. Therefore, either through the presence of the oxidation-related phases present in the material or through a disruption to the precipitation and formation of the cellular nanostructrue, a pinning-based coercivity after heat treatment has not been produced, and this is consistent throughout the $Sm_2(Co, Fe, Cu, Zr)_{17}$ composite magnets studied, irrespective of the amount of CaF_2 added. If the composite magnets are a nucleation-based coercivity mechanism, the increasingly concentrated insulating material phase, which may also remove Zr from the microstructure, also

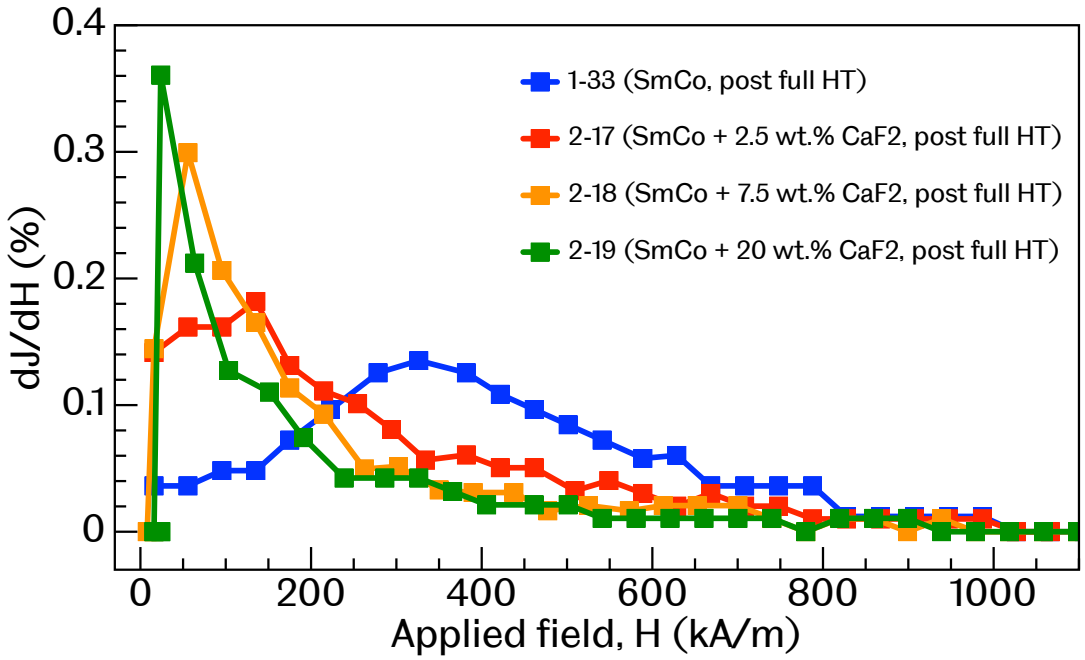

Figure 8.33: Rate of change of initial magnetisation curves for post-heat treatment $Sm_2(Co, Fe, Cu, Zr)_{17}$ magnet (1-33) and $Sm_2(Co, Fe, Cu, Zr)_{17}$ and CaF_2 composite magnets with varying concentration of insulating material.

becomes nucleation sites for reversed domains [9, 13], which could explain the negative relationship between the coercivity and concentration of CaF_2 after heat treatment.

In the post heat treatment $Sm_2(Co, Fe, Cu, Zr)_{17}$ and CaF_2 composite magnets, the deleterious effect on the magnetic properties; the remanence and the coercivity, combine produce a similar trend in the energy product, shown in figure 8.34.

The measured energy products show a similar trend to the coercivity and, while there is a relatively small loss in the $Sm_2(Co, Fe, Cu, Zr)_{17}$ and 2.5 wt.% CaF_2 composite magnet samples, from the addition of 5 wt.% onwards, the energy product rapidly approaches zero. The cumulative effects observed on the remanence and coercivity lead to a similar trend in the energy product. With oxidation phases present within the composite material, the $Sm_2(Co, Fe, Cu, Zr)_{17}$ and CaF_2 composite magnets after heat treatment could not be suitable for most REPM applications. However, there is potential for blended powder method high resistivity composite permanent magnets, as was shown before the heat treatment, where positive increases were observed in the bulk resistivity and coercivity profiles with concentration of CaF_2.

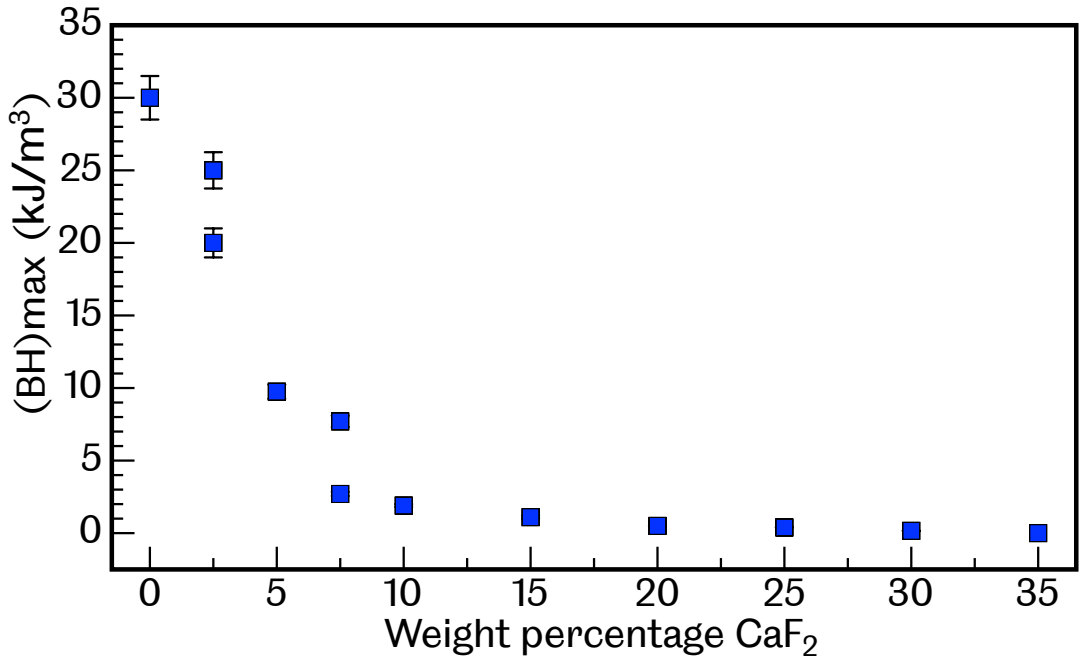

Figure 8.34: Energy product, $(BH)_{max}$ measured in post-heat treatment $Sm_2(Co, Fe, Cu, Zr)_{17}$ and CaF_2 composite magnets and plot against weight percentage of CaF_2.

8.8 Chapter summary

Our study of high resistivity blended $Sm_2(Co, Fe, Cu, Zr)_{17}$ and CaF_2 composite magnets has provided a number of insights into the processing and heat treatment of this type of material, designed for minimising eddy current effects during operation.

The SPS technique has been used to quickly and efficiently produce a wide number of $Sm_2(Co, Fe, Cu, Zr)_{17}$ and CaF_2 blended magnet prototypes. The blended powder method for high resistivity permanent magnets was shown to be capable after processing by SPS to produce an isotropic distribution of the insulating material. Future work is required to develop an optimised SPS processing parameters for the $Sm_2(Co, Fe, Cu, Zr)_{17}$ and CaF_2 blended powders to achieve full densification, with the hold time recommended as the best candidate for study. Hold pressure could also be investigated, although this would require a different mould and punch material with superior material properties at elevated temperature than graphite.

The effect of adding CaF_2 to form a composite magnet with $Sm_2(Co, Fe, Cu, Zr)_{17}$ gives significantly different results on both the material and magnetic properties before and after heat treatment. There is no significant evidence for the $Sm_2(Co, Fe, Cu, Zr)_{17}$ and CaF_2 phases interacting after processing powders by SPS.

After heat treatment however, oxidation-related oxides and Co-Fe type phases are prevalent at the surface. Sub-surface (below approximately 500 µm) there is evidence that CaF_2 and Zr interact, which affects the resistivity and coercivity of the post-heat treatment composite magnets.

The resistivity variation with weight percentage of CaF_2 before heat treatment appears to reach the percolation threshold at around 30 wt.% (0.53 volume fraction). It is possible to approximately double the resistivity of $Sm_2(Co, Fe, Cu, Zr)_{17}$ through the addition of 10 wt.% CaF_2. After heat treatment, the oxidation-related effects result in only a subtle increase in the resistivity with large concentrations of CaF_2.

The remanence of the composite magnets decreased with increasing weight addition of CaF_2 both before and after heat treatment. The replacement of the magnetic material within the volume expectedly reduces the remanence, although a decreasing relative density in the composite magnets further contributed to the decline.

The coercivity increased in the $Sm_2(Co, Fe, Cu, Zr)_{17}$ and CaF_2 composite magnets up to 20 wt.% addition of insulating material before heat treatment. Initial magnetisation curve analysis showed the CaF_2 phase within the microstructure increased the pinning of domain walls and increased the coercivity, before decoupling of the magnetic grains occurred in high weight additions of CaF_2, an effect which was shown to be consistent with FEM micromagnetic models. For permanent magnets which have nucleation-based coercivity mechanisms, as is the case in $Sm_2(Co, Fe, Cu, Zr)_{17}$ magnets before the heat treatment, it is possible to approximately maintain the remanence and improve the coercivity, energy product and resistivity: a 5 wt. % addition of CaF_2 to $Sm_2(Co, Fe, Cu, Zr)_{17}$ improved the resistivity by 17% and the energy product by 11%, although the 'squareness' of the demagnetisation loop was reduced.

After heat treatment, oxidation effects were shown to be significantly detrimental to both the resistivity enhancement and magnetic properties of the $Sm_2(Co, Fe, Cu, Zr)_{17}$ and CaF_2 composite magnets. Oxides and soft-magnetic phases dominate at the surface and an apparent reaction between CaF_2 phase and zirconium in the $Sm_2(Co, Fe, Cu, Zr)_{17}$ phase leads to the formation of $(Ca_{0.8}Zr_{0.2})F_2$, identified in phase analysis here. The presence and prevalence of these phases affect the precipitation and formation of the 2:17R cells, 1:5H cell walls and Zr rich lamellar phase, all of which are critical to the coercivity enhancement of $Sm_2(Co, Fe, Cu, Zr)_{17}$ permanent magnets.

For magnets which have nucleation-based coercivity, this study has shown it is possible to increase the electrical resistivity, thus effectively reducing eddy cur-

rent effects, and also improve the coercivity and energy product for blended powder REPM composites. Domain wall pinning-based coercivity permanent magnets require better control, as in the case of $Sm_2(Co, Fe, Cu, Zr)_{17}$, not to disrupt the delicate nanostructure, which lends to the coercivity of the REPM.

Chapter 9

Conclusions and future work

Conclusions

The work presented over the previous chapters has detailed the study of processing $Sm_2(Co, Fe, Cu, Zr)_{17}$ powders by way of SPS. Over cycle times of tens of minutes, optimal processing parameters were found which produced full density specimens in preparation for a required heat treatment. An issue of carbon uptake during the sinter process was shown to be insignificant to the bulk properties once steps were taken to remove minuscule surface material. As a powder consolidation method, the SPS technique was shown to occur at lower sinter temperatures and was much faster than conventional, pressure-less sintering methods used commercially for $Sm_2(Co, Fe, Cu, Zr)_{17}$. The only noticeable microstructural difference in the as-processed state between the two methods was the average grain size in the SPS processed material was a tenth of that in the conventional sinter processed sample studied.

Naturally, this work extended into the heat treatment of the SPS processed $Sm_2(Co, Fe, Cu, Zr)_{17}$ magnets, which is crucial to developing the hard magnetic properties of this type of microcrystalline and sintered REPM. In a study of the parameters in a typical heat treatment for $Sm_2(Co, Fe, Cu, Zr)_{17}$, the largest coercivities and energy products were found. However, the coercivities measured were notably lower than those developed in commercial magnets. With further optimisation and greater control over exposure to oxygen in the precursor powders and during the heat treatment, it is believed that the coercivity will improve to comparable values measured within the literature. Similarly, to better qualify the magnets produced by SPS requires a better method to induce texture within the magnet than those explored in this work. Either through greater magnetic fields to better align the powder particles, or through hot deformation methods, to enhance the remanent polarisation and energy product of the produced magnets. The latter method has

been shown possible with use of modified SPS apparatus and could be replicated in future studies of SPS processed $Sm_2(Co, Fe, Cu, Zr)_{17}$ magnets [34, 50]. However, while single specimen cycle times and energy costs (assumed) were reduced when the SPS technique was used to sinter $Sm_2(Co, Fe, Cu, Zr)_{17}$ magnets, the proceeding heat treatment, which is complex and over several hours, will mean the overall cost reduction or processing advantages from using the SPS technique are minor, therefore weakening the argument for using SPS to categorically produce microcrystalline $Sm_2(Co, Fe, Cu, Zr)_{17}$. Bespoke benefits from the rapid processing by SPS, such as an observed reduction in grain size leads that may improve mechanical properties or corrosion resistance, warrant further investigation and may justify small and unique production runs for particular $Sm_2(Co, Fe, Cu, Zr)_{17}$ applications.

The difficulties encountered in the project were mostly confined to the heat treatment of the $Sm_2(Co, Fe, Cu, Zr)_{17}$ magnets and should not detract from the overall viability of processing REPMs by SPS technique. The rapid processing of the SPS technique lends itself to a high-throughput approach to material development. Example of this was the systematic study of high-resistivity $Sm_2(Co, Fe, Cu, Zr)_{17}$ and varying concentration CaF_2 composite magnets for use in high temperature applications where eddy currents are generated. While the effect of oxidation masked the potential of these composite magnets after heat treatment, it was shown before heat treatment there was a beneficial effect of CaF_2 material on the resistivity and magnetic properties at low weight concentrations for a magnet that is defined by a nucleation based coercivity mechanism, much like Nd-Fe-B-type and $SmCo_5$ magnets. This area of research would benefit from TEM microscopy showing the influence and interaction of CaF_2 on the post-heat treatment $Sm_2(Co, Fe, Cu, Zr)_{17}$ cellular nanostructure. Disruption to the precipitated cell structure, which was assumed to occur with the effects of oxidation, is highly detrimental to the use of $Sm_2(Co, Fe, Cu, Zr)_{17}$ composites as permanent magnets. The application of these blended high-resistivity $Sm_2(Co, Fe, Cu, Zr)_{17}$ and CaF_2 magnets with minimised eddy current effects at high temperature will still be defined by achieving an optimal cellular nanostructure.

In further remarks; the batch processing nature of the SPS apparatus studied in this work can sinter a single specimen significantly quicker than a commercial vacuum induction furnace. However, commercial production of sintered REPMs utilise high volume processing methods. Arnold Magnetic Technologies produce their $Sm_2(Co, Fe, Cu, Zr)_{17}$ magnets from powders by sintering a large block of material and cutting into smaller specimens of a desired geometry or through the use of tooling which allows the mass production of several thousand magnets in one go within a large induction furnace [318].

Replicating such high volume production methods in SPS has been met with challenges, as there are limitations in the scale of sintered geometry. Maintaining the temperature distribution across increasing diameter specimens becomes very difficult [319, 320] and current generation SPS apparatus are limited by the power/current they can supply, which defines a maximum specimen diameter based upon the required current density to achieve the sinter temperature [321]. Current maximum diameter specimens achieved with commercial SPS equpment are around 400 mm[321, 322], which is much smaller than the diameters of around 1 m that are routinely produced by conventional commercial methods. Other than increasing volume, increasing production via automation and reducing down time is another area in development to make the SPS technique more appealing to the sintered permanent magnet industry. Automated SPS processing platforms, multi specimen tools and the utilisation of multiple chambers to reduce production cycle times by moving cooling specimens away from the sintering chamber are examples of this [322].

As a recommendation from the study of the literature and experience in the SPS processing technique for $Sm_2(Co, Fe, Cu, Zr)_{17}$ and composite permanent magnets; it is that the strength of the SPS technique lies in its use as a development/prototyping tool for new permanent magnet materials. New alloying compositions, non-equilibrium phases or composite materials can be rapidly produced and studied if the SPS platform is used, thus reducing lead times on research and development. This is crucial in current global material markets, where current trends seek to end a reliance on critical rare earth elements. Current production methods that can be implemented are near-net shape magnetic parts, which reduces the time and cost spent machining and minimises material wasteage. Several authors have explored non-disc geometries such as rectangles, domes and rings using specially designed moulds [320, 321]. While disc shaped magnets are inherent to the largest energy products in hard magnets [9], certain applications require specific magnetic fields and the geometry of the permanent magnet is designed to achieve this. If SPS can produce a wide array of geometries, it will also improve its practicality to the permanent magnet industry.

Development of new magnetic materials, in combination with the ability of the SPS technique in producing nanocrystalline microstructures and near-net shape parts, may be able to place the SPS method as a production technique for unique permanent magnet materials in bespoke applications. It is noted however, that as the work in this study has shown, much developmental work is required to perfect the processing methodology of REPMs by SPS to compare with those produced by conventional methodologies, which have had decades of optimisation.

Future work

- To complement the study of the magnetic properties of the $Sm_2(Co, Fe, Cu, Zr)_{17}$ and composite magnets after heat treatment, TEM microscopy should be used to establish a relationship with the heat treatment, and the presence of the CaF_2 or oxide phases, on the morphology and structure of the cellular nanostructure.

- The oxidation effects were attributed to oxidation of the precursor powder and allowing the specimen to cool in air after the homogenisation stage of the heat treatment. Future work would aim to implement greater control over the handling and storage of the $Sm_2(Co, Fe, Cu, Zr)_{17}$ powders, with the intention to reduce exposure to oxygen at a bare minimum. If the homogenisation stage (which is performed at 1170 °C for 2 hours under argon or vacuum atmosphere) could be conducted within the SPS vessel, it may offer greater control over oxidation and provide rapid cooling to room temperature via the water cooled hydraulic punches.

- Magnetic anisotropy is required to optimise the energy product of the SPS processed $Sm_2(Co, Fe, Cu, Zr)_{17}$ and CaF_2 composite magnets. The strength of magnetic fields for powder alignment available in this project only induced partial alignment. If a study of the maximum energy products was required, then future work would look to access larger magnetic fields or alternative methods, such as hot deformation, which may possible to achieve within the SPS apparatus available.

- The rapid processing of the SPS technique is off-set by the long heat treatment of $Sm_2(Co, Fe, Cu, Zr)_{17}$, and from a mass production point of view this may be counter-productive. Similarly, the addition of the CaF_2 to the composite material before heat treatment, and in a state defined by a nucleation-based coercivity mechanism, enhanced both the resistivity and coercivity. Therefore, it may warrant exploring blended powder permanent magnets which do not require prolonged heat treatments and/or are nucleation-based coercivity mechanism. This could utilise the rapid processing of the SPS technique to produce nanocrystalline Nd-Fe-B or Sm-Co-type REPMs with insulating material addition.

References

1. Coey, J. M. D. Advances in Magnetics - Hard Magnetic Materials : A Perspective. *IEEE Transactions on Magnetics* **47,** 4671–4681 (2011).
2. Gutfleisch, O. *et al.* Magnetic materials and devices for the 21st century: stronger, lighter, and more energy efficient. *Advanced Materials* **23,** 821–42 (Feb. 2011).
3. Gibson, M. & Parkinson, I. *Once Ignored on the Periodic Table, Don't Ignore Them Now: A Rare Earth Element Industry Overview* tech. rep. 416 (2011), 41.
4. Gambogi, J. *U.S. Geological Survey Mineral Commodity Summaries: Rare Earths* tech. rep. (2017), 134–135. arXiv: `arXiv:1011.1669v3`.
5. Goll, D., Kronmüller, H. & Stadelmaier, H. H. Micromagnetism and the microstructure of high-temperature permanent magnets. *Journal of Applied Physics* **96,** 6534–6545 (2004).
6. Ishak, D., Zhu, Z. & Howe, D. Eddy-Current Loss in the Rotor Magnets of Permanent-Magnet Brushless Machines Having a Fractional Number of Slots Per Pole. *IEEE Transactions on Magnetics* **41,** 2462–2469 (2005).
7. Chinnasamy, C., Jasinski, M. M., Patches, D. & Liu, J. High Electrical Resistivity Sm(Co,Fe,Cu,Zr) /Sm S Permanent Magnets With Layered Structure for Advanced Motors. *IEEE Transactions on Magnetics* **48,** 3166–3169 (2012).
8. Marinescu, M., Gabay, a. M., Liu, J. F. & Hadjipanayis, G. C. Fluoride-added Pr–Fe–B die-upset magnets with increased electrical resistivity. *Journal of Applied Physics* **105,** 07A711 (2009).
9. Coey, J. M. D. *Magnetism and Magnetic Materials* 614 (Cambridge University Press, Cambridge, United Kingdom, 2010).
10. O' Handley, R. C. *Modern Magnetic Materials: Principles and Applications* 740 (John Wiley and Sons, 2000).
11. Aharoni, A. *Introduction to the Theory of Ferromagnetism* 315 (Oxford University Press, Oxford, England, United Kingdom, 1996).

12. Spaldin, N. *Magnetic Materials: Fundamentals and Device Applications* 213 (Cambridge University Press, 2003).

13. Kronmuller, H. & Fahnle, M. *Micromagnetism and the Microstructure of Ferromagnetic Solids* 432 (Cambridge University Press, 2003).

14. Barkhausen, H. Two with help of new repeating rediscovered appearances by H Barkhausen - The silence during unmagnetising of iron. *Physikalische Zeitschrift* **20,** 401–403 (1919).

15. Sixtus, K. J. & Tonks, L. Propagation of large Barkhausen discontinuities. *Physical Review* **37,** 930–959 (1931).

16. Sixtus, K. J. & Tonks, L. Propagation of large Barkhausen discontinuities. II. *Physical Review* **42,** 419–435 (1932).

17. Brown, W. F. Theory of the approach to magnetic saturation. *Physical Review* **58,** 736–743 (1940).

18. Brown, W. F. The effect of dislocations on magnetization near saturation. *Physical Review* **60,** 139–147 (1941).

19. Gutfleisch, O. *et al.* Evolution of magnetic domain structures and coercivity in high-performance SmCo 2:17-type permanent magnets. *Acta Materialia* **54,** 997–1008 (Feb. 2006).

20. Strnat, K. & Strnat, R. M. W. Rare earth-cobalt permanent magnets. *Journal of Magnetism and Magnetic Materials* **100,** 38–56 (1991).

21. Hadjipanayis, G. C. Nanophase hard magnets. *Journal of Magnetism and Magnetic Materials* **200,** 373–391 (1999).

22. Rong, C.-b. *et al.* Effects of annealing on the coercivity of Sm(Co,Fe,Cu,Zr)z ribbons and its temperature dependence. *Journal of Physics D: Applied Physics* **39,** 437–440 (2006).

23. Kronmüller, H. & Goll, D. Analysis of the temperature dependence of the coercive field of Sm2Co17 based magnets. *Scripta Materialia* **48,** 833–838 (2003).

24. Chen, R.-j., Zhang, H.-w., Rong, C.-b., Sun, J.-r. & Shen, B.-g. Temperature dependence of the magnetization reversal in magnets. *Journal of Magnetism and Magnetic Materials* **305,** 191–195 (2006).

25. Fidler, J., Schrefl, T., Hoefinger, S. & Hajduga, M. Recent developments in hard magnetic bulk materials. *Journal of Physics: Condensed Matter* **16,** 455–470 (2004).

26. Liu, S. Magnetic alignment in powder magnet processing. *Journal of Applied Physics* **76,** 6757 (1994).

27. Gutfleisch, O. Controlling the properties of high energy density permanent magnetic materials by different processing. *Journal of Applied Physics* **33,** 157–172 (2000).

28. Cui, X. *et al.* Effects of alignment on the magnetic and mechanical properties of sintered Nd–Fe–B magnets. *Journal of Alloys and Compounds* **563,** 161–164 (June 2013).

29. Kronmüller, H., Fischer, R., Seeger, M. & Zern, A. Micromagnetism and microstructure of hard magnetic materials. *Journal of Physics D: Applied Physics* **29,** 2274–2283 (1996).

30. Woodcock, T. G. *et al.* Understanding the microstructure and coercivity of high performance NdFeB-based magnets. *Scripta Materialia* **67,** 536–541 (2012).

31. Hono, K. & Sepehri-Amin, H. Strategy for high-coercivity Nd-Fe-B magnets. *Scripta Materialia* **67,** 530–535 (2012).

32. Sepehri-Amin, H., Ohkubo, T., Gruber, M., Schrefl, T. & Hono, K. Micromagnetic simulations on the grain size dependence of coercivity in anisotropic Nd-Fe-B sintered magnets. *Scripta Materialia* **89,** 29–32 (2014).

33. Liu, J. *et al.* Grain size dependence of coercivity of hot-deformed Nd-Fe-B anisotropic magnets. *Acta Materialia* **82,** 336–343 (2015).

34. Castle, E. *et al.* High coercivity, anisotropic, heavy rare earth-free Nd-Fe-B by Flash Spark Plasma Sintering. *Scientific Reports* **7,** 1–12 (2017).

35. Muralidhar, S. *et al.* Temperature-dependent first-order reversal curve measurements on unusually hard magnetic low-temperature phase of MnBi. *Physical Review B* **95,** 1–9 (2017).

36. Zhang, D. *et al.* Magnetic properties and structure of bulk nanocrystalline Sm(Co, Cu, Fe, Zr)7.6 sintered magnet. *Journal of Applied Physics* **105,** 07A707 (2009).

37. Lu, N., Song, X., Liu, X. & Zhang, J. Preparation and magnetic properties of amorphous and nanocrystalline Sm2Co17 alloys. *Intermetallics* **18,** 1180–1184 (June 2010).

38. Manaf, A., Buckley, R., Davies, H. & Leonowicz, M. Enhanced magnetic properties in rapidly solidified Nd-Fe-B based alloys. *Journal of Magnetism and Magnetic Materials* **101,** 360–362 (1991).

39. Yue, M., Zhang, J., Liu, W. & Wang, G. Chemical stability and microstructure of Nd-Fe-B magnet prepared by spark plasma sintering. *Journal of Magnetism and Magnetic Materials* **271,** 364–368 (May 2004).

40. Wang, G., Liu, W., Huang, Y., Ma, S. & Zhong, Z. Effects of sintering temperature on the mechanical properties of sintered NdFeB permanent magnets prepared by spark plasma sintering. *Journal of Magnetism and Magnetic Materials* **349,** 1–4 (2014).

41. Sepehri-Amin, H., Une, Y., Ohkubo, T., Hono, K. & Sagawa, M. Microstructure of fine-grained Nd-Fe-B sintered magnets with high coercivity. *Scripta Materialia* **65,** 396–399 (2011).

42. Manaf, A., Buckley, R. A. & Davies, H. A. New nanocrystalline high-remanence Nd-Fe-B alloys by rapid solidification. *Journal of Magnetism and Magnetic Materials* **128,** 302–306 (1993).

43. Fidler, J. & Schrefl, T. Overview of Nd–Fe–B magnets and coercivity (invited). *Journal of Applied Physics* **79,** 5029 (1996).

44. Davies, H. A. Nanocrystalline exchange-enhanced hard magnetic alloys. *Journal of Magnetism and Magnetic Materials* **157-158,** 11–14 (1996).

45. Porwal, H. V. *et al.* Magnetic properties of nanocrystalline Ni3Fe compacts prepared by spark plasma sintering. *Intermetallics* **35,** 98–103 (2013).

46. Gutfleisch, O., Eckert, D., Schäfer, R., Müller, K. H. & Panchanathan, V. Magnetization processes in two different types of anisotropic, fully dense Nd-FeB hydrogenation, disproportionation, desorption, and recombination magnets. *Journal of Applied Physics* **87,** 6119–6121 (2000).

47. Gutfleisch, O. *et al.* Nanocrystalline high performance permanent magnets. *Journal of Magnetism and Magnetic Materials* **242-245,** 1277–1283 (2002).

48. Lee, R. W., Brewer, E. G. & Schaffel, N. A. Processing of Neodymium-Iron-Boron melt-spun ribbons to fully dense magnets. *IEEE Transactions on Magnetics* **21,** 1958–1963 (1985).

49. Gabay, A. M., Marinescu, M., Liu, J. F. & Hadjipanayis, G. C. Deformation-induced texture in nanocrystalline 2:17, 1:5 and 2:7 Sm-Co magnets. *Journal of Magnetism and Magnetic Materials* **321,** 3318–3323 (2009).

50. Castle, E., Sheridan, R., Grasso, S., Walton, A. & Reece, M. Rapid sintering of anisotropic, nanograined Nd-Fe-B by flash-spark plasma sintering. *Journal of Magnetism and Magnetic Materials* **417,** 279–283 (2016).

51. Huang, Y. L. *et al.* Diffusion of Nd-rich phase in the spark plasma sintered and hot deformed nanocrystalline NdFeB magnets. *Journal of Applied Physics* **111,** 10–14 (2012).

52. Kronmüller, H. & Goll, D. Coercivity of 2:17 Based Permanent Magnets. *Journal of Iron and Steel Research International* **13,** 39–47 (2006).

53. Kronmüller, H. & Goll, D. Micromagnetic theory of the pinning of domain walls at phase boundaries. *Physica B: Condensed Matter* **319,** 122–126 (2002).

54. Durst, K., Kronmuller, H. & Ervens, W. Investigations of the Magnetic Properties and Demagnetization Processes of an Extremely High Coercive Sm (Co , Cu , Fe , Zr) 7.6 Permanent Magnet I. Determination of Intrinsic Magnetic Material Parameters. *Physica Status Solidi (a)* **403,** 403–416 (1988).

55. Scholz, W. *et al.* Micromagnetic simulation of the pinning and depinning process in permanent magnets. *IEEE Transactions on Magnetics* **39,** 2920–2922 (Sept. 2003).

56. Strnat, K., Hoffer, J., Olson, J., Ostertag, W. & Becker, J. J. A Family of New Cobalt-Base Permanent Magnet Materials. *Journal of Applied Physics* **38,** 1001 (1967).

57. Buschow, K. H. & van der Goot, A. Intermetallic compounds in the system samarium-cobalt. *Journal of the Less-Common Metals* **14,** 323–328 (1967).

58. Schneider, G., Henig, E.-T., Lukas, H. L. & Petzow, G. Phase-relations in the Samarium-poor Sm-Co-Fe system. *Journal of Less-Common Metals* **110,** 159–170 (1985).

59. Perry, A. J. The constitution of copper-hardened samarium-cobalt permanent magnets. *Journal of the Less Common Metals* **51,** 153–162 (1977).

60. Derkaoui, S., Allibert, C. H., Delannay, F. & Laforest, J. The influence of zirconium on Sm(Co, Fe, Cu, Zr)7.2 alloys for permanent magnets II: Composition and lattice constants of the phases in heat-treated materials. *Journal of The Less-Common Metals* **136,** 75–86 (1987).

61. Williams, K. L., Bartlett, R. W. & Jorgensen, P. J. Contribution to the samarium-cobalt phase diagram. *Journal of Less-Common Metals* **37,** 174–176 (1974).

62. Khan, Y. A Contribution to the Sm-Co Phase Diagram. *Acta Crystallographica Section B: Structural Science, Crystal Engineering and Materials§* **B,** 861–864 (1974).

63. Yuan, Y., Delsante, S., Yi, J. & Borzone, G. A revision of the Sm-rich region of the Sm-Co system. *Journal of Alloys and Compounds* **508,** 309–314 (2010).

64. Yuan, Y., Yi, J., Borzone, G. & Watson, A. Thermodynamic modeling of the CoSm system. *Calphad: Computer Coupling of Phase Diagrams and Thermochemistry* **35,** 416–420 (2011).

65. Tawara, Y. & Strnat, K. Rare Earth-Cobalt Permanent Magnets Near 2-17 Composition. *IEEE Transactions on Magnetics* **12,** 954–958 (1976).

66. Kumar, K. RETM5 and RE2TM17 permanent magnets development. *Journal of Applied Physics* **63** (1988).

67. Ray, A. E. Metallurgical behavior of Sm(Co,Fe,Cu,Zr)z alloys. *Journal of Applied Physics* **55,** 2094–2096 (1984).

68. Senno, H. & Tawara, Y. Magnetic properties of Sm-Co-Fe-Cu alloys for permanent magnet materials. *Japanese Journal of Applied Physics* **1619** (1975).

69. Hori, T., Ojima, T., Tomizawa, S. & Yoneyama, T. Magnetic Properties Of a New Type of Rare-Earth Cobalt Magnets Sm2(Co, Cu, Fe, M)17. *IEEE Transactions on Magnetics* **2,** 13–15 (1977).

70. Nagel, H. & Menth, A. Hard magnetic properties of Sm-Co-Cu-Fe single phase 2-17 bulk samples. *IEEE Transactions on Magnetics* **12,** 59–61 (1976).

71. Fidler, J. Coercivity of Precipitation Hardened Cobalt Rare Earth 17:2 Permanent Magnets. *Journal of Magnetism and Magnetic Materials* **30,** 58–70 (1982).

72. Perry, A. & Menth, A. PERMANENT-MAGNETS BASED ON SM(CO,CU,FE)Z. *IEEE Transactions on Magnetics* **11,** 1423–1425 (1975).

73. Tang, W., Zhang, Y. & Hadjipanayis, G. C. Microstructure and magnetic properties of Sm(Co bal, Fe x, Cu 0.128, Zr 0.02)(7.0) magnets with Fe substitution. *Journal of Magnetism and Magnetic Materials* **221,** 268–272 (2000).

74. Mishra, R. K., Thomas, G., Yoneyama, T., Fukuno, A. & Ojima, T. Microstructure and properties of step aged rare earth alloy magnets. *Journal of Applied Physics* **52,** 2517–2519 (1981).

75. Maury, C., Rabenberg, L. & Allibert, C. H. Genesis of the cell microstructure in the Sm(Co, Fe, Cu, Zr) permanent magnets with 2:17 type. *Physica Status Solidi (a)* **140,** 57–72 (Nov. 1993).

76. Fidler, J., Skalicky, P. & Rothwarf, F. High resolution electron microscope study of Sm(Co, Fe, Cu, Zr)7.5magnets. *IEEE Transactions on Magnetics* **M,** 2041–2043 (1983).

77. Hadjipanayis, G. & Tang, W. High temperature 2:17 magnets: relationship of magnetic properties to microstructure and processing. *Magnetics, IEEE ...* **36,** 3382–3387 (2000).

78. Kronmüller, H., Durst, K., Ervens, W. & Fernengel, W. Micromagnetic analysis of precipitation hardened permanent magnets. *IEEE Transactions on Magnetics* **20,** 1569–1571 (1984).

79. Rabenberg, L., Mishra, R. K. & Thomas, G. Microstructures of precipitation-hardened SmCo permanent magnets. *Journal of Applied Physics* **53,** 2389–2391 (1982).

80. Tang, W., Zhang, Y. & Hadjipanayis, G. C. Effect of Zr on the microstructure and magnetic properties of Sm(Co bal, Fe 0.1, Cu 0.088, Zr x)8.5 magnets. *Journal of Applied Physics* **87,** 399 (2000).

81. Feng, H., Chen, H., Guo, Z., Yu, R. & Li, W. Twinning structure in Sm(Co,Fe,Cu,Zr)z permanent magnet. *Intermetallics* **18,** 1067–1071 (2010).

82. Arinicheva, O. A., Lileev, A. S., Reissner, M., Kubel, F. & Dormidontov, A. G. Effect of Homogenization Temperature on the Structure and Properties of Sintered Magnets Based on Sm(Co, Fe, Cu, Zr) z. *Metal Science and Heat Treatment* **56,** 595–598 (2015).

83. Romero, S. A., De Campos, M. F., De Castro, J. A., Moreira, A. J. & Landgraf, F. J. G. Microstructural changes during the slow-cooling annealing of nanocrystalline SmCo 2:17 type magnets. *Journal of Alloys and Compounds* **551,** 312–317 (2013).

84. Xiong, X. *et al.* The microstructure of sintered Sm(Co0.72Fe0.20Cu0.055Zr0.025)7.5 permanent magnet studied by atom probe. *Acta Materialia* **52,** 737–748 (2004).

85. Buschow, K. H. J. & van der Goot, a. S. Composition and crystal structure of hexagonal Cu-rich rare earth–copper compounds. *Acta Crystallographica Section B Structural Crystallography and Crystal Chemistry* **27,** 1085–1088 (1971).

86. Hadjipanayis, G. C. Magnetic hardening in Zr-substituted 2 : 17 rare-earth permanent magnets. *Journal of Applied Physics* **55,** 2091–2093 (1984).

87. Gopalan, R., Ohkubo, T. & Hono, K. Identification of the cell boundary phase in the isothermally aged commercial Sm(Co0.725Fe0.1Cu0.12Zr 0.04)7.4 sintered magnet. *Scripta Materialia* **54,** 1345–1349 (2006).

88. Goll, D., Stadelmaier, H. H. & Kronmuller, H. Samarium-cobalt 2:17 magnets: Analysis of the coercive field of Sm 2(CoFeCuZr)17 high-temperature permanent magnets. *Scripta Materialia* **63,** 243–245 (2010).

89. Lectard, E., Allibert, C. H. & Ballou, R. Saturation magnetization and anisotropy fields in the Sm(Co1-xCux)5 phases. *Journal of Applied Physics* **75,** 6277 (1994).

90. Durst, K., Kronmuller, H. & Ervens, W. Investigations of the Magnetic Properties and Demagnetization Processes of an Extremely High Coercive Sm(Co, Cu, Fe, Zr)7.6 Permanent Magnet II. The Coercivity Mechanism). *Physica Status Solidi (a)* **705,** 705–719 (1988).

91. Liu, J. F., Ding, Y. & Hadjipanayis, G. C. Effect of iron on the high temperature magnetic properties and microstructure of Sm(Co, Fe, Cu, Zr)z permanent magnets. *Journal of Applied Physics* **85,** 1670–1674 (1999).

92. Tang, W., Zhang, Y., Hadjipanayis, G. C. & Kronmüller, H. Influence of Zr and Cu content on the microstructure and coercivity in Sm(Co bal, Fe 0.1, Cu y, Zr x)8.5 magnets. *Journal of Applied Physics* **87,** 5308 (2000).

93. Liu, J., Zhang, Y. & Hadjipanayis, G. *High-temperature magnetic properties and microstructural analysis of Sm(Co,Fe,Cu,Zr)z permanent magnets* 1999.

94. Chen, C. H. *et al.* Magnetic pinning strength for the new Sm-TM for use up to 550°C. *Journal of Applied Physics* **87,** 6719 (2000).

95. Liu, S., Yang, J., Doyle, G. & Knhl, G. E. New Sintered High Temperature Sm-Co Based Permanent Magnet Materials. *IEEE Transactions on Magnetics* **35,** 3325–3327 (1999).

96. Lewis, L. H. & Jiménez-Villacorta, F. Perspectives on Permanent Magnetic Materials for Energy Conversion and Power Generation. *Metallurgical and Materials Transactions A* **44,** 2–20 (2013).

97. Zhu, Z. Q. & Howe, D. Electrical Machines and Drives for Electric, Hybrid, and Fuel Cell Vehicles. *Proceedings of the IEEE* **95,** 746–765 (2007).

98. McCallum, R., Lewis, L., Skomski, R., Kramer, M. & Anderson, I. Practical Aspects of Modern and Future Permanent Magnets. *Annual Review of Materials Research* **44,** 451–477 (2014).

99. Liu, J. F. & Walmer, M. H. Thermal stability and performance data for SmCo 2:17 high-temperature magnets on PPM focusing structures. *IEEE Transactions on Electron Devices* **52,** 899–902 (2005).

100. Chen, C. H. *et al.* Sm2(Co,Fe,Cu,Zr)17 magnets for use at temperature above 400 °C. *Journal of Applied Physics* **83,** 6706 (1998).

101. Liu, H., Chow, L. & Wu, T. *Design of a Permanent Magnet Motor with Wide Temperature Range* in *Industrial Electronics Society, IECON 2015 - 41st Annual Conference of the IEEE* (2015), 3816–3820.

102. Liu, S. & Hoffman, E. P. Application-Oriented Characterization of Sm,(Co,Fe,Cu,Zr)l, Permanent Magnets. *IEEE Transactions on Magnetics* **32,** 5091 (1996).

103. Fingers, R. & Rubertus, C. Application of high temperature magnetic materials. *IEEE Transactions on Magnetics* **36,** 3373–3375 (2000).

104. Chen, C. H., Walmer, M. S., Walmer, M. H., Liu, S. & Kuhl, G. E. Thermal stability of Sm-Tm high temperature magnets at 300-550°C. *IEEE Transactions on Magnetics* **36,** 3291–3293 (2000).

105. Tariq, A. R., Nino-Baron, C. E. & Strangas, E. G. Consideration of magnet materials in the design of PMSMs for HEVs application. *IEEE Power and Energy Society General Meeting,* 1–6 (2011).

106. Ma, B. M., Liang, Y. L. & Bounds, C. O. The effects of intrinsic coercivity on the thermal stability of Sm(Co0.70Fe0.21Cu0.06Zr0.03)7.6 sintered magnets up to 450 °C. *Journal of Applied Physics* **81,** 5612–5614 (1997).

107. Chen, C. H., Walmer, M. H., Kottcamp, E. H. & Gong, W. Surface reaction and Sm depletion at 550 °C for high temperature Sm-Tm magnets. *IEEE Transactions on Magnetics* **37,** 2531–2533 (2001).

108. Zhu, Z. Q., Ng, K., Schofield, N. & Howe, D. Improved analytical modelling of rotor eddy current loss in brushless machines equipped with surface-mounted permanent magnets. *IEEE Proceedings: Electric Power Applications* **151,** 641–650 (2004).

109. Liu, J. F., Zhang, Y., Dimitrov, D. & Hadjipanayis, G. C. Microstructure and high temperature magnetic properties of Sm(Co, Cu, Fe, Zr)z(z=6.7-9.1) permanent magnets. *Journal of Applied Physics* **85,** 2800 (1999).

110. Kardelky, S. *et al.* Corrosion behavior of Sm-Co-based permanent magnets in oxidizing environments. *IEEE Transactions on Magnetics* **40,** 2931–2933 (2004).

111. Pragnell, W. M., Williams, A. J. & Evans, H. E. The oxidation of SmCo magnets. *Journal of Applied Physics* **103,** 127–130 (2008).

112. Yang, Z. *et al.* The mechanism of high temperature oxidation of a SmCo-based magnetic alloy. *Corrosion Science* **61,** 72–82 (2012).

113. Yang, Z., Peng, X., Guo, Z., Li, W. & Wang, F. Internal oxidation of Sm(CobalFe0.22Cu0.08Zr0.02)7.5 alloy at 700°C. *Corrosion Science* **70,** 260–267 (2013).

114. Wang, X. *et al.* High temperature oxidation and its induced coercivity loss of a 2:17 type SmCo-based magnet. *Journal of Applied Physics* **117,** 1–11 (2015).

115. Wang, Q., Zheng, L., An, S., Zhang, T. & Jiang, C. Thermal stability of surface modified Sm2Co17-type high temperature magnets. *Journal of Magnetism and Magnetic Materials* **331,** 245–249 (2013).

116. Bernard-Granger, G., Benameur, N., Guizard, C. & Nygren, M. Influence of graphite contamination on the optical properties of transparent spinel obtained by spark plasma sintering. *Scripta Materialia* **60,** 164–167 (2009).

117. Bertrand, A. *et al.* A comprehensive study of the carbon contamination in tellurite glasses and glass-ceramics sintered by spark plasma sintering (SPS). *Journal of the American Ceramic Society* **97,** 163–172 (2014).

118. Frage, N. *et al.* Effect of the spark plasma sintering (SPS) parameters and LiF doping on the mechanical properties and the transparency of polycrystalline Nd-YAG. *Ceramics International* **38,** 5513–5519 (2012).

119. Morita, K., Kim, B.-n., Yoshida, H. & Hiraga, K. Densification behavior of a fine-grained MgAl 2 O 4 spinel during spark plasma sintering (SPS). *Scripta Materialia* **63,** 565–568 (2010).

120. Morita, K., Kim, B.-N., Yoshida, H., Hiraga, K. & Sakka, Y. Spectroscopic study of the discoloration of transparent MgAl2O4 spinel fabricated by spark-plasma-sintering (SPS) processing. *Acta Materialia* **84,** 9–19 (2015).

121. Tian, J., Zhang, S., Qu, X., Akhtar, F. & Tao, S. Behavior of residual carbon in Sm (Co, Fe, Cu, Zr)z permanent magnets. *Journal of Alloys and Compounds* **440,** 89–93 (2007).

122. Gong, W. Comparison on the magnetic and structural properties of Sm (Co 0.67-x, Fe 0.25, Cu 0.06, Zr 0.02, C x)8.0, where x = 0–0.15, melt spun ribbons and cast alloys. *Journal of Applied Physics* **4657,** 6–9 (2008).

123. Moore, M., Roth, S., Gebert, A., Schultz, L. & Gutfleisch, O. The effect of surface grain reversal on the AC losses of sintered Nd-Fe-B permanent magnets. *Journal of Magnetism and Magnetic Materials* **375,** 43–48 (2015).

124. Aoyama, Y., Miyata, K. & Ohashi, K. Simulations and experiments on eddy current in Nd-Fe-B magnet. *IEEE Transactions on Magnetics* **41,** 3790–3792 (2005).

125. Jassal, a., Polinder, H. & Ferreira, J. Literature survey of eddy-current loss analysis in rotating electrical machines. *IET Electric Power Applications* **6,** 743 (2012).

126. Duffin, W. J. *Electricity and Magnetism: Second Edition* 2nd, 423 (McGraw-Hill book Company Ltd., Maidenhead, 1973).

127. Guangliang, X. *et al.* Influence of Fe Content on Magnetic Properties of High Temperature Rare Earth Permanent Magnets Sm(CobalFexCu0.1Zr0.03)7.5(x=0.09–0.21). *Rare Metal Materials and Engineering* **37,** 396–399 (2008).

128. Gabay, A. M., Marinescu-jasinski, M., Liu, J. & Hadjipanayis, G. C. Internally Segmented Nd-Fe-B / CaF2 Sintered Magnets. *IEEE Transactions on Magnetics* **49,** 558–561 (2013).

129. Kara, H. *et al. Lanthanide Resources and Alternatives* tech. rep. March (2010), 64.

130. Kim, J. Y., Kwon, H. W., Lee, J. G. & Yu, J. H. Decomposition of DyF3 and its effect on magnetic performance of DyF3-doped Nd-Fe-B-type hot-deformed magnet. *Journal of Applied Physics* **117** (2015).

131. Ruoho, S., Haavisto, M., Takala, E., Santa-Nokki, T. & Paju, M. Temperature Dependence of Resistivity of Sintered Rare-Earth Permanent-Magnet Materials. *IEEE Transactions on Magnetics* **46,** 15–20 (Jan. 2010).

132. Gutfleisch, O., Verdier, M., Harris, I. R. & Ray, A. E. Characterisation of Rare Earth-Transition Metal Alloys with Resistivity Measurements. *IEEE Transactions on Magnetics* **29,** 2–4 (1993).

133. Li, W. *et al.* Effect of CaF2 Addition on the Microstructure and Magnetic and Electrical Properties of Sintered Nd-Fe-B Magnets. *IEEE Transactions on Magnetics* **50,** 1–4 (2014).

134. Pan, W., Li, W., Cui, L., Li, X. & Guo, Z. Rare earth magnets resisting eddy currents. *IEEE Transactions on Magnetics* **35,** 3343–3345 (1999).

135. Komuro, M., Satsu, Y., Enomoto, Y. & Koharagi, H. High electrical resistance hot-pressed NdFeB magnet for low loss motors. *Applied Physics Letters* **91** (2007).

136. Zheng, L., Li, W., Zhu, M., Ye, L. & Bi, W. Microstructure, magnetic and electrical properties of the composite magnets of Nd–Fe–B powders coated with silica layer. *Journal of Alloys and Compounds* **560,** 80–83 (May 2013).

137. Zheng, L. *et al.* Microstructure and properties of the composite magnets fabricated with Nd-Fe-B powders coated with CaF2. *Journal of Applied Physics* **709,** 2012–2015 (2014).

138. Zheng, L. *et al. Nd 2 Fe 14 B / CaF 2 Composite Magnet Synthesized by Liquid-Phase Coating* in *IEEE Transactions on Magnetics* **51** (IEEE transactions on magnetics, Beijing, PEOPLES R CHINA, 2015), 8–11.

139. Imaoka, N. *et al.* High electrical resistance composite magnets of Sm2Fe17N3 powders coated with ferrite layer for high frequency applications. *Journal of Applied Physics* **103,** 07E129 (2008).

140. Liu, Q., Zhang, L., Dong, X., Xu, F. & Komuro, M. Increased coercivity in sintered Nd-Fe-B magnets with NdF3 additions and the related grain boundary phase. *Scripta Materialia* **61,** 1048–1051 (2009).

141. Liu, Q. *et al.* Dysprosium Nitride-Modified Sintered Nd–Fe–B Magnets with Increased Coercivity and Resistivity. *Japanese Journal of Applied Physics* **49,** 093001 (2010).

142. Sawatzki, S., Dirba, I., Wendrock, H., Schultz, L. & Gutfleisch, O. Diffusion processes in hot-deformed Nd-Fe-B magnets with DyF3 additions. *Journal of Magnetism and Magnetic Materials* **358-359,** 163–169 (2014).

143. Zheng, L. *et al.* Microstructure and Properties of Die-Upset Nd-Fe-B Dy2O3 Composite Magnets. *IEEE Transactions on Magnetics* **49,** 3368–3371 (2013).

144. Gabay, A., Marinescu-Jasinski, M., Li, W. F., Liu, J. F. & Hadjipanayis, G. C. Nanocrystalline SmCo5 magnets with laminated structure and increased electrical resistivity. *Journal of Applied Physics* **109,** 07A719 (2011).

145. Gabay, A., Marinescu-Jasinski, M., Chinnasamy, C., Liu, J. & Hadjipanayis, G. Eddy-current-resistant SmCo5/CaF2 magnets produced via high-energy milling in polar and non-polar liquids. *Journal of Magnetism and Magnetic Materials* **324,** 2879–2884 (Sept. 2012).

146. Zheng, L., Cui, B., Zhao, L., Li, W. & Hadjipanayis, G. C. A novel route for the synthesis of CaF2-coated SmCo5 flakes. *Journal of Alloys and Compounds* **549,** 22–25 (2013).

147. Wang, Z. *et al.* Enhanced Electric Resistivity of Die-Upset Magnets By Segmented NdF3 Addition. *IEEE Transactions on Magnetics* **50,** 10–12 (2014).

148. German, R. M. *Sintering Theory and Practice* 550 (John Wiley and Sons, New York, 1996).

149. German, R. M. History of sintering: empirical phase. *Powder Metallurgy* **56,** 117–123 (2013).

150. Frenkel, J. Viscous Flow of crystalline bodies under the action of surface tension. *Journal of Physics: Condensed Matter* **9,** 385–395 (1945).

151. Kuczynski, G. Self-Diffusion In Sintering Of Metallic Particles. *Transactions of the American Institute of Mining and Metallurgical Engineers* **185,** 169–178 (1949).

152. Ashby, M. A first report on sintering diagrams. *Acta Metallurgica* **22,** 275–289 (1974).

153. Garay, J. Current-Activated, Pressure-Assisted Densification of Materials. *Annual Review of Materials Research* **40,** 445–468 (June 2010).

154. Garay, J. E., Anselmi-Tamburini, U. & Munir, Z. A. Enhanced growth of intermetallic phases in the Ni-Ti system by current effects. *Acta Materialia* **51,** 4487–4495 (2003).

155. Olevsky, E. A. Theory of sintering: from discrete to continuum. *Materials Science and Engineering: R: Reports* **23,** 41–100 (1998).

156. Duval, D. A. A. L. *Article of fused metallic oxide and process of producing the same* 1922.

157. Lenel, F. RESISTANCE SINTERING UNDER PRESSURE. *TRANSACTIONS OF THE AMERICAN INSTITUTE OF MINING AND METALLURGICAL ENGINEERS* **203,** 158–167 (1955).

158. Inoue, K. *Method of electrically sintering discrete bodies* 1967.

159. Goetzel, C. & de Marchi, V. Electrically Activated Pressure Sintering (Spark Sintering) of Titanium Powders. *Powder Metallurgy International* **3,** 80–87 (1971).

160. Munir, Z. A., Anselmi-Tamburini, U. & Ohyanagi, M. The effect of electric field and pressure on the synthesis and consolidation of materials: A review of the spark plasma sintering method. *Journal of Materials Science* **41,** 763–777 (2006).

161. Black, J. Electromigration—A brief survey and some recent results. *Electron Devices, IEEE Transactions on* **16,** 338–347 (1969).

162. Blech, I. A. Electromigration in thin aluminum films on titanium nitride. *Journal of Applied Physics* **47,** 1203–1208 (1976).

163. Ho, P. S. & Kwok, T. Electromigration in metals. *Reports on progress in physics* **52,** 301–3482 (1989).

164. Bertolino, N., Garay, J. & Munir, Z. A. Electromigration effects in Al-Au multilayers. *Scripta Materialia* **44,** 737–742 (2001).

165. Friedman, J. R., Garay, J. E., Anselmi-Tamburini, U. & Munir, Z. A. Modified interfacial reactions in Ag-Zn multilayers under the influence of high DC currents. *Intermetallics* **12,** 589–597 (2004).

166. Wang, C. H., Kuo, C. Y., Chen, H. H. & Chen, S. W. Effects of current density and temperature on Sn/Ni interfacial reactions under current stressing. *Intermetallics* **19,** 75–80 (2011).

167. Chen, C.-m. & Chen, S.-w. Electic Current Effects on Sn-Ag Interfacial Reaction. *Journal of Electronic M* **28,** 902–906 (1999).

168. Frei, J. M., Anselmi-Tamburini, U. & Munir, Z. A. Current effects on neck growth in the sintering of copper spheres to copper plates by the pulsed electric current method. *Journal of Applied Physics* **101** (2007).

169. Munir, Z. a., Quach, D. V. & Ohyanagi, M. Electric Current Activation of Sintering: A Review of the Pulsed Electric Current Sintering Process. *Journal of the American Ceramic Society* **94,** 1–19 (Jan. 2011).

170. Orrù, R., Licheri, R., Locci, A. M., Cincotti, A. & Cao, G. Consolidation/synthesis of materials by electric current activated/assisted sintering. *Materials Science and Engineering: R: Reports* **63,** 127–287 (Feb. 2009).

171. Stanciu, L. a., Kodash, V. Y. & Groza, J. R. Effects of heating rate on densification and grain growth during field-assisted sintering of α-Al2O3 and MoSi2 powders. *Metallurgical and Materials Transactions A* **32,** 2633–2638 (2001).

172. Rathel, J., Herrmann, M. & Beckert, W. Temperature distribution for electrically conductive and non-conductive materials during Field Assisted Sintering (FAST). *Journal of the European Ceramic Society* **29,** 1419–1425 (2009).

173. Weston, N. S., Derguti, F., Tudball, A. & Jackson, M. Spark plasma sintering of commercial and development titanium alloy powders. *Journal of Materials Science* **50,** 4860–4878 (2015).

174. Zhou, Y., Hirao, K., Yamauchi, Y. & Kanzaki, S. Densification and grain growth in pulse electric current sintering of alumina. *Journal of the European Ceramic Society* **24,** 3465–3470 (Jan. 2004).

175. Shen, Z., Johnsson, M., Zhao, Z. & Nygren, M. Spark plasma sintering of alumina. *Journal of the American Ceramic Society* **85,** 1921–1927 (2002).

176. Mamedov, V. Spark plasma sintering as advanced PM sintering method. *Powder Metallurgy* **45,** 322–328 (2002).

177. Omori, M. Sintering, consolidation, reaction and crystal growth by the spark plasma system (SPS). *Materials Science and Engineering A* **287,** 183–188 (2000).

178. Bonifacio, C. S., Holland, T. B. & Van Benthem, K. Evidence of surface cleaning during electric field assisted sintering. *Scripta Materialia* **69,** 769–772 (2013).

179. Hulbert, D. M. *et al.* The absence of plasma in "spark plasma sintering". *Journal of Applied Physics* **104** (2008).

180. Hulbert, D. M., Anders, A., Andersson, J., Lavernia, E. J. & Mukherjee, A. K. A discussion on the absence of plasma in spark plasma sintering. *Scripta Materialia* **60,** 835–838 (2009).

181. Saunders, T., Grasso, S. & Reece, M. J. Plasma formation during electric discharge (50V) through conductive powder compacts. *Journal of the European Ceramic Society* **35,** 871–877 (2014).

182. Hitchcock, D., Livingston, R. & Liebenberg, D. Improved understanding of the spark plasma sintering process. *Journal of Applied Physics* **117,** 1–6 (2015).

183. Anselmi-Tamburini, U., Garay, J. E. & Munir, Z. A. Fundamental investigations on the spark plasma sintering/synthesis process - II. Modeling of current and temperature distributions. *Materials Science and Engineering A* **407,** 24–30 (2005).

184. Xie, G. *et al.* Frequency effect on pulse electric current sintering process of pure aluminum powder. *Materials Science and Engineering A* **359,** 384–390 (2003).

185. Anselmi-Tamburini, U. *et al.* Spark plasma sintering and characterization of bulk nanostructured fully stabilized zirconia: Part I. Densification studies. *Journal of Materials Research* **19,** 3263–3269 (2004).

186. Anselmi-Tamburini, U., Garay, J. E. & Munir, Z. A. Fundamental investigations on the spark plasma sintering/synthesis process - III. Current effect on reactivity. *Materials Science and Engineering A* **407,** 24–30 (2005).

187. Garay, J. E., Glade, S. C., Anselmi-Tamburini, U., Asoka-Kumar, P. & Munir, Z. A. Electric current enhanced defect mobility in Ni3Ti intermetallics. *Applied Physics Letters* **85,** 573–575 (2004).

188. Trzaska, Z. & Monchoux, J. P. Electromigration experiments by spark plasma sintering in the silver-zinc system. *Journal of Alloys and Compounds* **635,** 142–149 (2015).

189. Song, X., Liu, X. & Zhang, J. Neck formation and self-adjusting mechanism of neck growth of conducting powders in spark plasma sintering. *Journal of the American Ceramic Society* **89,** 494–500 (2006).

190. Yue, M., Zhang, J., Tian, M. & Liu, X. B. Microstructure and magnetic properties of isotropic bulk Nd[sub x]Fe[sub 94-x]B[sub 6] (x=6,8,10) nanocomposite magnets prepared by spark plasma sintering. *Journal of Applied Physics* **99,** 08B502 (2006).

191. Shongwe, M. *et al.* Effect of starting powder particle size and heating rate on spark plasma sintering of FeNi alloys. *Journal of Alloys and Compounds* **678,** 241–248 (2016).

192. Olevsky, E. A., Kandukuri, S. & Froyen, L. Consolidation enhancement in spark-plasma sintering: Impact of high heating rates. *Journal of Applied Physics* **102** (2007).

193. Zhang, Z. H., Wang, F. C., Wang, L. & Li, S. K. Ultrafine-grained copper prepared by spark plasma sintering process. *Materials Science and Engineering A* **476,** 201–205 (2008).

194. Onoda, G. Y. & Toner, J. Fractal Dimensions of Model Particle Packings Having Multiple Generations of Agglomerates. *Communications of the American Ceramic Society* **69,** 278–279 (1986).

195. Anselmi-Tamburini, U., Garay, J. E. & Munir, Z. A. Fast low-temperature consolidation of bulk nanometric ceramic materials. *Scripta Materialia* **54,** 823–828 (2006).

196. Xie, G. *et al. Effect of Interface Behavior between Particles on Properties of Pure Al Powder Compacts by Spark Plasma Sintering.* 2001.

197. Grasso, S., Sakka, Y. & Maizza, G. Pressure Effects on Temperature Distribution during Spark Plasma Sintering with Graphite Sample. *Materials Transactions* **50,** 2111–2114 (2009).

198. Constantinides, S. *A Manufacturing and Performance Comparison Between Bonded and Sintered Permanent Magnets* tech. rep. (Arnold Magnetic Technologies, 2006), 54.

199. Hadfield, D. History of the Development of Sintered Permanent Magnets. *Powder Metallurgy* **22,** 132–138 (1979).

200. Chen, Y. C. *et al.* Unique high-temperature performance of highly condensed MnBi permanent magnets. *Scripta Materialia* **107,** 131–135 (2015).

201. Lu, Q., Zhou, C. & Yue, M. Enhanced Magnetic Properties and Thermal Stability of Nd2Fe14B/SmCo5 Composite Permanent Magnets Prepared by Spark Plasma Sintering. *IEEE Transactions on Magnetics* **51,** 14 (2015).

202. Rama Rao, N. *et al.* Structural and magnetic studies on spark plasma sintered SmCo5/Fe bulk nanocomposite magnets. *Journal of Magnetism and Magnetic Materials* **312,** 252–257 (May 2007).

203. Su, K. P. *et al.* A feasible approach for preparing remanence enhanced NdFeB based permanent magnetic composites. *Journal of Applied Physics* **109,** 2–5 (2011).

204. Saito, T. Magnetic properties of anisotropic Sm-Fe-N bulk magnets produced by spark plasma sintering method. *Journal of Magnetism and Magnetic Materials* **320,** 1893–1897 (2008).

205. Saito, T. & Kikuchi, K. Production of Sm–Fe–N bulk magnets by the spark plasma sintering method with dynamic compression. *Journal of Alloys and Compounds* **673,** 195–198 (2016).

206. Yue, M., Zhang, J., Xiao, Y., Wang, G. & Li, T. New Kind of NdFeB Magnet Prepared by Spark Plasma Sintering. *IEEE Transactions on Magnetics* **39,** 3551–3553 (2003).

207. Saito, T., Takeuchi, T. & Kageyama, H. Production of Bulk Amorphous and Nanocomposite Sintering Method. *IEEE Transactions on Magnetics* **40,** 2880–2882 (2004).

208. Yue, M. *et al.* Microstructure and magnetic properties of anisotropic Nd–Fe–B magnets produced by spark plasma sintering technique. *Materials Science and Engineering: B* **131,** 18–21 (2006).

209. Liu, Z. W. *et al.* Microstructure and property evolution of isotropic and anisotropic NdFeB magnets fabricated from nanocrystalline ribbons by spark plasma sintering and hot deformation. *Journal of Physics D: Applied Physics* **44,** 025003 (2010).

210. Liu, Y. *et al.* Magnetic properties and microstructure studies of hot-deformed Nd-Fe-B magnets with Zr addition. *IEEE Transactions on Magnetics* **46,** 2566–2569 (2010).

211. Wuest, H., Bommer, L., Weissgaerber, T. & Kieback, B. Magnetic and structural properties of spark plasma sintered nanocrystalline NdFeB-powders. *Journal of Magnetism and Magnetic Materials* **392,** 74–78 (2015).

212. Saito, T., Sajima, Y. & Nishio-Hamane, D. Enhancement of magnetic properties by Zn addition in Nd-Fe-B hot-deformed magnets produced by spark plasma sintering method. *Journal of Alloys and Compounds* **687,** 662–666 (2016).

213. Hu, Z. H., Dong, H., Ma, D. W. & Luo, C. Enhanced magnetic and mechanical properties of die-upset Nd-Fe-B magnets prepared by spark plasma sintering via alloy powder blends. *Journal of Magnetism and Magnetic Materials* **401,** 169–172 (2016).

214. Zagar, K., Kocjan, A. & Kobe, S. Magnetic and microstructural investigation of high-coercivity net-shape Nd-Fe-B-type magnets produced from spark-plasma-sintered melt-spun ribbons blended with DyF3. *Journal of Magnetism and Magnetic Materials* **403,** 90–96 (2016).

215. Mo, W. *et al.* Microstructure and magnetic properties of NdFeB magnet prepared by spark plasma sintering. *Intermetallics* **15,** 1483–1488 (2007).

216. Zhang, D. T. *et al.* Nanocrystalline SmCo5 magnet synthesized by spark plasma sintering. *Journal of Applied Physics* **107,** 09A701 (2010).

217. Xu, W., Song, X., Zhang, Z. & Liang, H. Experimental and modeling studies on phase stability of nanocrystalline magnetic Sm2Co7. *Materials Science and Engineering: B* **178,** 971–976 (Sept. 2013).

218. Rama Rao, N. *et al.* Structural and magnetic studies on spark plasma sintered SmCo5/Fe bulk nanocomposite magnets. *Journal of Magnetism and Magnetic Materials* **312,** 252–257 (May 2007).

219. Todd, R. I., Zapata-Solvas, E., Bonilla, R. S., Sneddon, T. & Wilshaw, P. R. Electrical characteristics of flash sintering: Thermal runaway of Joule heating. *Journal of the European Ceramic Society* **35,** 1865–1877 (2015).

220. Yu, M., Grasso, S., Mckinnon, R., Saunders, T. & Reece, M. J. Review of flash sintering: materials, mechanisms and modelling. *Advances in Applied Ceramics* **116,** 24–60 (2017).

221. Zhang, Z., Song, X. & Xu, W. Phase evolution and its effects on the magnetic performance of nanocrystalline SmCo7 alloy. *Acta Materialia* **59,** 1808–1817 (2011).

222. An, S., Zhang, T. & Jiang, C. Evolution of phase and microstructure in anisotropic nanocrystalline SmCo6.1Si0.9 magnets. *Journal of Applied Physics* **115,** 043901 (Jan. 2014).

223. Matsumoto, H. *et al.* Microstructures and magnetic properties of spark plasma sintered Fe–Cr–Co type and Sm2Co17 type magnets. *Journal of Magnetism and Magnetic Materials* **272-276,** E1873–E1875 (May 2004).

224. Poudyal, N. & Ping Liu, J. Advances in nanostructured permanent magnets research. *Journal of Applied Physics* **46,** 043001 (Jan. 2013).

225. Nishida, Y., Endo, M. & Sakurada, S. A modeling study of domain wall pinning in magnets. *Journal of Magnetism and Magnetic Materials* **324,** 1948–1953 (2012).

226. Stoner, E. C. & Wohlfarth, E. P. A Mechanism of Magnetic Hysteresis in Heterogeneous Alloys. *Philisophical Transactions of the Royal Society of London. Series A, Mathematical and Physical Sciences* **240,** 599–642 (1948).

227. Aharoni, A. Theoretical search for domain nucleation. *Reviews of Modern Physics* **34,** 227–238 (1962).

228. Callen, E., Liu, Y. J. & Cullen, J. R. Initial magnetization, remanence, and coercivity of the random anisotropy amorphous ferromagnet. *Physical Review B* **16,** 263–270 (1977).

229. Hadjipanayis, G. C. & Gong, W. Magnetic hysteresis in melt-spun Nd-Fe-Al-B-Si alloys with high remanence. *Journal of Applied Physics* **64,** 5559–5561 (1988).

230. Nakatani, Y., Uesaka, Y. & Hayashi, N. Direct solution of the Landau-Lifshiftz-Gilbert equation for micromagnetics. *Japanese Journal of Applied Physics* **28,** 2485–2507 (1989).

231. Gabay, A. M., Lileev, A. S. & Menushenkov, V. P. Simulation of intergranular interaction in sintered magnets. *Journal of Magnetism and Magnetic Materials* **109,** 213–220 (1992).

232. Koehler, T. & Fredkin, D. Finite element methods for micromagnetics. *IEEE Transactions on Magnetics* **28,** 1239–1244 (1992).

233. Fidler, J. & Schrefl, T. Micromagnetic modelling - the current state of the art. *Journal of Physics D: Applied Physics* **33,** R135–R156 (2000).

234. Fukunaga, H. & Inoue, H. Effect of strength of intergrain exchange interaction on magnetic properties of nanocomposite magnets. *The Japanese Journal of Applied Physics Part 1 - Regular papers, Short notes & Review papers* **31,** 1347–1352 (1992).

235. Schrefl, T. Finite elements in numerical micromagnetics Part I: granular hard magnets. *Journal of Magnetism and Magnetic Materials* **207,** 45–65 (1999).

236. Rave, W., Ramstöck, K. & Hubert, A. Corners and nucleation in micromagnetics. *Journal of Magnetism and Magnetic Materials* **183,** 329–333 (1998).

237. Ulbrich, T. C. *et al.* Magnetization reversal in a novel gradient nanomaterial. *Physical Review Letters* **96,** 1–4 (2006).

238. Fredkin, D. R. & Koehler, T. R. Numerical micromagnetics: Prolate spheroids. *IEEE Transactions on Magnetics* **25,** 3473–3475 (1989).

239. Schrefl, T. & Fidler, J. Numerical simulation of magnetization reversal in hard magnetic materials using a finite element method. *Journal of Magnetism and Magnetic Materials* **111,** 105–114 (1992).

240. Bance, S. *et al.* Grain-size dependent demagnetizing factors in permanent magnets. *Journal of Applied Physics* **116,** 233903 (2014).

241. Schrefl, T., Fidler, J. & Kronmuller, H. Remanence and coercivity in isotropic nanocrystalline permanent magnets. *Physical Review B: Condense Matter and Materials Physics* **49,** 6100–6113 (1994).

242. Fischer, R., Schrefl, T., Kronmuller, H. & Fidler, J. Grain-size dependence of remanence and coercive field of isotropic nanocrystalline composite permanent magnets. *Journal of Magnetism and Magnetic Materials* **3,** 35–49 (1996).

243. Fischer, R. & Kronmüller, H. Static computational micromagnetism of demagnetization processes in nanoscaled permanent magnets. *Physical Review B* **54,** 7284–7294 (1996).

244. Fischer, R. & Kronmüller, H. The role of the exchange interaction in nanocrystalline isotropic Nd2Fe14B-magnets. *Journal of Magnetism and Magnetic Materials* **191,** 225–233 (1999).

245. Schmidts, H. F. & Kronmüller, H. Size dependence of the nucleation field of rectangular ferromagnetic parallelepipeds. *Journal of Magnetism and Magnetic Materials* **94,** 220–234 (1991).

246. Schrefl, T., Fidler, J. & Kronmüller, H. Nucleation fields of hard magnetic particles in 2D and 3D micromagnetic calculations. *Journal of Magnetism and Magnetic Materials* **138,** 15–30 (1994).

247. Yi, M., Gutfleisch, O. & Xu, B. X. Micromagnetic simulations on the grain shape effect in Nd-Fe-B magnets. *Journal of Applied Physics* **120** (2016).

248. Fidler, J. & Schrefl, T. Micromagnetic modelling of nanocrystalline magnets and structures. *Journal of Magnetism and Magnetic Materials* **203,** 28–32 (1999).

249. Kronmüller, H. Theory of Nucleation Fields in Inhomogeneous Ferromagnets. *Physica Status Solidi (B)* **144,** 385–396 (1987).

250. Kim, A. S., Camp, F. E. & Stadelmaier, H. H. Relation of remanence and coercivity of Nd,(Dy)-Fe,(Co)-B sintered permanent magnets to crystallite orientation. *Journal of Applied Physics* **76,** 6265–6267 (1994).

251. Schrefl, T., Schmidts, H. F., Fidler, J. & Kronmüller, H. Nucleation of reversed domains at grain boundaries. *Journal of Applied Physics* **73,** 6510–6512 (1993).

252. Kronmüller, H. & Goll, D. Pinning of domain walls in composite particles. *Physica B: Condensed Matter* **403,** 237–241 (2008).

253. Skomski, R., Zhou, J., Kashyap, A. & Sellmyer, D. J. Domain-wall pinning at inhomogenities of arbitrary cross-sectional geometry. *IEEE Transactions on Magnetics* **40,** 2946–2948 (2004).

254. Streibl, B., Fidler, J. & Schrefl, T. Domain wall pinning in high temperature Sm(Co, Fe, Cu, Zr)7-8 magnets. *Journal of Applied Physics* **87,** 4765 (2000).

255. Scholz, W., Fidler, J., Schrefl, T., Suess, D. & Matthias, T. Micromagnetic three-dimensional simulation of the pinning field in high temperature Sm(Co,Fe,Cu,Zr)[sub z] magnets. *Journal of Applied Physics* **91,** 8492 (2002).

256. Scholz, W., Fidler, J., Schrefl, T., Suess, D. & Matthias, T. Micromagnetic simulation of domain wall pinning in Sm(Co,Fe,Cu,Zr)z magnets. *Journal of Magnetism and Magnetic Materials* **242,** 1356–1358 (2002).

257. Chen, R.-j., Wang, J.-z. & Zhang, H.-w. Simulation of magnetization behaviours of Sm(Co, Fe, Cu, Zr)z magnet with low Cu content. *Chinese Physics B* **18,** 2582–2588 (2009).

258. Fidler, J. *et al.* Micromagnetic modelling and magnetization processes. *Journal of Magnetism and Magnetic Materials* **272-276,** 641–646 (May 2004).

259. Goll, D., Kleinschroth, I., Sigle, W. & Kronmuller, H. Melt-spun precipitation-hardened Sm-2(Co, Cu, Fe, Zr)(17) magnets with abnormal temperature dependence of coercivity. *Applied Physics Letters* **76,** 1054–1056 (2000).

260. Gabay, A. M., Tang, W., Zhang, Y. & Hadjipanayis, G. C. Anomalous temperature dependence of coercivity and reversal mechanism in bulk-hardened rare earth-cobalt magnets. *Applied Physics Letters* **78,** 1595–1597 (2001).

261. Corte-Real, M. M., De Campos, M. F., Zhang, Y., Hadjipanayis, G. C. & Liu, J. F. Coercivity analysis in Sm(CoFeCuZr)z magnets with abnormal temperature behavior. *Physica Status Solidi (A) Applied Research* **193,** 302–313 (2002).

262. Liu, J. F., Chui, T., Dimitrov, D. & Hadjipanayis, G. C. Abnormal temperature dependence of intrinsic coercivity in Sm(Co, Fe, Cu, Zr)z powder materials. *Applied Physics Letters* **73,** 3007 (1998).

263. Tang, W., Gabay, A., Zhang, Y., Hadjipanayis, G. & Kronmuller, H. Temperature dependence of coercivity and magnetization reversal mechanism in Sm(Co bal Fe 0.1 Cu y Zr 0.04)7.0 magnets. *IEEE Transactions on Magnetics* **37,** 2515–2517 (2001).

264. Rong, C.-B., Zhang, H.-W., Chen, R.-J., Shen, B.-G. & He, S.-L. Micromagnetic investigation on the coercivity mechanism of the SmCo5/Sm2Co17 high-temperature magnets. *Journal of Applied Physics* **100,** 123913 (2006).

265. Bance, S. *et al.* Thermal Activation in Permanent Magnets. *Jom* **67,** 1350–1356 (2015).

266. Atallah, K., Chin, R., Arshad, W. M. & Lendenmann, H. Rotor Eddy-Current Loss in Permanent-Magnet Brushless AC Machines. *IEEE Transactions on Magnetics* **46,** 2701–2707 (July 2010).

267. Scholz, W., Fidler, J., Schrefl, T., Suess, D. & Matthias, T. Micromagnetic three-dimensional simulation of the pinning field in high temperature Sm(Co,Fe,Cu,Zr)[sub z] magnets. *Journal of Applied Physics* **91,** 8492 (2002).

268. Livingston, J. D. & Martin, D. L. Microstructure of aged (Co,Cu,Fe)7Sm magnets. *Journal of Applied Physics* **48,** 1350–1354 (1977).

269. Howe, D., Jewell, G., Dudding, J. & Grossinger, R. Pulsed field magnetometry. *IEEE Transactions on Magnetics* **29,** 2980–2982 (1993).

270. Singh, Y. Electrical Resistivity Measurements: a Review. *International Journal of Modern Physics: Conference Series* **22,** 745–756 (2013).

271. Van der Pauw, L. J. *A method of measuring the resistivity and Hall coefficent on lamellae of arbitrary shape* 1958.

272. Ramadan, A. A., Gould, R. D. & Ashour, A. On the Van der Pauw method of resistivity measurements. *Thin Solid Films* **239,** 272–275 (1994).

273. Kasl, C. & Hoch, M. J. R. Effects of sample thickness on the van der Pauw technique for resistivity measurements. *Review of Scientific Instruments* **76,** 1–5 (2005).

274. Weiss, J. D., Kaplar, R. J. & Kambour, K. E. A derivation of the van der Pauw formula from electrostatics. *Solid-State Electronics* **52,** 91–98 (2008).

275. Koon, D. W., Bahl, A. A. & Duncan, E. O. Measurement of contact placement errors in the van der Pauw technique. *Review of Scientific Instruments* **60,** 275–276 (1989).

276. Fawcett, T. G., Needham, F., Crowder, C. & Kabekkodu, S. Advanced Materials Analyses Using the Powder Diffraction File. *Proceedings of the 10th National Conference on X-ray Diffraction and ICDD Workshop,* 1–3 (2009).

277. Mettler-Toledo. *Operating instructions for solids and liquids determination for MS-DNY-43* Greifensee, Switzerland, 2010.

278. Buschow, K. H. J., Naastepad, P. A. & Westendorp, F. F. Preparation of SmCo5 permanent magnets. *Journal of Applied Physics* **40,** 4029–4032 (1969).

279. Engqvist, H. & Uhrenius, B. Determination of the average grain size of cemented carbides. *International Journal of Refractory Metals and Hard Materials* **21,** 31–35 (2003).

280. Schneider, C. A., Rasband, W. S. & Eliceiri, K. W. NIH Image to ImageJ: 25 years of image analysis. *Nature Methods* **9,** 671–675 (2012).

281. Goldstein, J. *et al. Scanning Electron Microscopy and X-Ray Microanalysis* 3rd ed., 689 (Springer US, 2003).

282. Gazulla, M. F., Rodrigo, M., Orduña, M. & Gómez, C. M. Determination of Carbon, Hydrogen, Nitrogen and Sulfur in Geological Materials Using Elemental Analysers. *Geostandards and Geoanalytical Research* **36,** 201–217 (2012).

283. Dean, J. S., Harding, J. H. & Sinclair, D. C. Simulation of impedance spectra for a full three-dimensional ceramic microstructure using a finite element model. *Journal of the American Ceramic Society* **97,** 885–891 (2014).

284. Geuzaine, C. & Remacle, J. F. Gmsh: A 3-D finite element mesh generator with built-in pre- and post-processing facilities. *International Journal for Numerical Methods in Engineering* **79,** 1309–1331 (2009).

285. Morley, N. A., Finkel, A. C., Yang, W. & Reeves-mclaren, N. Magnetic and Structural Characterization of NiFe / Fe 30 Co 70 Bilayers. **50** (2014).

286. Hall, R. C. Single crystal anisotropy and magnetostriction constants of several ferromagnetic materials including alloys of NiFe, SiFe, AlFe, CoNi, and CoFe. *Journal of Applied Physics* **30,** 816–819 (1959).

287. Chen, Y. *et al.* Designing and tuning magnetic resonance with exchange interaction. *Advanced Materials* **27,** 1351–1355 (2015).

288. Scholtz, W. *et al.* Scalable Parallel Micromagnetic Solvers for Magnetic Nanostructures. *Computational Materials Science* **28,** 366–383 (2003).

289. Schrefl, T., Roitner, H. & Fidler, J. Dynamic micromagnetics of nanocomposite NdFeB magnets. *J. Appl. Phys.* **81,** 53–56 (1997).

290. Bokhonov, B. B. *et al.* Carbon uptake during Spark Plasma Sintering: investigation through the analysis of the carbide "footprint" in a Ni–W alloy. *RSC Adv.* **5,** 80228–80237 (2015).

291. De Campos, M. F. *et al.* A model relating remanence and microstructure of SmCo5 magnets. *Journal of Alloys and Compounds* **267,** 257–264 (1998).

292. Pyrhönen, J., Jokinen, T. & Hrabovcová, H. *Design of Rotating Electrical Machines* (John Wiley and Sons, London, 2009).

293. Mackie, A. J., Dean, J. S. & Goodall, R. Material and magnetic properties of Sm2(Co, Fe, Cu, Zr)17permanent magnets processed by Spark Plasma Sintering. *Journal of Alloys and Compounds* **770,** 765–770 (2019).

294. Eclipse Magnetics. *Samarium Cobalt Magnets, SmCo Magnets Datasheet* tech. rep. (Eclipse Magnetics, Sheffield, 2016), 6.

295. ARNOLD MAGNETIC TECHNOLOGIES. *RECOMA® 35E datasheet* tech. rep. (Arnold Magnetic Technologies, Sheffield, 2016), 2.

296. Goodall, R., Weber, L. & Mortensen, A. The electrical conductivity of microcellular metals. *Journal of Applied Physics* **100,** 044912 (2006).

297. Weber, L., Dorn, J. & Mortensen, A. On the electrical conductivity of metal matrix composites containing high volume fractions of non-conducting inclusions. *Acta Materialia* **51,** 3199–3211 (2003).

298. Weber, L., Fischer, C. & Mortensen, A. On the influence of the shape of randomly oriented, non-conducting inclusions in a conducting matrix on the effective electrical conductivity. *Acta Materialia* **51,** 495–505 (2003).

299. Gao, R., Zhang, D., Li, H. & Zhang, J. Effects of the degree of grain alignment on the hard magnetic properties of sintered NdFeB magnets. *Applied Physics A: Materials Science & Processing* **67,** 353–356 (Sept. 1998).

300. Ruwei, G., Hua, L., Shouting, J., Liangmo, M. & Meiying, Q. Investigations on magnetization reversal processes in oriented sintered Nd-Fe-B alloys. *Journal of Magnetism and Magnetic Materials* **95,** 205–212 (1991).

301. Livingston, J. D. A review of coercivity mechanisms (invited). *Journal of Applied Physics* **52,** 2544–2548 (1981).

302. Gao, R. W. *et al.* Effect of the intergrain interactions on the coercivity and its angular dependence for Nd(FeCo)B sintered magnets. *Journal of Magnetism and Magnetic Materials* **224,** 125–131 (2001).

303. Mackie, A. J., Hatton, G. D., Hamilton, H. G. C., Dean, J. S. & Goodall, R. Carbon uptake and distribution in Spark Plasma Sintering (SPS) processed Sm(Co, Fe, Cu, Zr)z. *Materials Letters* **171,** 14–17 (2016).

304. Tang, W., Zhang, Y. & Hadjipanayis, G. C. Sm(Co, Fe, Cu, Zr)z magnets fabricated by simple processing. *Applied Physics Letters* **77,** 421 (2000).

305. Yan, A., Gutfleisch, O., Gemming, T. & Müller, K. H. Microchemistry and magnetization reversal mechanism in melt-spun 2:17-type Sm-Co magnets. *Applied Physics Letters* **83,** 2208–2210 (2003).

306. Mao, S. *et al.* Evolution and effects of surface degradation layer of Sm2Co17 magnets at high temperatures. *Journal of Applied Physics* **115,** 043912 (2014).

307. Deng, X. *et al.* Phase transitions in nanocrystalline barium titanate ceramics prepared by spark plasma sintering. *Journal of the American Ceramic Society* **89,** 1059–1064 (2006).

308. Mehrizi, S. & Heydarzadeh Sohi, M. Electrical resistivity and magnetic properties of electrodeposited nanocrystalline CoFe thin films. *Journal of Materials Science: Materials in Electronics* **26,** 7381–7389 (2015).

309. ARNOLD MAGNETIC TECHNOLOGIES. *RECOMA® 28E datasheet* tech. rep. (Arnold Magnetic Technologies, Sheffield, 2014), 2.

310. Palit, M., Rajkumar, D., Pandian, S. & Kamat, S. Effect of grain size on microstructure and magnetic properties of Sm2(Co,Cu,Fe,Zr)17 permanent magnets. *Materials Chemistry and Physics* **2,** 1–9 (2016).

311. Gabay, A. M., Marinescu, M., Li, W. F., Liu, J. F. & Hadjipanayis, G. C. Dysprosium-saving improvement of coercivity in Nd-Fe-B sintered magnets by Dy2S3 additions. *Journal of Applied Physics* **109,** 6–11 (2011).

312. Komuro, M., Satsu, Y. & Suzuki, H. Increase of coercivity and composition distribution in fluoride-diffused NdFeB sintered magnets treated by fluoride solutions. *IEEE Transactions on Magnetics* **46,** 3831–3833 (2010).

313. Zheng, L. *et al.* Microstructure, magnetic properties and electrical resistivity of Nd-Fe-B / NdF 3 Composite Magnets. *IEEE Transactions on Magnetics* **50,** 1–4 (2014).

314. Scher, H. & Zallen, R. Critical density in percolation processes. *The Journal of Chemical Physics* **53,** 3759 (1970).

315. Zern, a., Seeger, M., Bauer, J. & Kronmüller, H. Microstructural investigations of exchange coupled and decoupled nanocrystalline NdFeB permanent magnets. *Journal of Magnetism and Magnetic Materials* **184,** 89–94 (1998).

316. Goll, D., Seeger, M. & Kronmüller, H. Magnetic and microstructural properties of nanocrystalline exchange coupled PrFeB permanent magnets. *Journal of Magnetism and Magnetic Materials* **185,** 49–60 (1998).

317. Grönefeld, M. & Kronmüller, H. Calculation of strayfields near grain edges in permanent magnet material. *Journal of Magnetism and Magnetic Materials* **80,** 223–228 (1989).

318. Arnold-Magnetic-Technologies. *Magnet Manufacture Process*

319. Olevsky, E. A., Bradbury, W. L., Haines, C. D., Martin, D. G. & Kapoor, D. Fundamental Aspects of Spark Plasma Sintering : I . Experimental Analysis of Scalability. *Journal of the American Ceramic Society* **95,** 2406–2413 (2012).

320. Voisin, T. *et al.* Temperature control during Spark Plasma Sintering and application to up-scaling and complex shaping. *Journal of Materials Processing Technology* **213,** 269–278 (2013).

321. Anselmi-Tamburini, U. & Groza, J. R. Critical assessment : electrical field / current application – a revolution in materials processing / sintering. *Materials Science and Technology* **33,** 1855–1862 (2017).

322. Guillon, O. *et al.* Field-assisted sintering technology/spark plasma sintering: Mechanisms, materials, and technology developments. *Advanced Engineering Materials* **16,** 830–849 (2014).